KfK 5054
Februar 1993

Results of SFD Experiment CORA-13 (OECD International Standard Problem 31)

S. Hagen, P. Hofmann, V. Noack,
G. Schanz, G. Schumacher, L. Sepold

Hauptabteilung Ingenieurtechnik
Institut für Materialforschung
Institut für Neutronenphysik und Reaktortechnik
Projekt Nukleare Sicherheitsforschung

Kernforschungszentrum Karlsruhe

Kernforschungszentrum Karlsruhe

Hauptabteilung Ingenieurtechnik
Institut für Materialforschung
Institut für Neutronenphysik und Reaktortechnik
Projekt Nukleare Sicherheitsforschung

KfK 5054

Results of SFD Experiment CORA-13 (OECD International Standard Problem 31)

S. Hagen, P. Hofmann, V. Noack, G. Schanz, G. Schumacher, L. Sepold

Kernforschungszentrum Karlsruhe GmbH, Karlsruhe

Kernforschungszentrum Karlsruhe GmbH
Postfach 3640, 7500 Karlsruhe 1

ISSN 0303-4003

Abstract

The CORA experiments carried out in an out-of-pile facility at the Kernforschungszentrum Karlsruhe (KfK), Federal Republic of Germany, are part of the international "Severe Fuel Damage" (SFD) program.

The experimental program is to provide information on the failure mechanisms of Light Water Reactor (LWR) fuel elements in a temperature range from 1200°C to 2000°C and in a few cases up to 2400°C.

In the CORA experiments two different bundle configurations are tested: PWR (Pressurized Water Reactor) and BWR (Boiling Water Reactor) bundles. The PWR-type assemblies usually consist of 25 rods with 16 electrically heated fuel rod simulators and nine unheated rods (full-pellet and absorber rods). Bundle CORA-13, a PWR-type assembly, contained two Ag/In/Cd - steel absorber rods. The test bundle was subjected to temperature transients of a slow heatup rate in a steam environment, i.e. the transient phase of the test was initiated with a temperature ramp rate of 1 K/s. The temperature escalation due to the exothermal zircaloy(Zry)-steam reaction started at about 1100 °C at an elevation of 850 mm (1000 s after onset of the transient), leading to a temperature plateau of 1850 °C and after initiation of quenching to maximum temperatures of approximately 2000°C to 2300°C. CORA-13 was terminated by quenching with water from the bottom with a flooding rate of 1 cm/s.

Rod destruction started with the failure of the absorber rod cladding at about 1200 C, i. e. about 250 K below the melting regime of steel. Penetration of the steel cladding was presumably caused by a eutectic interaction between steel and the zircaloy guide tube. As a consequence, the absorber-steel-zircaloy melt relocated radially outward and axially downward. Besides this melt relocation the test bundle experienced severe oxidation and partial melting of the cladding, fuel dissolution by Zry/UO_2 interaction, complete Inconel grid spacer destruction, and relocation of melts and fragments to lower elevations in the bundle. An extended flow blockage has formed at the axial midplane.

Quenching of the hot test bundle by water resulted, besides additional fragmentation of fuel rods and shroud, in an additional temperature increase in the upper bundle region. Coinciding with the temperature response an additional hydrogen buildup was detected. During the flooding phase 48 % of the total hydrogen were generated.

Ergebnisse des SFD-Experiments CORA-13 (Internationales OECD-Standardproblem Nr. 31)

Zusammenfassung

Die CORA-Experimente, die in einer Out-of-pile-Versuchsanlage des Kernforschungszentrums Karlsruhe (KfK) durchgeführt werden, sind Teil des internationalen Severe-Fuel-Damage-Programms (SFD) zur Untersuchung schwerer Kernschäden in Leichtwasserreaktoren.

Mit Hilfe der CORA-Versuche sollen die Versagensmechanismen von LWR-Brennelementen im Temperaturbereich von 1200°C bis 2000°C, und in einigen Fällen bis 2400°C, ermittelt werden.

In den CORA-Experimenten werden zwei verschiedene Bündeltypen getestet: DWR (Druckwasserreaktor)- und SWR (Siedewasserreaktor)-Bündel. Die DWR-Anordnung besteht üblicherweise aus 25 Stäben mit 16 elektrisch beheizten Brennstabsimulatoren und neun unbeheizten Stäben (Vollpellet-Stäbe und Absorberstäbe). Bündel CORA-13, vom Typ DWR, war mit zwei Ag/In/Cd - Stahl Absorberstäben bestückt. Das Brennstabbündel war einer Temperaturtransiente mit langsamer Aufheizrate in Dampfatmosphäre ausgesetzt. Die transiente Phase des Versuchs wurde mit einer Temperaturanstiegsrate von 1 K/s eingeleitet. Die Temperatureskalationsphase, hervorgerufen durch die exotherme Zirkaloy(Zry)-Dampf-Reaktion, begann bei etwa 1100 °C. Die maximalen Bündeltemperaturen betrugen in der transienten Phase 1850 °C, in der Flutphase 2000°C bis 2300 °C. Versuch CORA-13 wurde durch Fluten mit Wasser (quenching) mit einer Flutrate von 1 cm/s, beginnend an der Bündelunterkante, beendet.

Die Stabzerstörung begann mit dem Versagen der Absorberstabhülle bei etwa 1200 °C, d. h. ungefähr 250 K unterhalb des Schmelzbereichs von Stahl. Die Zerstörung der Stahlhülle war sicherlich durch die eutektische Wechselwirkung zwischen Stahl und dem Führungsrohr aus Zirkaloy hervorgerufen.

Als Folge dieser Wechselwirkung verlagerte sich die Absorber-Stahl-Zirkaloy-Schmelze radial nach außen und axial nach unten. Zusätzlich zur Verlagerung der Absorberschmelze erlitt das Versuchsbündel eine starke Oxidation und ein teilweises Schmelzen der Hülle, Brennstoffauflösung durch die Zry/UO_2-Wechsel-

wirkung, vollständige Zerstörung des Inconel-Abstandshalters sowie Verlagerung von Schmelzen und Bruchstücken in den unteren Teil des Bündels. Eine ausgeprägte Kühlkanalblockade hat sich in der axialen Mitte des Bündels gebildet.

Das Abschrecken des heißen Testbündels mit kaltem Wasser ergab neben einer zusätzlichen Fragmentierung von Brennstäben und Kühlmittelführungsrohr (Shroud) einen zusätzlichen Temperaturanstieg im oberen Bündelbereich. Gleichzeitig mit dieser Temperaturerhöhung wurde eine zusätzliche Wasserstoffproduktion beobachtet. Allein während der Flutphase wurden 48 % des gesamten Wasserstoffs erzeugt.

Inhaltsverzeichnis

1. Introduction

The TMI-2 accident has demonstrated that a severe fuel damage transient will not necessarily escalate to an uncontrolled core melt down accident if the design basis accident limits are exceeded. Therefore, comprehensive research programs have been initiated in various countries to investigate the relevant fuel rod bundle damage mechanisms that occur in an uncovered core, after an increase of temperature.

In the Federal Republic of Germany at the Kernforschungzentrum Karlsruhe (KfK) the Severe Fuel Damage (SFD) Program is now co-ordinated by the Project Nuclear Safety Research (PSF) as successor of Project Nuclear Safety (PNS) and LWR Safety Project Group (PRS). As part of this program, out-of-pile experiments (the CORA-Program) are being conducted at the Hauptabteilung Ingenieurtechnik (HIT). These experiments are designed to provide information on the behavior of Light Water Reactor (LWR) fuel elements under severe fuel damage (SFD) conditions, up to complete meltdown. The results of the out-of-pile experiments will also be used for the assessment of the SFD computer codes.

In the frame work of international co-operation the out-of-pile experiments are contributing confirmatory and complementary information to the results obtained from the limited number of in-pile tests. The investigation of the basic phenomena of the damage process is supported by separate-effect tests.

The most important aspects concerning fuel rod failure and subsequent core degradation are the chemical interactions amongst the fuel element components in competition with the oxidation of the cladding in steam, which causes also the temperature escalation.

The melt formation starts around 1200°C by chemical interactions of the Inconel spacer grids and absorber materials (Ag, In, Cd) for PWR with the Zircaloy cladding /1/. The dissolution of the UO_2 pellets by liquid Zircaloy starts far below the UO_2 melting point /2/.

Melt formation, relocation, blockage formation and finally fragmentation of fuel elements during reflooding characterize the degraded core and the potential of long term coolability. Furthermore the influence of internal pressure of the fuel

rods (ballooning and bursting) and external pressure of the system (solid contact between pellets and cladding) on the bundle meltdown behavior is investigated.

Finally the investigation of the influence of pre-oxidation and steam availability is included in the program.

The tests performed in the CORA-facility are listed in the test matrix (Table 1). The original test matrix was directed towards the behavior of PWR fuel elements only. In 1988 discussion showed that in most countries using nuclear energy, information on the behavior of BWRs in severe accident conditions was needed. In consequence, five planned PWR experiments were replaced by BWR tests in the revised test matrix. Also the original sequence of tests was changed, as one can see from the test numbers.

In this report test CORA-13 is discussed. CORA-13 is the second PWR test which is terminated by quenching. The first PWR quenching test CORA-12 resulted in an unexpected remarkable temperature increase in the upper part of the bundle during the quenching process. The temperature peak was caused by a strong steam-zircaloy reaction in coincidence with a peak in the hydrogen production. This behavior shows the strong influence of the Zircaloy oxidation also in the quenching process.

CORA-13 should give additional information on the increase of temperature and hydrogen production in response to the fast cooling of a hot bundle. In this test the bundle was quenched at a much higher temperature, due to the smaller lag between the time of shutdown of electrical heating and that of flooding of the bundle.

Test CORA-13 was also chosen as OECD-CSNI International Standard Problem 31 (ISP-31). This is the second Standard Problem on early phase core meltdown behaviour. It is in close relationship with the first one (ISP-28) which is based on the Phebus B9$^+$ experiment. In comparison with Phebus B9$^+$, CORA-13 contained absorber rods and was terminated by quenching from the bottom.

2. Description of the CORA test facility

The CORA out-of-pile facility is designed to investigate the behavior of LWR fuel elements under severe fuel damage accident conditions. In the experiments the decay heat is simulated by electrical heating. Great emphasis is given to the fact that the test bundles contain all materials used in light-water reactor fuel elements to investigate the different material interactions. Pellets, claddings, grid spacers, absorber rods and the pertinent guide tubes are typical of those of commercial LWRs with respect to their compositions and radial dimensions.

The CORA facility is situated within the reactor hall of the now disused FR2 reactor at the Nuclear Research Center Karlsruhe. Fig. 1 gives the simplified flow diagram of the facility. The geometrical arrangement of the different CORA components is given in Fig. 2.

The central part of the facility is the fuel rod bundle. The bundle is enclosed in a Zry-shroud with ZrO_2 fibre insulation. A high temperature radiation shield surrounds the bundle, leaving an annular space. The bundle is connected to the power supply system at its upper and lower end.

Below the bundle sits the quench unit with a water-filled quench cylinder, which can be raised towards the bundle with a controlled speed. The cylinder is guided by three rods, which also connect the electric power to the bundle lower end. At the beginning of the test the water level is 220 mm below the "zero elevation" of the bundle. The "zero elevation" corresponds to the lower end of the pellets in the heated rods.

The bundle upper end is fixed in the bundle head plate. The plate is connected by a funnel-shaped tube to the surge condenser. The surge condenser is double-walled, leaving access to the bundle end fittings above the bundle head funnel.

The steam is produced in the steam generator, superheated and guided to the lower end of the bundle, entering at "zero elevation". The steam not consumed within the bundle is condensed in two parallel condensors and the hydrogen produced is fed to the off-gas system after dilution with air to attain a low H_2 concentration.

Bundle design

The location of the bundle within the facility is shown in Figs. 3 and 4. Details of the high temperature shield are given in Figs. 5 and 6. The arrangement of the fuel rod simulators within the bundle is given in Fig. 7. Figure 8 presents the individual main components of the bundle; i.e. the heated and unheated fuel rods and the (Ag, In, Cd) absorber rods. Characteristic data of the bundle are given in Tables 2, 2a and 2b.

Fuel rod simulators

Two types of fuel rod simulators are used: electrically heated rods and unheated solid rods. Altogether 25 rods made up of 16 heated and 7 unheated rods and two absorber rods have been used. Vertical cross- sections of the rods are shown in Fig. 8. The heated fuel rod simulator is sheathed with a standard PWR Zircaloy cladding tube. The central part of the internal heater consists of a 6 mm diameter tungsten rod surrounded by UO_2 annular pellets. The tungsten heater has an effective length of 1024 mm. At the top and bottom the tungsten heater is screwed into Mo-electrodes of 300 mm length which fit directly into the Zircaloy cladding. The molybdenum electrodes are connected to copper electrodes and both are insulated from the Zircaloy cladding by a flame-sprayed ZrO_2 layer. The Zircaloy cladding is sealed to the copper electrodes by swage-lock fittings with an insulating sleeve. To the upper and lower copper electrodes flexible copper power cables are connected. The fuel rod simulator is screwed into the bundle flange from the top, sealing it hermetically. The bundle flange thus gives the fixed point for the axial thermal movement of the rod.

The unheated fuel rod simulator has the same configuration as the fuel rods in PWR-type reactors: solid UO_2 pellets inside the original Zry-4 cladding. The unheated fuel rod simulator is introduced through the bundle flange from below. At the lower end it extends to -200 mm elevation i.e. to 20 mm above the initial water level of the quench cylinder.

The two absorber rods are also made from original components. The (Ag80,In15,Cd5) absorber material is sheathed in stainless steel and this rod is surrounded by a Zry-4 guide tube. The absorber rods are connected in the same way to the bundle flange as the unheated rods.

Three spacers are used in the bundle to maintain the positions of the rods. Original PWR-type spacers have been used. The material of the middle spacer is Inconel 718. The upper and lower spacer are made of Zircaloy-4. The distances from the top end of the spacers to "zero elevation" are +880 mm, +496 mm and -5 mm.

The bundle head funnel (Fig. 3) is made of copper and is water-cooled by the double-walled outer chamber. To make the cooling more effective the space around the rods inside this chamber is filled with water. In consequence, the upper ends of the heated rods (the copper electrode inside the Zry-cladding) and the connectors for the pressure capillaries and thermocouples of the unheated rods are surrounded by water.

At the lower end the heated fuel rod simulators are cooled by the water inside the quench cylinder. The gross volume of water inside the quench cylinder (230 mm ID) amounts to about 70 l. The initial water level is at the -220 mm elevation. The electrode is made out of molybdenum from 0 to 300 mm length and the remaining part consists of copper. The electrode is flame-sprayed with a 0.2 mm thick layer of ZrO_2 and surrounded by the Zry-4 cladding. The unheated rod contacts the water of the quench cylinder only through the thermocouple connections.

The bundle is surrounded by a Zry-4 shroud of 1.2 mm thickness (Figs. 7 and 8). The shroud conducts the steam through the bundle. The steam enters at 180° into the lower end (0 mm). To minimize the heat losses from the shroud, it is surrounded by an insulating layer of ZrO_2 fibre of 19 mm (0.75 inch) thickness. Since the ZrO_2 has a low heat conductivity and heat capacity, the shroud temperature can follow the bundle temperature closely. Since the Zry shroud participates in the interaction with steam, the resulting oxidation energy contributes substantially to the bundle heat-up.

The steam inlet at 0 mm elevation is connected to the stainless steel steam distribution tube (Fig. 4 and 5). This tube extends down into the water of the quench cylinder thus forming a lower closure. The time history of the water level in the quench cylinder (Fig. 9) shows that there is no net condensation of steam in the quench cylinder.

At an elevation of 36 mm the steam distribution tube joins into the shroud. From here the shroud extends in vertical direction for 1195 mm and the insulation for 1000 mm. To protect the thermocouple compensation cables, which are laid on outside the shroud insulation, the shroud and its insulation are extended in the upward direction at 50° and 210° by 110 mm and by 305 mm, respectively.

The annuli between the shroud and the high temperature shield on one hand and the high temperature shield and pressure containment on the other hand are closed at the upper end by fibre ceramic layers of 38 mm thickness.

High-temperature shield

To keep the heat losses as low as possible, the bundle is surrounded by a high temperature shield (HTS). The vertical and the horizontal cross-sections of the high temperature shield are given in Figures 3 to 6. The high temperature shield consists mainly of ceramic fibre plates. The inner layer of plates consists of ZrO_2, and the outer one of Al_2O_3. The fibre ceramics are excellent insulators and have a low density which results in a low heat capacity. The thermal shock behaviour of the fibre ceramics is also excellent.

The mechanical strength of the high temperature shield is provided by outer walls of stainless steel (0,9 mm). The fibre ceramic plates are attached to the stainless steel cover by ceramic nails. The inner ZrO_2 layer is 38 mm thick, and the outer Al_2O_3 layer is 76 mm thick, separated by a gap of 23 mm. The distance from the inner insulation surface to the centre of the bundle is 153 mm.

The high temperature shield is located within the pressure tube. In the pressure tube a large number of flanges allow access to the bundle. Through theses holes and their extensions in the temperature shield, the bundle can be inspected during the test with the help of the videoscope systems. In test CORA-13 three windows were used: in the 120° direction at the 390, 590 and 790 mm elevations. The size of the windows was 30 mm high and 40 mm wide.

Power Supply

In CORA-13 16 rods out of 25 were heated. The rods can be separately connected to three available power systems, each of which can supply a different voltage. Thus the radial power distribution of the bundle can be varied. In this test the

power input was the same for all rods. Since the voltages and currents of the individual rods are measured, the power input for each rod can be determined.

The power input is controlled by computer. The time-dependent power history is programmed before the test. The power is controlled by measuring the currents of the group and setting the voltage necessary to obtain the desired power. During the test the programmed power can be overridden and manually controlled. The power of each of the three groups can be increased or decreased as required. The electric heating is done by direct current to avoid generating eddy currents in the containment structures.

3. Test conduct and initial boundary conditions

The test sequence can be divided into three phases (Fig. 9):

1. 0 - 3000 s: gas preheat phase;
2. 3000 - 4900 s: transient phase;
3. 4900 s: cooling phase.

During the gas pre-heat phase of 8 g/s preheated argon flows through the bundle and a low constant electric power input of about 0.65 kW (Fig. 9). During this period the temperature in the insulation reaches a level which is high enough to avoid steam condensation. To keep the videoscope windows clear, a total flow of 1 g/s argon is directed to the front of the windows of the videoscopes. The pressure in the system is controlled to 0,22 MPa.

During the transient phase the temperature increase is initiated by raising the electric power input from 6 to 27 kW at a constant rate (Fig. 12). At 3300 s an steam flow of 6 g/s is added to the system. The cooling phase is initiated by the rise of the quench cylinder at 4870 s and the shut down of the electric power at 4900 s. The average velocity of the rising quench cylinder was 1 cm/s. Details are given in Fig. 29.

The boundary conditions during the tests are given in detail, starting at Fig. 10, and are discussed in the following pages. The overpressure in the system is shown

in Fig. 11. The increase of the pressure is initiated by the quench process and is then relieved by opening of the outlet valves.

The measured electrical power input during the transient phase, together with voltage, current and calculated resistance are given in Figs. 12 through 15. In Fig. 12 the power input to the bundle, as measured at the end of the electrodes, is given. The voltages of the three rod groups are shown in Fig. 13. The deviations in the second half of the transient are caused by melt relocations within the bundle, which influence the resulting resistance and with it the voltage necessary to produce the preset power. The resulting current (Fig. 14) to give a linearly increasing power is nearly constant. This is caused by the strong temperature dependence of the electric resistance. The resistance of the bundle (Fig. 15) increases by a factor of about 3 during the test. The stronger increase of the resistance in the second half of the test is caused by the influence of the chemical power production as a result of the exothermal Zry-steam interaction. The energy input in Fig. 21 includes only the electrical power.

The heated rod consists of the central 1024 mm long tungsten heater (6 mm diameter), and the upper electrode (300 mm molybdenum; 669 mm copper) and the lower electrode (300 mm molybdenum; 189 mm copper). The electrodes have a diameter of 8.6 mm. The diameter of the copper electrodes is reduced from 8.6 mm to 7.5 mm for 82 mm at the top and for 155 mm at the bottom. Large flexible copper cables provide the connection to the electrical systems. The resistance of the flexible cables to the points where the voltage is measured for the determination of the power, was less than 1 mΩ.

The resistivities R of tungsten, molybdenum and copper are given in the following 3 equations:

$$R_W = -2.61\ 10^{-2} + 2.63\ 10^{-4}\ T_W + 2.20\ 10^{-8}\ T^2_W$$

$$R_{Mo} = 2.249\ 10^{-2} + 5.36\ 10^{-5}\ T_{Mo} + 1.38\ 10^{-7}\ T^2_{Mo} - 2.22\ 10^{-11}\ T^3_{Mo}$$

$$R_{Cu} = -7.89\ 10^{-3} + 9.90\ 10^{-5} T_{Cu} - 5.49\ 10^{-8}\ T^2_{Cu} + 3.16\ 10^{-11}\ T^3_{Cu}$$

with T in Kelvin and R in $m\Omega \cdot mm^2/m$.

Figure 22 gives the "gas" temperature measured at the entrance of the bundle. The increase at about 3400 s shows the influence of the additional steam. The steam heats up the connecting tube from the steam superheater. Furthermore the introduction of the steam increases the gas flow velocity; by these effects the gas temperature is increased at the entrance of the bundle.

For experimental reasons the steam superheater has to be slowly heated up in flowing argon, which only can be released through the facility. In consequence, at the starting point of the test, the entering gas has already a temperature of 525°C and the bundle has already been heated up by the passing gas. In Tables 3 and 4 temperatures at 0 seconds and 3000 seconds for the different components are given. For the heated and unheated rods the measured temperatures at different radial positions do not exhibit significant differences, so that only one value is given.

The lower end of the bundle is cooled during the test by the water of the quench cylinder. As a result some water evaporates. The amount can be determined by measuring the water level in the quench cylinder. In Fig. 25 the position of the upper edge of the quench cylinder together with the water level is shown. At a time of 300 seconds before the test the quench cylinder was refilled to the upper edge. The difference between upper edge and water level gives the amount of evaporated water which is given in g/s in Fig. 26. Most of the time the evaporation rate is below 0.15 g/s, but in the last 200 seconds it reaches 1 g/s (compared to the steam input of 6 g/s), see Figs. 26 and 27.

The steam flow in the bundle is shown in Fig. 27. These values are determined from the steam concentration measured at 700 mm elevation during a pre-test under identical conditions. For comparison the evaporation from the quench cylinder is given in Fig. 28.

The movement of the water level during the quench phase is given in Fig. 29. Here the positions of the upper edge of the quench cylinder and the water level in the cylinder are shown. For experimental reasons the quench cylinder was not raised with a constant velocity, but in steps. The average velocity was 1 cm/s.

To quench the bundle at a high temperature, the movement of the quench cylinder was started 30 s before the shutdown of the electrical power. The time histories of the power shut down and quench cylinder movement are given in

Fig. 30. During the shutdown of the power the water level had already reached the 150 mm elevation.

About 90 s after shutdown of the electrical power, the quench cylinder reached the 1100 mm elevation and the water level the 950 mm elevation. To compensate for the evaporation a constant water flow was added to the quench water.

We assume that the water that disappeared from the quench cylinder had evaporated. In this case the amount of evaporated water can be calculated from the difference of the water level to the upper edge of the quench cylinder taking into account the feed water. Additional water was added from 4950 s on. The difference between the water level and the upper edge of the quench cylinder, corrected for the additional water input, is shown as function of time in Fig. 31

Fig. 32 gives the rate of evaporation in mm/s obtained by differentiation of the curve of Fig. 31. Finally in Fig. 33 the rate of evaporation in g/s is given, calculated with the effective volume of the quench tank.

After the test the water level in the quench cylinder decreases according to Fig. 34. The evaporation has two heat sources. First the heat capacity of the facility, and secondly argon which flows through the facility for the cooldown of the steam superheater and passes around the quench cylinder.

At the beginning of the test the water level is at the -220 mm elevation. The water temperature in the quench cylinder is measured at the -250 mm and -350 mm elevations. Before quenching the thermocouple signals give the temperatures as a function of time at these fixed elevations. During the quench process the water column is passes the thermocouples so that the thermocouple signals reflect the temperatures as a function of axial height. The measured temperatures are shown in Fig. 35.

During the transient the water temperatures increase to 85 and 70°C due to heat conduction of the heated fuel rod simulators immersed into the water of the quench cylinder and due to the radiation from the bundle. During the quench process the temperatures decrease to about 30°C.

Fig. 36 gives the temperatures at two positions together with the position of the quench cylinder as a function of time. If, for instance, the quench cylinder has

moved from -220 mm to -100 mm elevation the thermocouples measure the temperature of the water at an elevation that is 120 mm lower, i.e. the temperature of water that was originally at -370 mm and -470 mm.

In Fig. 35 at about 4910 s and 5000 s deviations from a smooth course can be seen. They are caused by the movement of the water with a stratified temperature distribution. At about 2000 s for control reasons the quench cylinder was moved down and back up again to the same position, so that the thermocouples came into contact with the water of higher temperature at the higher elevations. At about 4200 s melt from the bundle had dropped into the water and caused mixing of the stratified water layers. In consequence, the thermocouple at -250 mm was influenced by the colder water from the lower layers and the thermocouple at -350 mm from the warmer water of the upper layers.

4. Temperature response, hydrogen generation, and bundle end state

4.1 Temperature measurements of the bundle

The temperature in the bundle was measured with high-temperature thermocouples with WRe5/WRe26 wires and HfO_2 insulating material. The sheath was made of tungsten + zircaloy. Thermocouples with "Ker" in the name were additionally shielded with a ZrO_2 tube. The exact number can be seen from Table 7. The compensation cables are sheathed with stainless steel.

As test CORA-13 was terminated by quenching it was necessary to move the quench cylinder filled with water along the bundle length. Therefore, all thermocouples had to be introduced from the top. Unfortunately, this resulted in a strong attack at the compensation cables in the upper part of the bundle after beginning of the escalation. This is the reason for the irregular behavior of temperature traces after 4200 s.

The presentation of the temperature measurements are grouped in two ways. First, the temperatures for special components are given, as for heated rods, unheated rods, etc. in Figures 37-52. Secondly, for comparative reasons the temperature measurements of different components are grouped for the same axial elevations in Figures 53-59.

The maximum temperatures reached during the transient and the quench phase are listed in Table 4a.

The failure times and temperatures of the two absorber rods, of three unheated fuel rods and of one heated rod are provided with Table 4b.

4.1.1 Temperatures of the components

In Fig. 37 the temperature measurements at heated rods are shown. The positions of the thermocouples of the heated rods are given in Fig. 38. There are two thermocouples installed at each elevation between 1350 mm and -50 mm. Always one rod of the inner ring and one rod of the outer ring are chosen.

The temperature rise shows the same general features already found in earlier tests. With the increase of the electrical power input, first the temperature rises proportional to the power. Having reached about 1000°C, the exothermal Zry/steam reaction adds an increasing contribution to the energy input, resulting in a temperature escalation. The escalation starts at 950 mm and 750 mm elevation. For the outer fuel rod simulator 3.7 the escalation is delayed at 750 mm by about 150 s. A possible reason for this delay could be the heat losses due to the window at 790 mm adjacent to this rod. The escalation at the 550 mm elevation follows 200 s later. The escalation at 1150 mm develops before that at the 350 mm elevation.

After about 4500 s the temperature measurement is strongly disturbed. The increase of the temperature measurement at the lower positions at about 4500 s is not reliable, as the compensation cables pass the upper part of the bundle, where the temperature increased strongly. Only the thermocouples at 1350 mm survived up to the beginning of quenching at 4870 s. At 1350 mm elevation the temperature in the time period of 3900 s to 4900 s shows only a very modest increase at the heated rods. The very disturbed temperature traces at 950 mm elevation indicate a nearly constant behaviour. The thermocouples that survived at 950 mm and 1350 mm indicate a temperature increase with the beginning of the quench process. But the height of the temperature peak at 950 mm is not reliable due to the disturbance of the temperature measurements.

The temperatures in the unheated rods are shown in Fig. 39. Their positions within the bundle are given in Fig. 40. The course of the temperature is very similar to that on the heated rods. The escalation starts at 850 mm elevation, followed by 950 mm and 750 mm with not much delay. About 100 s later the escalation of rod 6.6 can be seen at 650 mm and at 550 mm. The thermocouple at 550 mm elevation in rod 4.2 (in the neighbourhood of a window) shows the escalation - analog to that at 420 mm - 300 s later.

The temperature measurement at 1050 mm and 1150 mm elevation, at which thermocouples survived up to the end of the test, suggest that there seems to be a plateau in the temperature course before the final rise due to quenching. Also for the temperature at 1350 mm a plateau is indicated between 4500 s and the quench rise. The temperature value of this plateau (1000 °C) is in good agreement with the temperature measured at the heated rods at this elevation. Also the rise of the temperature with the beginning of the quench process is in good agreement with the temperature measured at the heated rods. the temperatures of the spacer are shown

The temperatures of the spacer are shown in Fig. 41. On each spacer two thermocouples were fixed to the outside of the spacer at the 30° and 210° sides. The measured temperatures are very similar to those measured in the unheated rods, showing the flat radial temperature profile within the bundle.

The temperatures of the guide tube and in the absorber rods are given in Fig. 42 and 43. At the guide tubes the thermocouples were fixed to the outer surface of the tube. In the absorber rods the thermocouples were placed into the absorber close to the SS-cladding.

The temperatures of the guide tubes at 750 mm and 950 mm elevation are practically the same as those in the unheated rods. At 1150 mm elevation the temperature is slightly higher than the one at the same elevation in the unheated rods. At 1350 mm elevation the temperature is 50°C to 100°C lower in heated than in unheated rods and does not show the rise between 4300 and 4500 s. The temperatures of the 550, 350, 150, and -50 mm elevation (Fig. 42, lower picture) are similar to those measured in the unheated rods.

The temperatures of the absorber rods are given in Fig. 43. The results are very similar to those measured at the guide tube at the same elevation confirming the

flat radial temperature gradient in the bundle. At about 3600 s, when 800°C are reached, one can recognize the delay of the temperature increase due to melting of the absorber.

On the surface of the bundle we have measured the temperature at 950 mm and 750 mm elevation (Fig. 44). The positions are given in the inserted schematic pictures. The 8 WRe thermocouples entering the test section from the bundle head plate were additionally protected by ZrO_2 tubes, which resulted in a longer survival time. The small deviation between the thermocouple responses at the same elevation shows the reliability of the measurement. Good agreement with the temperature measured in the unheated rods up to the end of the escalation (4200 s), confirmes again the flat radial temperature profile and indicates that the time constant of the thermocouple protected by a ZrO_2 tube is short enough to give reliable measurements. The measurement also confirms the nearly constant temperature between 4200 s and the beginning of the quench process, found for the temperature of the unheated rods at the upper end of the bundle. The comparison of the measurements at 750 mm and 950 mm in the upper part of Fig. 45 shows the small deviation of the temperature between 750 mm and 950 mm elevation. In the lower part of Fig. 45 the results of measurements with 4 ZrO_2 tube-protected thermocouples placed at the inner side of the shroud are added. For these 12 thermocouples a good agreement was found, too.

The temperatures at the inner side of the shroud at 950 mm and 750 mm are given in Fig. 46. In Fig. 47 the measurements of all ceramic-protected thermocouples on the inside of the shroud are compared. Contrary of the thermocouples located at the upper half of the bundle those at 550 mm and 350 mm elevation had to be introduced from the lower end of the bundle. In consequence, the compensation cables were influenced by the high temperature at the upper part of the bundle and this resulted in the failure at the end of the escalation. The timing of the escalation is very similar to that of the increase in temperature of the guide tube at the same elevation (Fig. 42) and to that on the outside of the shroud (Fig. 48).

The temperatures measured at the outside of the shroud (still inside the shroud insulation) are given in Fig. 48. In the upper part of the bundle the temperatures at the outside of the shroud are very similar to those measured inside, confirming the reliability of the temperature measurement in the area, where the thermocouples have survived. The strong increase of the temperature below 150

mm elevation at about 4500 s is not reliable. It is probably caused by failure of the compensation cables in the upper part of the bundle.

The "gas" temperatures above the shroud are given in Fig. 49 and Fig. 50 at the elevations 1350 mm and 1250 mm, respectively. The thermocouples, introduced through the bundle head plate, survived the test. Both measurements show the strong increase of the temperature during the quench process: 800°C at 1350 mm and 600°C at 1250 mm elevation.

The temperatures at the surface and inside the shroud insulation at 950 and 550 mm of are given in Fig. 51. All positions are shown in Fig. 52. One can recognize the strong delay of the temperature increase compared to that of the bundle and the strong axial gradient of the surface temperature.

4.1.2 Temperatures at fixed elevations

To better recognize the general tendencies of the temperature distribution in the bundle and also to get an approximate proof of the reliability of the temperature measurement, we have collected the temperature measurements for different components at a fixed elevation in one figure. The sequence is chosen in the order from high to low elevations in Figures 53 to 59.

The measurements at 1450 to 1491 mm (Fig. 53) give the temperature at the lower side of the bundle head plate (1471 mm), at 20 mm inside the bundle head plate (1491 mm), and at the entrance to the off-gas system (1450 mm). The temperature before quenching at the lower end of the bundle head plate stays below 300°C, the position 20 mm inside the plate below 180°C, and the temperature at the exit to the off-gas system below 250°C. During the quench process both the temperature in the off-gas system and on the lower end of the bundle head plate are strongly increasing to 800°C and 600°C, respectively.

At 1350 mm elevation the temperatures of the heated and unheated rods are very similar. After the initial increase up to 600°C at 4100 s, the rise levels out for about 300 s. Then the temperature rises up faster to about 1000°C to stay their nearly constant till the beginning of quenching. The temperature of the guide tube and the "gas" temperature, both are up to 4100 s - the beginning of the melting in the bundle - again very similar to those of the fuel rod simulators. The

further course is less smooth and reaches only about 800°C at the beginning of the quench process. For all measurements the quenching starts a steep temperature increase. Only the "gas" thermocouple survives and shows a temperature increase of about 800°C.

At the 1250 mm elevation (Fig. 54) the flattening of the temperature rise has nearly disappeared. The thermocouple failed before the plateau could be formed. As at the following elevations always a plateau has been formed before the quench peak, also here a plateau can be assumed at about 1500°C. The "gas" temperature measurement shows no plateau similar to that of the gas temperature at 1350 mm in Fig. 53. The quench peak causes a temperature increase at about 600 mm.

At the 1150 mm elevation (Fig. 54) from about 4100 s on - when the escalation starts in the lower part of the bundle - we get an acceleration of the temperature increase which, after 4500 s, is slowing down to a plateau. Also here a temperature peak is found during quenching. The much lower temperature on the shroud insulation shows the good insulating property of the ZrO_2 fibre material.

The temperature of the unheated rod at the 1050 mm elevation (Fig. 54) shows the same course with an earlier escalation. The plateau again has a temperature of about 1850°C.

At 950 mm (Fig. 55) elevation the temperature measurements at heated rods, unheated rods, guide tube and absorber, and with the ceramic-protected thermocouples show only a small deviation from each other. The escalation reached its maximum at 4200 s. After this a temperature plateau at 1850°C formed that extends up to the beginning of the quench peak.

At 850 mm (Fig. 55) and 750 mm (Fig. 56) the escalation starts first so that the plateau is already reached at 4100 s. At the 850 mm elevation the escalation is only slightly faster than at 750 mm. The measurements with the ceramic-protected thermocouples at 750 mm elevation clearly show the formation of the temperature plateau berfore formation of the quench peak.

At the 550 mm elevation (Fig. 57) the escalation is delayed by about 200 s. Again the escalation at 350 mm developes 200 s later. No thermocouples have survived

up to the time after the escalation, but from the comparison of the temperature at the surface of the high-temperature shield, one can assume that the temperature of a possible plateau was not higher than 1850°C.

At 150 mm, 50 mm, and -50 mm (Fig. 55) it must be assumed, that also after 4500 s no escalation of the temperature had developed. The increase at 150 mm is not realistic, but due to a compensation cable failure in the upper part of the bundle. The appearance of the bundle at 150 mm elevation and below it clearly shows that temperatures much above 1000°C are not realistic. The temperatures on the inner side of the high-temperature shield also show only a modest increase, with no escalation.

4.1.3 Temperature measurements in the High-Temperature Shield

The overview of the positions of thermocouples in the High-Temperature Shield is shown in Fig. 60 and Fig. 61. The temperatures are given in Figs. 62 to 73. In Figs. 62 to 70 the temperatures are compared always for the same radial distance; either for different axial elevations or for different azimuthal positions. The High-Temperature Shield has measurement planes at 153 mm (inner surface), 192 mm, 255 mm, and 293 mm (outer surface). In Fig. 71 to Fig. 73 the radial comparison of the measurements is shown.

The measurements at the inner surface of the High-Temperature Shield (153 mm radius) are given in Fig. 62a. One can recognize a strong axial dependence. From 90 mm to 990 mm elevation the maximum temperature increases from 300°C to 1350°C. The temperature increase is delayed with increasing height in the bundle. There is a qualitative difference in the temperature decrease at 890 mm, 990 mm on one hand and the temperatures at the lower positions on the other hand. In the lower part the close neighbourhood of the water-filled quench cylinder, reduces the temperature early. The temperature in the two upper positions declines slower.

The measurements outside the 1.5 inch HfO_2 fibre insulation at 192 mm radius are given in Fig. 62b. Here we get a much slower decrease of the temperature with increasing time. The slower decrease can even better be seen in Fig. 63a + 63b, from temperature measurements up to 10 000 s.

The temperatures at the inner surface are compared for different azimuthal directions (165°/345° and 75°/255°) in Figs. 64 to 66. The thermocouple at 390 mm elevation and 345° seems not to be positioned exactly on the surface but at a small distance inside the insulation, which results in a lower temperature and a delayed decline at quenching.

In Fig. 67 + Fig. 68 the temperatures are compared at a radius of 192 mm for different azimuthal directions.

The temperatures at 255 mm and 293 mm radius for different elevations are given in Fig. 69 and Fig. 70. The maxima at 5000 s for 293 mm radius (outer surface) and the somewhat higher temperatures, compared to the measurement at 255 mm, indicate that there is some additional heat transport also along the stainless steel outer surface wall of the High-Temperature Shield from top to bottom.

The temperature measurements for different radial positions at the same elevation are given in Figs. 71 to 73. There is a steep gradient visible for the maximum temperature in the High-Temperature Shield. In the inner 1.5 inch HfO_2 fibre insulation the temperature decreases to 1100°C at 950 mm elvation and to 750°C at 550 mm elevation. Due to the heat transportation the maximum is reached the later, the larger the radius (outer positions) is.

4.2 Hydrogen generation

The hydrogen produced during the test by the steam/Zr reaction is usually measured at two different positions, i.e. above the test section and in the mixing chamber (see Fig. 1).

A schematic diagram of the probes, gas lines, and gas analysis system is provided in Fig. 74. To dilute the gas taken at the location above the test section a dilution chamber with flow meters is installed (Fig. 74a). The off-gas mixture which contains hydrogen among other gases is transported to the spectrometer via capillary tubes. It is analyzed by two quadrupole mass spectrometers of the type Leybold PQ 100. The ion currents representing the concentrations of the respective gases are determined. From these data the mass production rate of hydrogen as well as of the other gases is calculated with the ratio of the partial

pressure of the particular gas to that of argon (the carrier gas) and multiplied by the argon flow rate through the test bundle.

The measured hydrogen data for test CORA-13 are given in Fig. 75 with a maximum of ca. 700 mg/s. They are derived from the ion current obtained from the gas probes at the outlet of the test section.

The spike in the H_2 production during quenching results from the intensified oxidation of the remaining metallic zircaloy. It is the increased flow rate (two-phase flow) that causes an enhancement in oxidation and thus in the H_2 buildup /3/. The percentage of the total hydrogen generated from 4870 s on (onset of quenching) amounts to 48 %.

Based on the accumulated H_2 production of 210 g the oxidation energy is determined to be 31.9 MJ which corresponds to 49 % of the total energy input (electic supply plus exothermal energy).

Also on the basis of 210 g H_2 the percentage of zirconium oxidation was calculated to be 60 % (referred to a bundle length of 1.2 m and a total mass of zircaloy of 8.0 kg that includes cladding and shroud). This percentage is an integral value and does not reflect local differences.

The fraction of steam consumed during the transient (heatup) phase, i. e. prior to quenching, was calculated to be 21 %. This, too, is an integral (average) value that is based on a flow rate of 6 g/s and a time at temperature above 1400 °C of 800 s.

4.3 Mass distribution and blockage formation

An axial profile of voids and structure material, respectively, can be obtained by using the epoxying process. As can be seen in Fig. 76 the epoxy resin is filled into the mould from the bottom end. By wheighing the resin left in the supply container after each step, i.e. when the resin level has raised in the bundle by 1 cm, the difference of mass allows the calculation of the void volume of the bundle as a function of axial height. The filling process is slow enough so that the reading at the scale can be taken per cm. The result of the specific mass of resin as

a function of elevation (g/cm) shows in Fig. 77a the axial distribution of voids because a higher amount of resin is equivalent to a larger void volume.

The smoothed solid-line curve in Fig. 77a was obtained from the data (crosses) by filtering, i.e. by using a Fourier transformation where higher frequencies were cut off by a low-pass filter. The smoothed curve is used for further evaluation.

Fig. 77b presents the axial distribution of the structural material. For the evaluation of this profile the cut bundle segments were wheighed. These data consist of the mass of the structure, the mass of the heater elements, and the mass of the epoxy resin. The lack of material between 1050 mm and 1100 mm is artificial (air entrainment).

Applying the cross-sectional areas of the mould inside, and the epoxy resin, the area of the structural material is evaluated, designated "blocked area inside the shroud" (Fig. 78):

> *Blocked area = (Cross section mould inside - cross section epoxy - cross section of shroud remnants) referred to cross section shroud inside.*

As the shroud of the axial center (hot region) was removed together with the fiber insulation after the test, the remnants of the shroud which were present during the filling process were excluded in the evaluation. It was assumed that there had been no shroud.

The result is almost a reversed profile of that in Fig. 77a. The area is given as percentage where 100 % means full blockage. A partial blockage between 400 mm and 500 mm is apparent. The melt that had left the bundle during the transient is taken as lost material and is therefore not included in this diagram.

The same results as of Fig. 78 are depicted as relative volume distribution referred to the pretest flow channel area in Fig. 78a. The figure presents the difference of the flow channel area before the test and after the test referred to the flow channel area before the test. So, the original (pretest) cross-sectional area is 0 % and the total blockage of the coolant channel means 100 %.

The axial mass distribution of Fig. 79 results from the profiles of Figs. 77 a and 77 b. These data represent the mass of the structure and the mass of the heater elements. The masses of the epoxy resin and of the shroud are eliminated:

> *Specific mass = Mass of wheighed samples - Epoxy mass - Mass of shroud remnants referred to the pertinent axial segment.*

Fig. 79a provides the same results as Fig. 79 but gives the axial mass distribution in relative units referred to the original specific mass. The original mass (pretest value) is 100 %.

5. Posttest appearance of the entire bundle and of cross sections

The posttest appearance of test bundle CORA-13 is documented with Figs. 80 through 107.

A view of the insulated bundle is shown with Fig. 80. The strong reaction between shroud and fuel rods with the ZrO_2 insulation can be seen in Figs. 81 through 85.

The overview of the bundle after removal of its insulation (Fig. 86) demonstrates that the zircaloy shroud is gone in the hot region and remained intact in the lower region, i.e. up to about 350 mm (Figs. 97, 101, 102, 106, and 107). The shroud remnants above the heated zone are of a light grey color. The pieces are heavily oxidized and very brittle (Figs. 93, 98, and 103).

The appearance of the de-clad fuel rods and melt is so that the predominant color is black (from UO_2) and that rods are glued together (Figs. 87, 88, 89, 90, 94, 95, 99 and 100). An extensive interaction between the UO_2 and the zirconium of the cladding has taken place in the hot region. At time of this reaction the cladding was mainly of metallic composition. Only parts of the cladding that did not react with the fuel were completely oxidized.

The oxidized cladding in the upper part is clearly to be seen in Figs. 104 and 105 where the oxide shell appears white or grey and deformed due to the "flowering" phenomenon.

After visual inspection, photographic documentation, and collecting of fragments the test bundles were encapsulated in epoxy resin and sectioned according to the list in Table 5.

For encapsulation of the bundle the epoxy system Rütapox 0273 with the hardener designated LC (Epoxy resin and hardener manufactured by Bakelite GmbH, D-5860 Iserlohn 7) was chosen. The bundle was filled starting from the bottom, through the steam inlet line, to avoid air entrainment in the encapsulant (see Fig. 76). Approximately 19 kg were required to fill the bundle of 120 by 120 mm to an elevation above the top of the shroud, i.e. 1300 mm. The epoxy showed some heating during the curing stage but the shrinkage effect was negligible. After epoxying the bundle the resin was allowed to harden for one week.

A saw with a 2.3 mm-thick diamond blade (mean diamond size 138 μm) of 500 mm OD was used to do the cutting of the slabs at 3200 rpm. The thicknesses of the slabs from the epoxied bundle can be taken from Table 5.

The macrophotographs of the cross sections from -45 mm to 1098 mm are presented in Figs. 109 and 110. The figure at the lowest elevation represents a cut through the bottom grid spacer (Zircaloy-4), the one at the highest elevation a cut above the heated section of the bundle. All cross sections above 500 mm show that material is missing by its relocation to lower positions. In addition it can be seen that

- interactions between UO_2 and zirconium have taken place
- the upmost grid spacer made of zircaloy was included in the interaction process (at 848 mm)
- cladding remnants are completely oxidized
- the cladding remnants are deformed: "flowering".

The relocated material has been solidified at elevations below 500 mm with partial flow blockages to be found at 448 mm and mainly at 498 mm. Elevation 498 mm is above the Inconel spacer which has been dissolved when the temperature had reached 1200°C at this axial location. The fact that most of the once molten material has been relocated here demonstates that the temperature was low enough for solidification of the melt. The first melt that "froze" at 498 mm was probably absorber rod melt from upper positions. Failure of the absorber

rods occurs in the same temperature regime (about 1200°C) where the Inconel spacer is dissolved by the zirconium.

Ten cross sections of the slabs were selected for grinding and polishing. These are the following elevations:

13-e top	148 mm
13-g top	248 mm
13-i top	348 mm
13-j top	398 mm
13-k top	448 mm
13-l top	498 mm
13-m top	548 mm
13-p top	698 mm
13-s top	848 mm
13-v top	998 mm.

Before grinding and polishing of the samples the selected cross sections were infiltrated by "Araldit" resin to close up residual pores.

The procedure of preparation for the metallographic examination is given with Table 6. The steps described in the list were performed using a semi-automatic machine with a closed water circuit for grinding and an automatic lubricant feeder for the polishing steps. The cross sections were studied in the as-polished condition.

6. Oxidation status of the bundle

The following statements are based on the visual observation of the complete bundle and horizontal cross sections, and a comprehensive series of ZrO_2 scale thickness measurements on many fuel rod peripheries and various positions around the shroud, performed at several elevations within the lower half of the bundle. Clad melting and internal clad oxidation by chemical interaction with the fuel, the processes competing with the external oxidation by steam, are also discussed.

6.1 Axial variation of steam oxidation

The measured ZrO_2 scale thickness increases from an unimportant range of some µm at 148 mm elevation to a still tolerable order of 100 µm at 248 mm, but at 348 mm complete conversion of the cladding has occurred locally (Tab. 8).

At higher elevations the destructive mechanical consequences of severe cladding oxidation and the competing degradation processes restrict the respective evaluation: On the basis of a Pilling-Bedworth factor of 1.5 to 1.56 the 725 µm original cladding wall would convert to roughly 1100 µm of ZrO_2. The measured values, however, cannot be used to confirm this more precisely. Lower values observed can easily be explained by spalling of partial layers or tube wall thinning during melt agglomeration at the respective side of the cladding periphery (see single values in Tab. 8).

In Fig. 111 the axial distribution of the measured ZrO_2 scale thickness is drawn. Broad scatter bands for the lower elevations indicate considerable local variations. For the upper half of the bundle the presence of any residual metallic cladding can be excluded although the obtainable data are scarce.

The axial distribution of peak temperatures in the bundle, measured during the transient and the quenching phase (see Table 4a) is included in Fig. 111. The temperatures and the availability of steam were high enough for dramatic additional oxidation to occur if residual metallic materials were available in the upper bundle half. Even above the heated zone, up to roughly 1300 mm elevation, no metal-

lic cladding residues are expected. For this reason the test was also not suitable to detect any consequences of local and temporal steam starvation.

On the other hand the completeness of the oxidation over an axial range of roughly 1000 mm together with the integral value of hydrogen generation allows to estimate the percentage of cladding which has relocated as or contributed to metallic melt. The steam oxidation of such a melt has to be neglected in this estimation, since it cannot be quantified. This is justified because the specific surface and the temperatures at the final location of melts are both reduced. The described estimation gives a value of ca. 28 % of relocated and of ca. 72 % of in situ oxidized cladding and shroud material.

On the basis of published results of oxidation kinetic studies (4,5) the axial and lateral variation of measured scale thicknesses can be evaluated towards an estimation of the corresponding temperature variations: At 148 mm elevation a maximum scale thickness of 24 µm (Tab. 8) and a maximum temperature of 1050 °C (Tab. 4a) were measured. Under isothermal conditions this scale would grow within roughly 5 min at this temperature. If this "effective duration" is used as a commonly valid fitting factor for all other positions and temperatures, a surely simplified treatment, the temperature values given in Tab. 9 are deduced. Nevertheless, and especially if some microstructural indications for peak temperature ranges are included, a fairly consistent picture of the local variations of maximum temperatures reached in the test is obtained.

6.2 Local variation of scale thickness

The lateral variation of scale thicknesses was measured from the shroud diagonally across the bundle at several elevations (Tab. 10). As a general trend the thickness maxima shift from the bundle center towards one of the corners (Fig. 112). A three dimensional representation of the ZrO_2 scale thickness variation over one half of the bundle at 348 mm elevation is given in Fig. 113. The corresponding field of temperatures reached within the bundle can be discussed as follows: At 148 mm the maximum of the bundle temperature field is oriented towards the 210 ° side. It is pointing to the 210 ° / 120 ° corner at 348 mm and reaches the bundle center at 398 mm elevation. This angular movement of the hot zone along the axial direction is not correlated with the steam inlet position (0 mm, 180 °) and the position of a window (400 mm, 120 °). It might correspond with the

"imported" heat from relocated melt and the resulting partial blockages.

6.3 Shroud oxidation

At the lower elevations the internal and external oxidation of the shroud is only slightly below that of the fuel rods of the outer row. At the higher elevations the differences to the fuel rods and across the shroud wall are increasing (Tab. 10, Fig. 112). In Fig. 114 the internal scale thickness ranges measured for the different sides and elevations are drawn. The shroud is completely converted to ZrO_2 or destroyed at the 448 mm elevation and not preserved above.

The external scales, in contrast, seem to stagnate at a level of roughly 50 to 150 µm, independent of further bundle temperature increase with increasing elevation (Fig. 115). This must be an indication of "steam starvation": Under those conditions of limited steam supply the available steam is almost completely consumed and the oxidation rate is therefore independent of the temperature. It is quite reasonable to assume that the ingress of steam between the shroud and its external insulation layer of fiber material is limited enough for steam starvation to develop.

7. First results of the destructive post-test examinations

The destructive post-test examinations of the bundle showed strong chemical interactions over the whole bundle length. In the upper half of the bundle the (Ag,In,Cd) absorber rods and Zircaloy guide tubes as well as a great part of the Zircaloy cladding of the fuel rods have been molten off (Figure 116). The relocated materials solidified, according to their solidification temperatures, at different axial elevations. The Inconel grid spacer at the 500 mm elevation acts as an additional material catcher for the relocated liquid and/or solid materials. For this reason the blockage formation at this elevation is most extended.

As a result of the high temperatures in the upper part of the bundle the interactions of the materials with steam are very fast and the resulting reaction products and melts are all ceramic in nature. Figure 117 shows the bundle cross-section at elevation 848 mm. One can still recognize a part of the completely oxidized upper

Zircaloy grid spacer. A great part of the Zircaloy cladding and UO_2 pellets have disappeared; only in the outer ring of the fuel rods some oxidized cladding remnants are still present.

The solidified material at the bundle cross-section elevation of 498 mm (Inconel grid spacer location) is mainly ceramic (Figure 118). On solidification large pores have formed. Cladding of nearly all fuel rod simulators was molten off or dissolved by local contacts between zircaloy and the steel cladding of the absorber rods. Also the UO_2 fuel has been chemically attacked and partially dissolved (liquefied). At some locations a pronounced cracking of the ceramic material occurred during quenching of the bundle. The resulting unusual crack pattern can be recognized in Figure 118; similar observations were made in in-pile quench tests.

In the lower half of the bundle ($\leq$ 400 mm) the two absorber rods are still present. The gap between the Zircaloy guide tube and stainless steel cladding of the absorber rods has been filled with the relocated absorber alloy (Figure 119). The damage of the fuel rods in the vicinity of the absorber rods is stronger than further away. The Ag of the absorber alloy attacks the Zircaloy cladding and dissolves it above about 1250 °C very quickly. The composition of the melts at this elevation is rather homogeneous; the high Zr content of about 52 wt.% reflects the strong interactions between the absorber alloy and Zircaloy.

The chemical composition of the various melts at different cross-section elevations was quantitatively determined by SEM/EDX examinations and is listed in Table 11 and plotted in Figure 120 as a function of the axial bundle elevation. The results indicate that below 400 mm all melts are metallic in nature. Sometimes the solidified melts contain small quantities of ceramic phases. Above 500 mm all melts are ceramic in nature, the other materials are UO_2 and ZrO_2. In between (400 - 500 mm) both types of melts can be detected. Figure 5 shows the variation in the composition of the metallic and ceramic melts as function of the bundle elevation. One can recognize the strong decrease of U and strong increase of Ag in the solidified melts going from the top to the bottom of the bundle. No stainless steel or absorber alloy elements or their corresponding reaction products are present in the upper half of the bundle, but U, Zr and oxygen.

More SEM/EDX examination results will be given in /6/.

8. Summary of the major results

The general behavior of bundle CORA-13, a typical PWR-type fuel element with Ag/In/Cd absorber rods that was tested under severe accident conditions can be described as follows.

- Temperature escalation due to the zirconium-steam reaction starts in the upper, i.e. hotter bundle half at about 1100 °C and propagates from there downwards and upwards. The maximum temperatures were 1850 °C and 2300 °C for the transient and quenching phase, respectively.

- In presence of PWR absorber material (Ag,In,Cd) the sequence of failure starts with the release, relocation and resolidification of the (Ag,In,Cd) melt. Most of the melt reacts with the Zircaloy cladding and guide tube while forming a metallic melt of the type (Ag,In,Zr). Due to its zirconium content this melt is capable of dissolving UO_2 even below the melting point of Zircaloy (1760 °C).

- The non-oxidized part of the Zircaloy cladding first melts in the upper bundle zone because of the higher temperatures prevailing there. Due to the progressing chemical dissolution of UO_2, melts consisting of (Zr, U, O) develop with different contents of uranium and oxygen and relocate into the bottom part of the bundle after the ZrO_2 layer has failed. While the melt solidifies in the colder zone, coolant channel blockages develop which are different in size.

- Thick ZrO_2 layers on the external cladding tube surfaces prevent substantial amounts of metallic Zircaloy melt from running off so that it remains in contact with the UO_2 fuel as well as with the ZrO_2 shell and dissolves both chemically. This causes thin oxide layers to rupture locally and the (Zr, O, U) metallic melt to escape.

- Most of the melt relocates along the surfaces (candling) and, to a minor extent, in the free fall as droplets, i.e. without contact to the surfaces of the materials (slumping). Film flow type of melt relocation along the rods could not be observed.

- On account of the different solidification temperatures of the melts a stratification develops such that the metallic lumps of melt rich in absorber material are superimposed by metallic and/or ceramic (Zr, U, O) blockages formed later.

- Besides the formation of solidified lumps of melts at "cold spots" within the lower part of the bundle, debris of absorber material, cladding, and fuel fragments of various sizes accumulates at the very bottom (below the bundle). The smallest particles consist of UO_2 powder and are of the order of micrometers in size.

- Water quenching (flooding) of the hot degraded fuel rod bundle causes additional fragmentation and an enhanced Zircaloy/steam interaction resulting in a renewed temperature rise, a meltdown of material, and in an additional strong hydrogen generation.

9. References

/1/ S. Hagen, P. Hofmann, G. Schanz, L. Sepold, "Interactions in Zry/UO_2 Fuel Rod Bundles with Inconel Spacers at Temperatures above 1200°C; (Posttest Results of Severe Fuel Damage Experiments CORA-2 and CORA-3)", KfK 4378, 1990.

/2/ S. Hagen, P. Hofmann, G. Schanz, G. Schumacher, L. Sepold, "Chemical-Physical Behavior of LWR Core Components in Severe Reactor Accident", IAEA Meeting on "Behavior of Core Materials and Fission Product Release in Accident Conditions in LWRs", Aix en Provence, France, 16-20 March 1992.

/3/ S. Hagen, F. Seibert, L. Sepold, P. Hofmann, G. Schanz, G. Schumacher, "Influence of Reflood in the CORA Severe Fuel Damage Experiments", Heat Transfer and Fuel Behavior in Nuclear Reactor Accidents, 27th ASME/AIChE/ ANS National Heat Transfer Conference, Minneapolis, 28-31 July 1991, AIChE Symposion Series 283, Vol. 87, ISBN-0-8169-0548-7, pp. 120-129.

/4/ S. Leistikow and G. Schanz, "Oxidations Kinetics and Related Phenomena of Zircaloy-4 Fuel Cladding Exposed to High Temperature Steam and Steam-Hydrogen Mixtures Under PWR Accident Conditions", Nucl. Eng. Des. 103, 65 (1987).

/5/ J.T. Prater and E.L. Courtright, "High Temperature Oxidation of Zircaloy-4 in Steam and Steam-Hydrogen Environments", NUREG/CR-4476, PNL-5558, U.S. Nuclear Regulatory Commission (1986).

/6/ J. Burbach, "Ergebnisse von REM-Mikrobereichsanalysen des DWR-Bündel-abschmelzexperiments CORA-13", KfK 5162, in preparation

10. Acknowledgements

Various kinds of support for preparation, conduct, and evaluation of the experiment are gratefully acknowledged.

The fuel elements were designed by Mr. H. Junker. The test rods were assembled by Mr. E. Mackert, the test bundles by Messrs. H. Giesmann and R. Röder. The authors would like to thank Messrs. H. Benz, W. Rötzel, and H.J. Röhling for test preparations and conduct.

Mr. K.P. Wallenfels is acknowledged for arrangement of camera and video systems and for the preparation of temperature measurements. Messrs. R. Huber, H. Malauschek, and Ms. I. Schub prepared and conducted the on-line measurements of the off-gas samples.

Mr. W. Rötzel's effort in the posttest photography is greatly appreciated. The authors would like to thank Mr. L. Anselment for sectioning of the epoxied bundle and for preparation of the metallographic samples, Mr. H. Metzger for investigation of the metallographic samples by optical microscope, and Mr. J. Burbach for the SEM investigations.

List of Tables

Table 1: CORA experiments performed up to test CORA-13

Test No.	Max. Cladding Tempera-tures	Absorber Material	Other Test Conditions	Date of Test
2	≈ 2000°C	-	UO_2 refer., inconel spacer	Aug. 6, 1987
3	≈ 2400°C	-	UO_2 refer., high temperature	Dec. 3, 1987
5	≈ 2000°C	Ag, In, Cd	PWR-absorber	Febr. 26, 1988
12	≈ 2000°C	Ag, In, Cd	quenching	June 9, 1988
16	≈ 2000°C	B_4C	BWR-absorber	Nov. 24, 1988
15	≈ 2000°C	Ag, In, Cd	rods with internal pressure	March 2, 1989
17	≈ 2000°C	B_4C	quenching	June 29, 1989
9	≈ 2000°C	Ag, In, Cd	10 bar system pressure	Nov. 9, 1989
7	< 2000°C	Ag, In ,Cd	57-rod bundle, slow cooling	Febr. 22, 1990
18	< 2000°C	B_4C	59-rod bundle, slow cooling	June 21, 1990
13	≈ 2200°C	Ag, In, Cd	OECD/ISP; quench initiation at higher temperature	Nov. 15, 1990

Table 2: Design characteristics of test bundle CORA-13

Bundle type:		PWR
Bundle size:		25 rods
Number of heated rods:		16
Number of unheated rods:		7
Pitch:		14.3 mm
Rod outside diameter:		10.75 mm
Cladding material:		Zircaloy-4
Cladding thickness:		0.725 mm
Rod length:	- heated rods: (elevation - unheated rods (elevation	1960 mm - 489 to 1471 mm) 1672 mm - 201 to 1471 mm)
Heated pellet stack:		1000 mm
Heater material:		Tungsten (W)
Heater	- length - diameter	
Fuel pellets	- heated rods: - unheated rods:	UO_2 annular pellets UO_2 full pellets
Pellet stack	- heated rods: - unheated rods:	O to 1000 mm - 199 to 1295 mm
U-235 enrichment		0.2 %
Pellet outer diameter (nominal)		9.1 mm
Grid spacer	- material: - length: - location:	Zircaloy -4, Inconel 718 Zry 42 mm Inc 38 mm lower (Zry) -5 mm center (Inc) + 496 mm top (Zry) + 880 mm
Shroud	- material - wall thickness - outside dimensions - elevation	Zircaloy -4 1.2 mm 89.4 x 90.4 mm 36 mm to 1231 mm
Shroud insulation	 - insulation thickness - elevation	ZrO_2 fibre 19 mm 36 mm to 1036 mm

Table 2: (Continuation)

Mo electrode	- length	300 mm
	- diameter	8,6 mm
Cu electrode	- length	189 mm (lower end)
	- length	669 mm (upper end)
	- diameter	8,6 mm
Absorber rod	- number of rods	2
	- material and composition	80Ag,15In,5Cd (wt.%)
	- cladding	Stainless steel
	- cladding OD	11,2 mm
	- cladding ID	10,2 mm
	- length	1660 mm
	- absorber material	-189 mm to + 1300 mm
Absorber rod guide tube	- material	Zircaloy -4
	- OD	13,8 mm
	- wall thickness of tube	0,8 mm
Plenum Volume	- heated rods	$12 \cdot 10^{-6}$ m^3
	- unheated rods	$87 \cdot 10^{-6}$ m^3

Table 2a: Total specific mass data of bundle CORA-13

Tungsten heater elements	8.70 kg/m
UO_2	11.24 kg/m
Zircaloy in rods	3.45 kg/m
Zircaloy in absorber rods	0.43 kg/m
Stainless steel in absorber rods	0.26 kg/m
Ag/In/Cd absorber	1.62 kg/m
Inconel grid spacer	0.11 kg
Zircaloy grid spacer	0.14 kg
Zircaloy of shroud	2.60 kg/m
Total zircaloy	6.48 kg/m

Table 2b: Areas of bundle CORA-13

Cross section areas [m^2]:	
Tungsten UO_2 Zircaloy cladding	$4.524 \cdot 10^{-4}$ $1.077 \cdot 10^{-3}$ $5.252 \cdot 10^{-4}$
Absorber (Ag/In/Cd) Stainless steel cladding Zircaloy guide tube	$1.634 \cdot 10^{-4}$ $3.362 \cdot 10^{-5}$ $6.535 \cdot 10^{-5}$
Zircaloy shroud	$3.888 \cdot 10^{-4}$
Total area inside the shroud	$8.038 \cdot 10^{-3}$

Table 3: Temperatures [°C] of test CORA-13 at 0 seconds for different components

	Components						
Elevation [mm]	Heated rod	Unheated rod	Absorber rod	Guide tube	Shroud	Shroud isolation	HTS 153 mm
1350	200	250	(210)	210			
1250	(250)	265	(250)	(250)			(75)
1150	290	280	(290)	290	210	102	(75)
1050	(300)	310	(300)	(300)	(240)	(105)	(75)
950	310	318	313	313	270	107	75
850	(320)	328	(322)	(322)	(280)	(110)	74
750	330	338	333	233	290	113	74
620	(343)	348	(350)	(350)	(303)	(115)	73
550	350	356	357	357	315	116	73
420	(363)	368	(370)	(370)	(328)	(119)	72
350	370	373	380	380	335	121	72
250	(380)	382	(390)	(390)	(350)	(123)	71
150	390	392	(405)	405	360	125	70
50	400	(402)	(410)	(410)	(345)	162	70
-50	300	295	(295)	(295)			(70)

() = no thermocouple at this elevation, calculated value

Table 4: Temperatures [°C] of test CORA-13 at 3000 seconds for different components

	Components					
Elevation [mm]	Heated rod	Unheated rod	Absorber rod	Guide tube	Shroud	Shroud isolation
1350	240	297	(245)	245		
1250	(305)	320	(305)	(305)		
1150	360	345	(360)	360	265	118
1050	(380)	375	(380)	(380)	(305)	(118)
950	395	397	395	395	345	118
850	(402)	405	(402)	(402)	(352)	(126)
750	410	410	408	408	358	133
620	(418)	415	(415)	(415)	(365)	(134)
550	420	417	420	420	370	135
420	(430)	423	(427)	(427)	(378)	(136)
350	435	426	432	432	383	137
250	(433)	431	(440)	(440)	(388)	(134)
150	431	435	(445)	445	395	133
50	430	(427)	(445)	(455)	(360)	174
-50	320	320	(320)	(320)		

Table 5: List of cross sections for test bundle CORA-13

Sample	Sample length	Elevation bottom	Elevation top	Remarks
13-a	48 mm	-93 mm	-45 mm	Lower remnant
cut	2 mm			Lower grid spacer
13-b	41 mm	-43 mm	- 2 mm	
cut	2 mm			
13-c	48 mm	0 mm	48 mm	
cut	2 mm			
13-d	48 mm	50 mm	98 mm	
cut	2 mm			
13-e	48 mm	100 mm	148 mm	top polished: 148 mm
cut	2 mm			
13-f	48 mm	150 mm	198 mm	
cut	2 mm			
13-g	48 mm	200 mm	248 mm	top polished: 248 mm
cut	2 mm			
13-h	48 mm	250 mm	298 mm	
cut	2 mm			
13-i	48 mm	300 mm	348 mm	top polished: 348 mm
cut	2 mm			
13-j	48 mm	350 mm	398 mm	top polished: 398 mm
cut	2 mm			
13-k	48 mm	400 mm	448 mm	top polished: 448 mm
cut	2 mm			
13-l	48 mm	450 mm	498 mm	top polished: 498 mm
cut	2 mm			
13-m	48 mm	500 mm	548 mm	top polished: 548 mm
cut	2 mm			

13-n	48 mm	550 mm	598 mm	
cut	2 mm			
13-o	48 mm	600 mm	648 mm	
cut	2 mm			
13-p	48 mm	650 mm	698 mm	top polished: 698 mm
cut	2 mm			
13-q	48 mm	700 mm	748 mm	
cut	2 mm			
13-r	48 mm	750 mm	798 mm	
cut	2 mm			
13-s	48 mm	800 mm	848 mm	top polished: 848 mm
cut	2 mm			
13-t	48 mm	850 mm	898 mm	
cut	2 mm			
13-u	48 mm	900 mm	948 mm	
cut	2 mm			
13-v	48 mm	950 mm	998 mm	top polished: 998 mm
cut	2 mm			
13-w	48 mm	1000 mm	1048 mm	
cut	2 mm			
13-x	48 mm	1050 mm	1098 mm	
cut	2 mm			
13-y	48 mm	1100 mm	1148 mm	
cut	2 mm			
13-z	48 mm	1150 mm	1198 mm	
cut	2 mm			
13-z1	48 mm	1200 mm	1248 mm	
cut	2 mm			
13-z2	48 mm	1250 mm	1298 mm	Upper remnant

Table 6: Procedure for the metallographic preparation of the CORA samples

	Horizontal grinding	Grinding	Lapping	Polishing		
Abrasive	Corrundum disc 120 µm Diamond disc 64 µm	Diamond disc 20 µm	Petrodisc-M or DP Net*)	PAW cloth	PAN-W	NAP cloth
Particle size			Diamond spray 6 µm	6 µm	3 µm	1 µm
Lubricant	Water	Water	W. lubric. **)	W. lub.	W. lub.	W. lub.
Revolutions of disc	300 rpm	300 rpm	150 rpm (Net) or 300 rpm (Petrod.)	150 U/min	150 U/min	150 U/min
Pressure	200-400 N	200-300 N	200 N	100 N	100 N	100 N
Time	to level	25 min	30 min	30 min	60 min	60 min

*) Petrodisc-M and DP Net are registered trade marks of Struers company

**) "White lubricant" of Struers; liquid on an oil/alcohol/glycerin basis

Positions of thermocouples in unheatd rods (CORA-13)

Slot Number	Elevation [mm]	Rod Number
135	1350	4.4
136	1350	2.4
131	1250	2.6
101	1150	6.6
102	1050	2.2
103	950	6.4
104	850	2.4
105	750	4.4
106	750	4.2
201	620	2.6
202	550	6.6
205	550	4.2
203	420	2.2
204	350	6.4
231	250	2.4
232	150	4.4
238	-50	2.4

Positions of thermocouples in absorber rods (CORA-13)

Slot Number	Elevation [mm]	Rod Number
107	950	6.2
108	750	4.6
206	550	6.2
207	350	4.6

Positions of thermocouples in heated rods (CORA-13)

Slot Number	Elevation [mm]	Rod Number
132	1350	3.3
133	1350	1.3
114	1150	5.1
113	1150	5.3
112	950	7.5
111	950	5.5
110	750	3.7
109	750	3.5
208	550	5.5
209	550	7.5
210	350	5.3
211	350	5.1
212	150	3.3
213	150	1.3
233	50	3.5

Positions of thermocouples in heated rods (CORA-13)

Slot Number	Elevation [mm]	Rod Number
234	50	3.7
235	-50	3.5
236	-50	3.7

Positions of thermocouples in guide tube (CORA-13)

Slot Number	Elevation [mm]	Rod Number
134	1350	6.2
117	1150	4.6
116	950	6.2
115	750	4.6
214	550	6.2
215	350	4.6
216	150	4.6
237	-50	6.2

Positions of thermocouples in ceramic tube, shroud inner surface (CORA-13)

Slot Number	Elevation [mm]	Direction of TE
120	950	120°
121	950	210°
118	750	120°
119	750	210°
217	550	210°
218	350	210°

Positions of thermocouples in ceramic tube (CORA-13)

Slot Number	Elevation [mm]	Direction of TE
129	950	300° l
128	950	210° l
127	950	120° l
126	950	30° l
125	750	300° r
124	750	210° r
123	750	120° r
122	750	30° r

Positions of thermocouples at the grid spacer (CORA-13)

Slot Number	Elevation [mm]	Direction of TE
130	860	210°
221	860	30°
137	475	210°

Positions of thermocouples at the grid spacer (CORA-13)

Slot Number	Elevation [mm]	Direction of TE
138	475	30°
139	-26	210°
141	-26	30°

Positions of thermocouples for gas (CORA-13)

Slot Number	Elevation [mm]	Direction of TE
223	1350	120°
222	1250	300°

Positions of thermocouples in ceramic tube, shroud outer surface (CORA-13)

Slot Number	Elevation [mm]	Direction of TE
229	1150	210° r
228	1150	120° l
227	950	210° m
226	950	120° m
225	750	210° l
224	750	120° r
230	550	120° r
241	550	210° l
242	350	120° r
243	350	210° l
244	150	120° l
245	150	210° r
142	50	120° l
143	50	210° r

Positions of thermocouples in shroud insulation (CORA-13)

Slot Number	Elevation [mm]	Direction of TE
148	1150	30°
246	950	210°
247	950	30°
248	950	210°
249	750	30°
250	750	210°
251	550	210°
252	550	210°
253	550	30°
144	350	210°
145	350	30°
146	150	210°
147	50	30°

Table 7: Position of Thermocouples

Table 8: **Range of measured ZrO_2 scale thickness at different axial elevations of the CORA-13 bundle, given as minimum/average/ maximum values in μm; in addition single values are given for elevations 448 mm and above**

148 mm:	8 / 16,3 / 24 μm
248 mm:	25 / 63,2 / 120 μm
348 mm:	130 / 520 / 1150 μm
398 mm:	420 / 910 / 1150 μm
448 mm:	650 / 1120 / 1150 μm

single values

448 mm:	1094, 1330, 1860 (shoud)
498 mm:	1500 (melt agglomeration)
548 mm:	1575 (melt aggl.), 770 (clad melt relocation), 1100 - 1200
698 mm:	1525 (melt aggl.), 900, 400 (clad melt relocation)
848 mm:	920, 950
998 mm:	no residues of completely converted cladding

Table 9: **Coarse estimation of axial distribution and lateral variation range of peak temperatures in the bundle CORA-13 as based on ZrO_2 scale thickness measurements; minimum / average / maximum values in °C**

Elevation (mm)	Peak temperature lower limit / average / higher limit (°C)
148	920 / 1000 / 1050*
248	1060 /1260 / 1420
348	1450 / 1610 / 1700*,[1]
398	1590 / 1660 / >1700[2]
448	1630 / 1700 / > 1700[3]

**: measured temperature values available*

1: clad melting indicates T > 1760 °C

2: Zr/ZrO_2 eutectic indicates T > 1900 °C

3: α-Zr(O) liquid indicates T > 2000 °C

Table 10: **Lateral variation of ZrO_2-scale thickness in μm, diagonally across the bundle CORA-13, at different axial elevations; maximum and minimum values for shroud and fuel rods are given in parentheses**

elevation (mm)	shroud ext.	shroud int.	1.1 left	1.1 right	2.2 left	2.2 right	3.3 left	3.3 right	4.4 left	4.4 right	5.5	6.6	7.7
448	650 (45-650)	1100 (750-1340)	compl. conv.		compl. conv.		compl. conv.		compl. conv.		melt	c.c.	c.c.
398	450 (50-640)	450 (400-750)	550 (530-680)	650	600 (600-900)	900	compl. conv.		compl. conv.		melt	c.c.	c.c. (melt)
348	120 (50-470)	120 (120-800)	130 (130-132)	130	190 (150-500)	500	550 (400-800)	720	not measurable		c.c.	c.c.	(680-820)
248	22 (22-78)	22 (22-80)	25 (25-28)	28	30 (30-50)	50	50 (50-75)	64	65 (65-78)	78	(86-95)	(96-120)	(80-85)
148	6 (6-16)	6 (6-16)	8 (8-10)	9	8 (8-12)	12	14 (14-20)	16	16 (16-22)	22	(20-24)	(20-24)	(16-20)

List of Figures

APPENDIX

Data of the pre-transient phase of test CORA-13

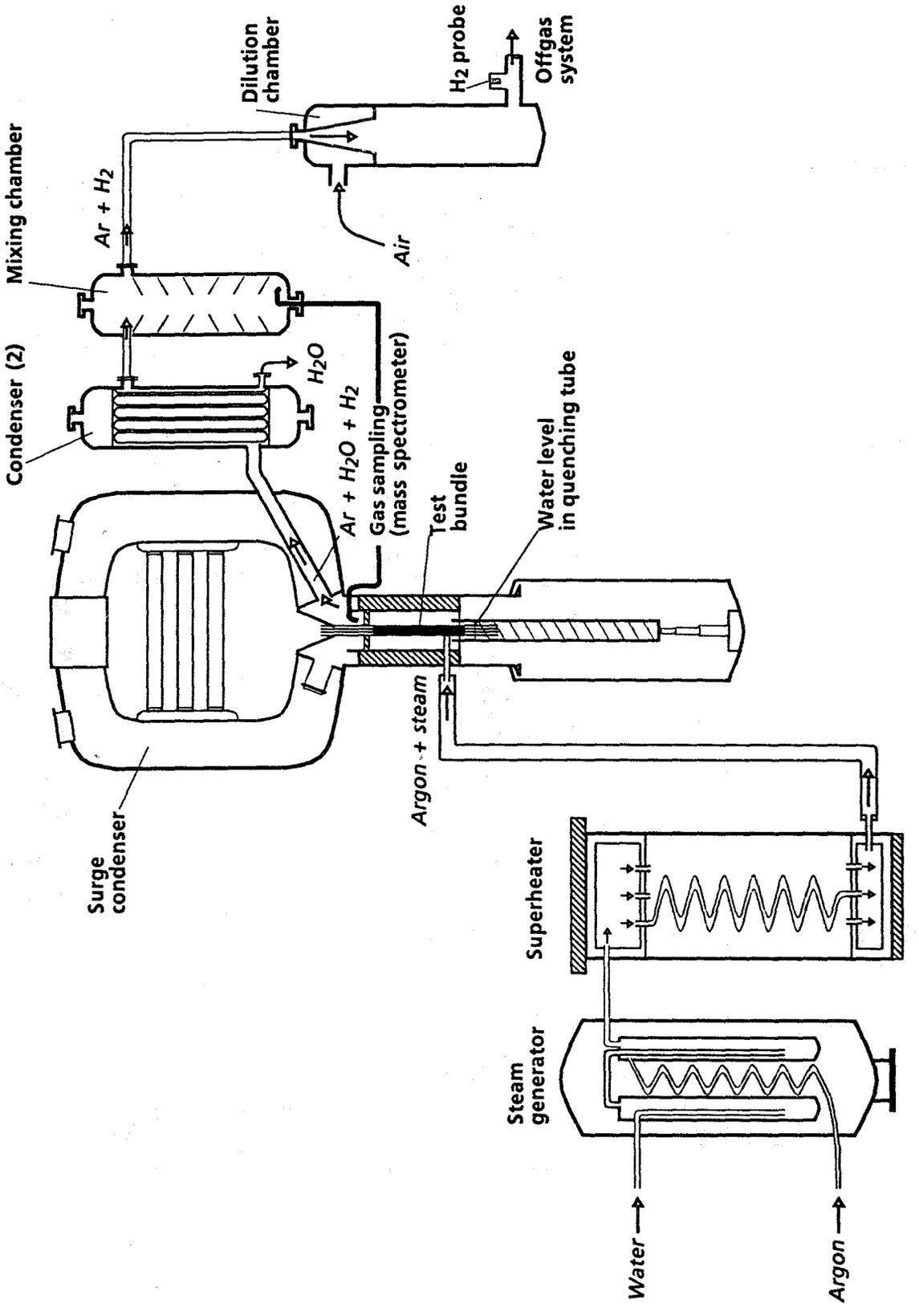

Fig. 1: SFD Test Facility (Simplified flow diagram)

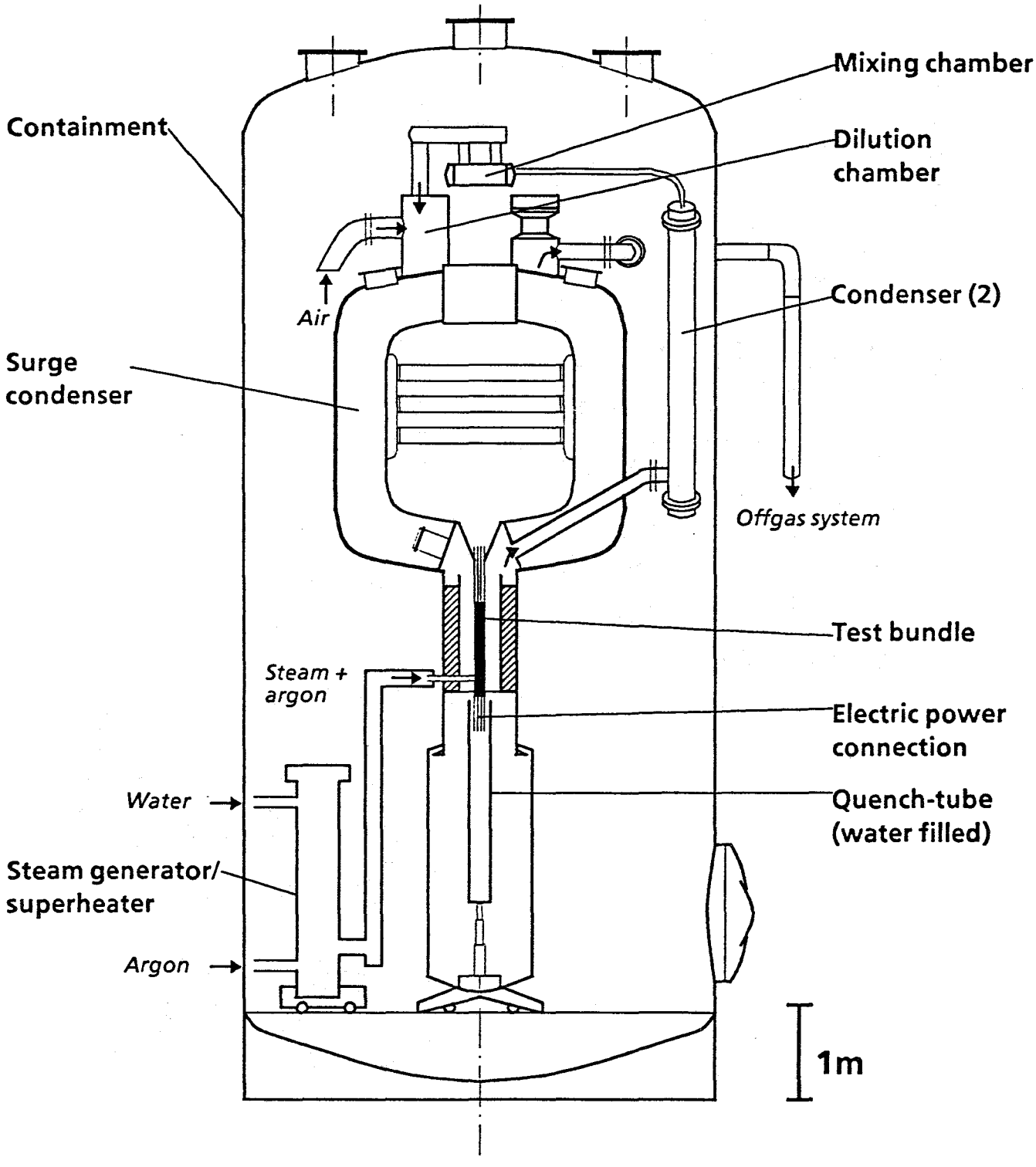

Fig. 2: SFD Test Facility CORA (Main components)

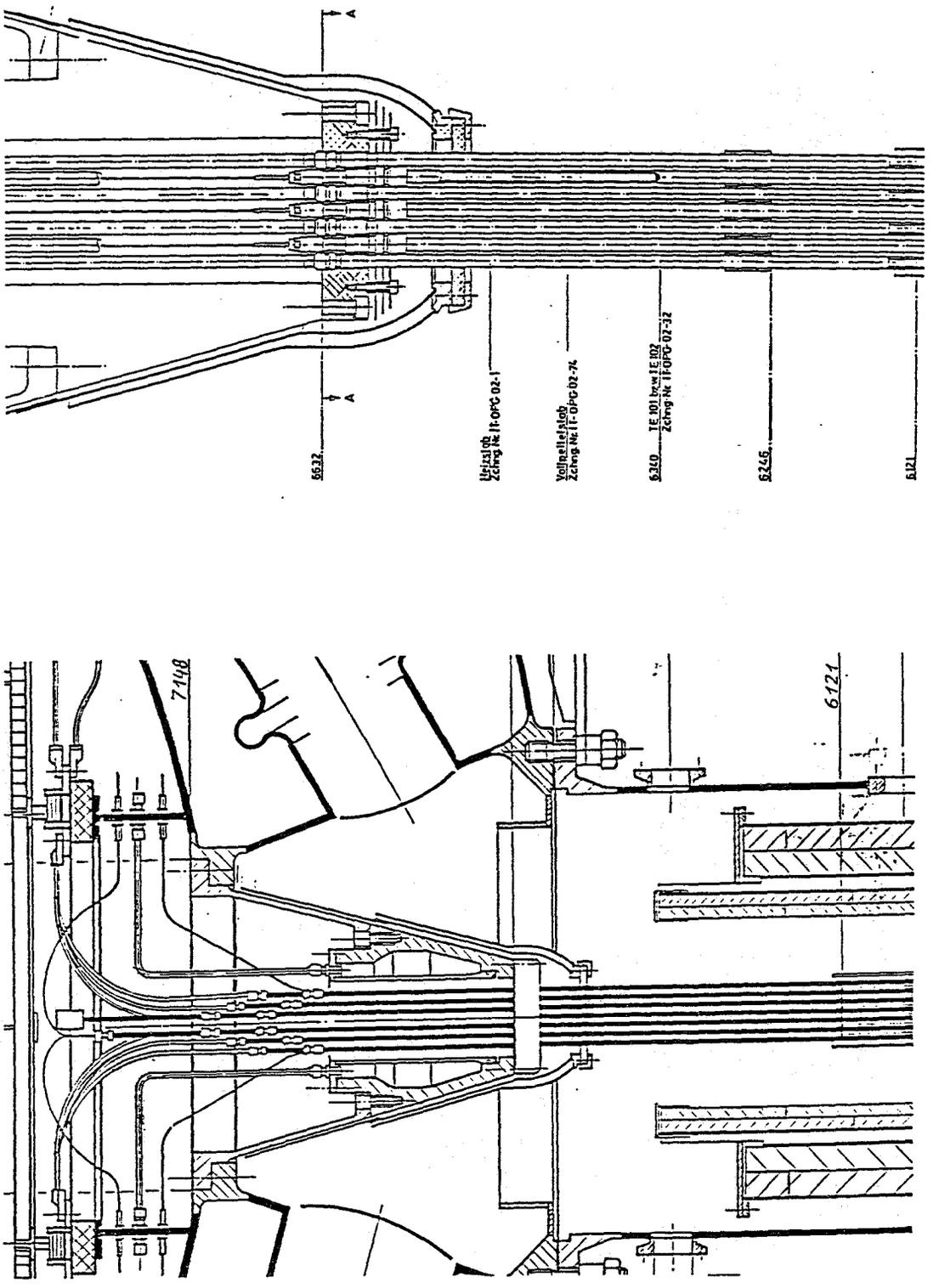

Fig. 3: High temperature shield with bundle; upper end

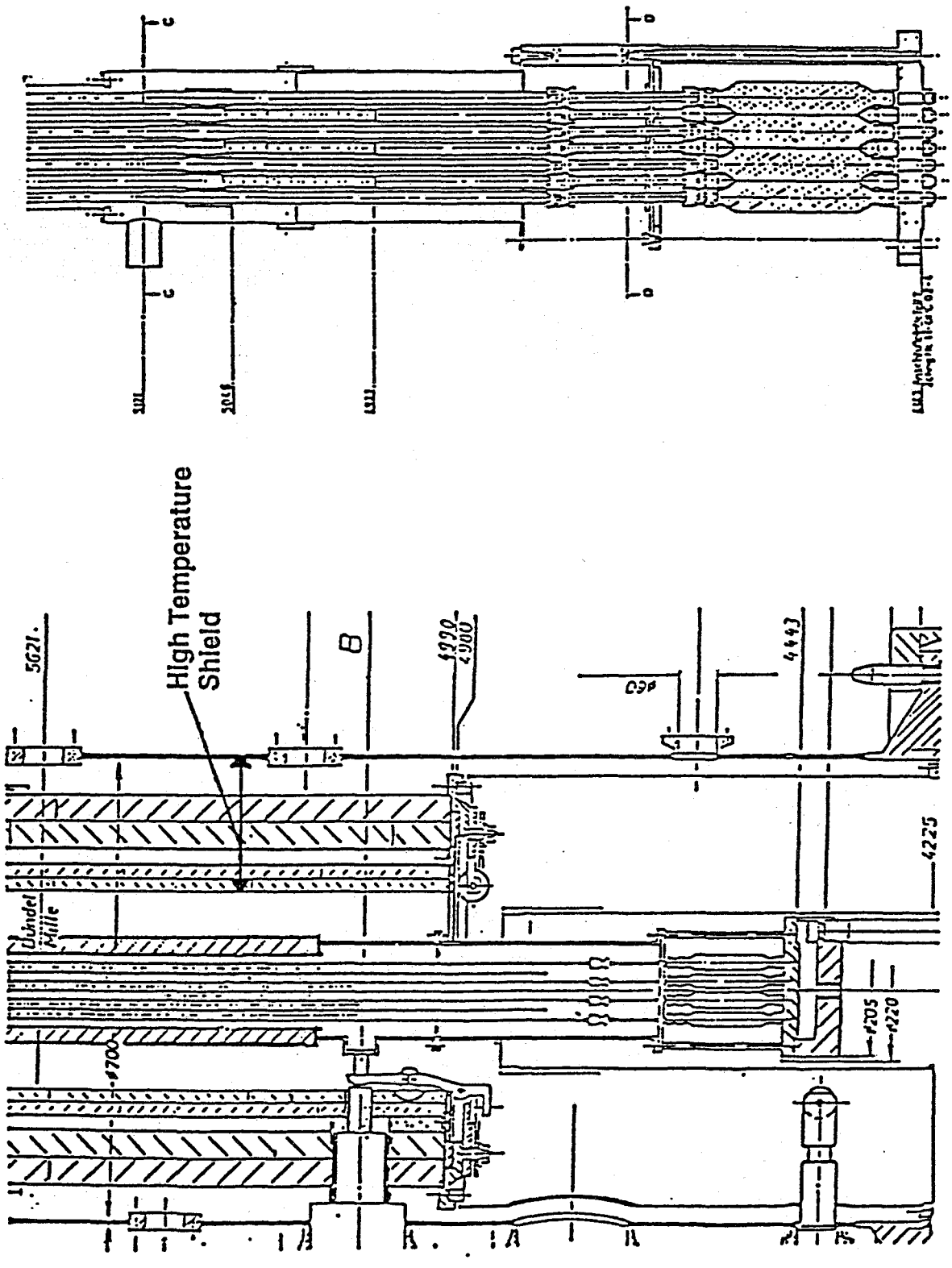

Fig. 4: **High temperature shield with bundle; lower end**

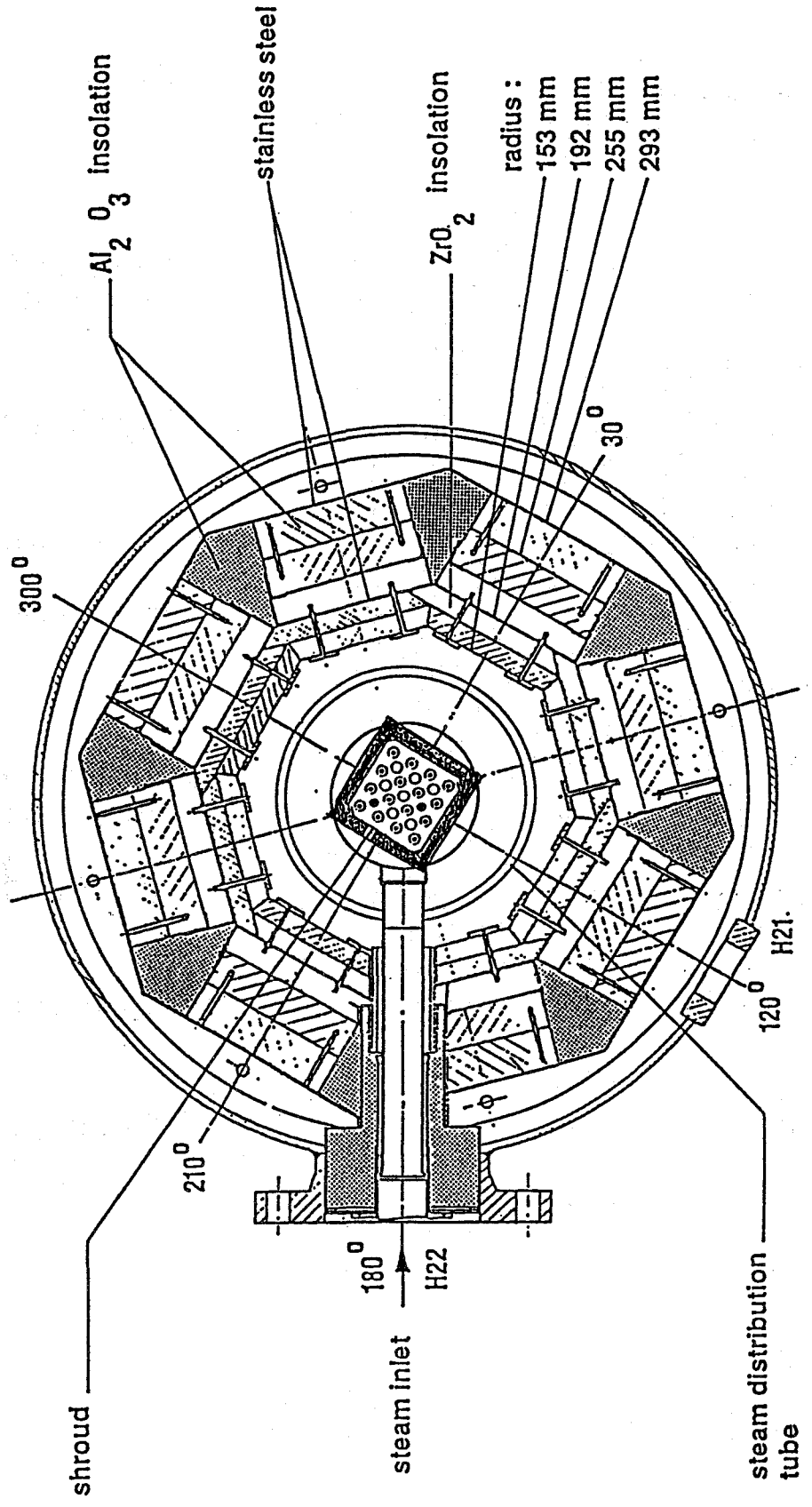

Fig. 5: Horizontal cross section of the high temperature shield

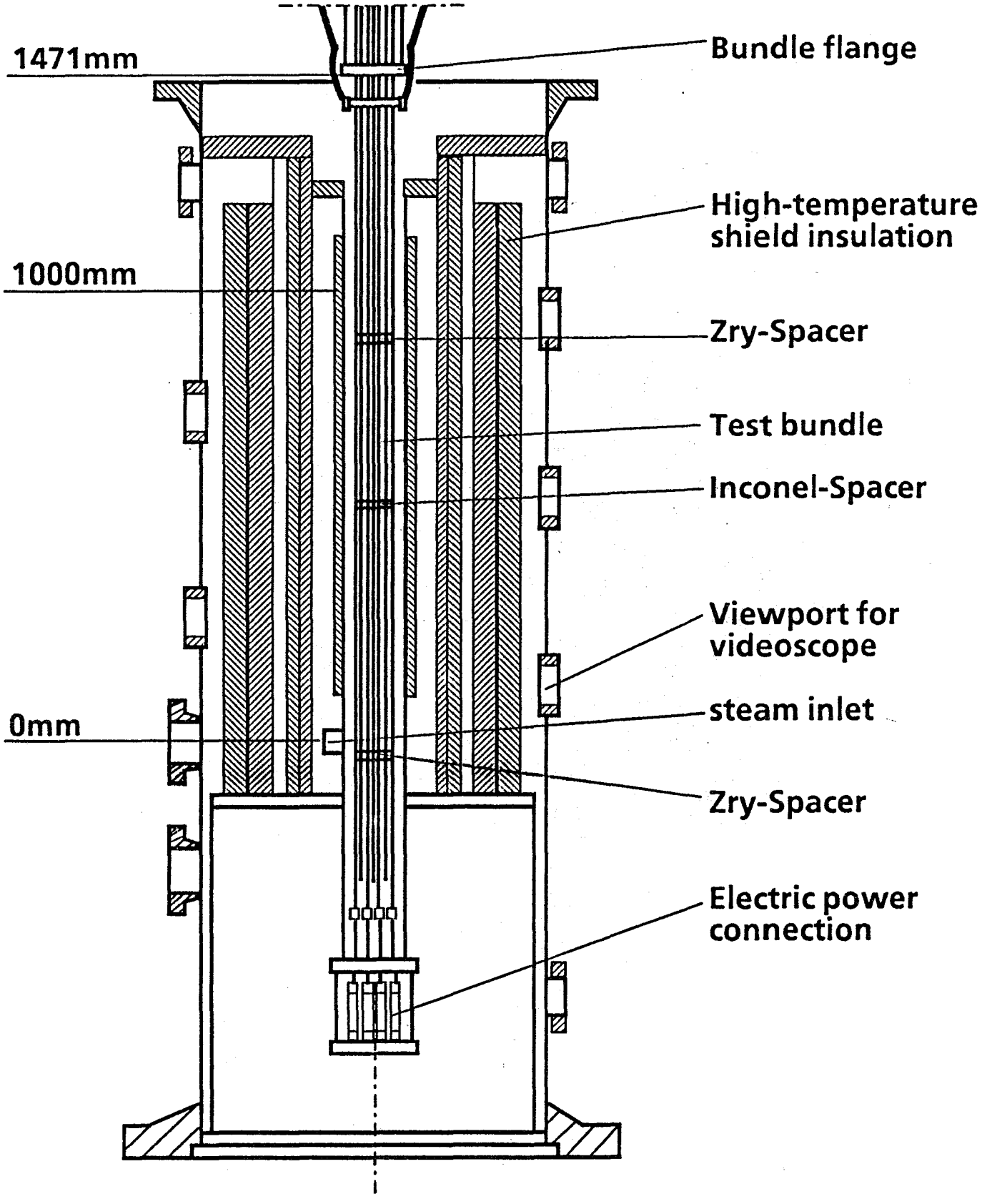

Fig. 6: CORA bundle arrangement

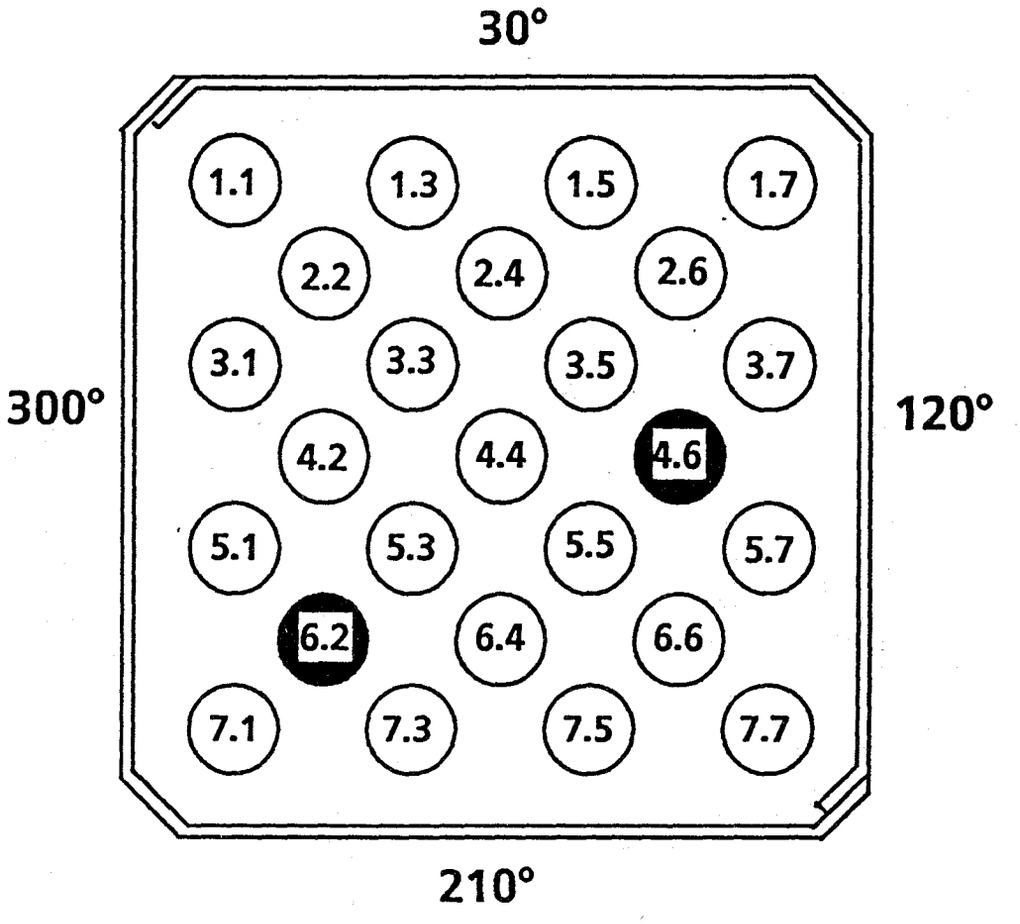

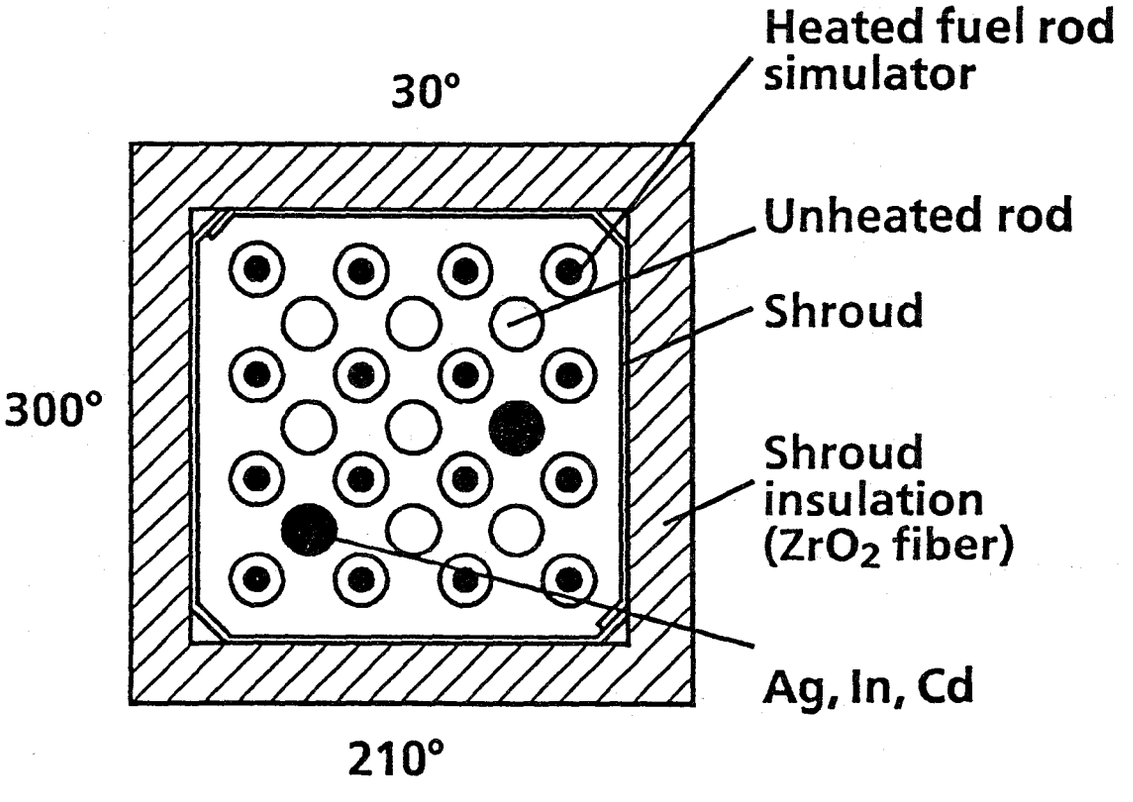

Fig. 7: Rod designation of test bundle CORA-13

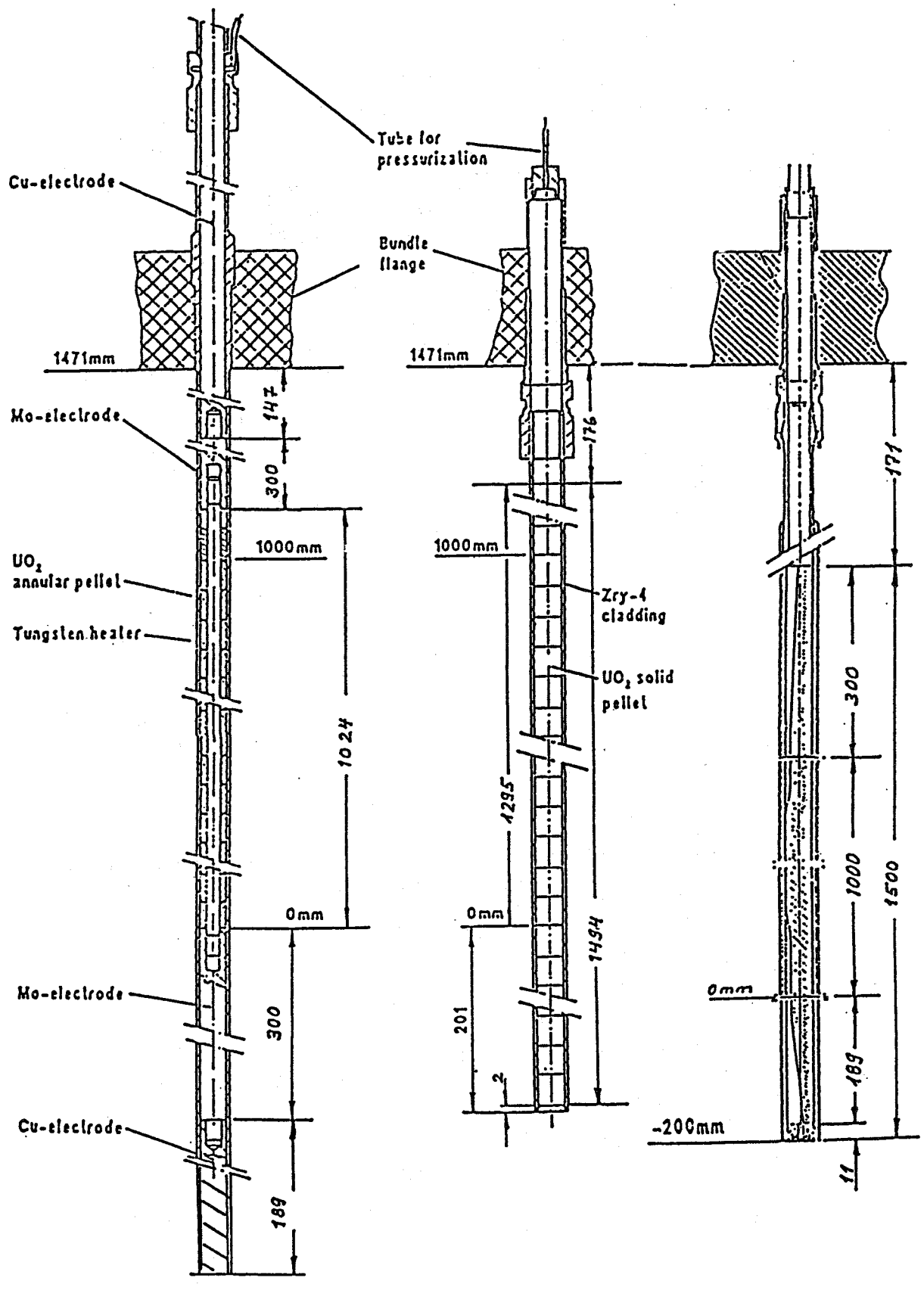

Fig. 8: Rod types used in the CORA experiments

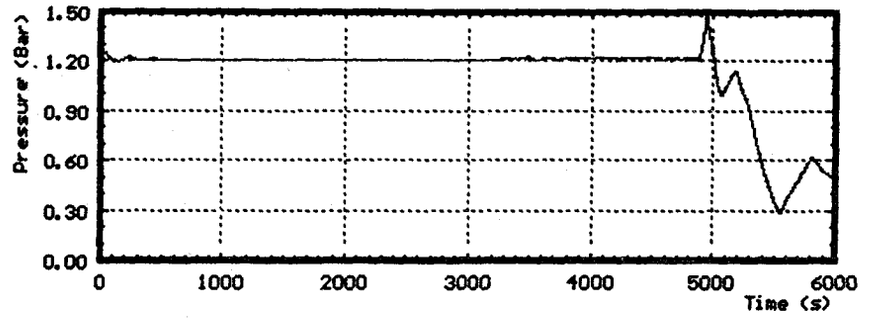

system overpressure

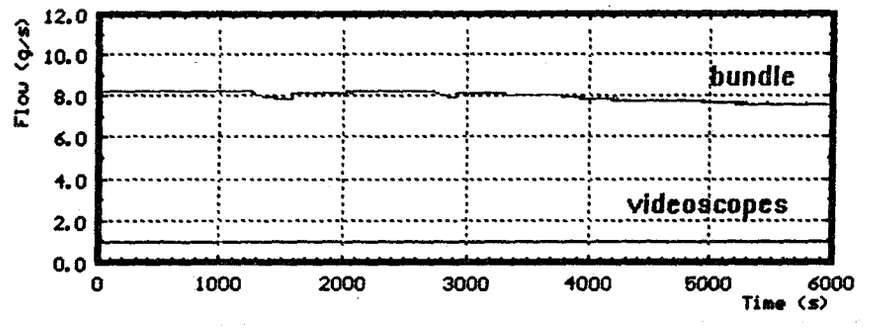

Argonflow

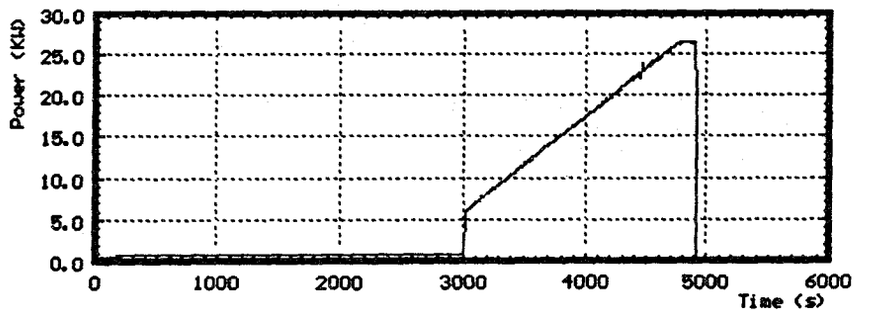

power

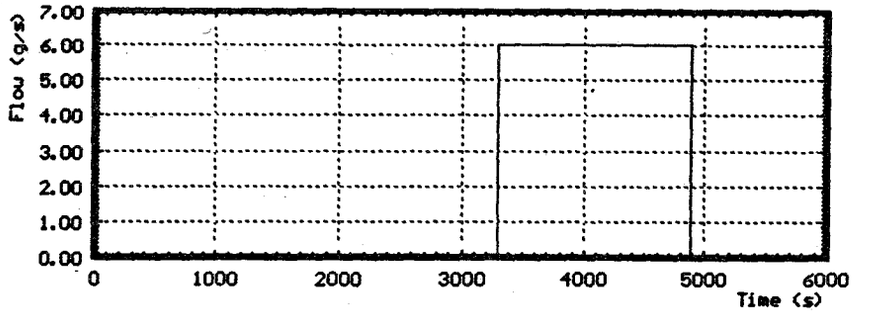

steam production

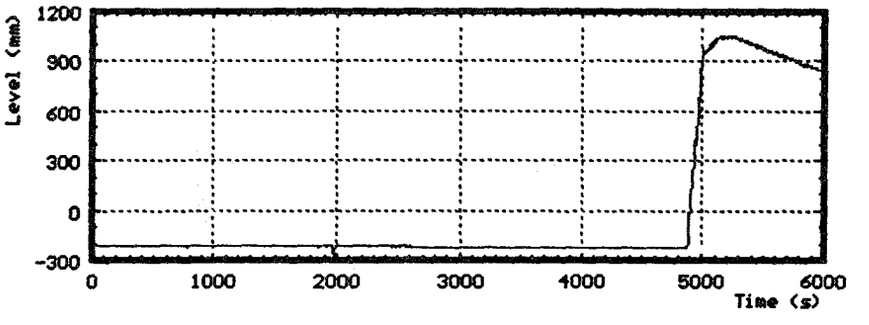

quench level

Fig. 9: System pressure, argonflow, steam input, power, and quench level during test CORA-13

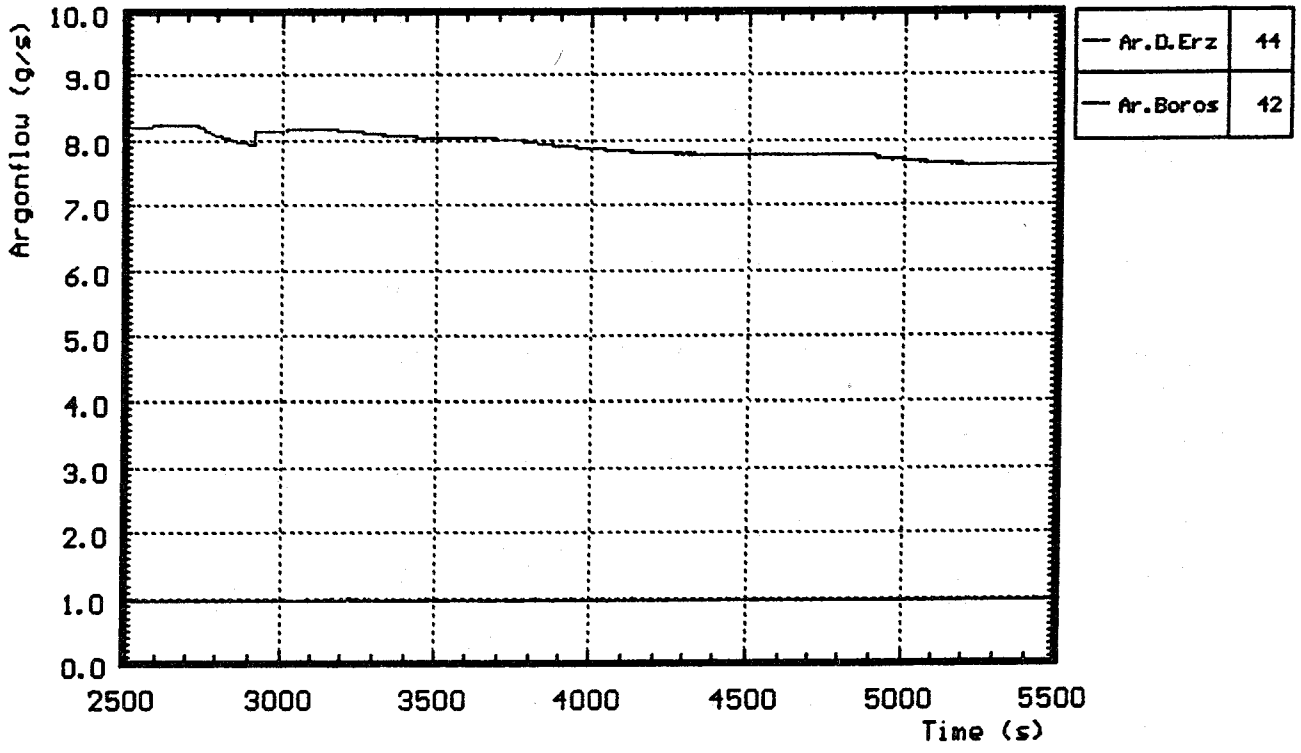

Fig. 10: Argonflow through bundle and videoscopes (CORA-13)

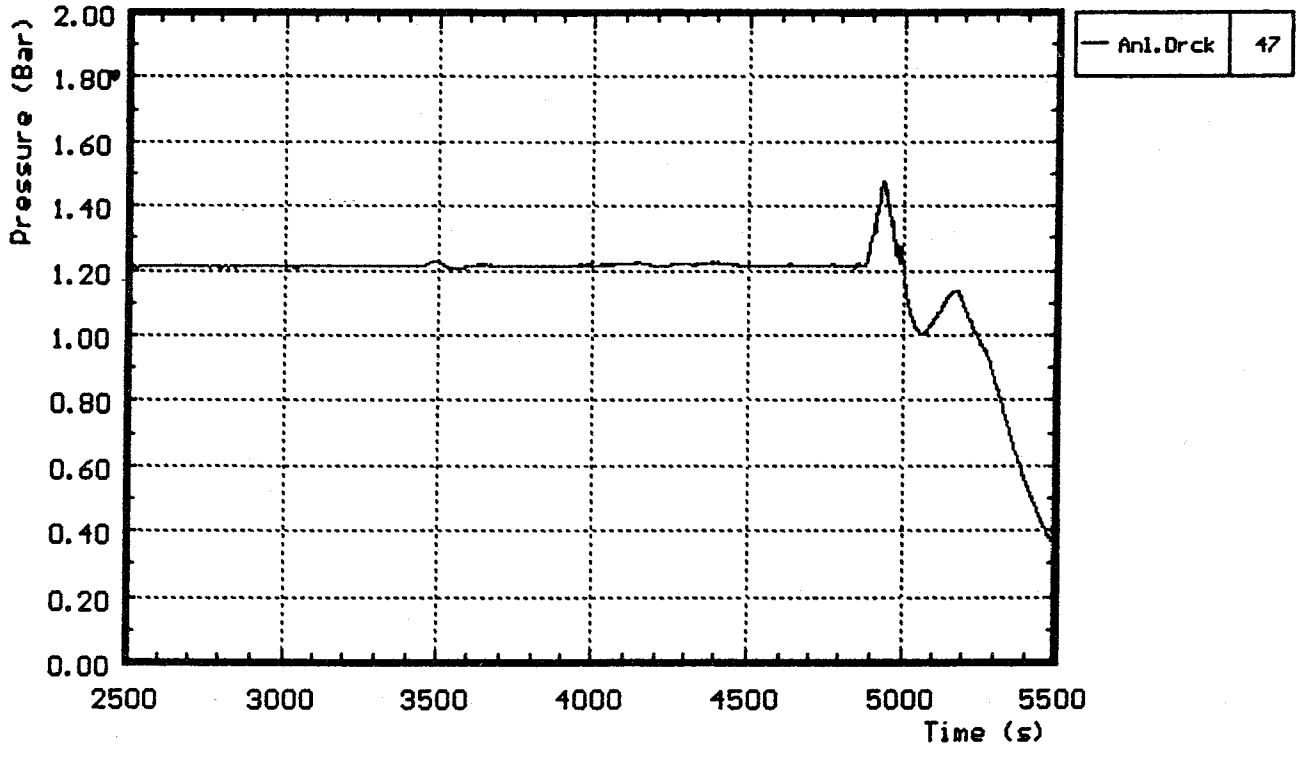

Fig. 11: System overpressure (CORA-13)

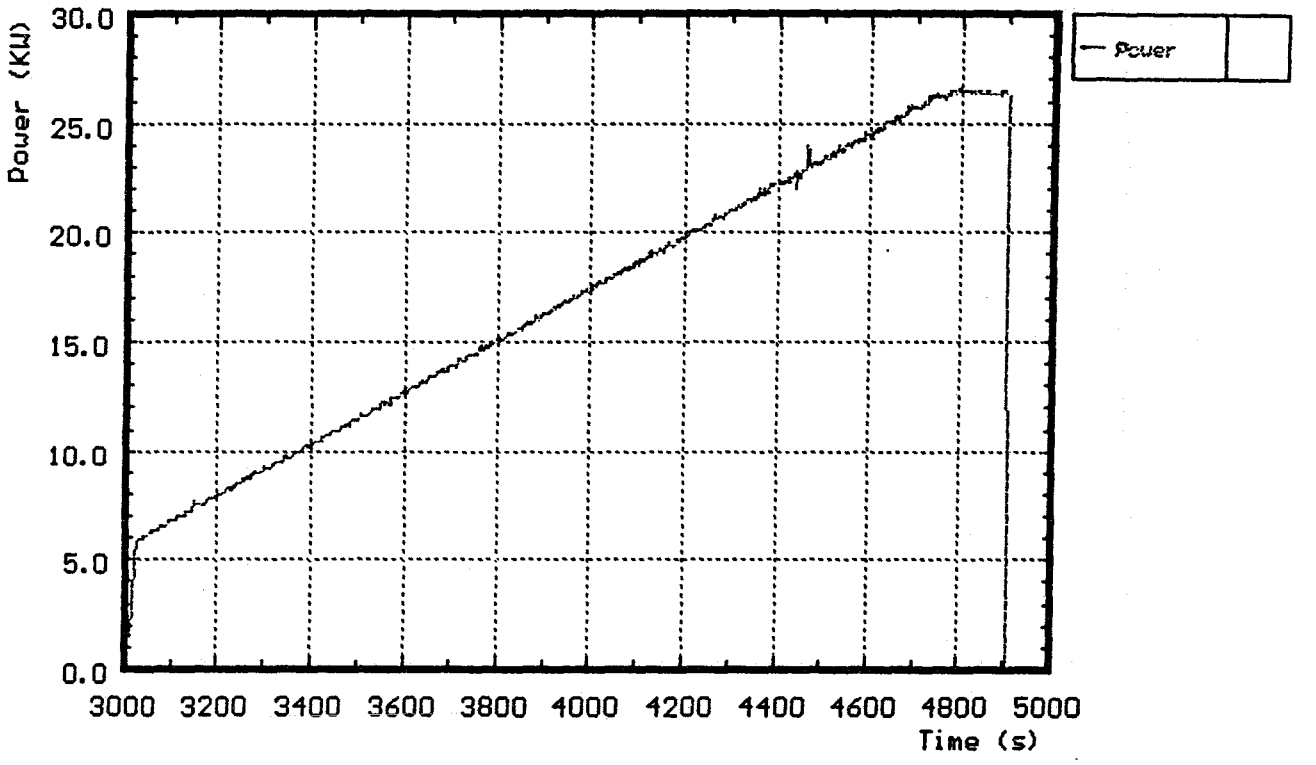

Fig. 12: Electric power input (CORA-13)

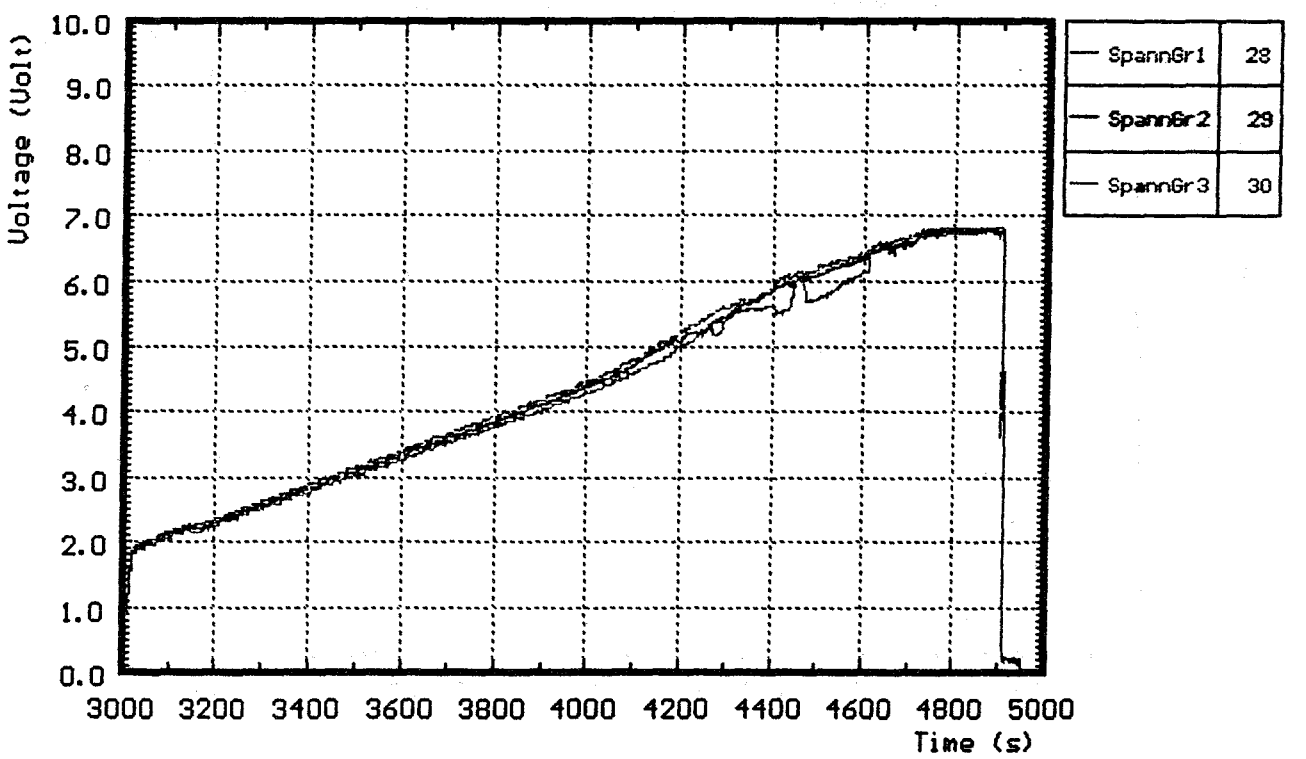

Fig. 13: Voltage input for the 3 rod groups (CORA-13)

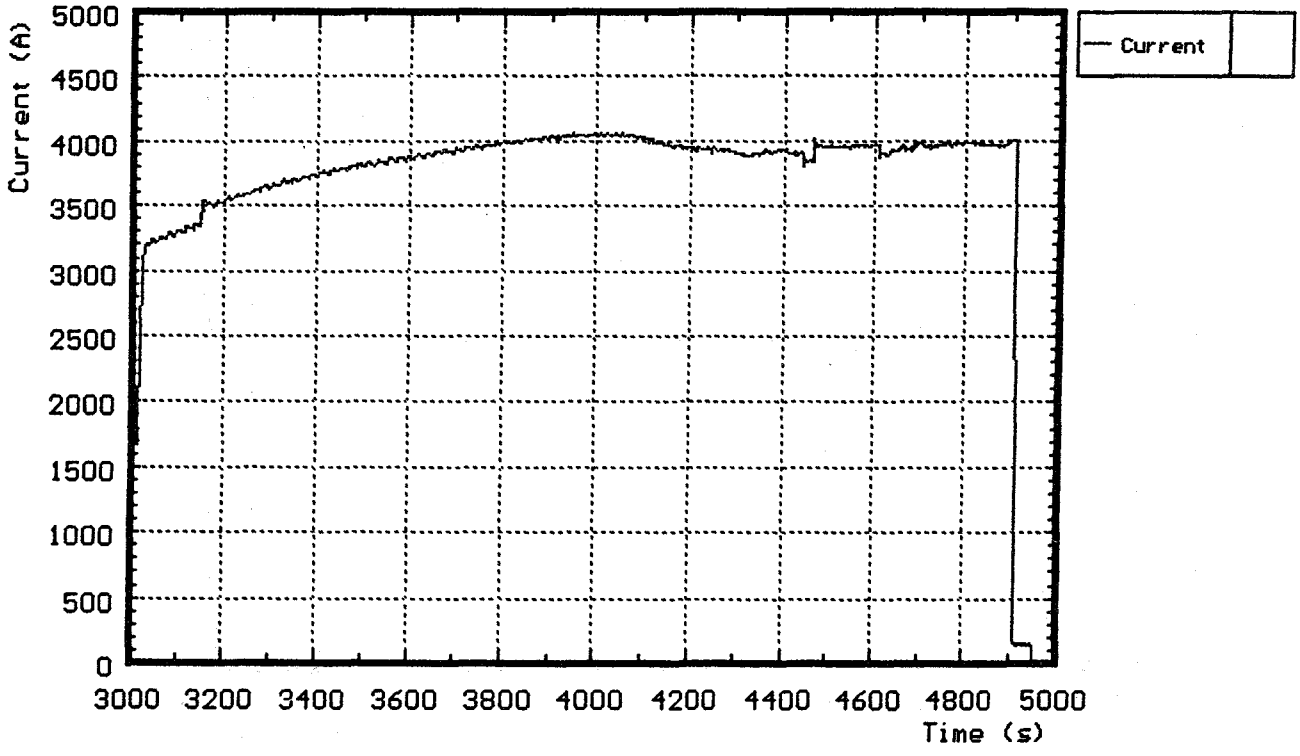

Fig. 14: Total electric current (CORA-13)

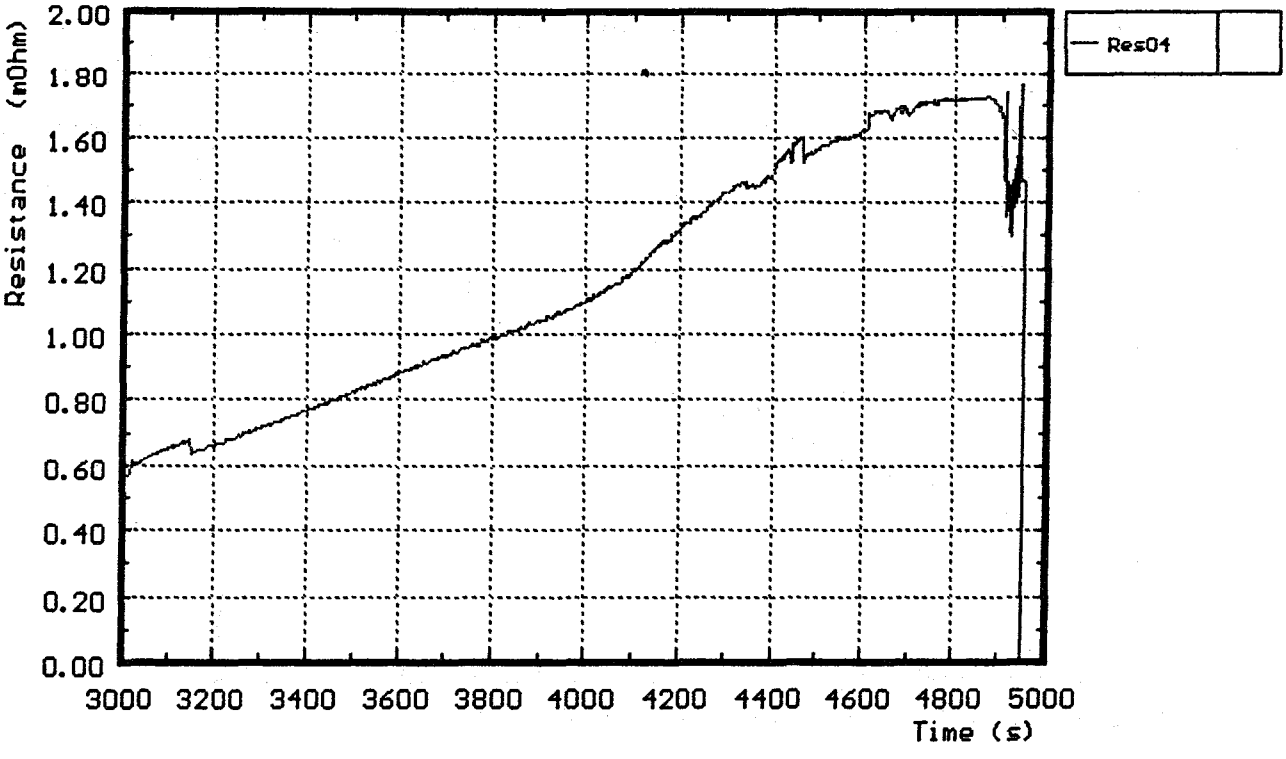

Fig. 15: Total Resistance of heaters (CORA-13)

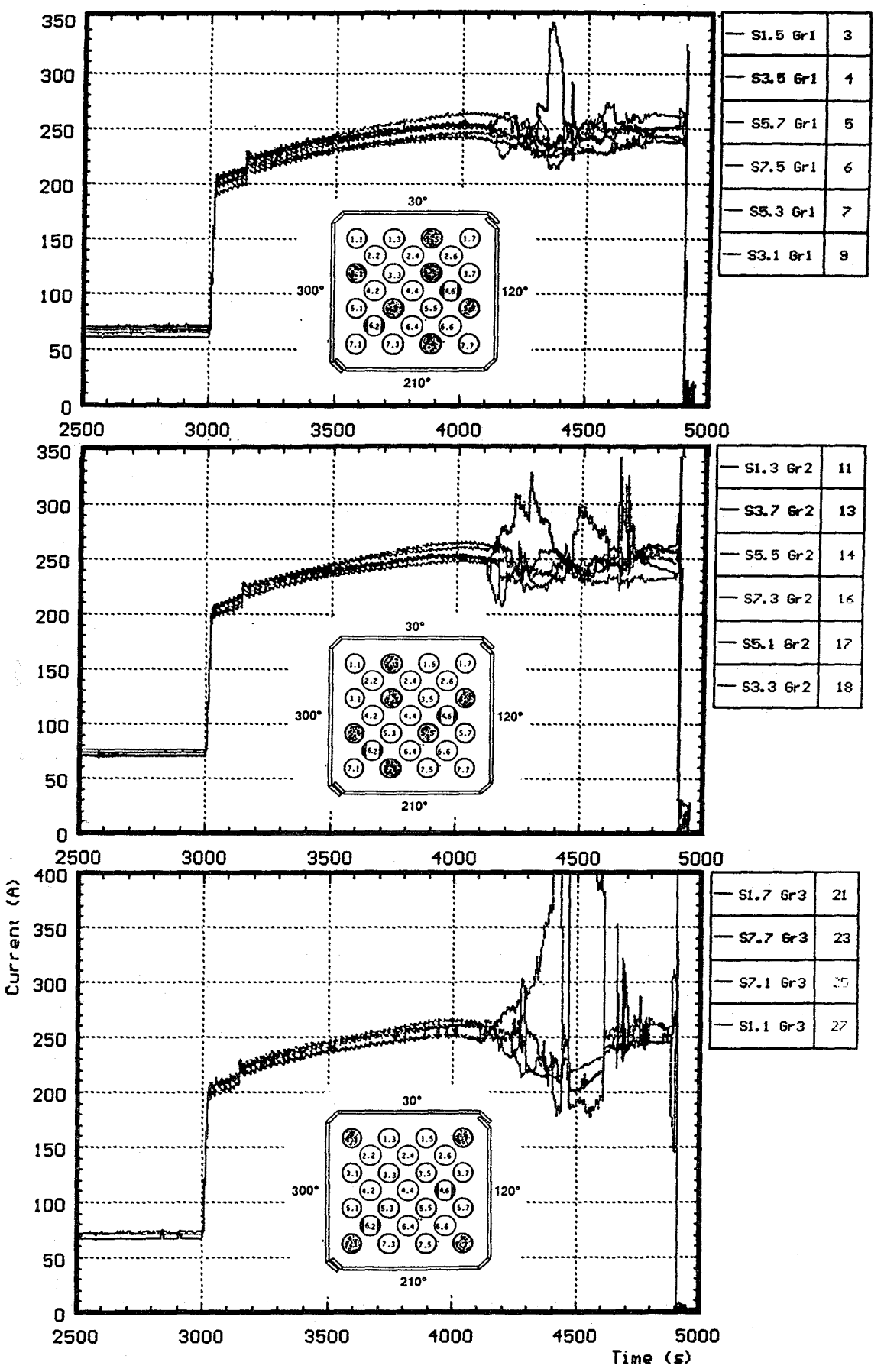

Fig. 16: Readings of currents within the three rod groups (CORA-13)

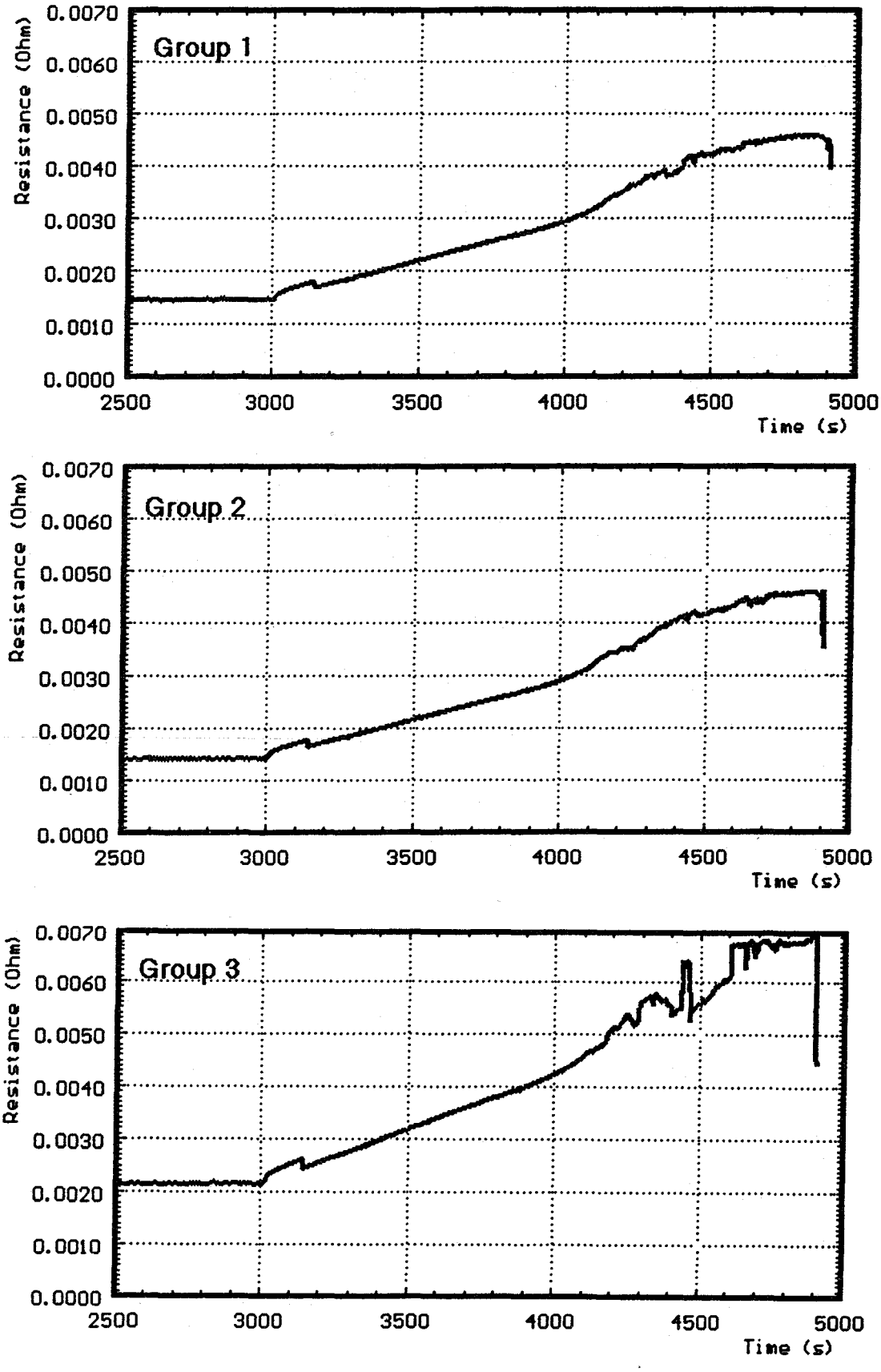

Fig. 17: Resistance of rod groups 1, 2 and 3 (CORA-13)

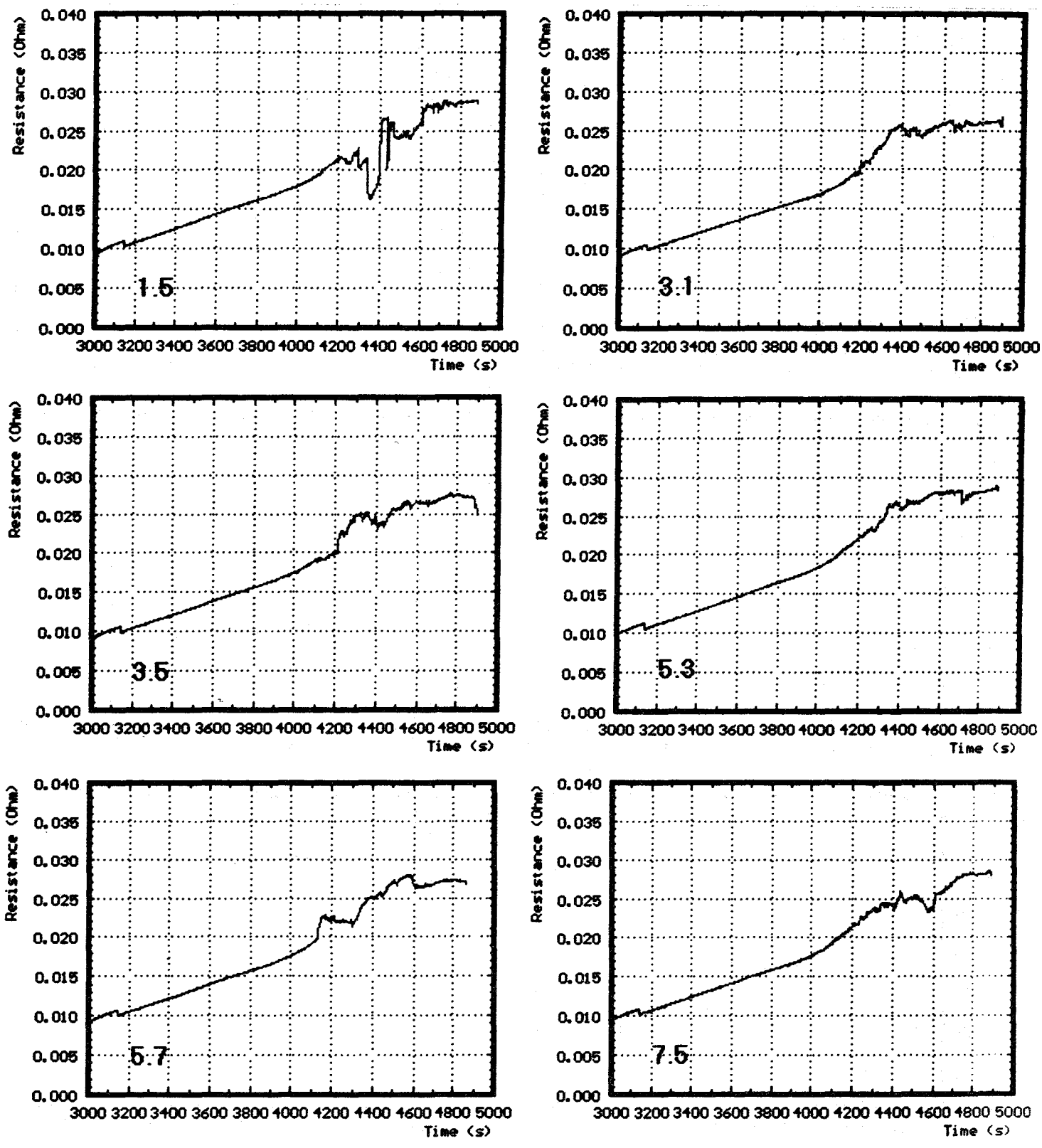

Fig. 18: Resistance of the single rods of group 1 (CORA-13)

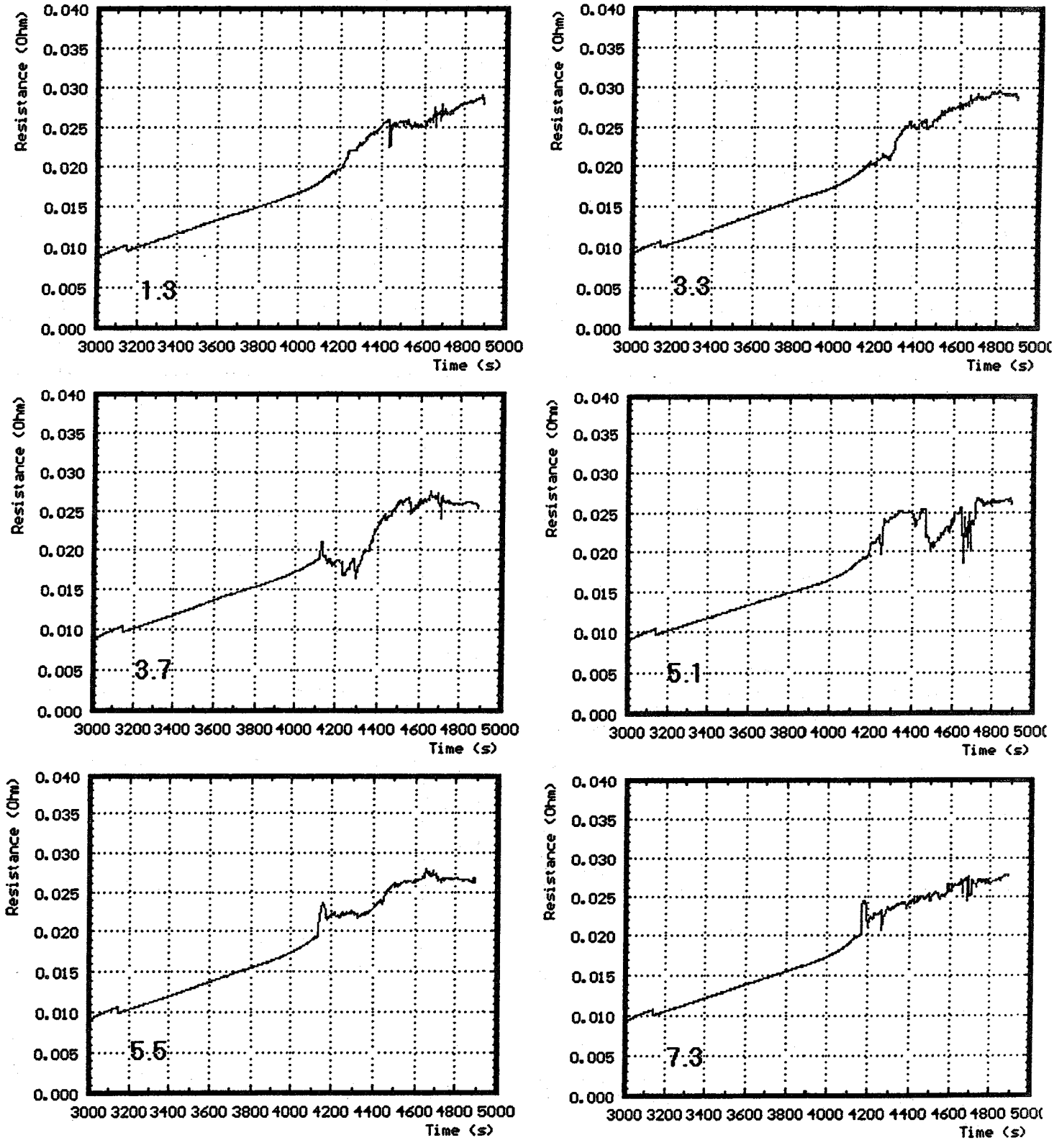

Fig. 19: Resistance of the single rods of group 2 (CORA-13)

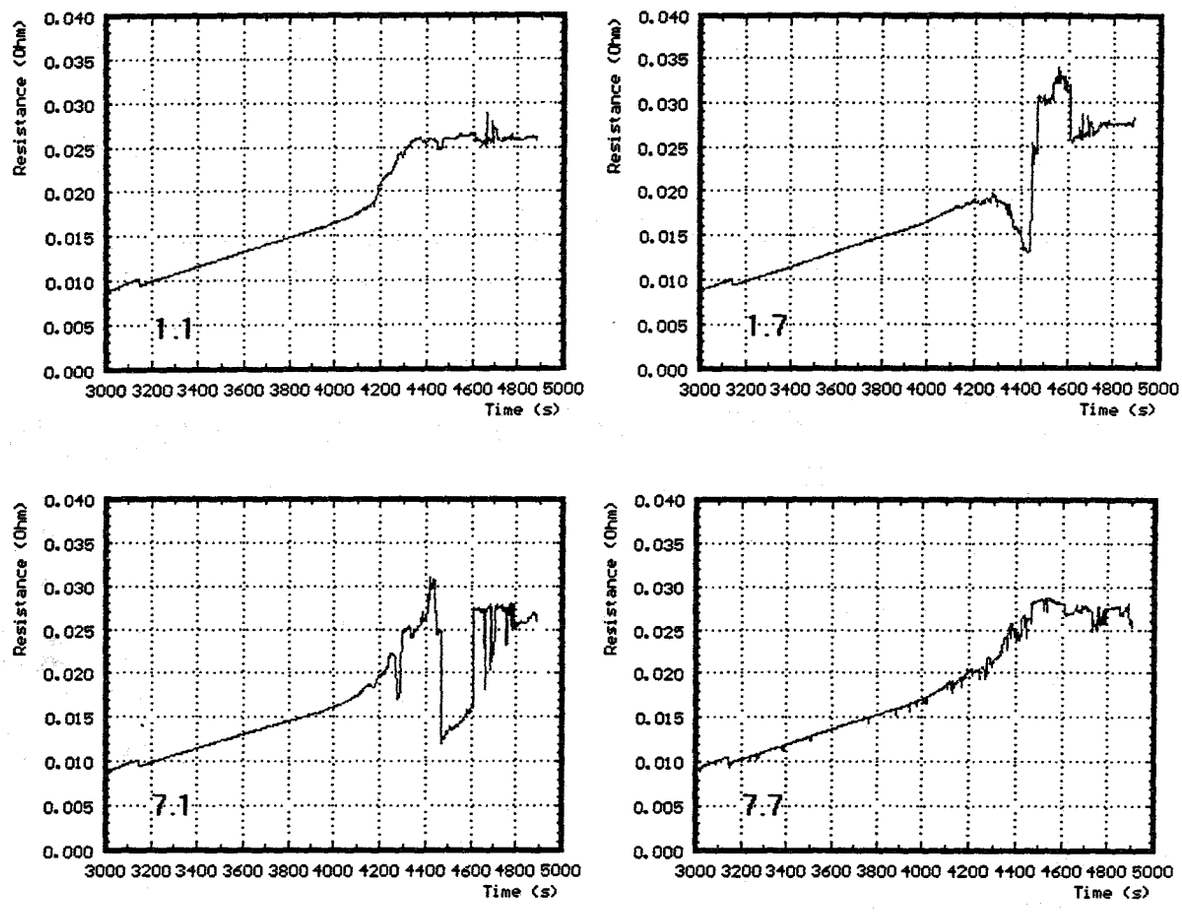

Fig. 20: Resistance of the single rods group 3 (CORA-13)

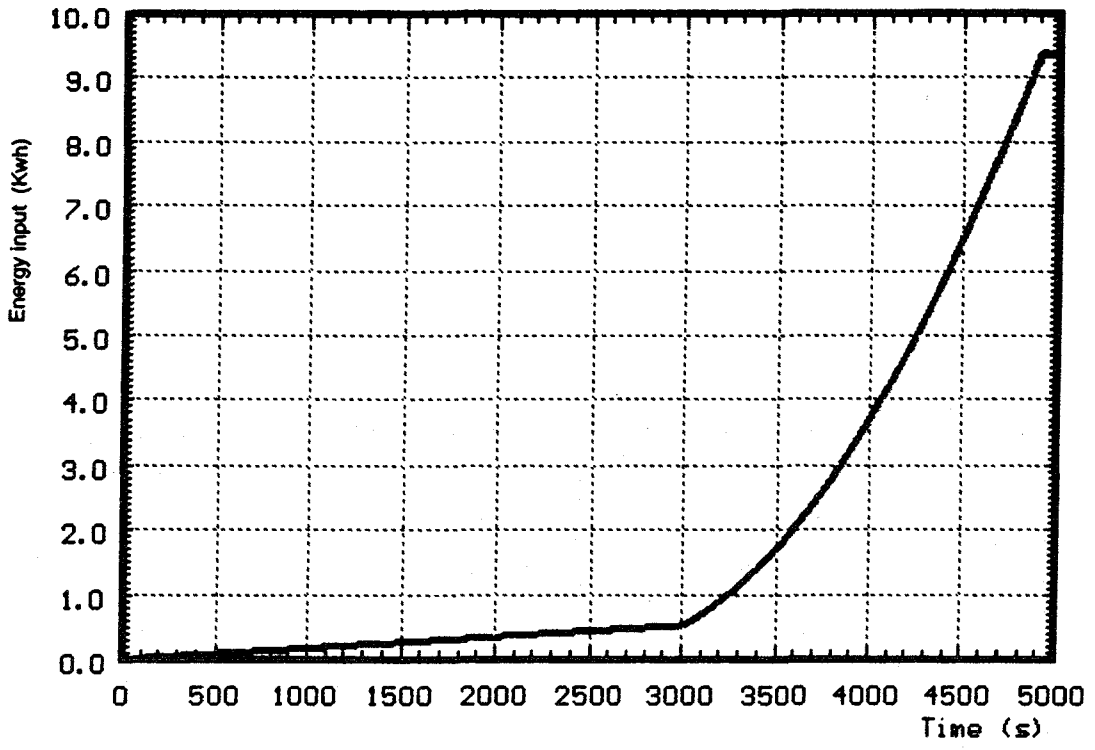

Fig. 21: Energy input for the entire test time of CORA-13

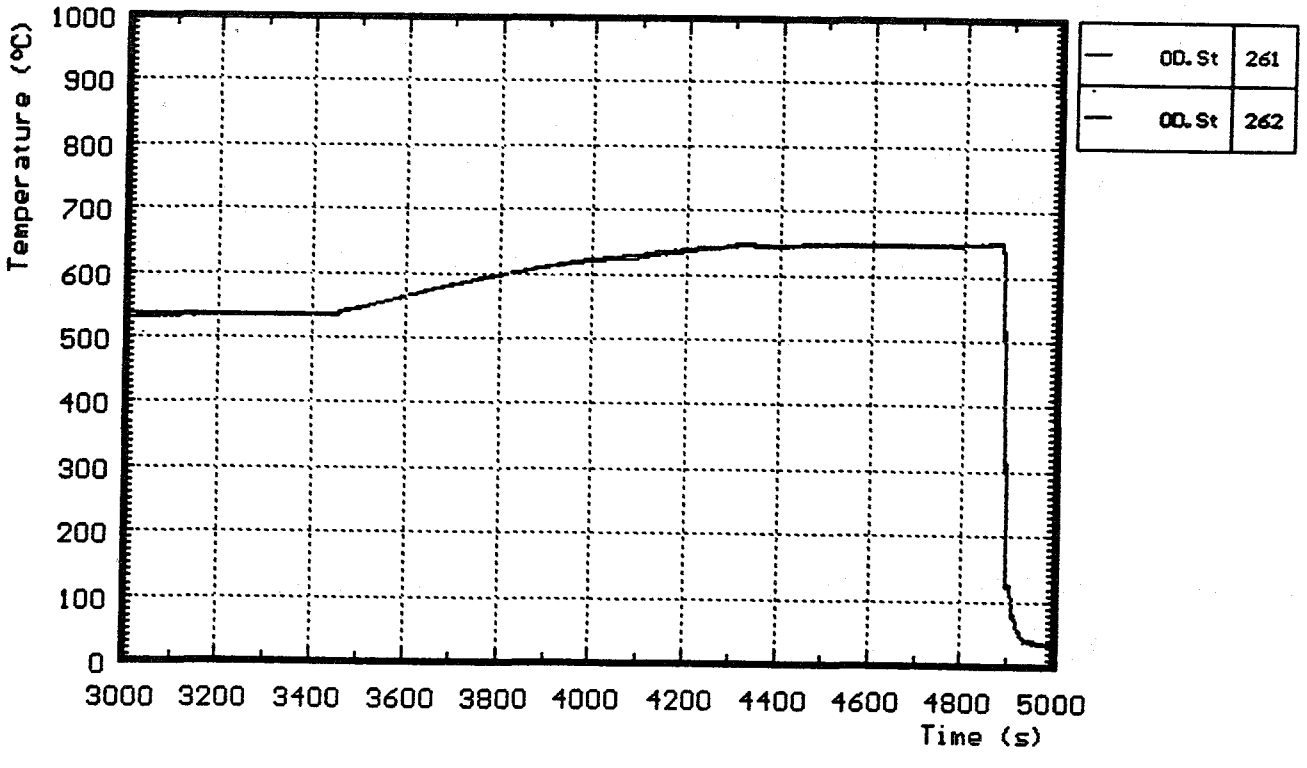

Fig. 22: Temperatures at steam inlet (CORA-13)

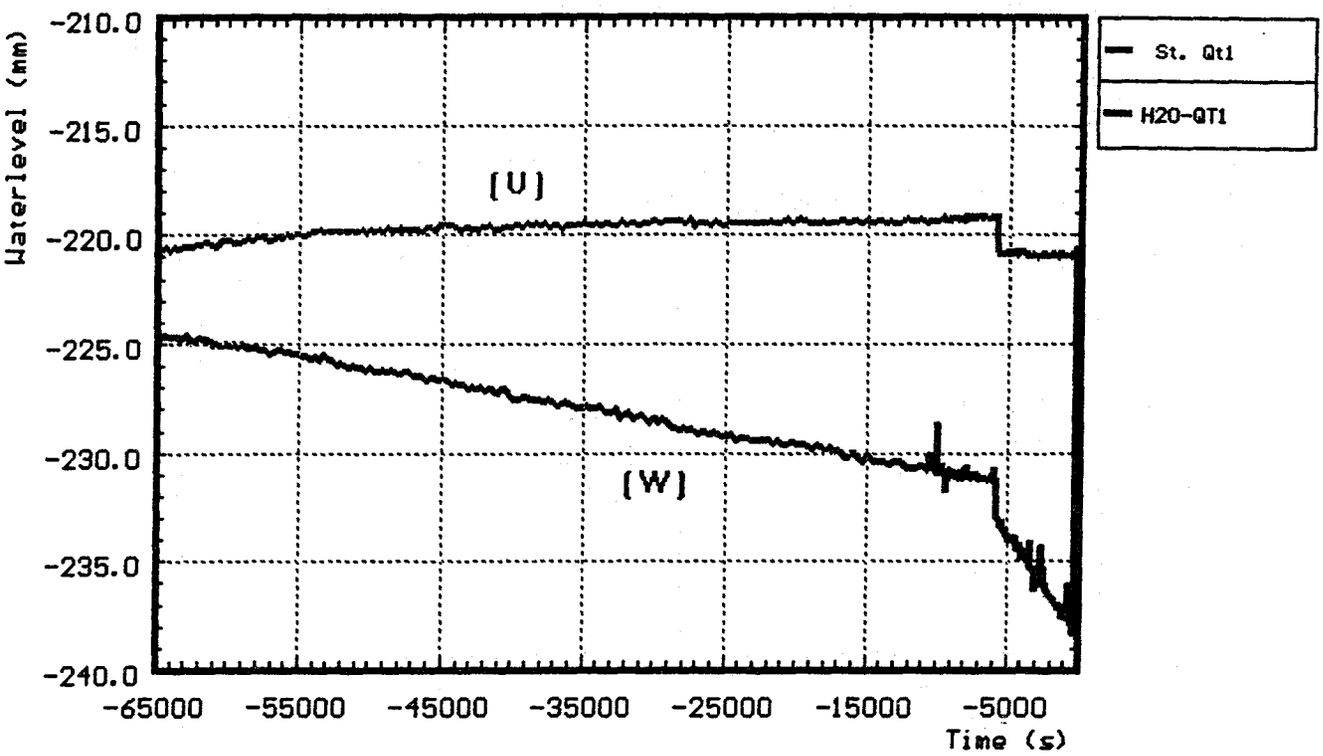

Fig. 23: Changes of water level as a function of time prior to transient of CORA-13

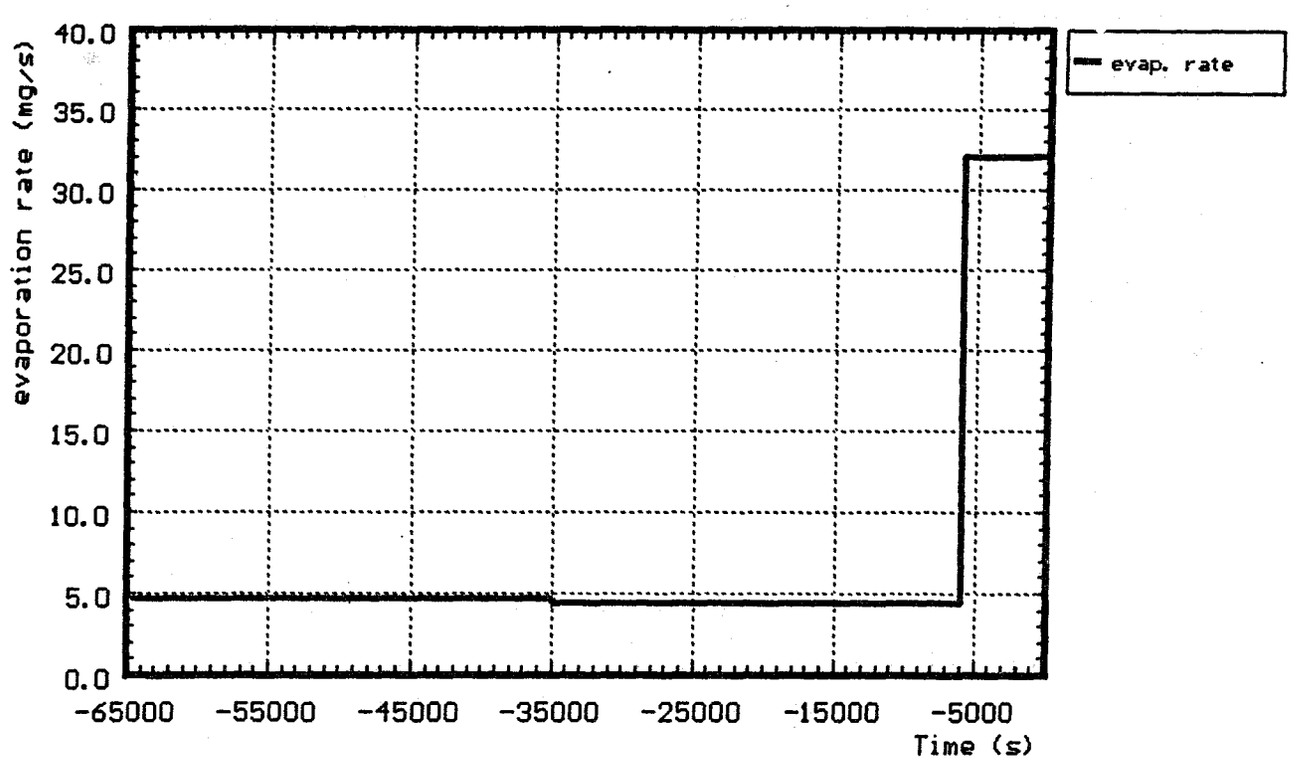

Fig. 24: Evaporation rate as a function of time prior to transient of CORA-13

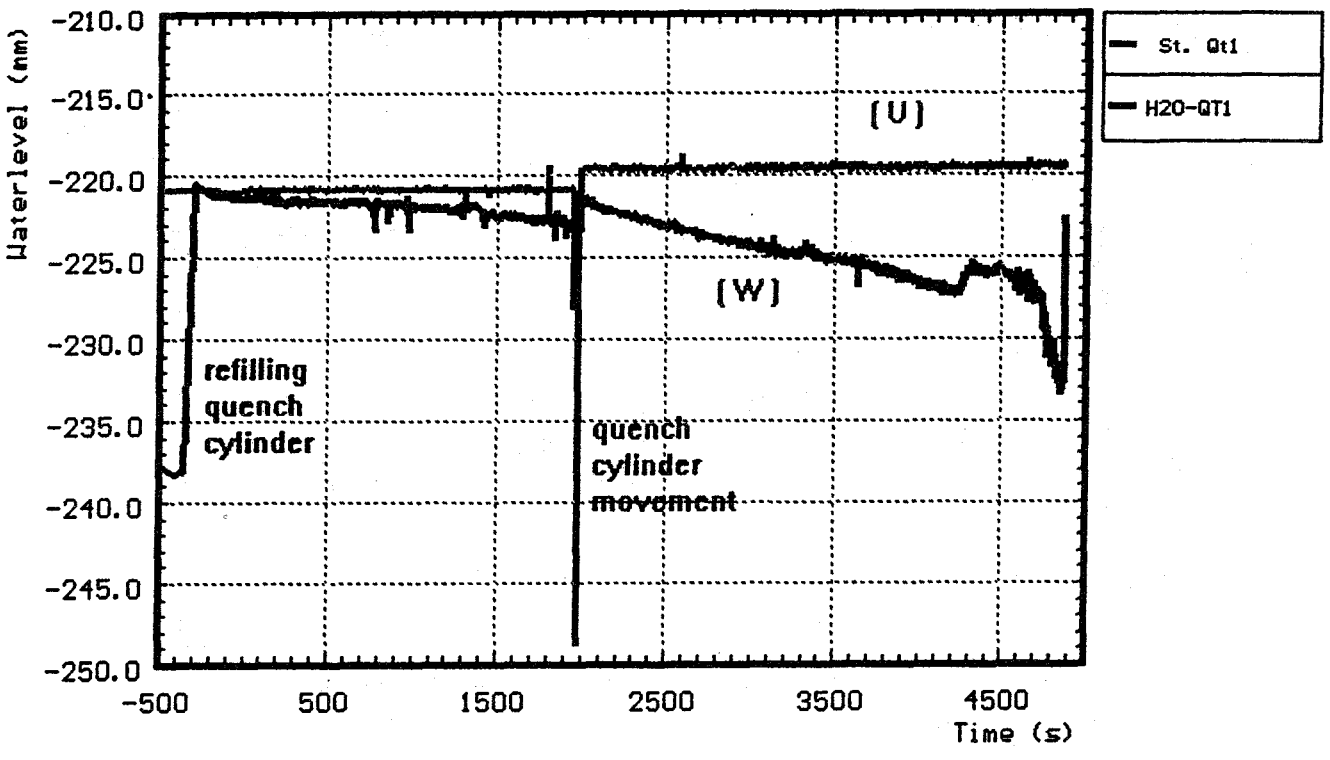

Fig. 25: Upper edge of quench cylinder (U) and waterlevel (W) (CORA-13)

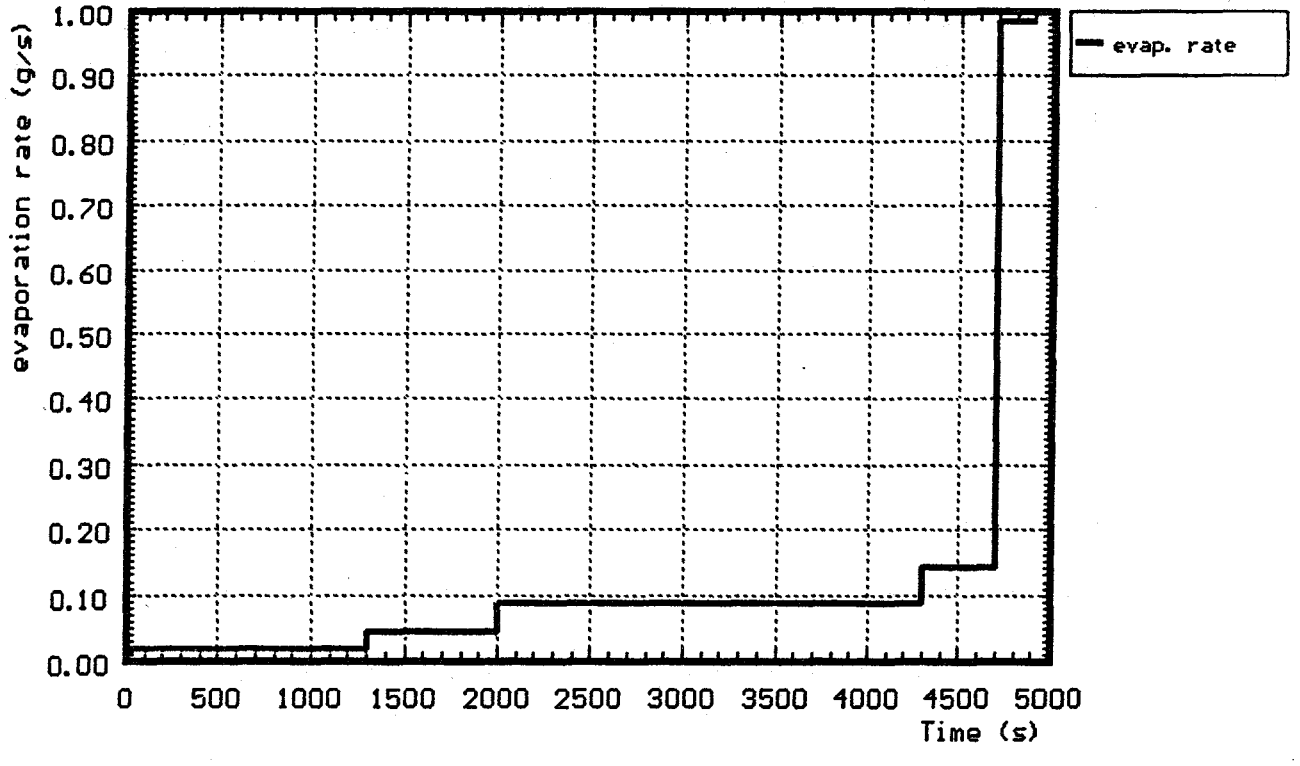

Fig. 26: Evaporation rate during the transient (CORA-13)

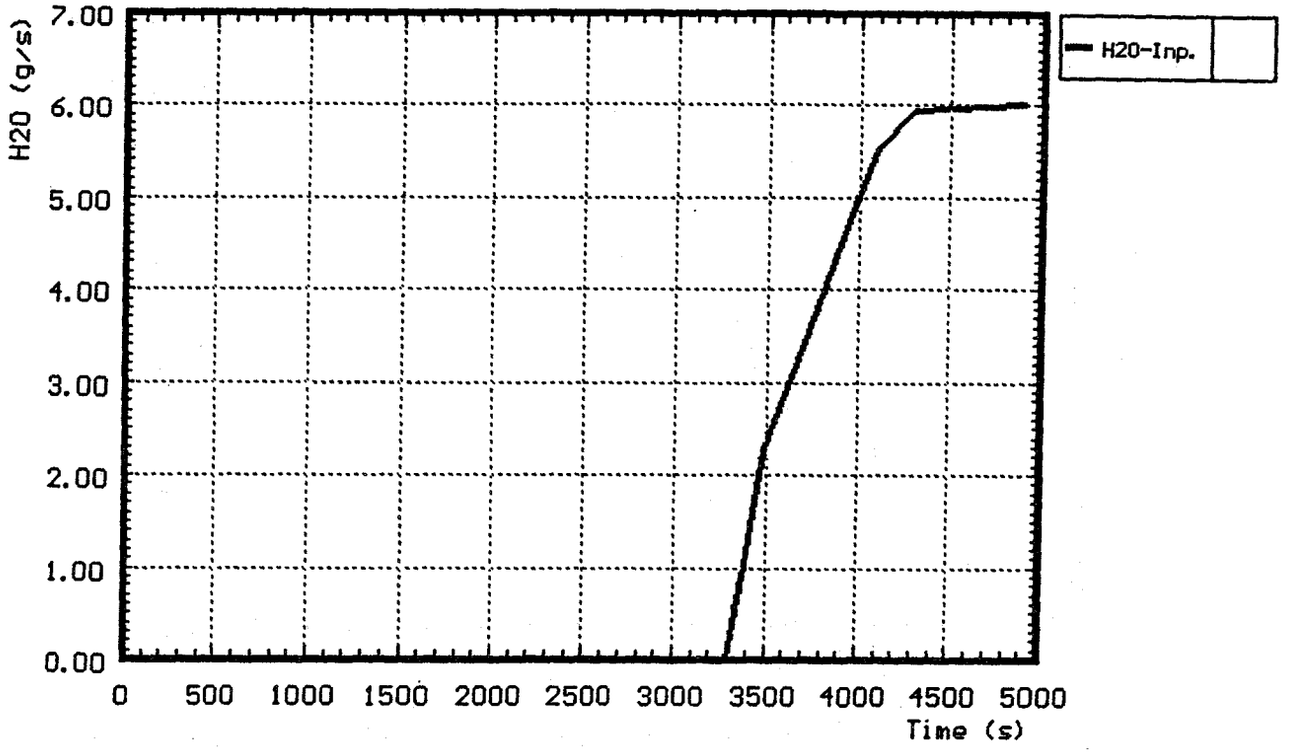

Fig. 27: Steam input into bundle CORA-13

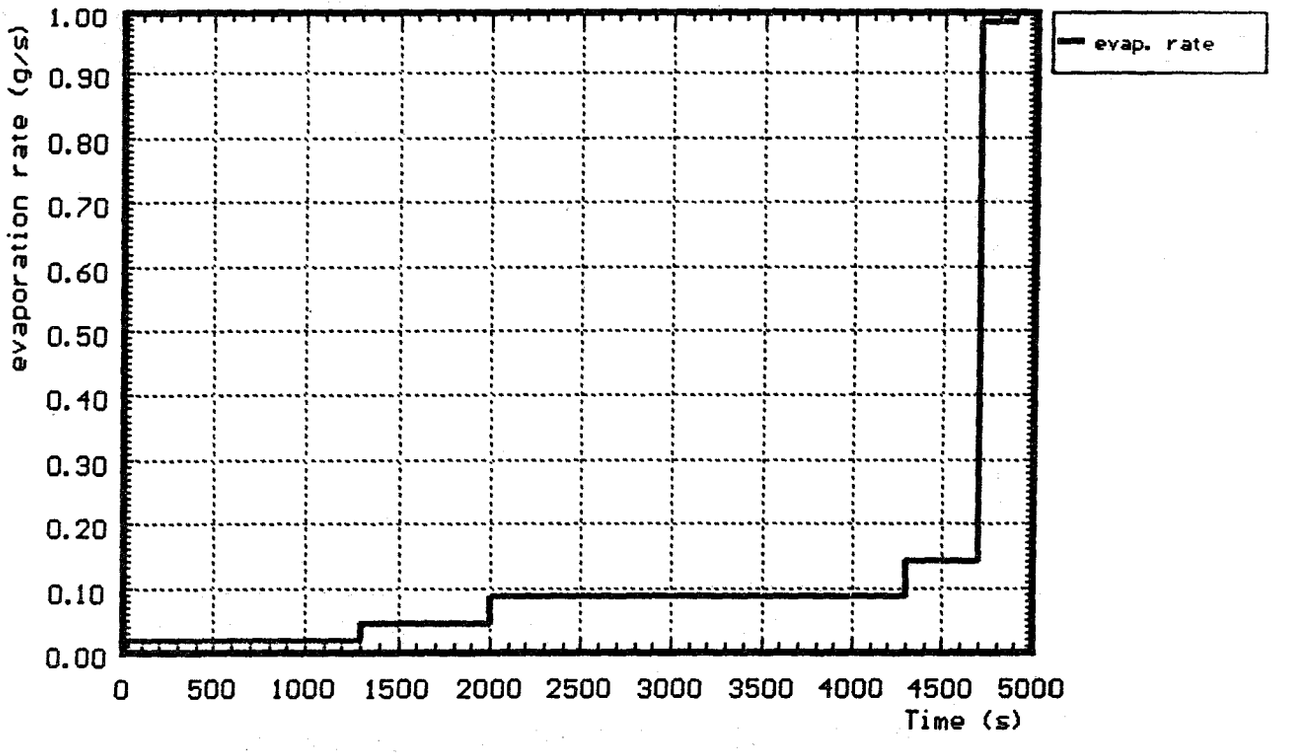

Fig. 28: Evaporation rate during the transient of CORA-13

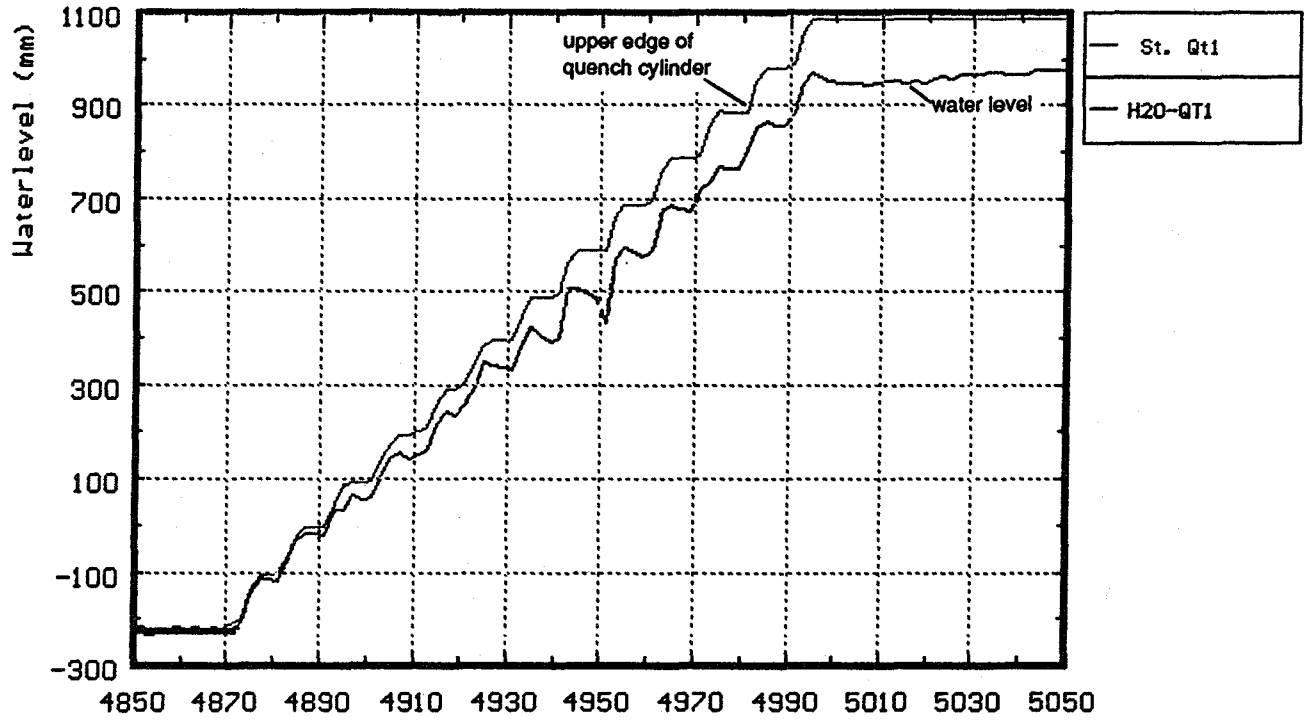

Fig. 29: Position of upper edge and water level in the quench cylinder (CORA-13)

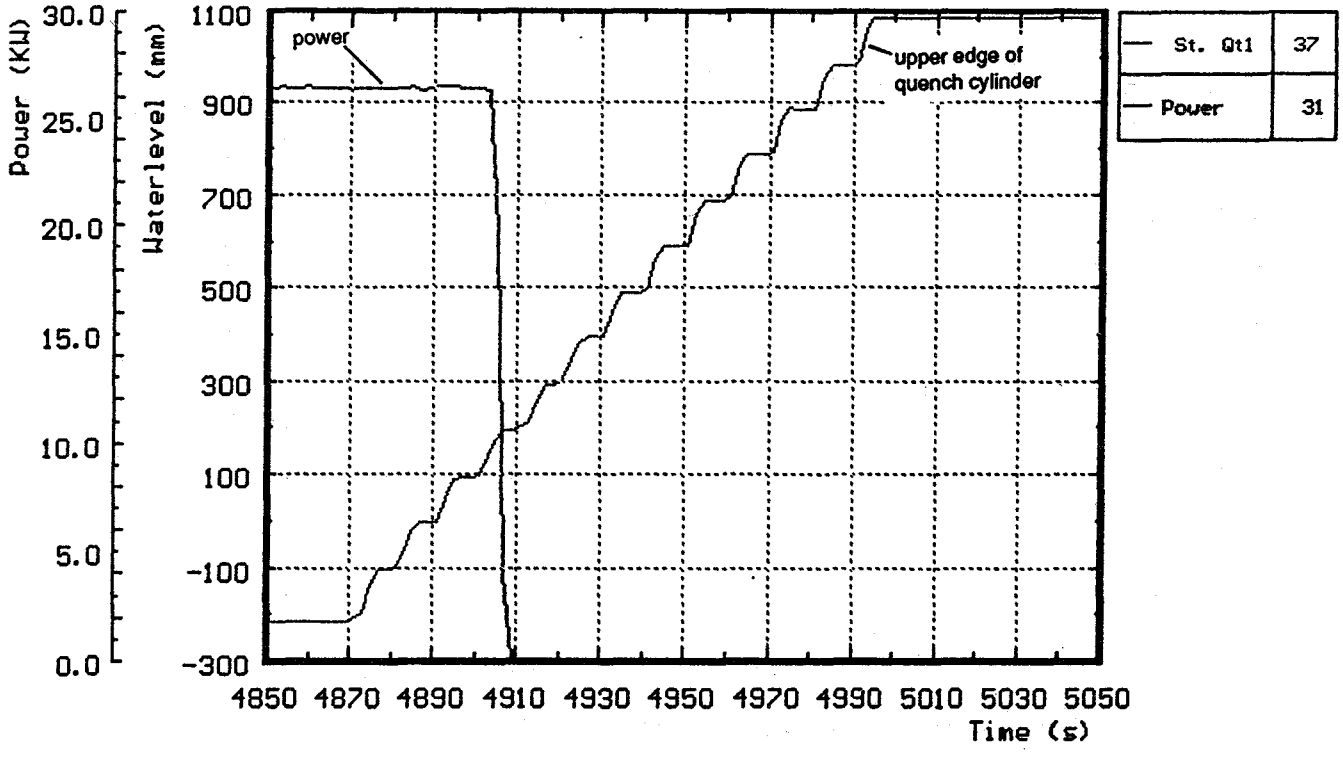

Fig. 30: Movement of the quench cylinder compared to power input (CORA-13)

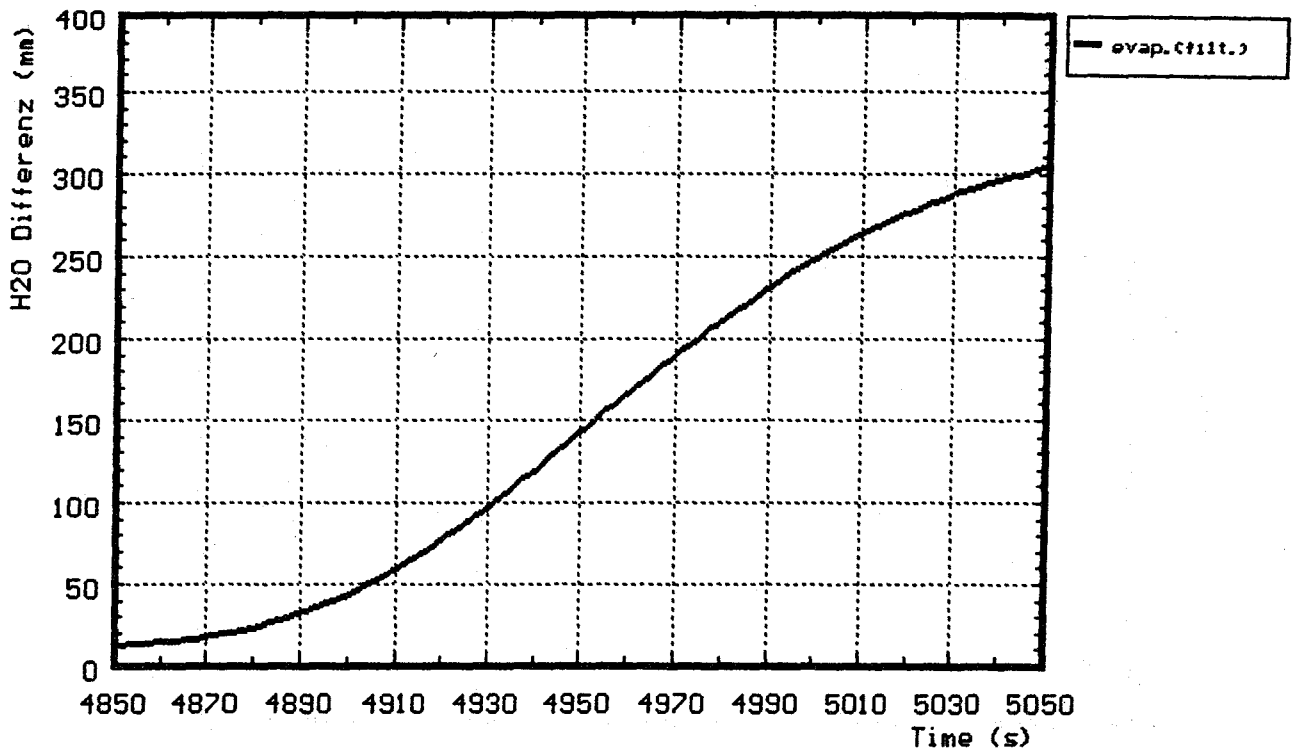

Fig. 31: Evaporated water from quench cylinder during the quench process (corrected for additional water input) (CORA-13)

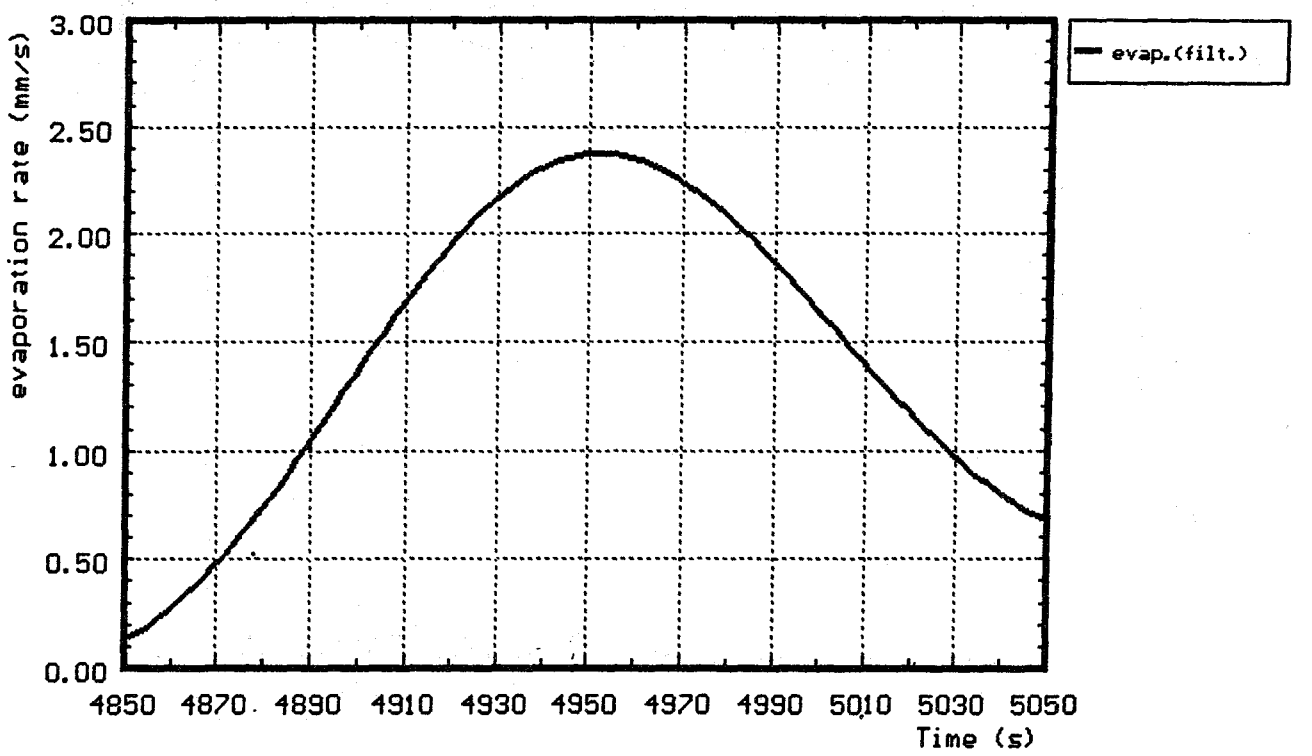

Fig. 32: Rate of evaporation during the quench process (CORA-13)

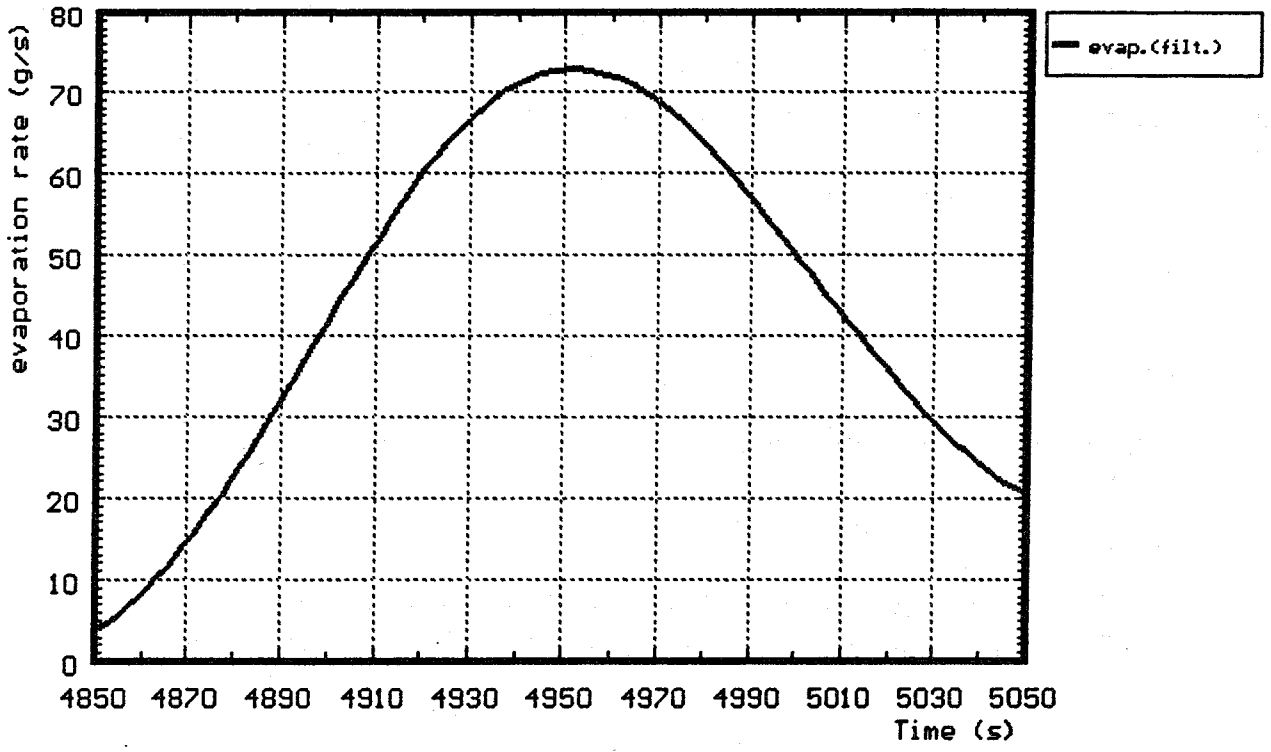

Fig. 33. Evaporation rate (g/s) during the quench process

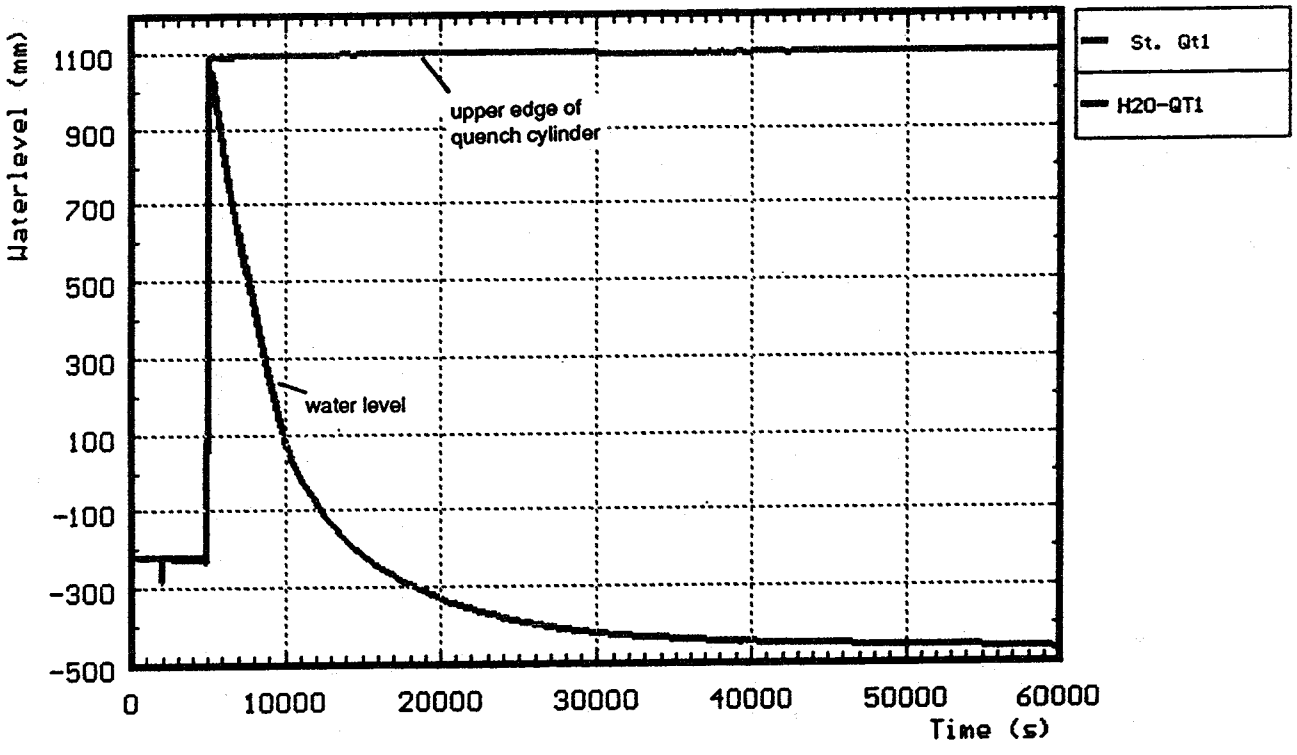

Fig. 34: Water level in the quench cylinder after the quench process

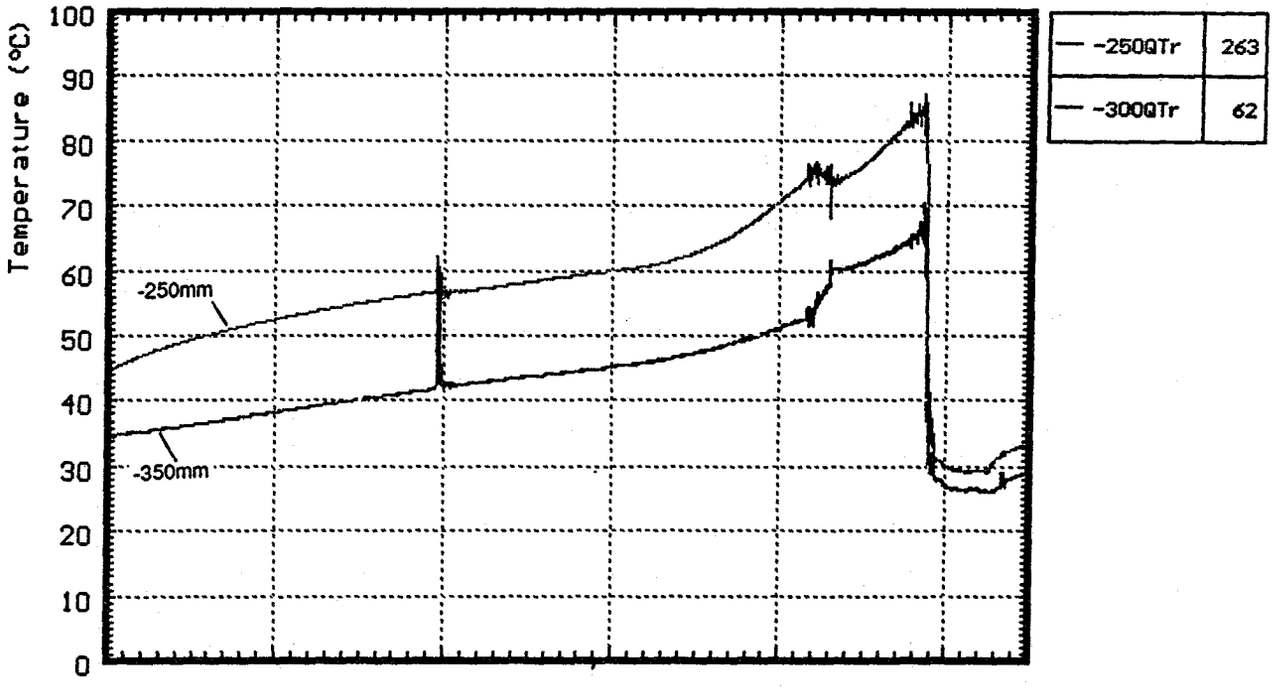

Fig. 35: Water temperatures in the quench cylinder at -250 mm and -300 mm (CORA-13)

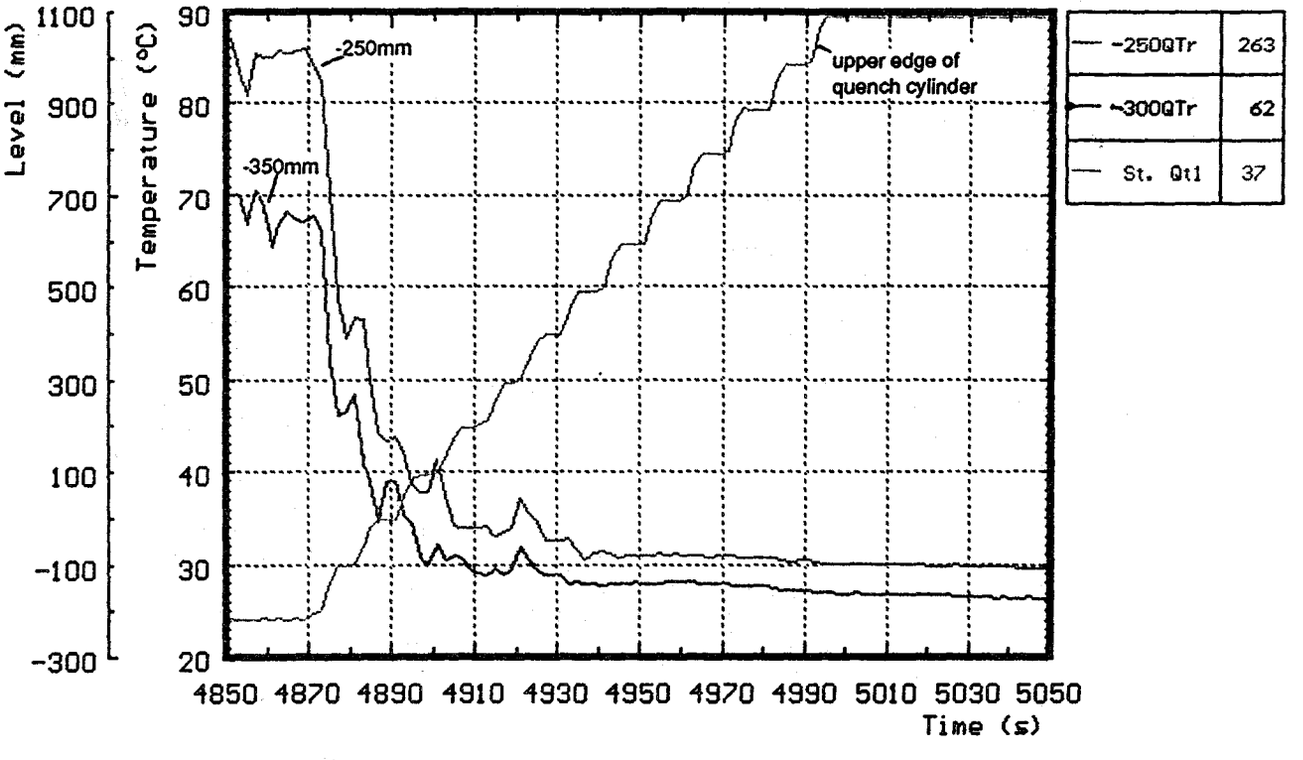

Fig. 36: Comparison of temperatures in the quench cylinder with the level of the quench cylinder (CORA-13)

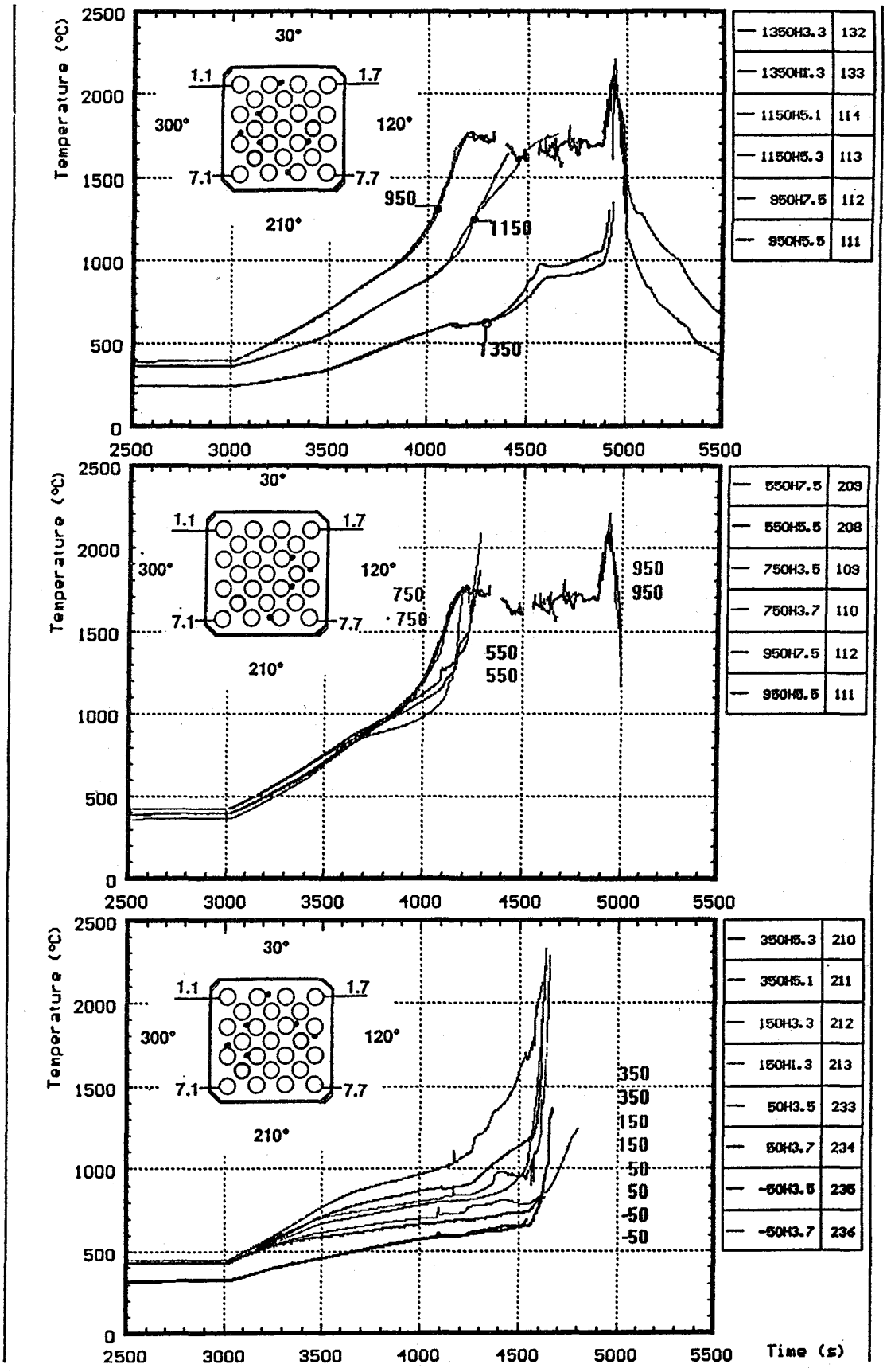

Fig. 37: Temperatures of the heated rods (CORA-13)

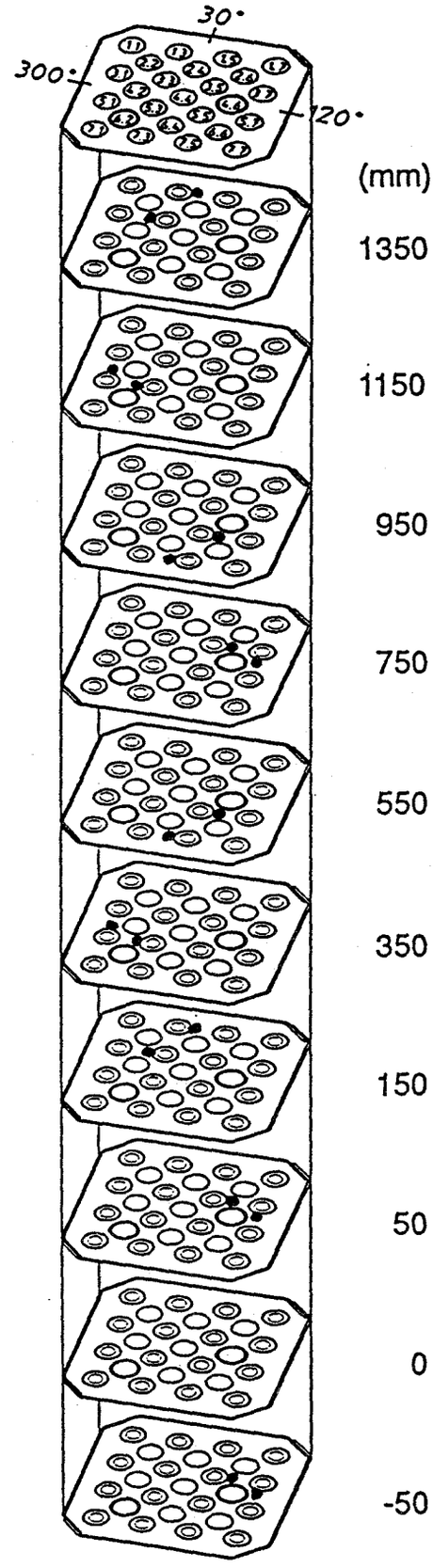

Fig. 38: Thermocouple locations at the heated rods (CORA-13)

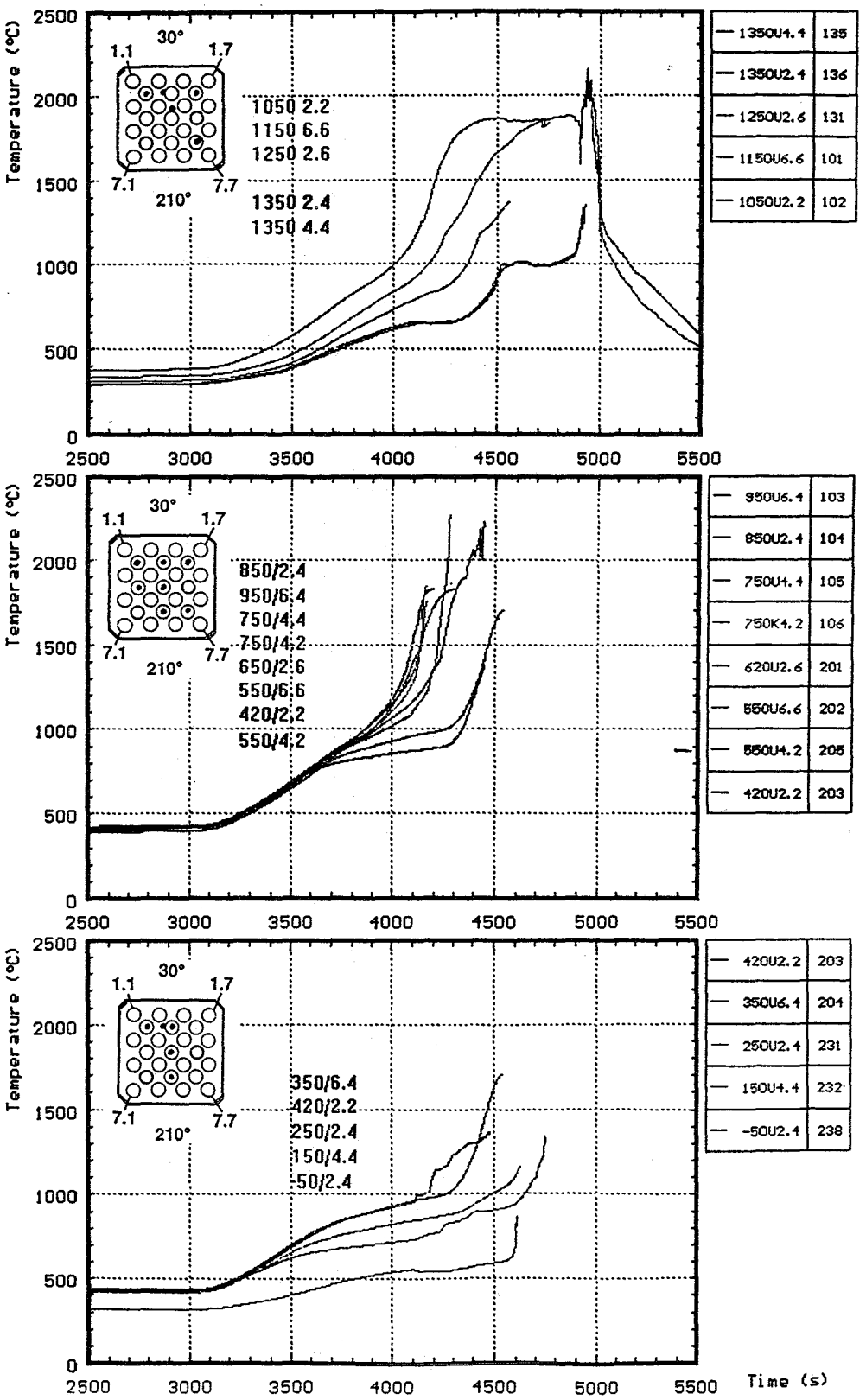

Fig. 39: Temperatures of the unheated rods (CORA-13)

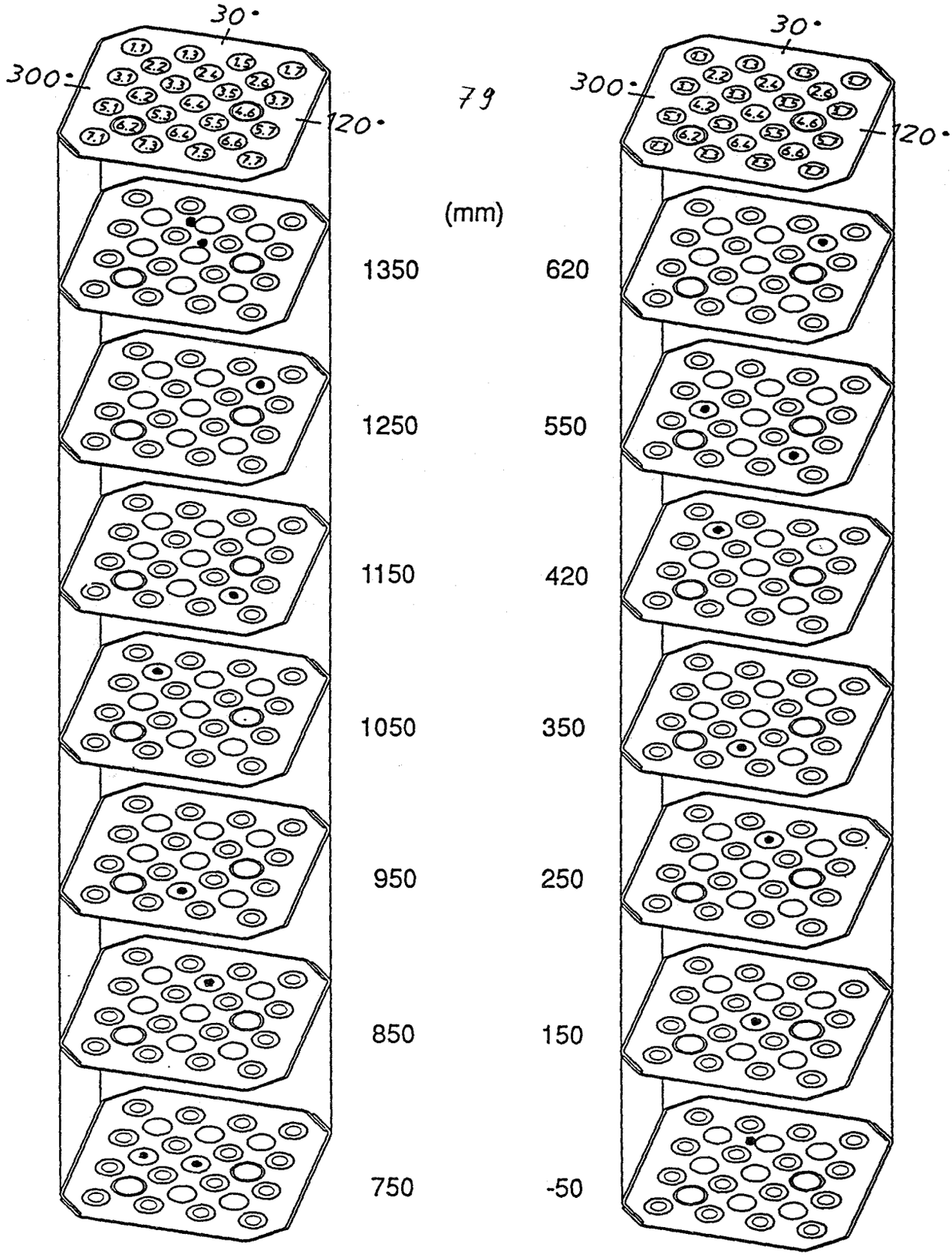

Fig. 40: Thermocouples at and in the unheated rods (CORA-13)

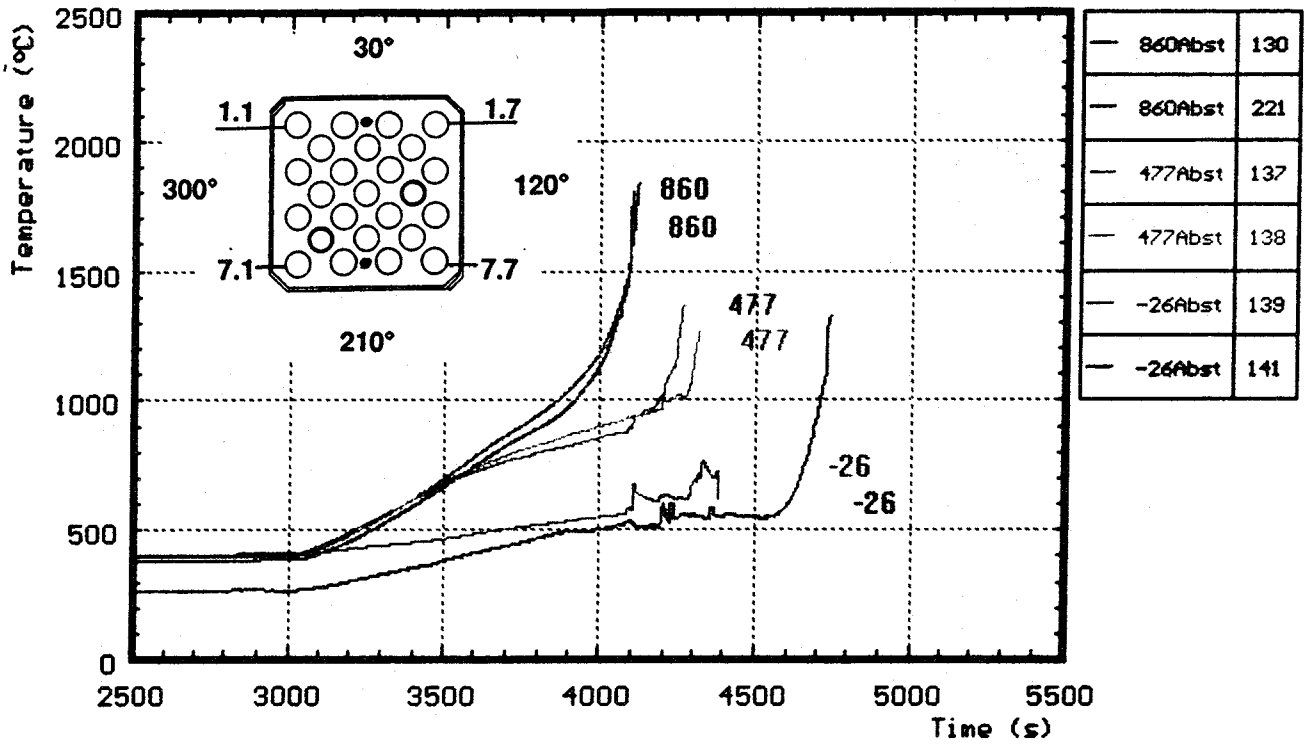

Fig. 41: Temperatures of the spacers (CORA-13)

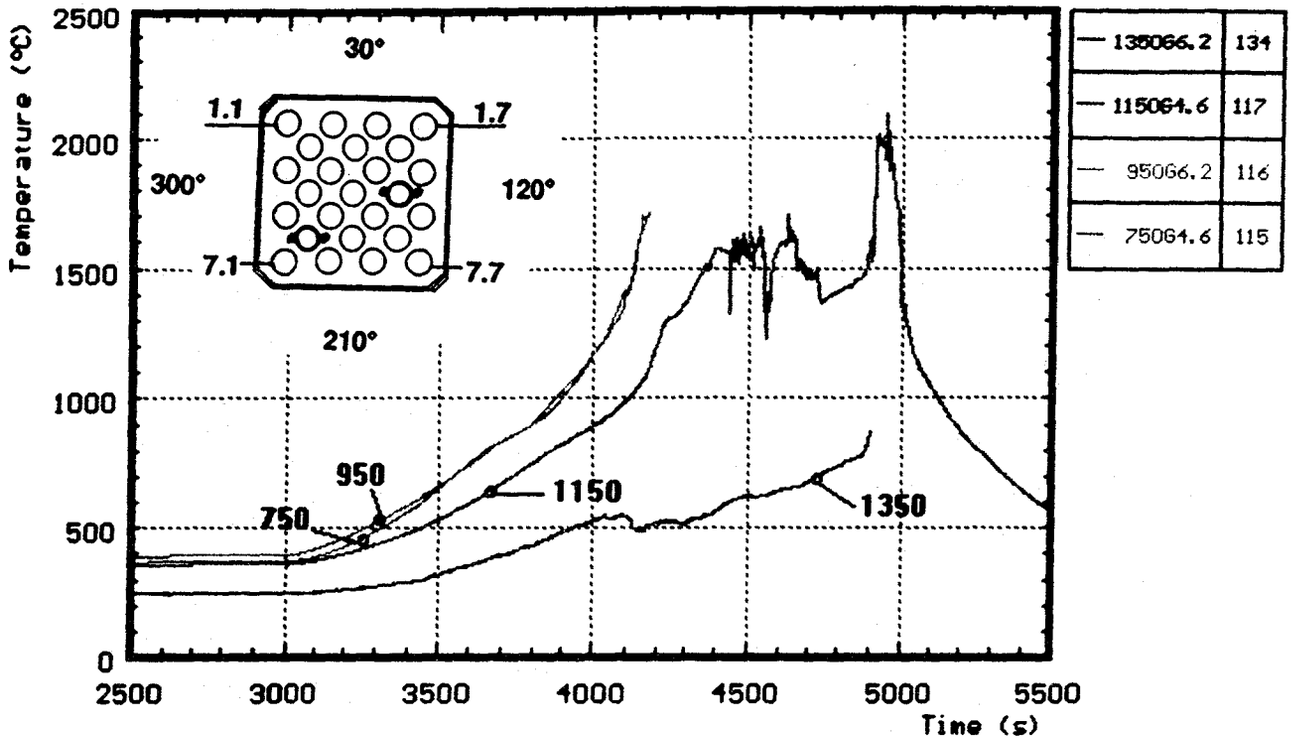

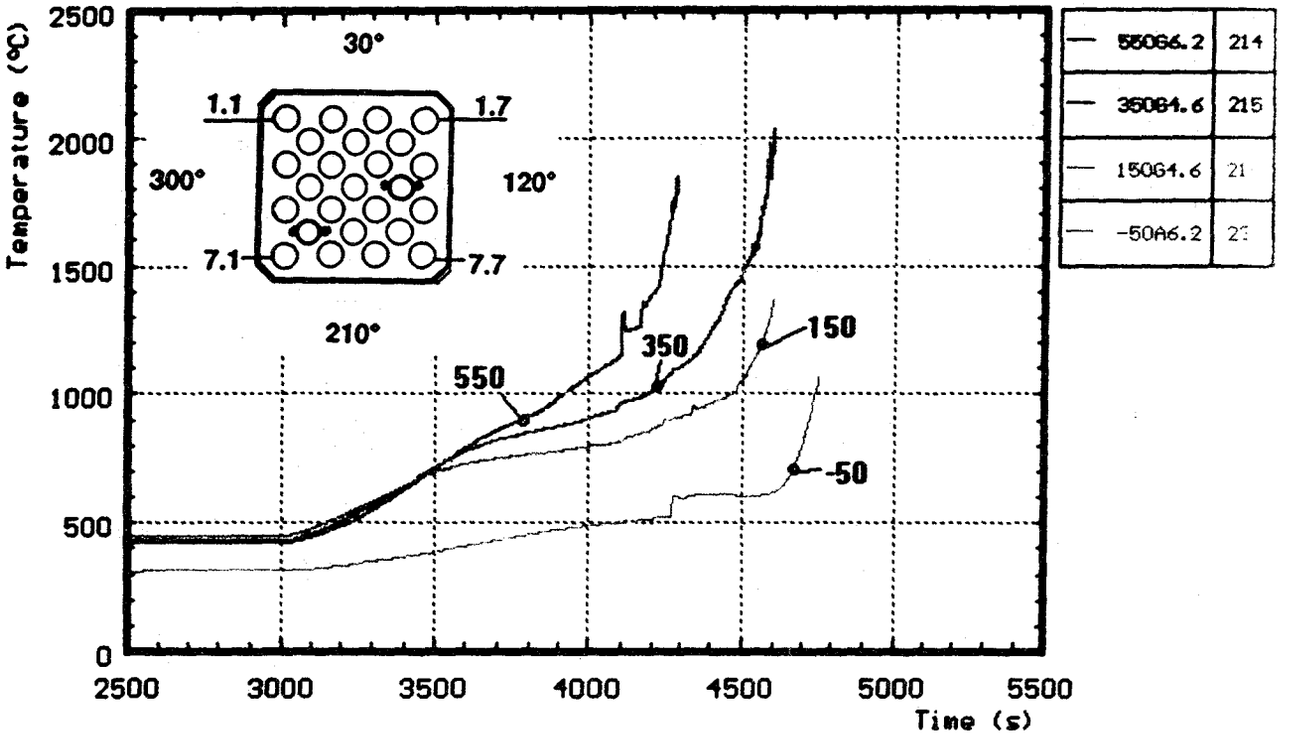

Fig. 42: Temperatures of the guide tubes (CORA-13)

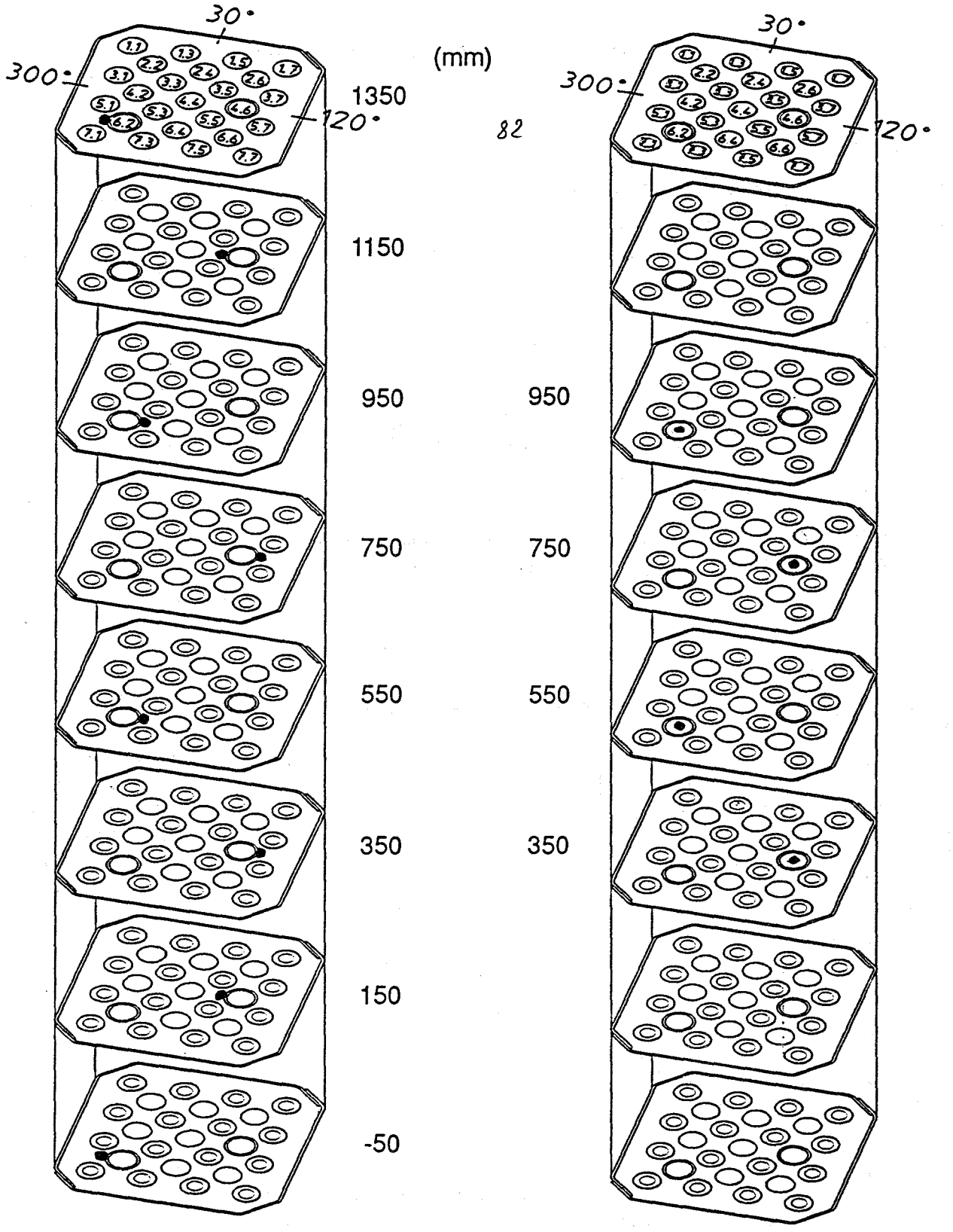

CORA-13

Fig. 42a: TC on the guide tube / TC in the absorber rod

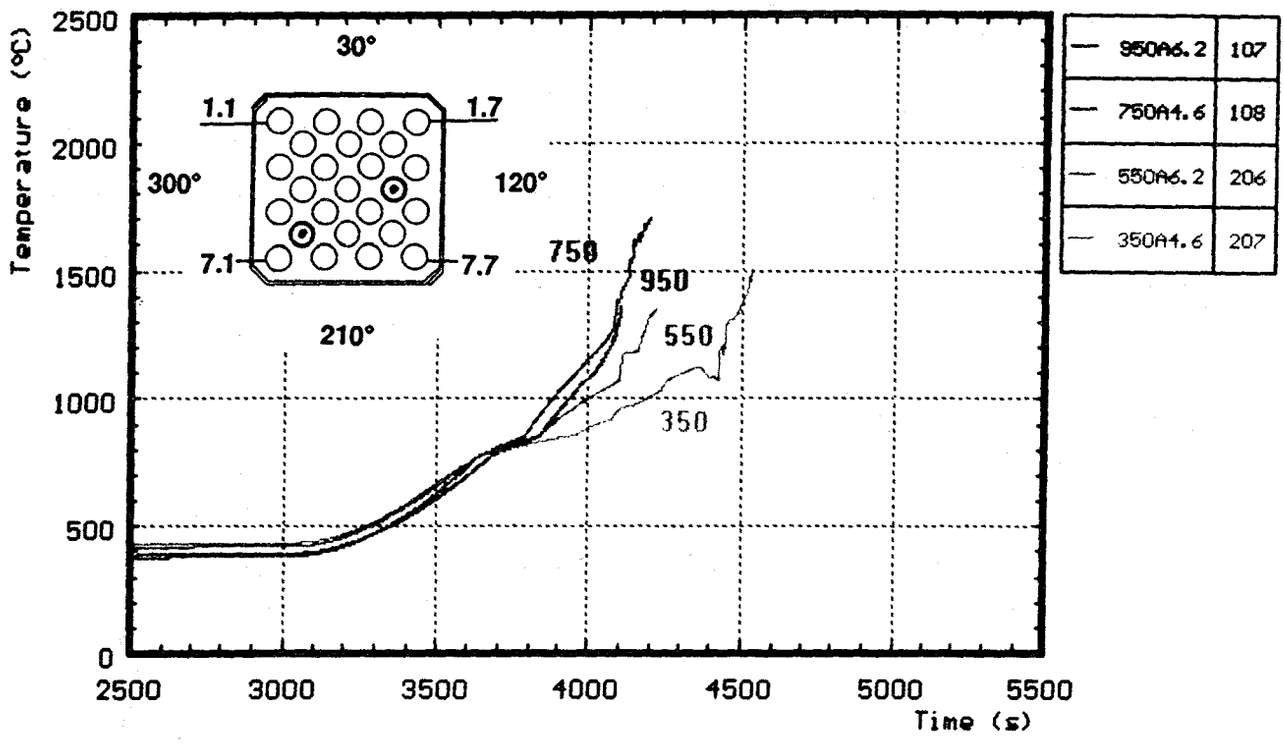

Fig. 43: Temperatures of the absorber rods (CORA-13)

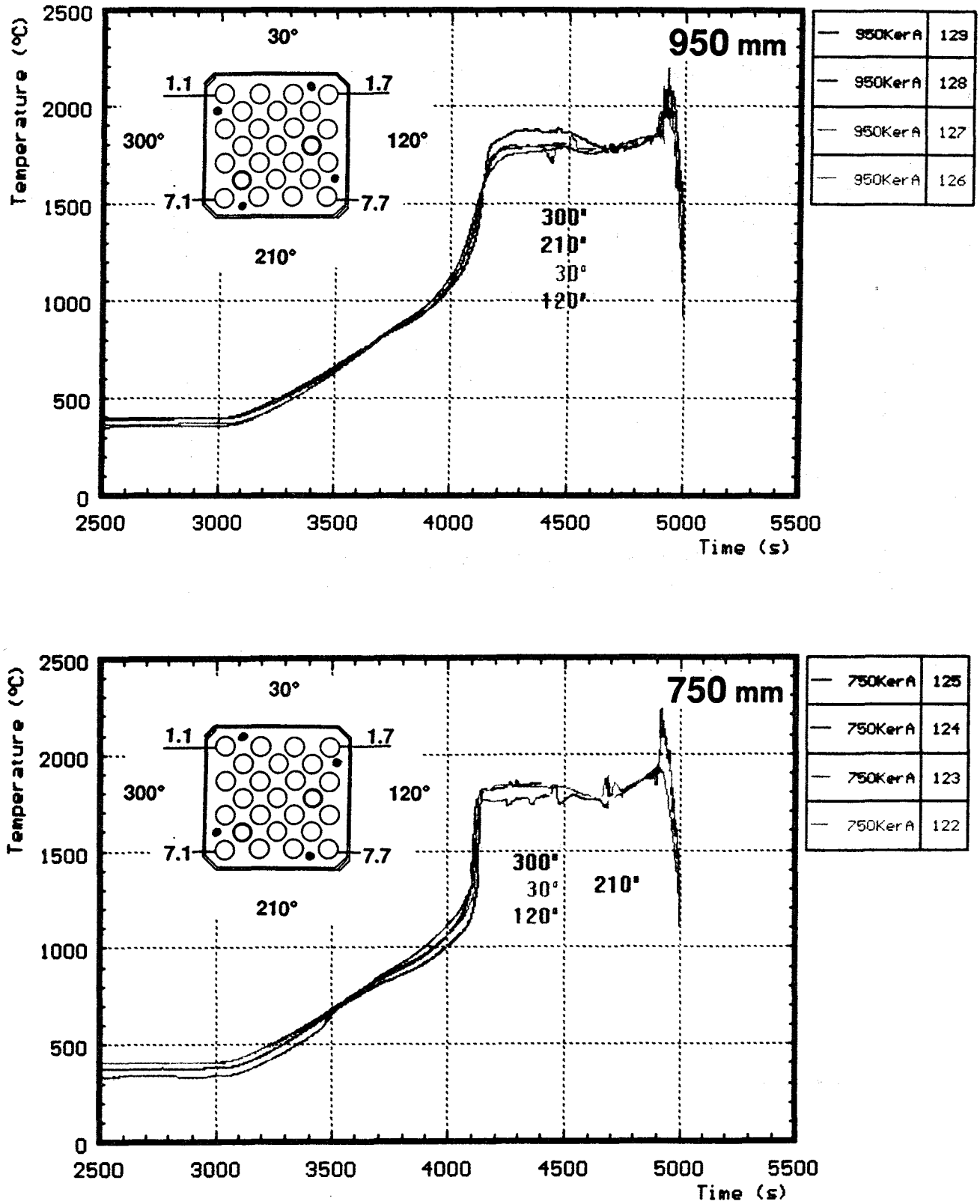

Fig. 44: Temperatures at the outside channel of the bundle CORA-13

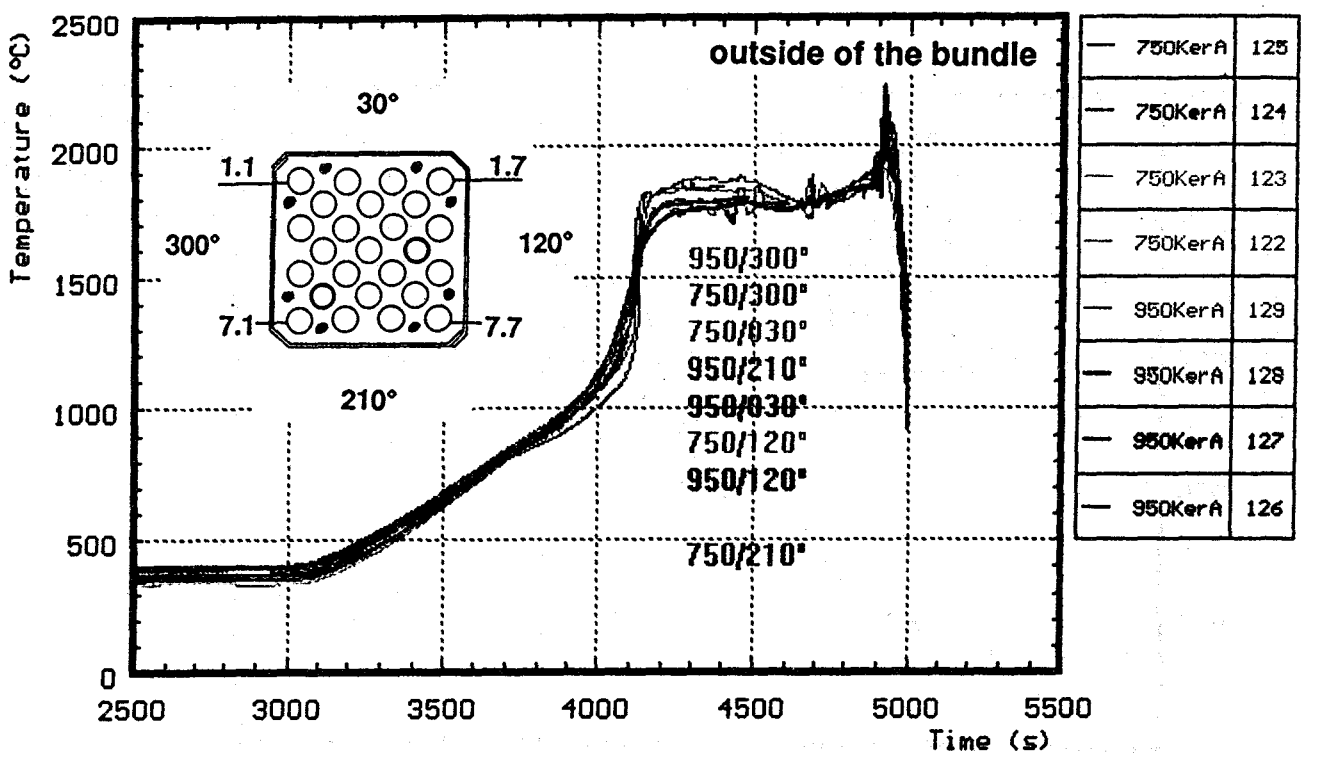

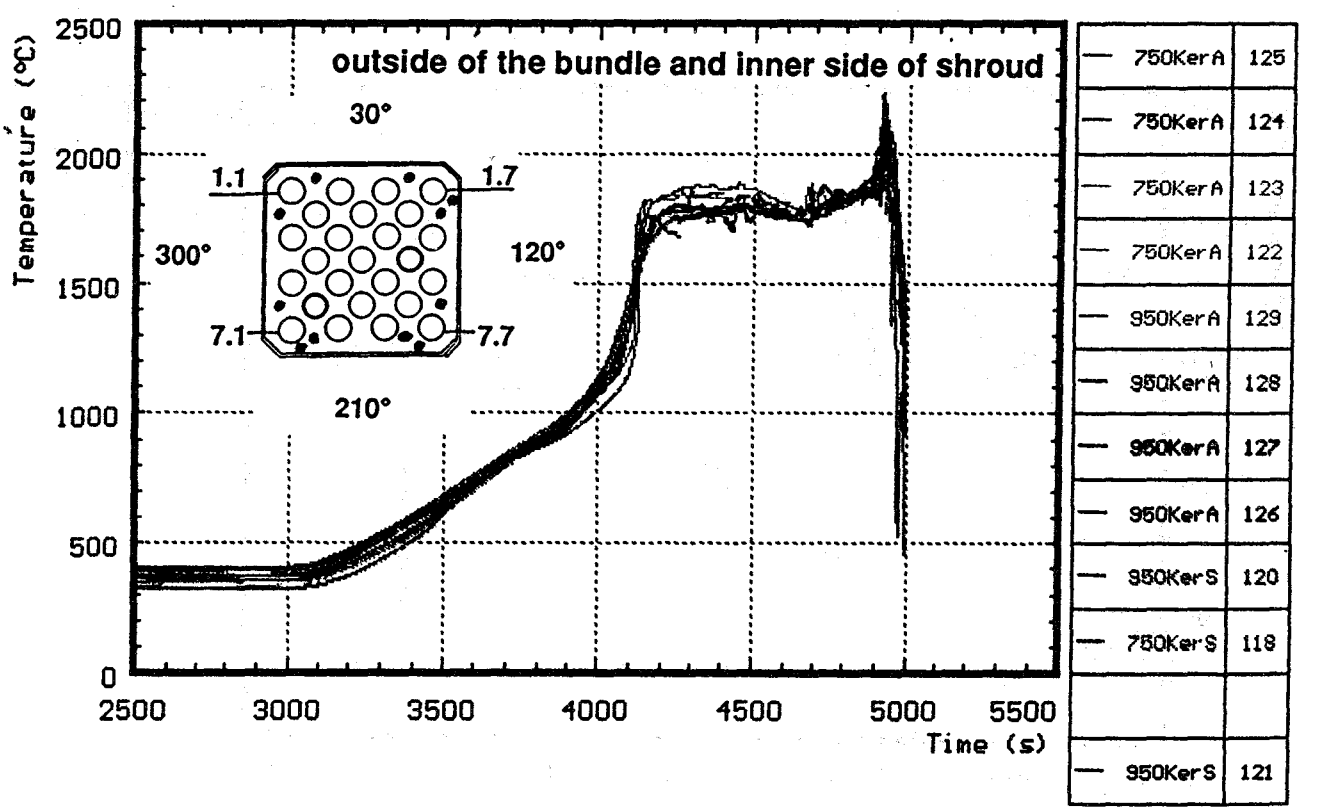

Fig. 45: ZrO_2-protected thermocouples at 950 and 750 mm (CORA-13)

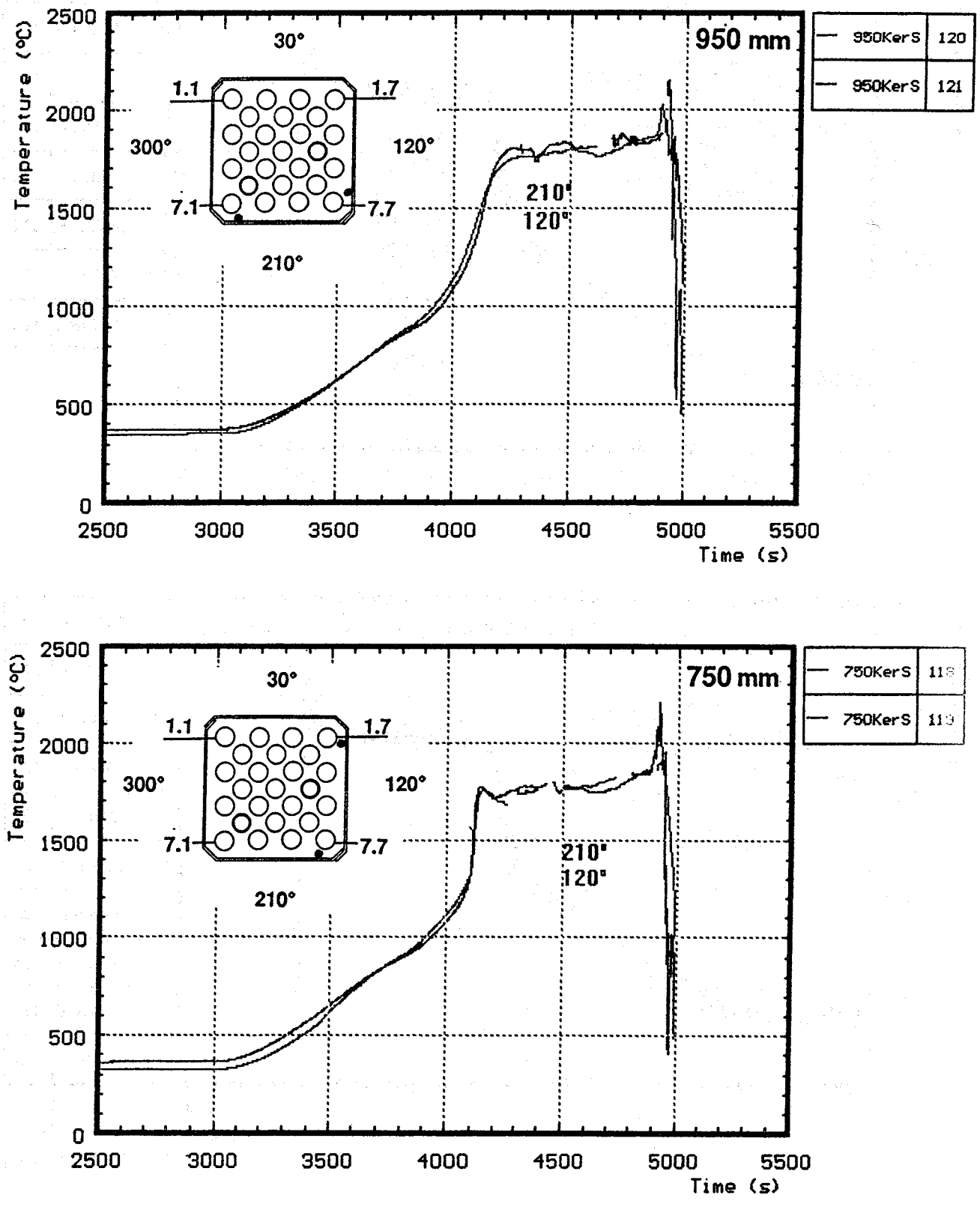

Fig. 46: Temperatures of the inner side of shroud (CORA-13)

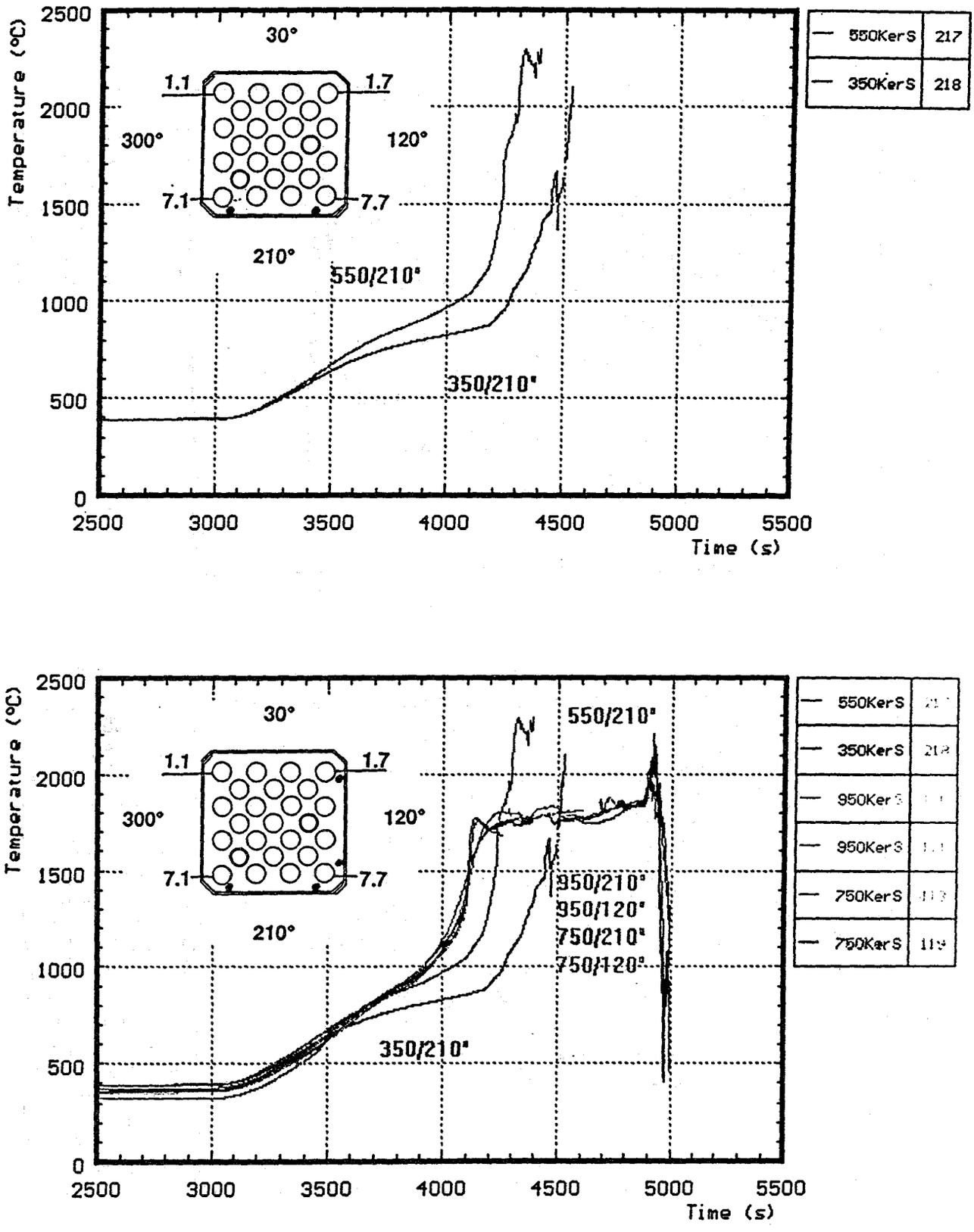

Fig. 47: Temperatures of the inner side of shroud (CORA-13)

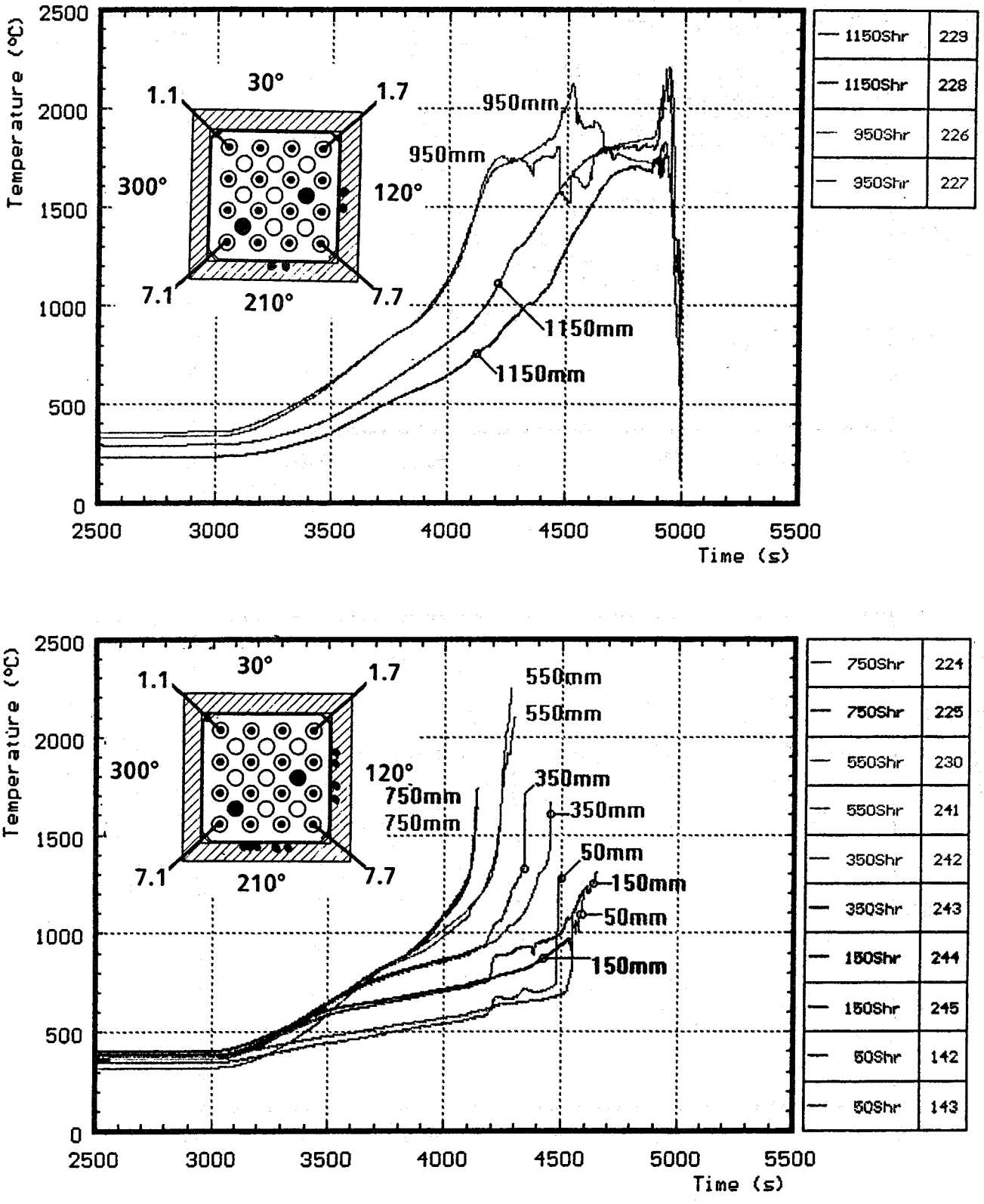

Fig. 48: Temperatures of the outer side of shroud (CORA-13)

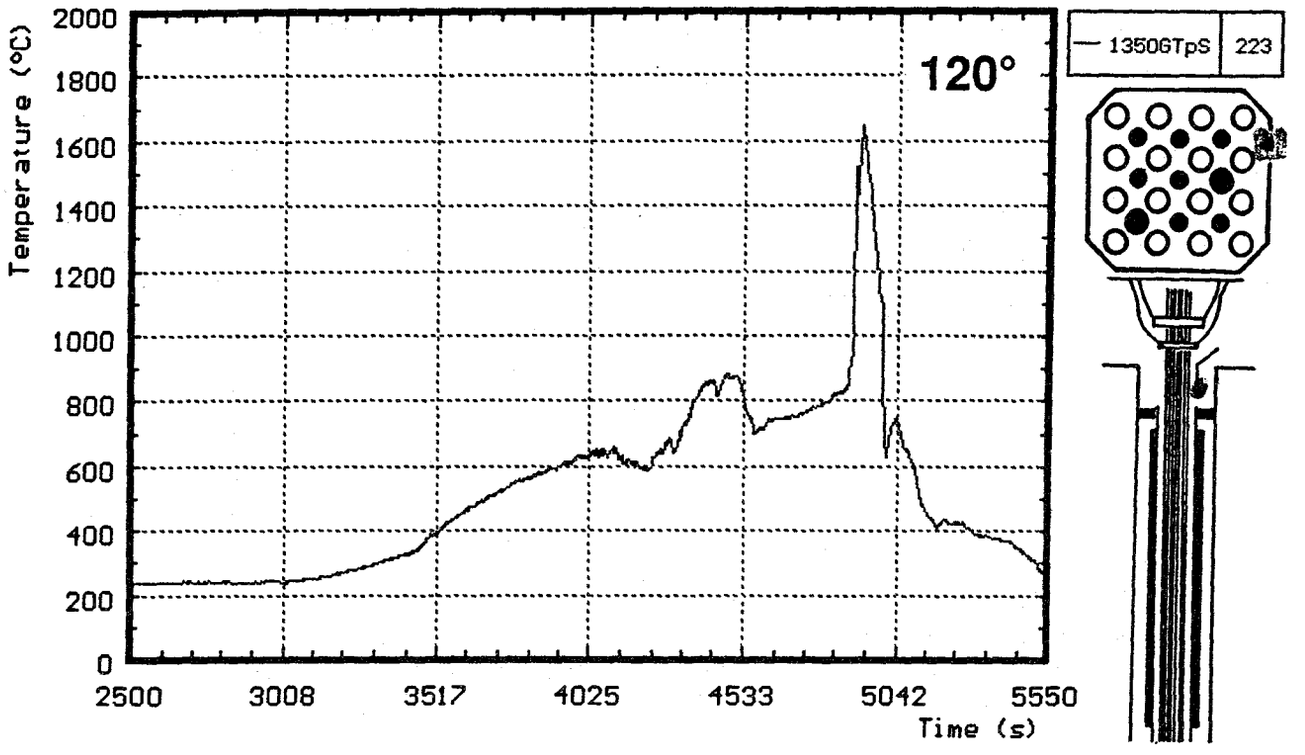

Fig. 49: Gas temperature above the shroud at 1350 mm elevation (CORA-13)

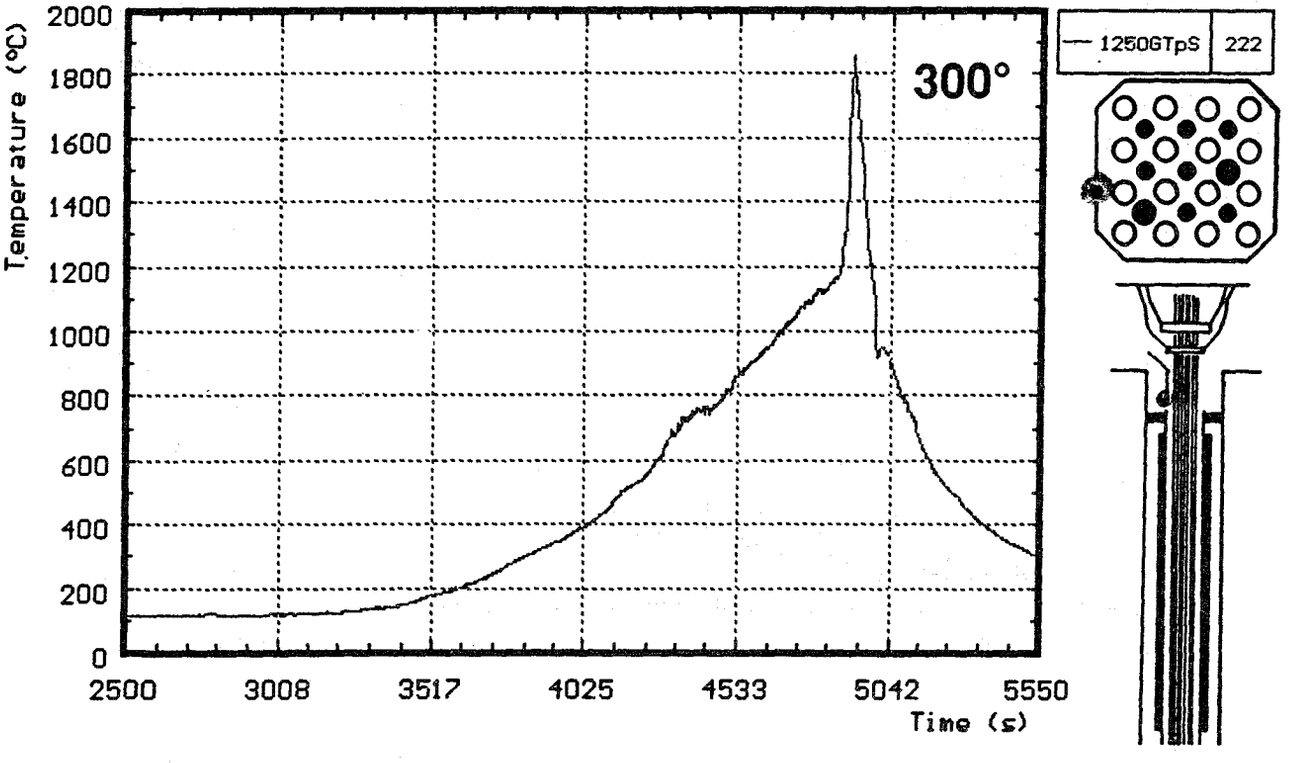

Fig. 50: Gas temperature above the shroud at 1250 mm elevation (CORA-13)

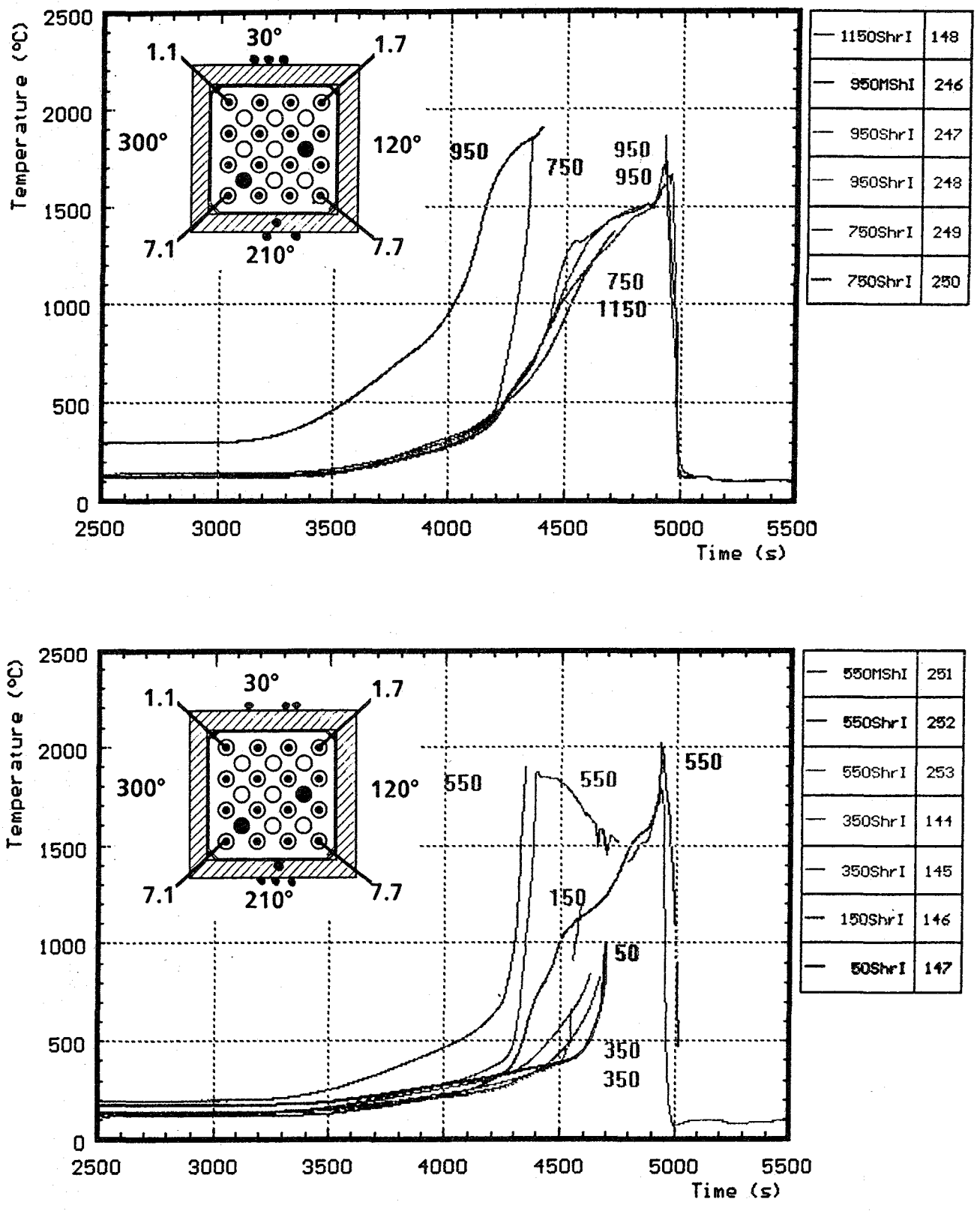

Fig. 51: Temperatures outside and within the shroud insulation (CORA-13)

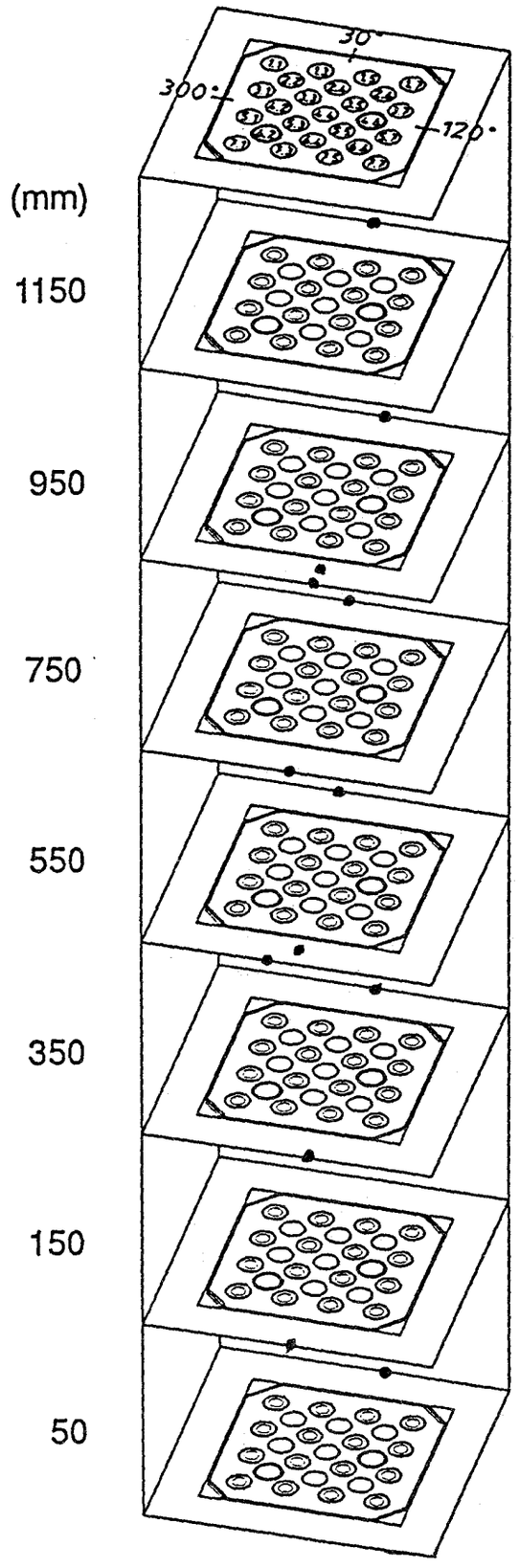

Fig. 52: Location of the thermocouples outside and within the shroud insulation (CORA-13)

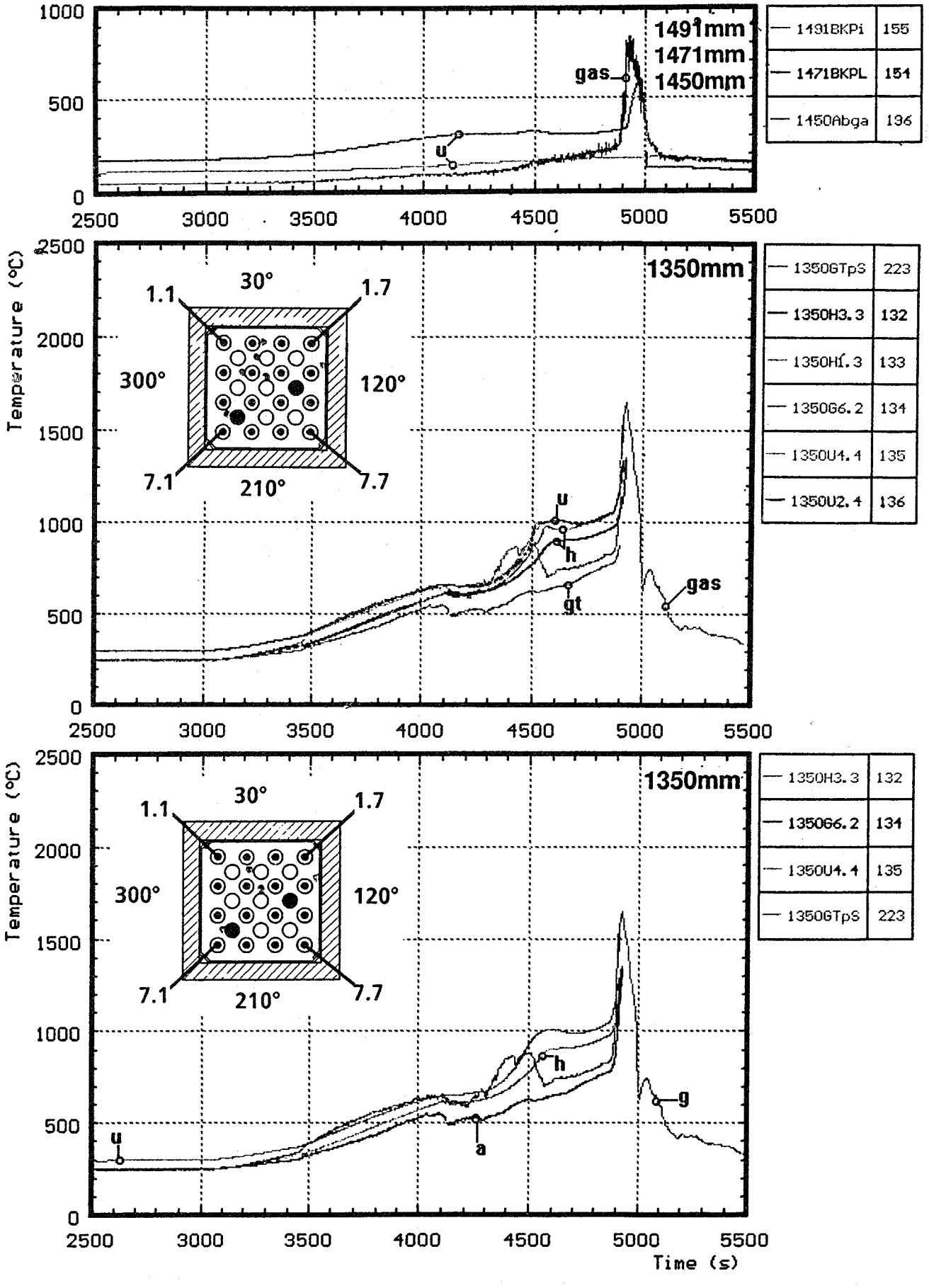

Fig. 53: Temperatures at fixed elevations (CORA-13)

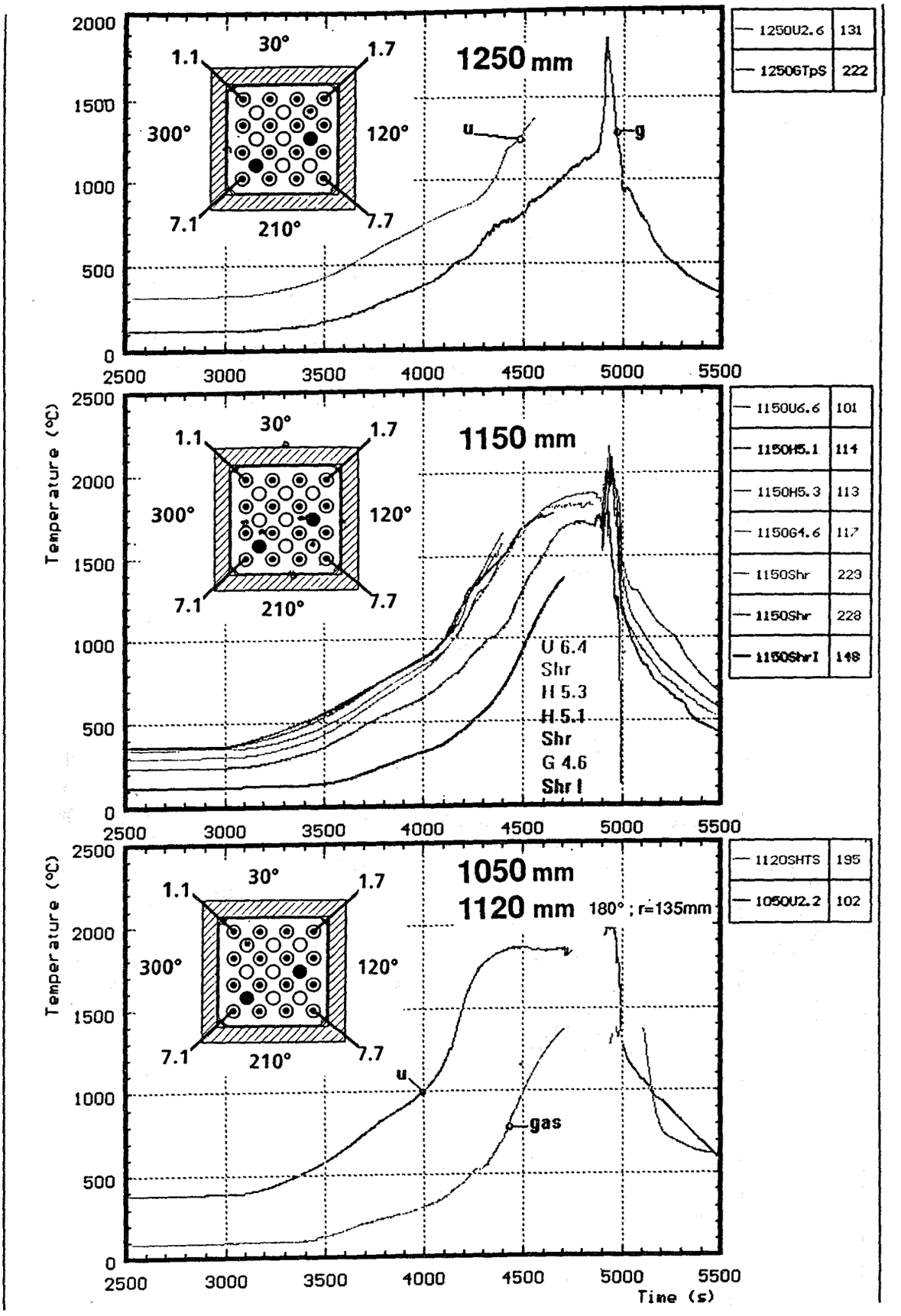

Fig. 54: Temperatures at fixed elevations (CORA-13)

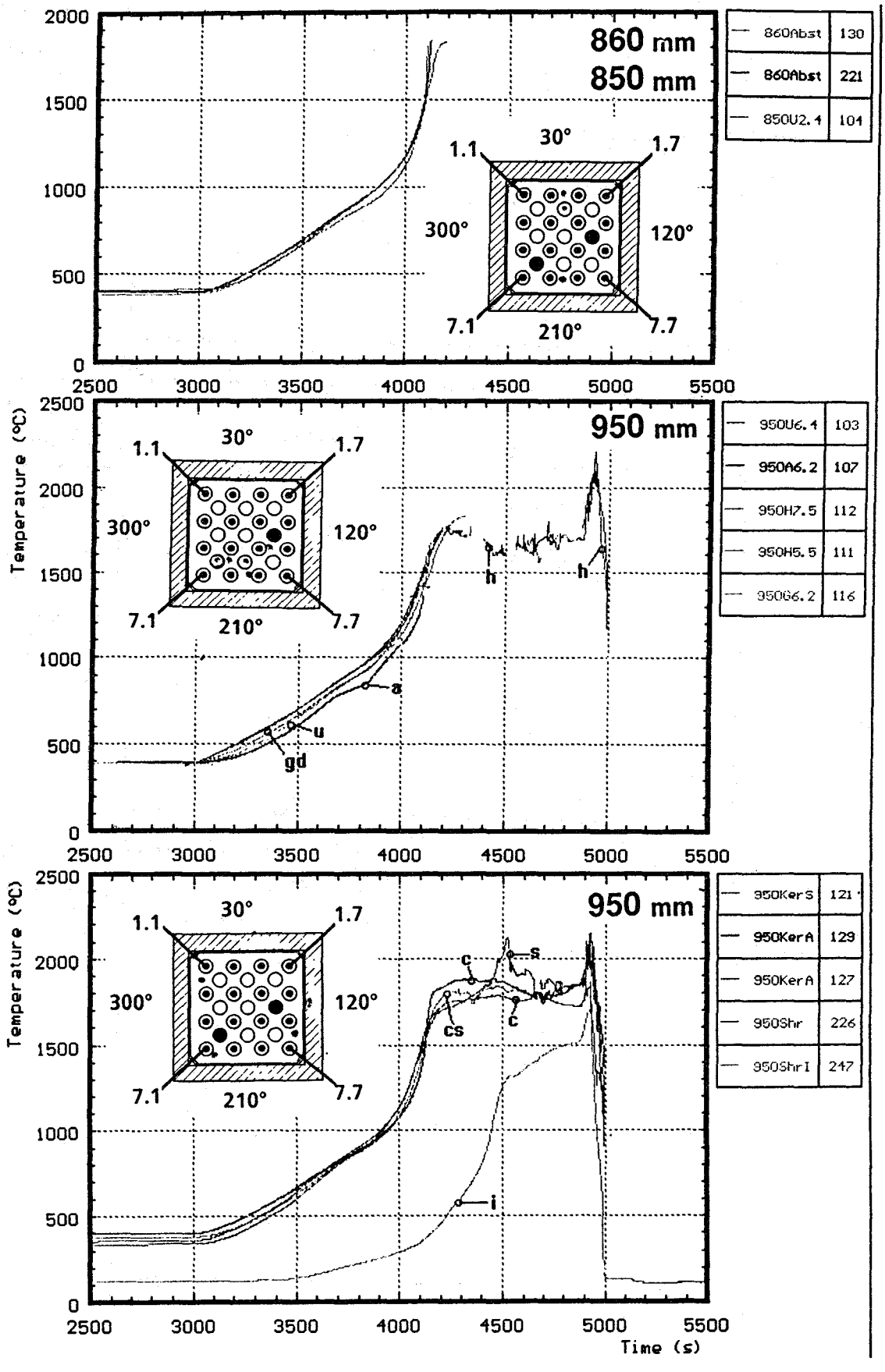

Fig. 55. Temperatures at fixed elevations (CORA-13)

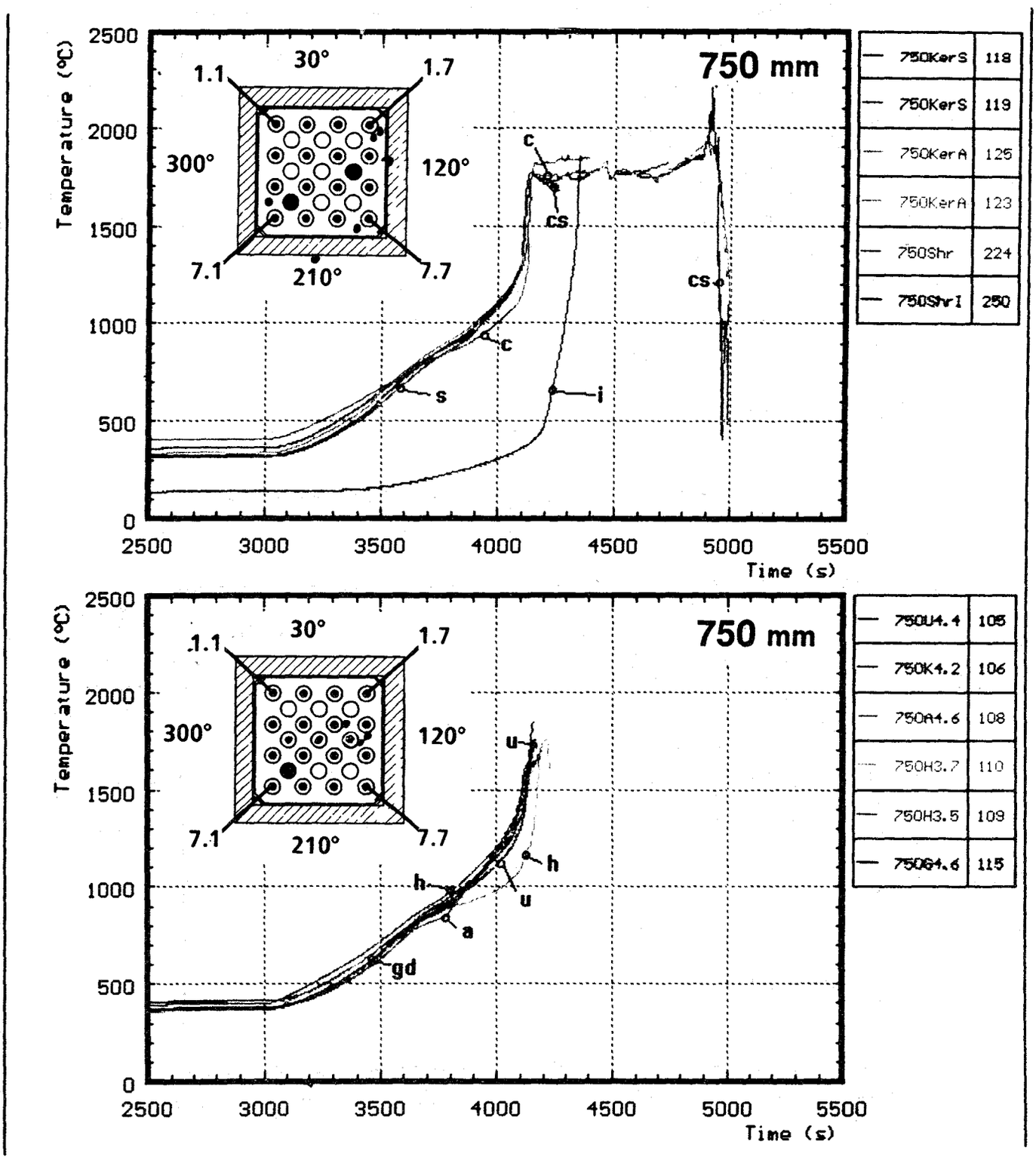

Fig. 56: Temperatures at fixed elevations (CORA-13)

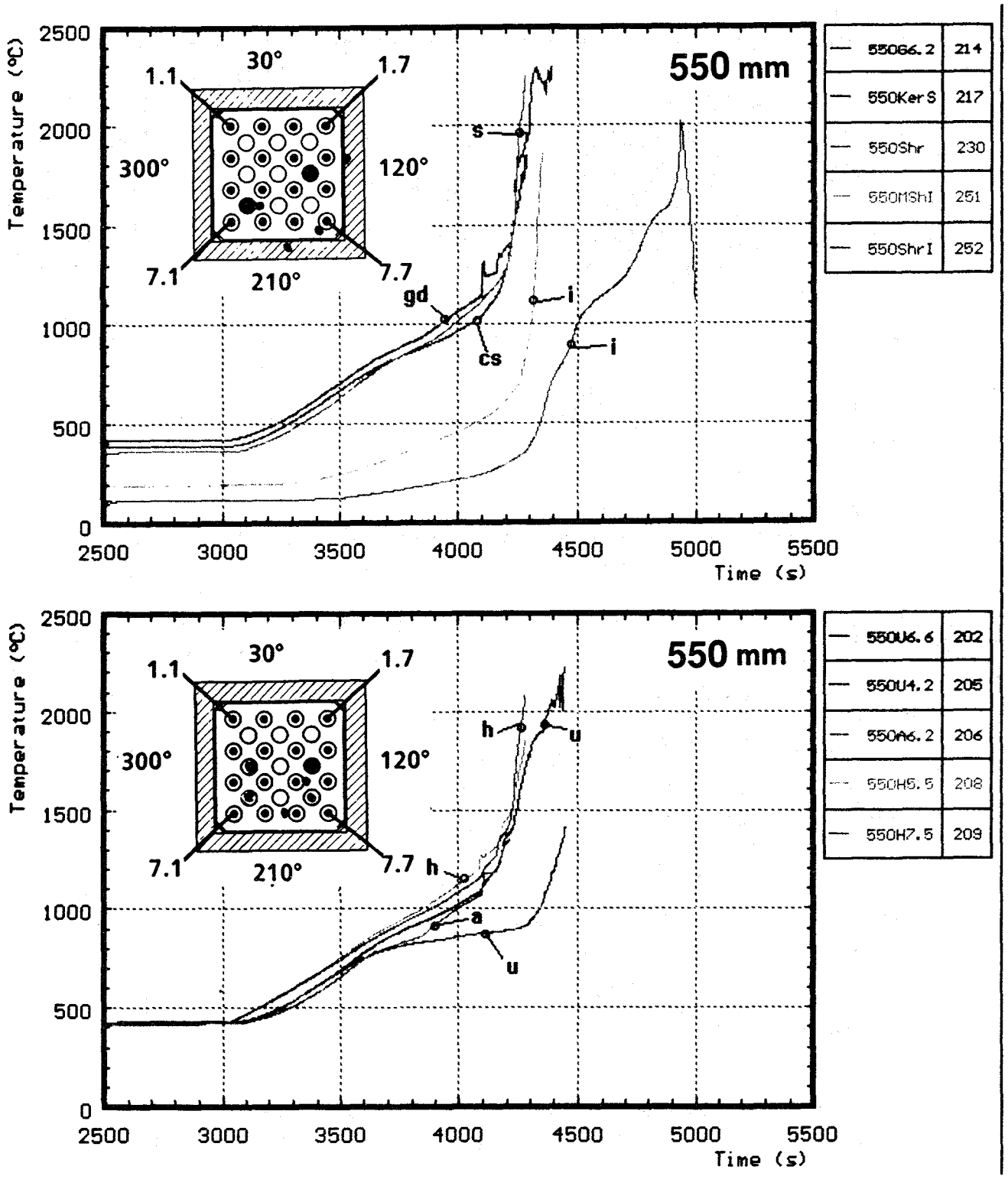

Fig. 57: Temperatures at fixed elevations (CORA-13)

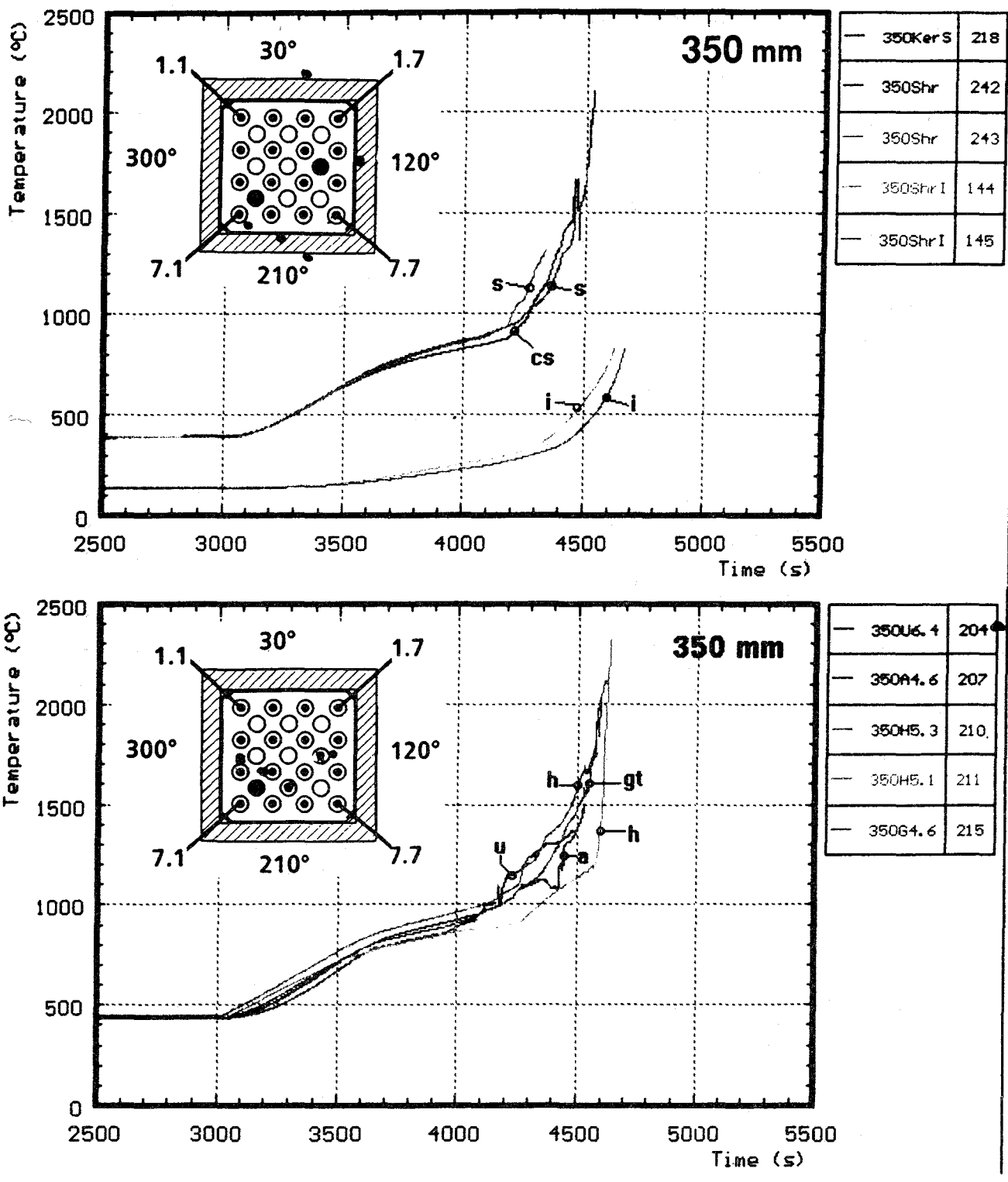

Fig. 58: Temperatures at fixed elevations (CORA-13)

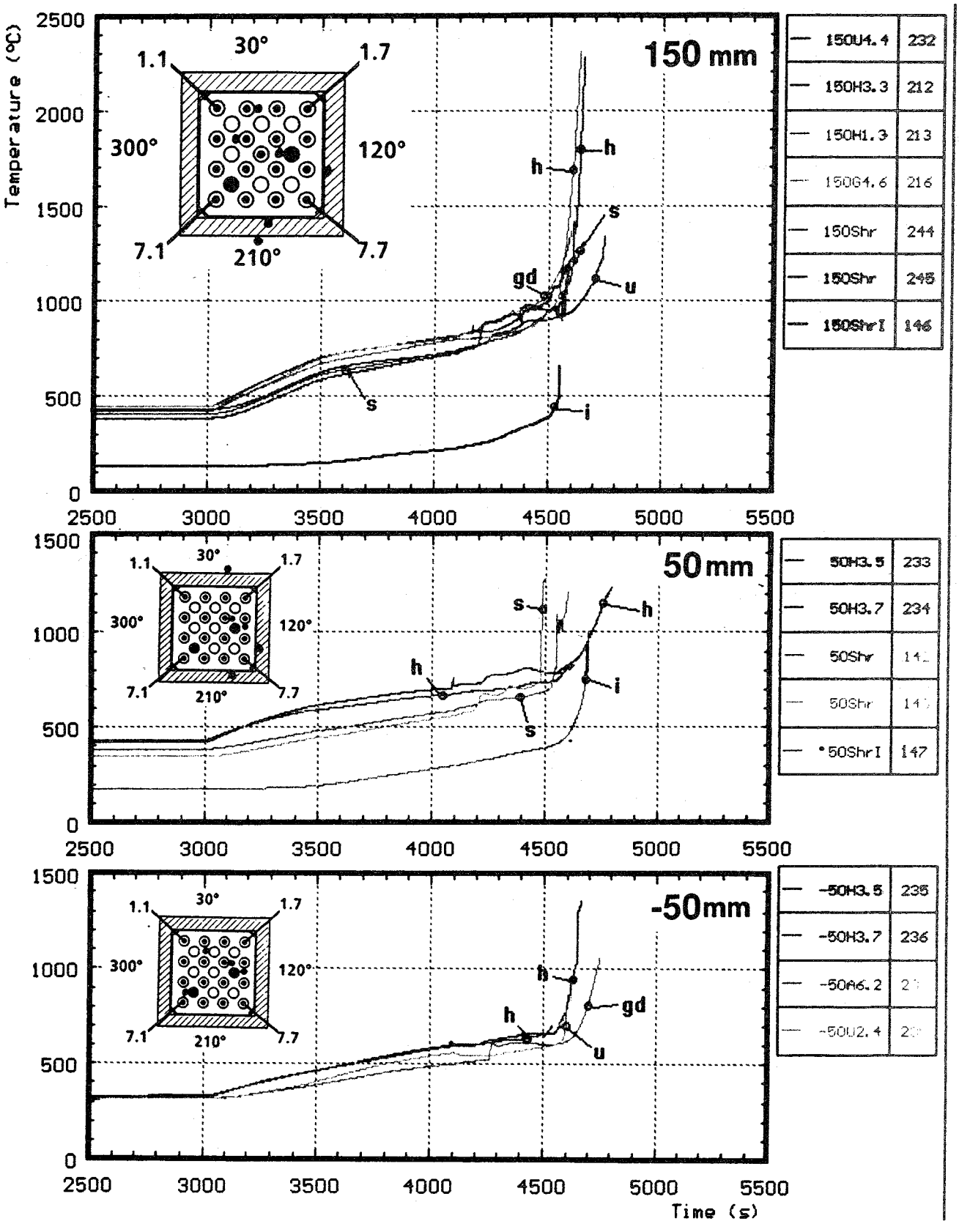

Fig. 59: Temperatures at fixed elevations (CORA-13)

ANGLE		75°					165°		255°				345°			
RADIUS (mm)		153	172	192	255	293	153	192	153	172	192	255	153	192	255	293
ELEVATION IN BUNDLE (mm)	1250													169 234Ni		
	1150													170 235Ni		189 245Ni
	990						161 78Ni						187 1B			
	950							163 229Ni						171 236Ni	178 242Ni	190 246Ni
	890	181 20B							185 7B							
	750							164 230Ni						172 237Ni		
	590						183 21B									
	550			162 126Ni	176 130Ni	180 244Ni		165 231Ni			168 127Ni	177 131Ni		173 238ni		191 247Ni
	390						184 22B						188 23B			
	350							166 232Ni								
	150							167 233Ni						174 240Ni	179 243Ni	192 248Ni
	90	182 33B							186 26B							
	0															
	-50													175 241Ni		

Fig. 60: Positions of thermocouples at the high-temperature shield (HTS) for test CORA-13

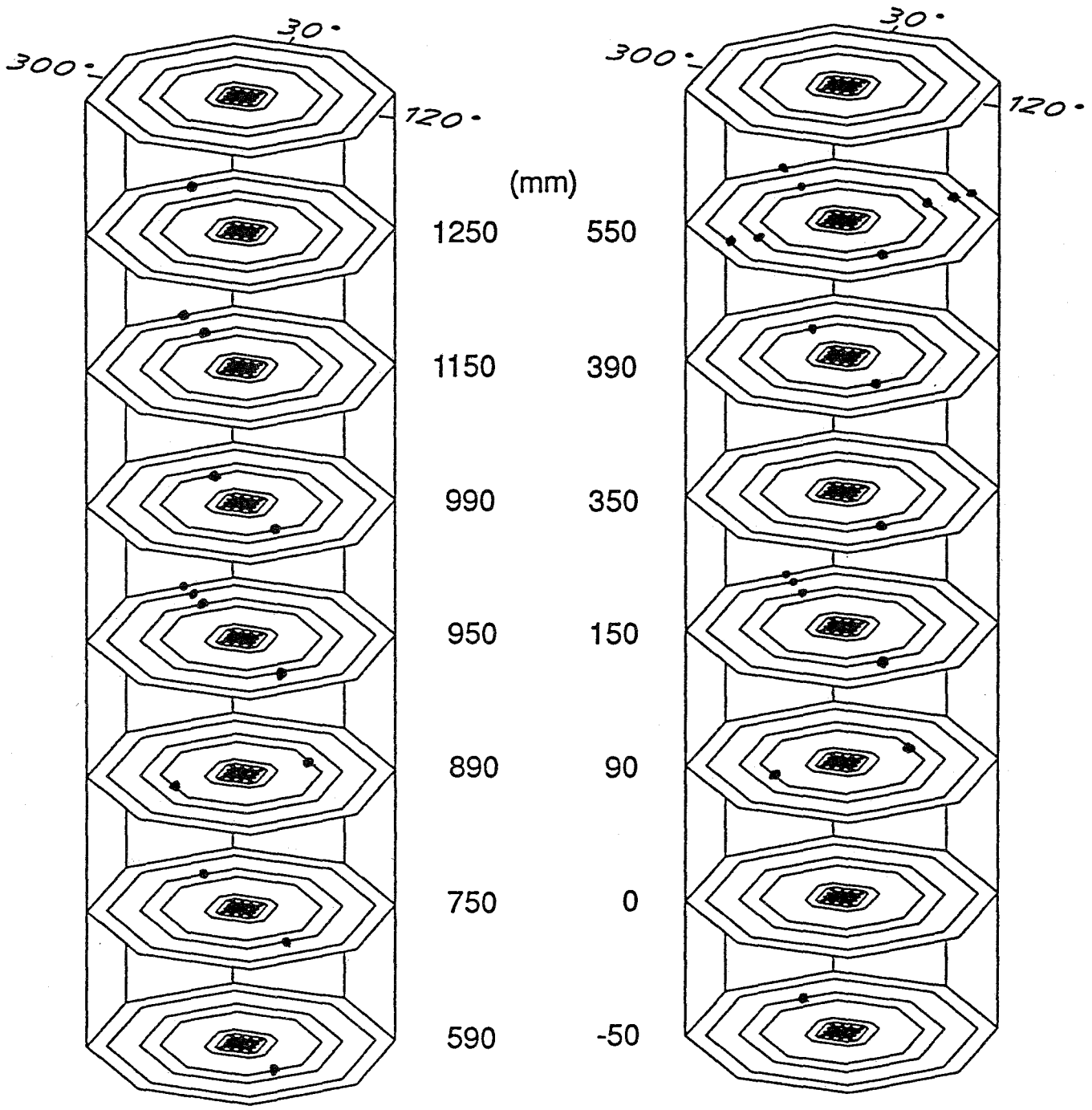

Fig. 61: Locations of thermocouples in the high-temperature shield (CORA-13)

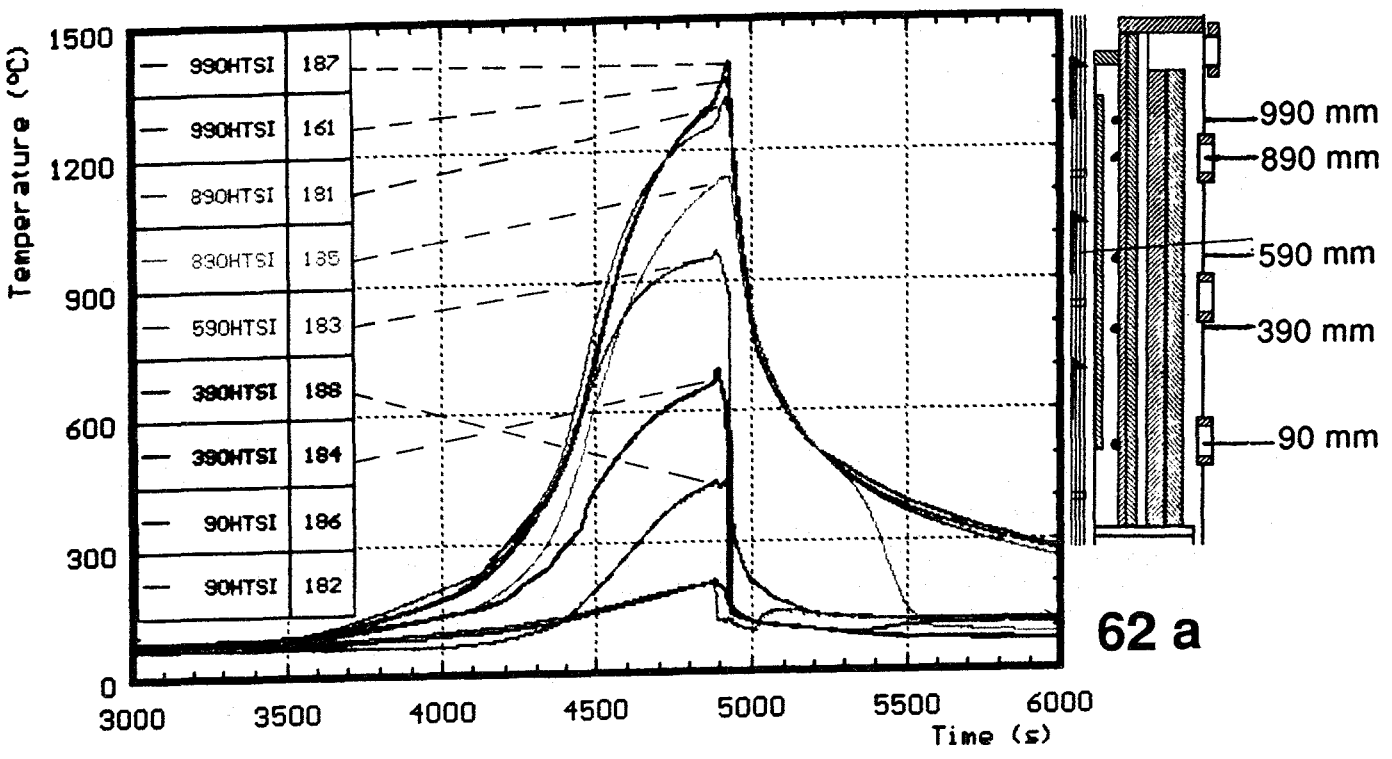

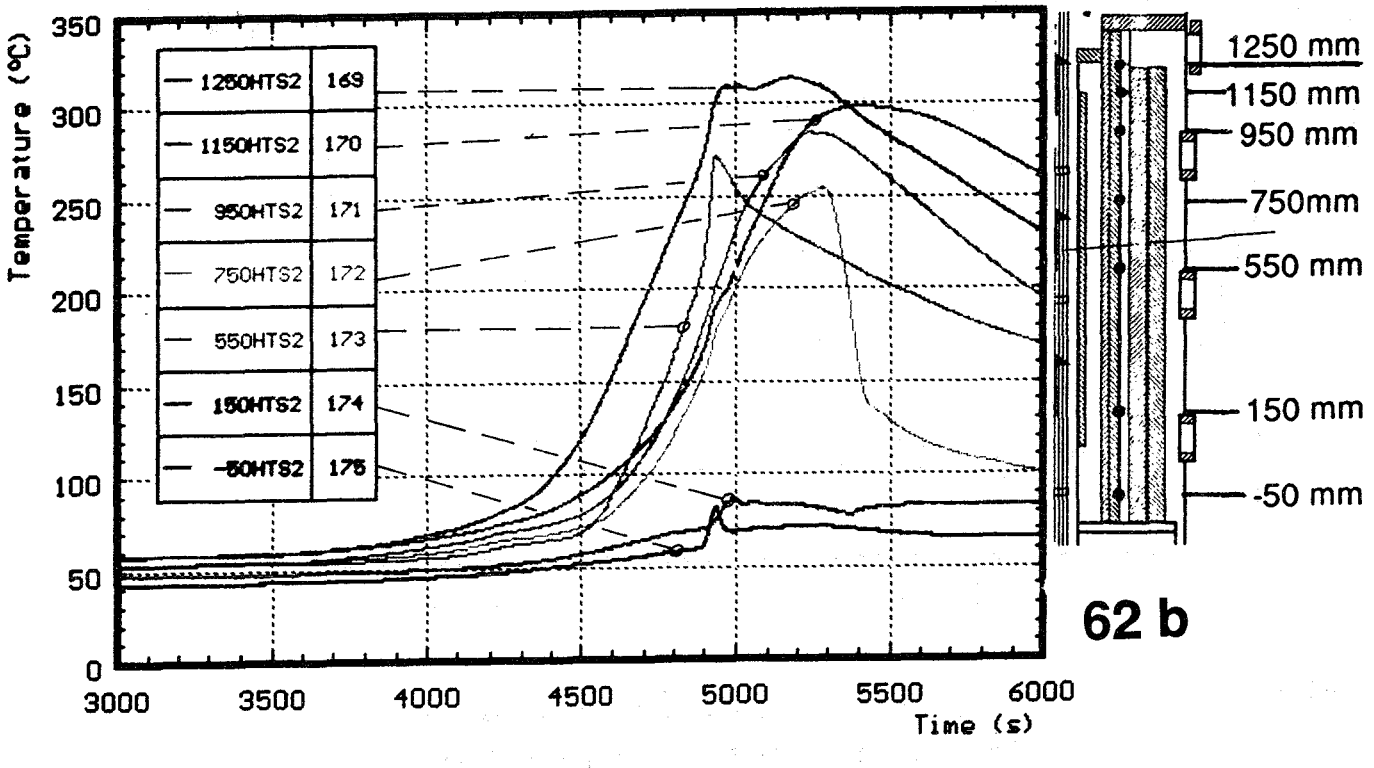

Fig. 62: Temperatures of HTS at inner surface 345°, (a) 153 mm radius; (b) 192 mm radius; (CORA-13)

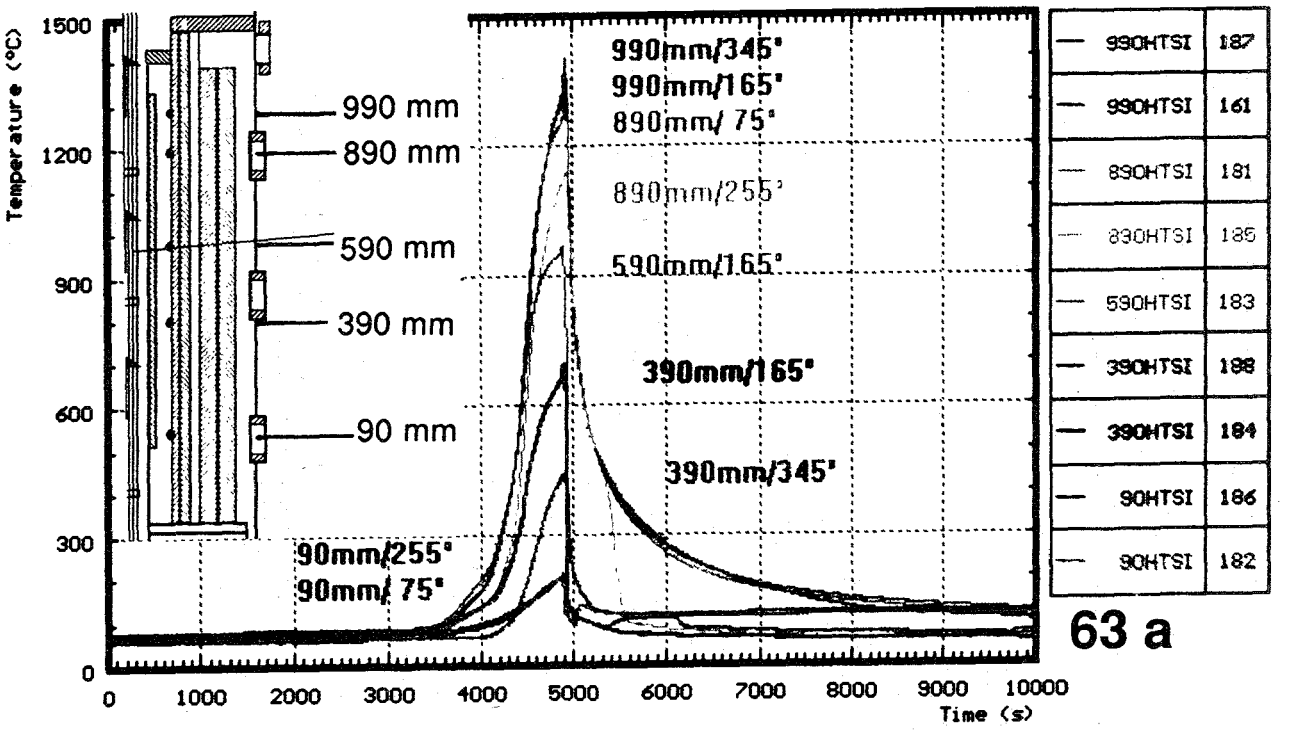

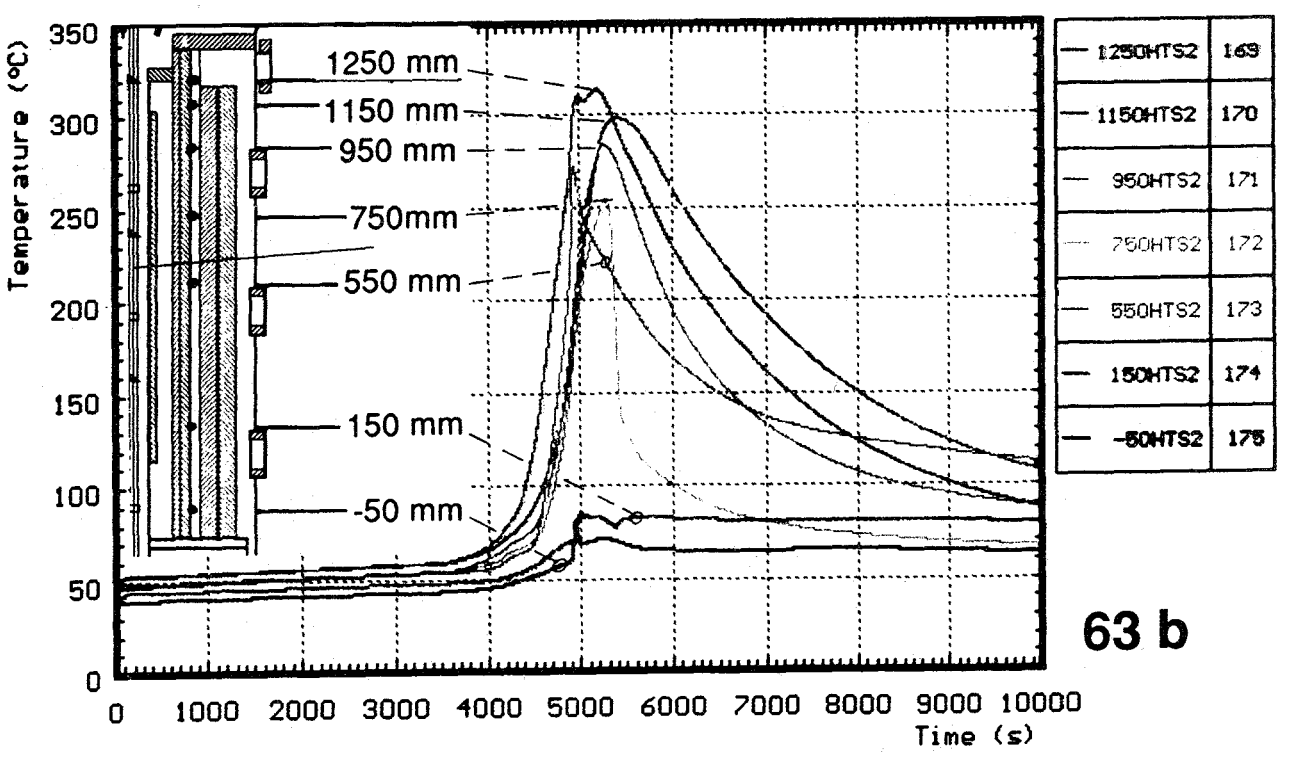

Fig. 63: Temperatures of HTS at inner surface 345°, (a) 153 mm radius; (b) 192 mm radius; (CORA-13)

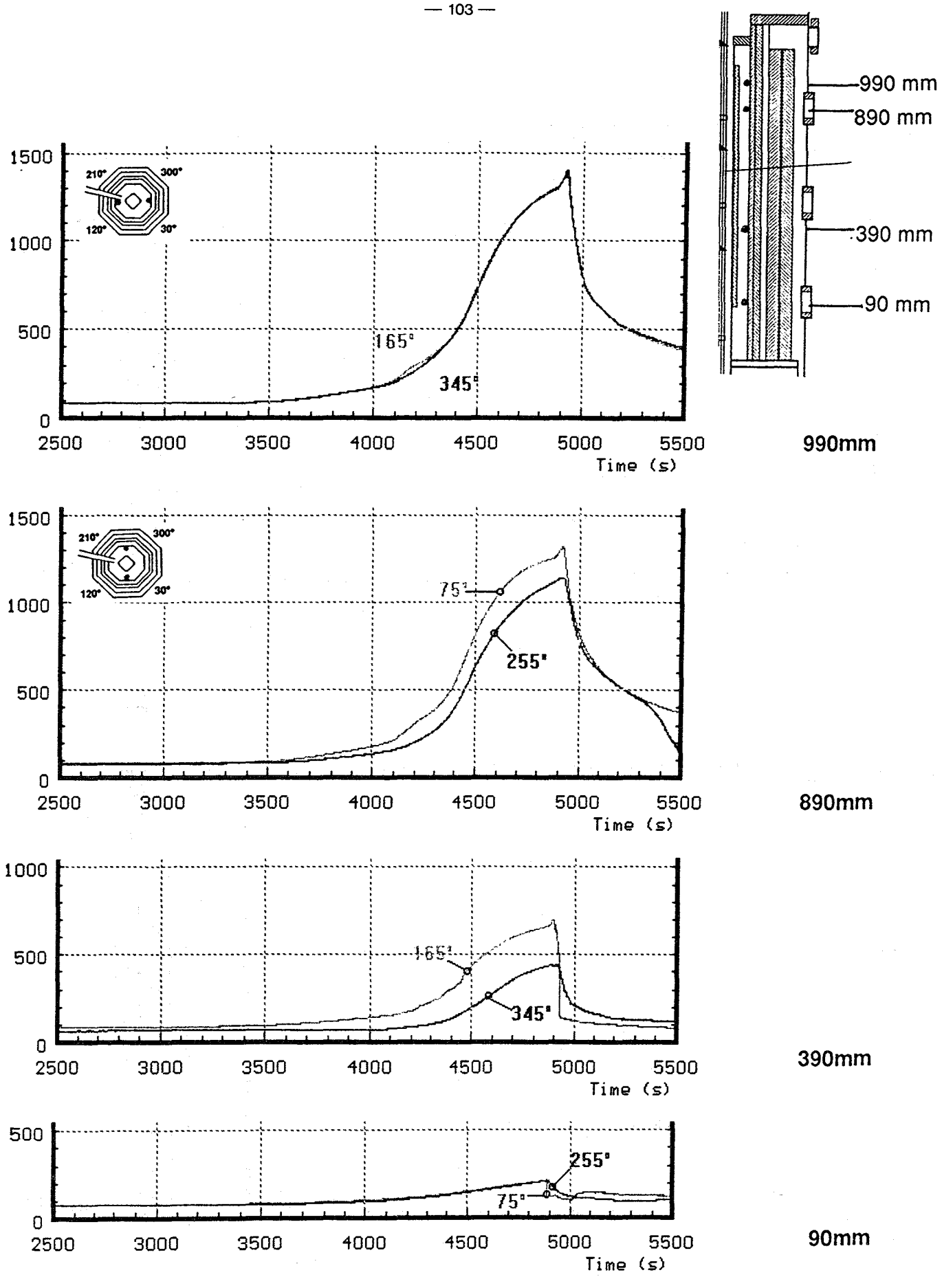

Fig. 64: Temperatures of HTS comparison at the inner surface, 153 mm radius (CORA-13)

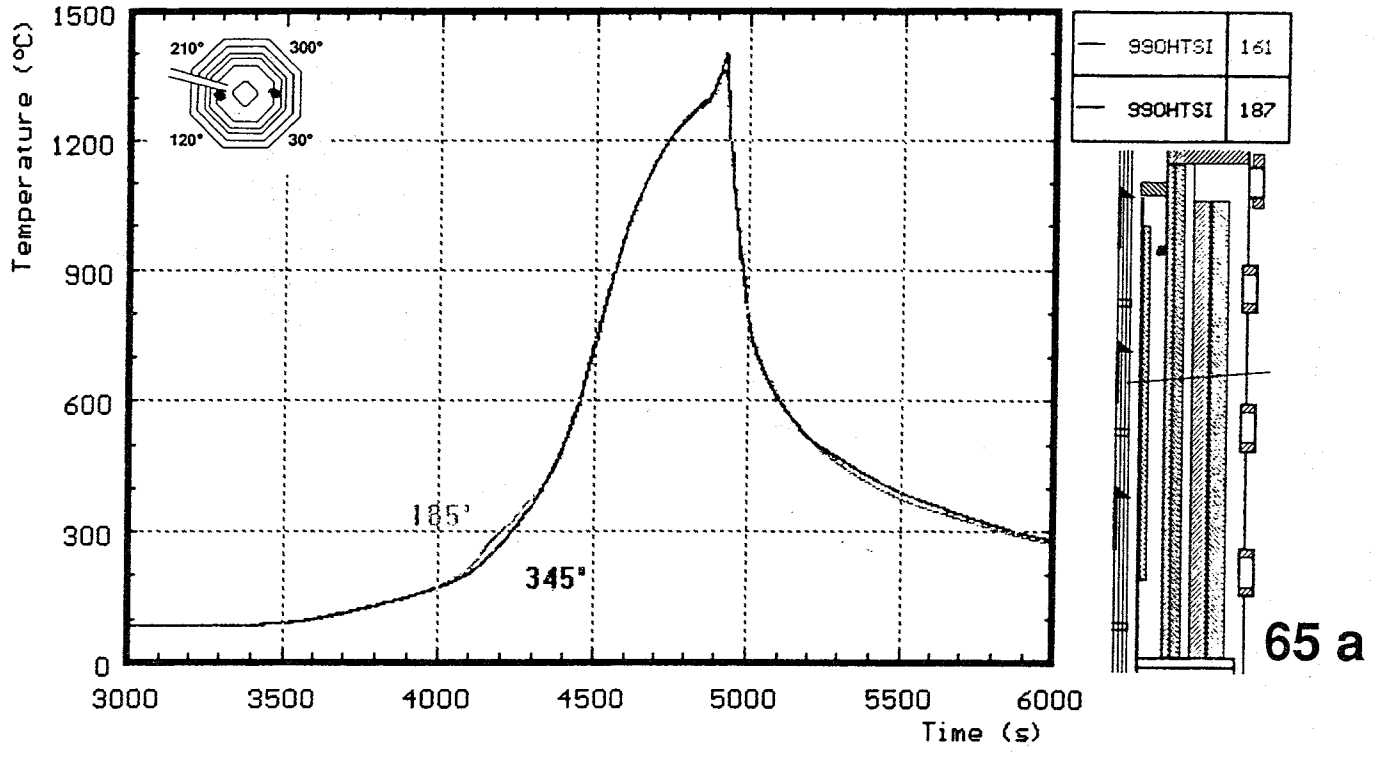

65 a

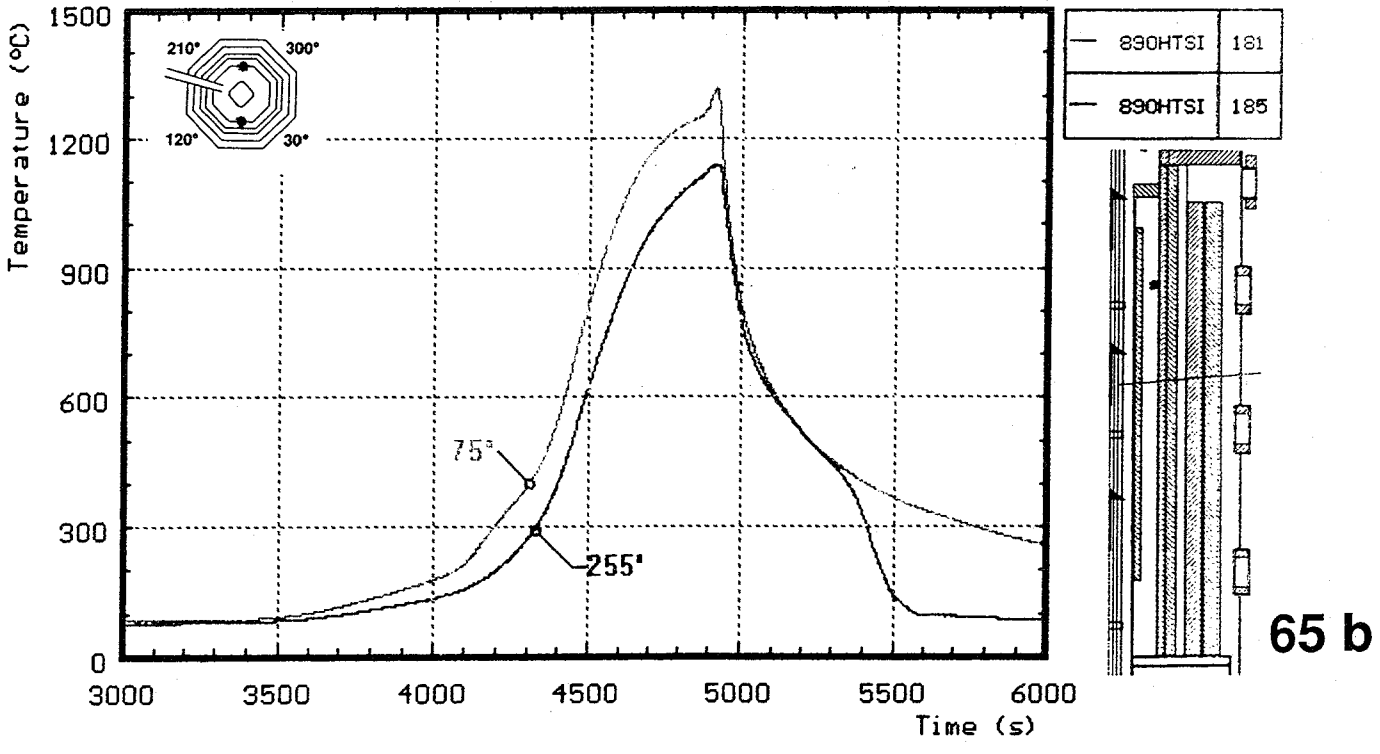

65 b

Fig. 65: Temperature of HTS (CORA-13); Comparison at the inner surface (153 mm radius) (a) at 990 mm, (b) at 890 mm elevation

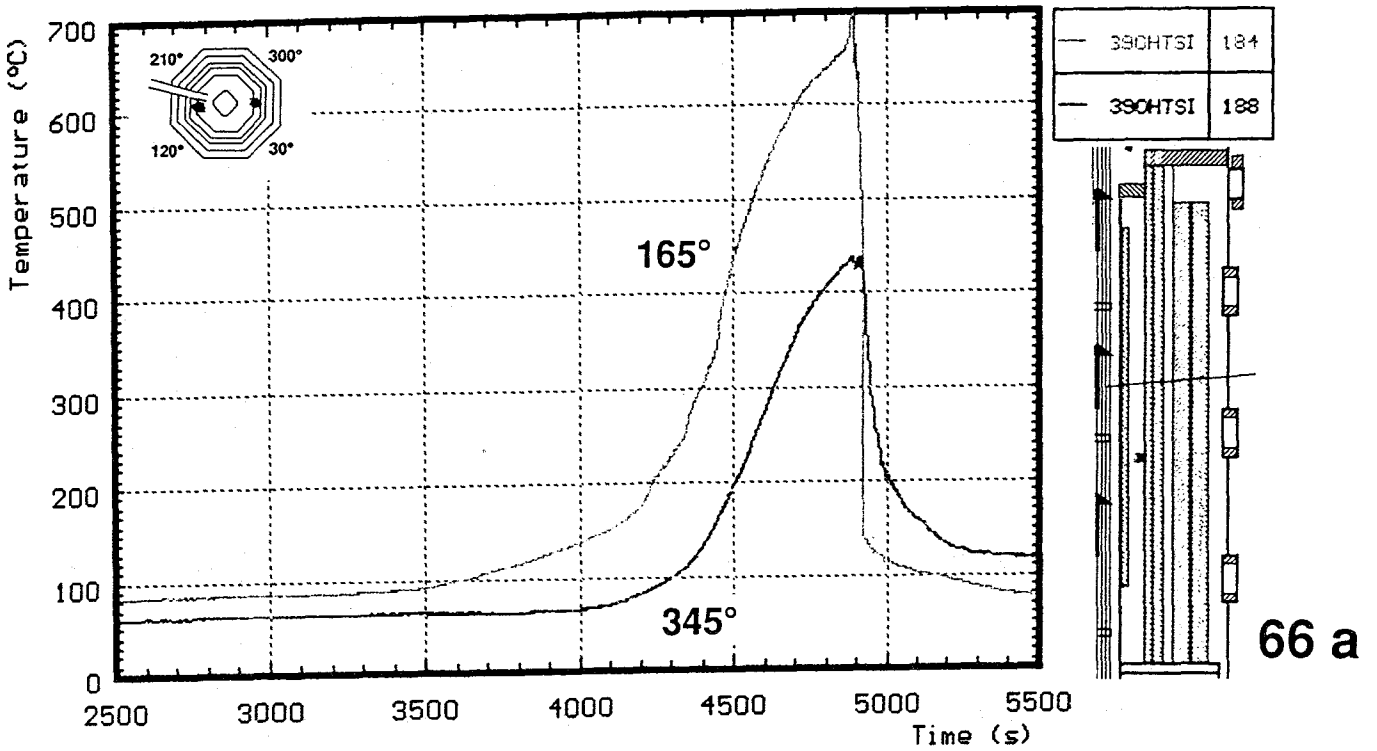

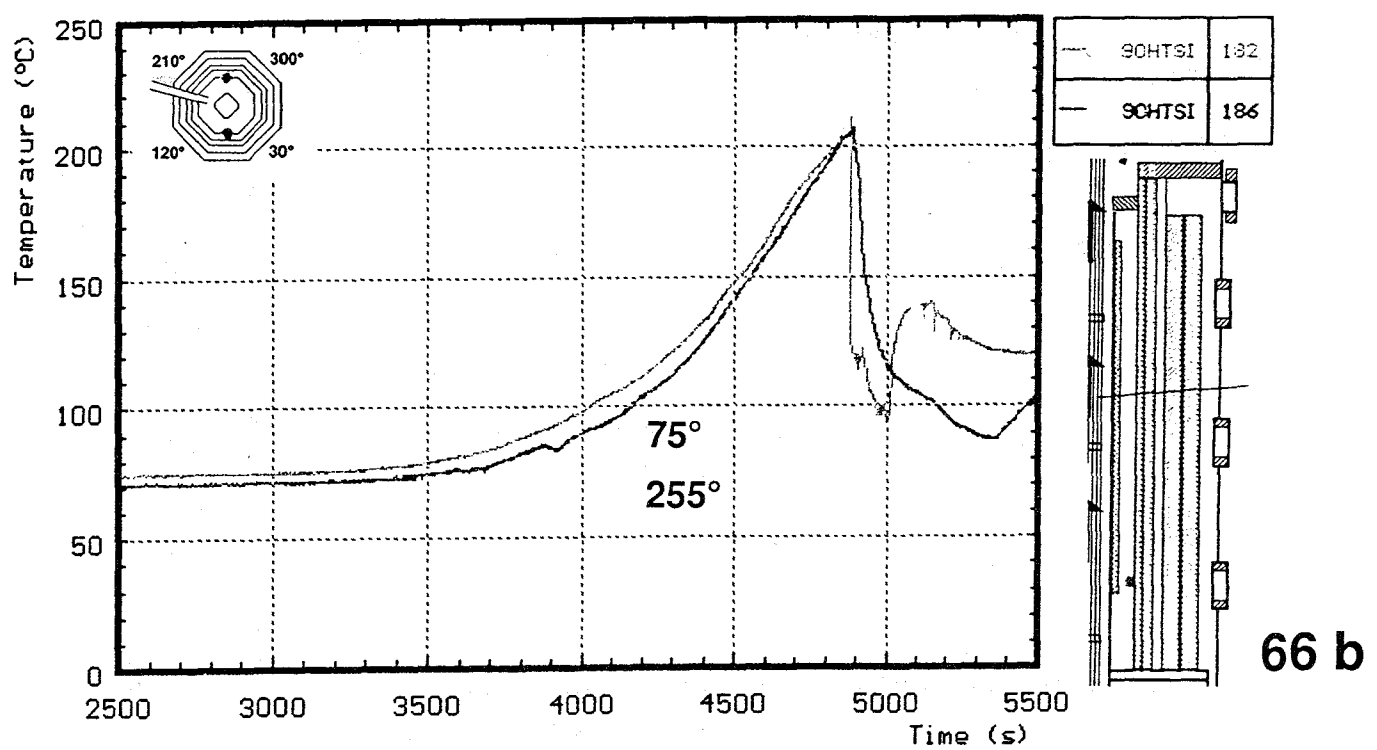

Fig. 66: Temperature of HTS (CORA-13); Comparison at the inner surface (153 mm radius) (a) at 390 mm, (b) at 90 mm elevation

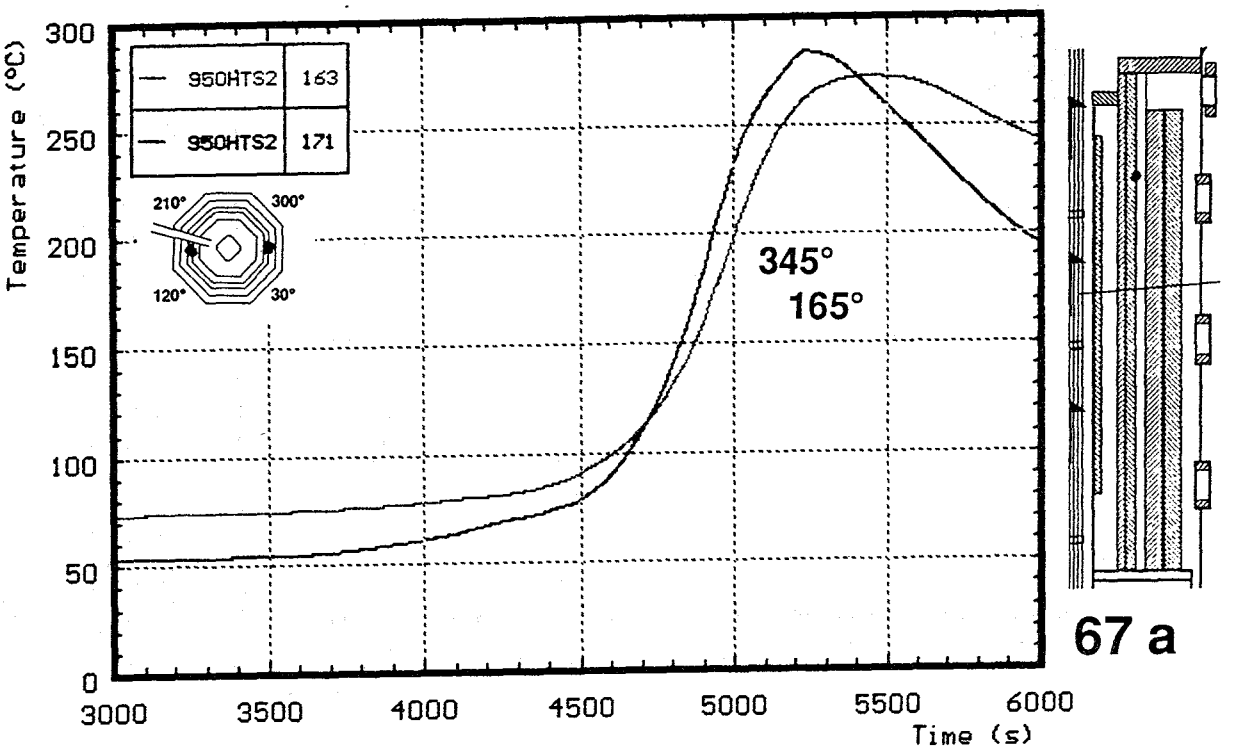

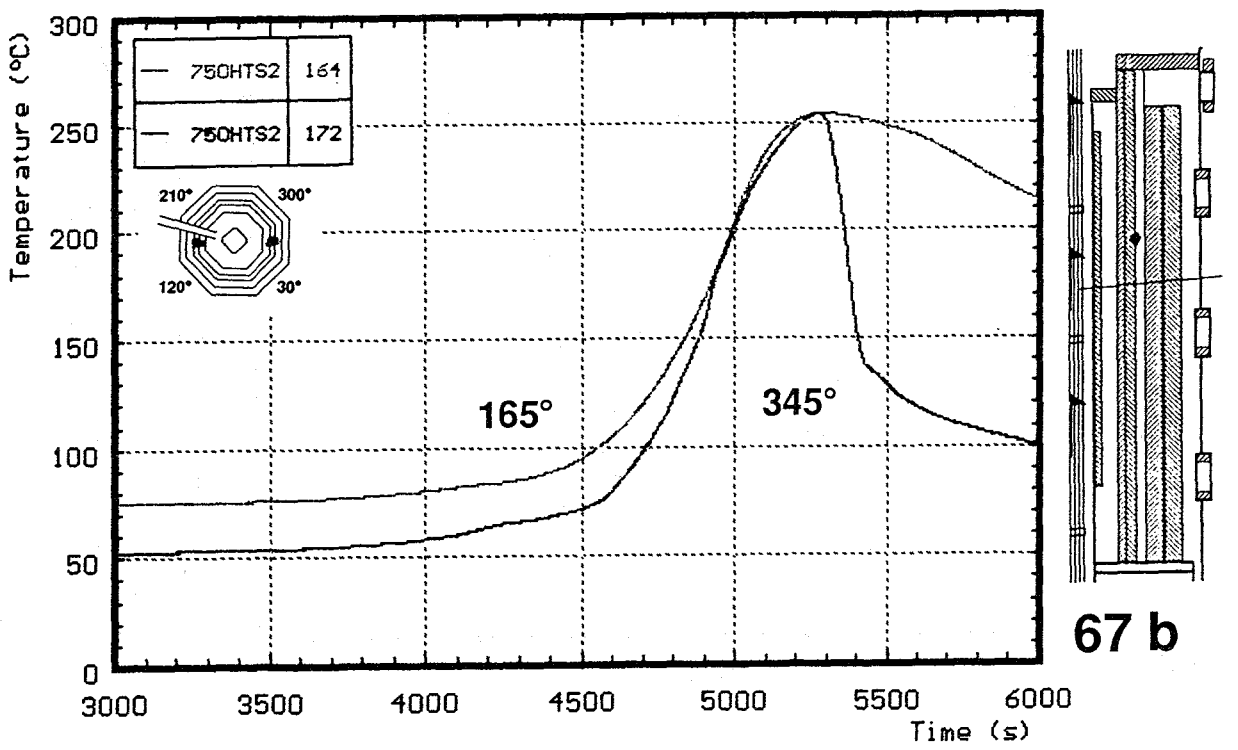

Fig. 67: Temperature of HTS (CORA-13); Comparison at 192 mm radius at (a) 950 mm elevation, (b)750 mm elevation

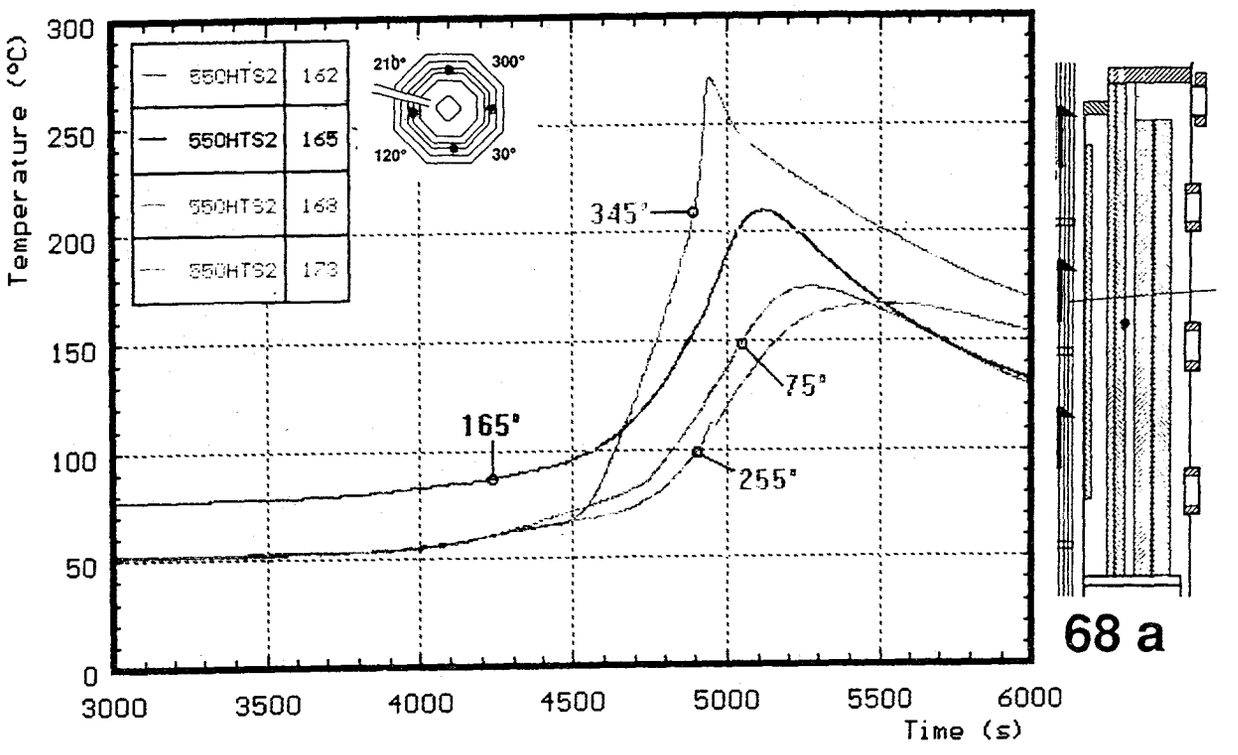

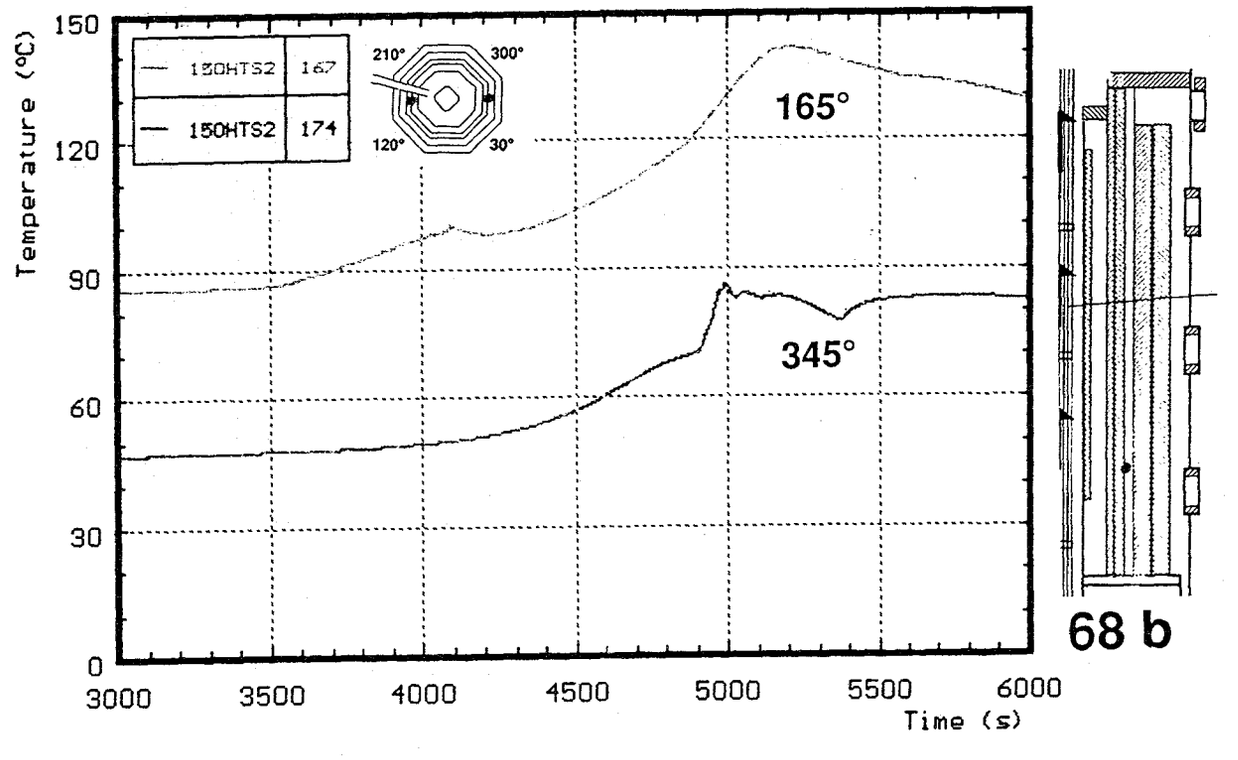

Fig. 68: Temperature of HTS (CORA-13); Comparison at 192 mm radius at (a) 550 mm elevation, (b) 150 mm elevation

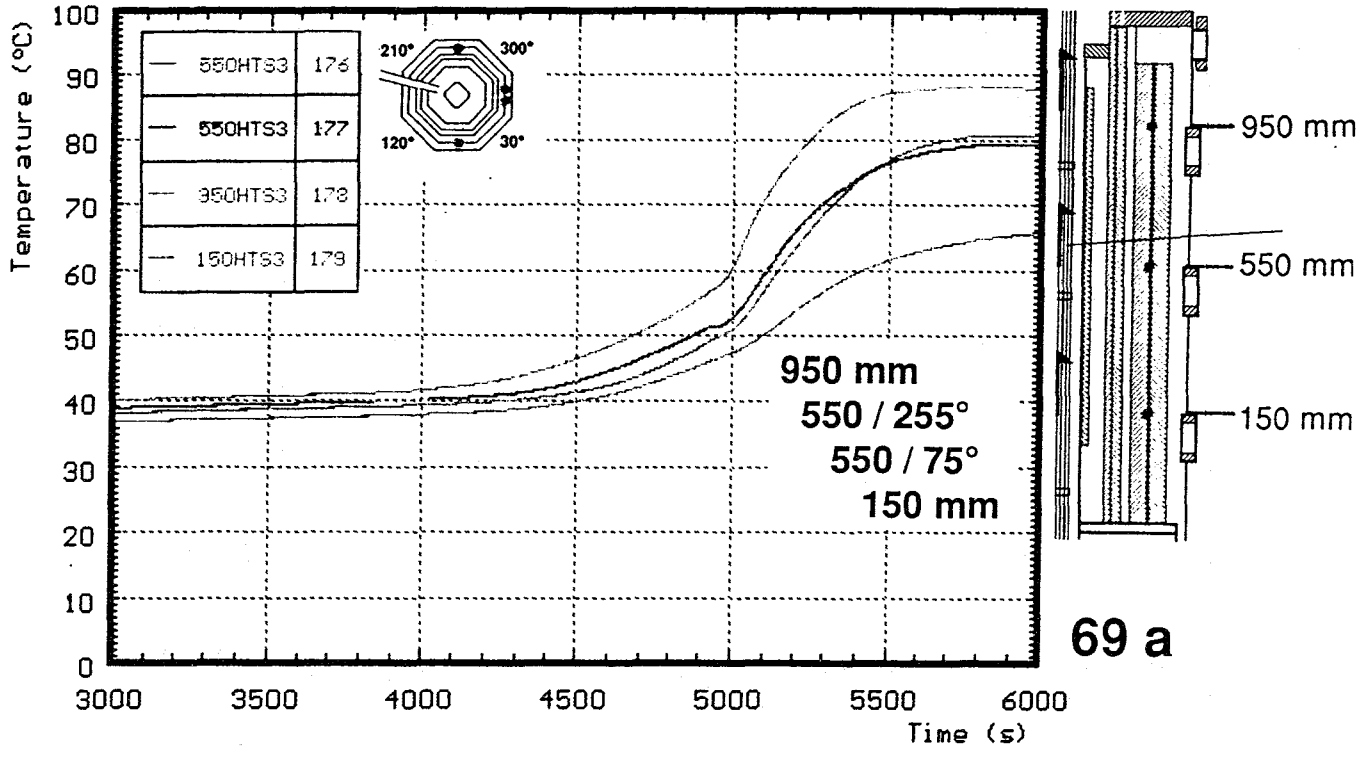

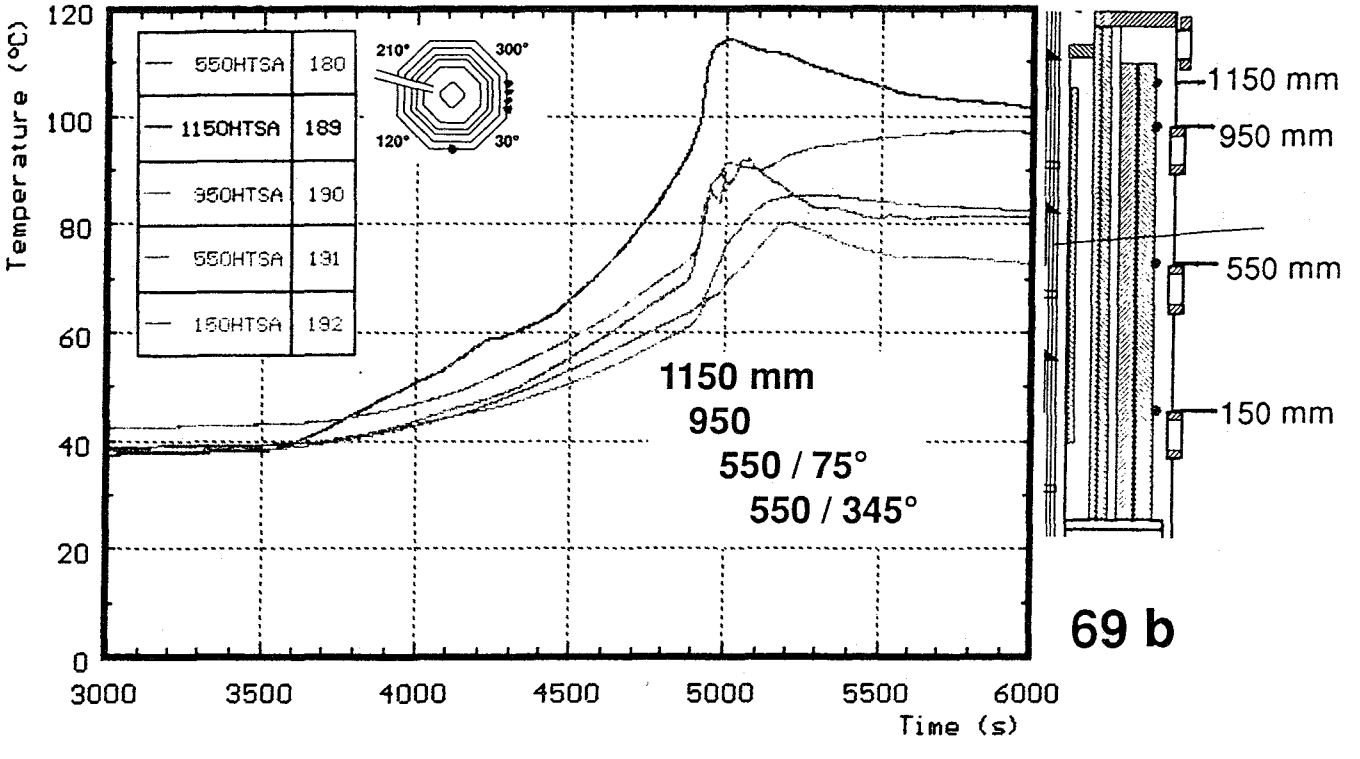

Fig. 69: Temperature of HTS (CORA-13); (a) 255 mm radius, (b) 293 mm radius

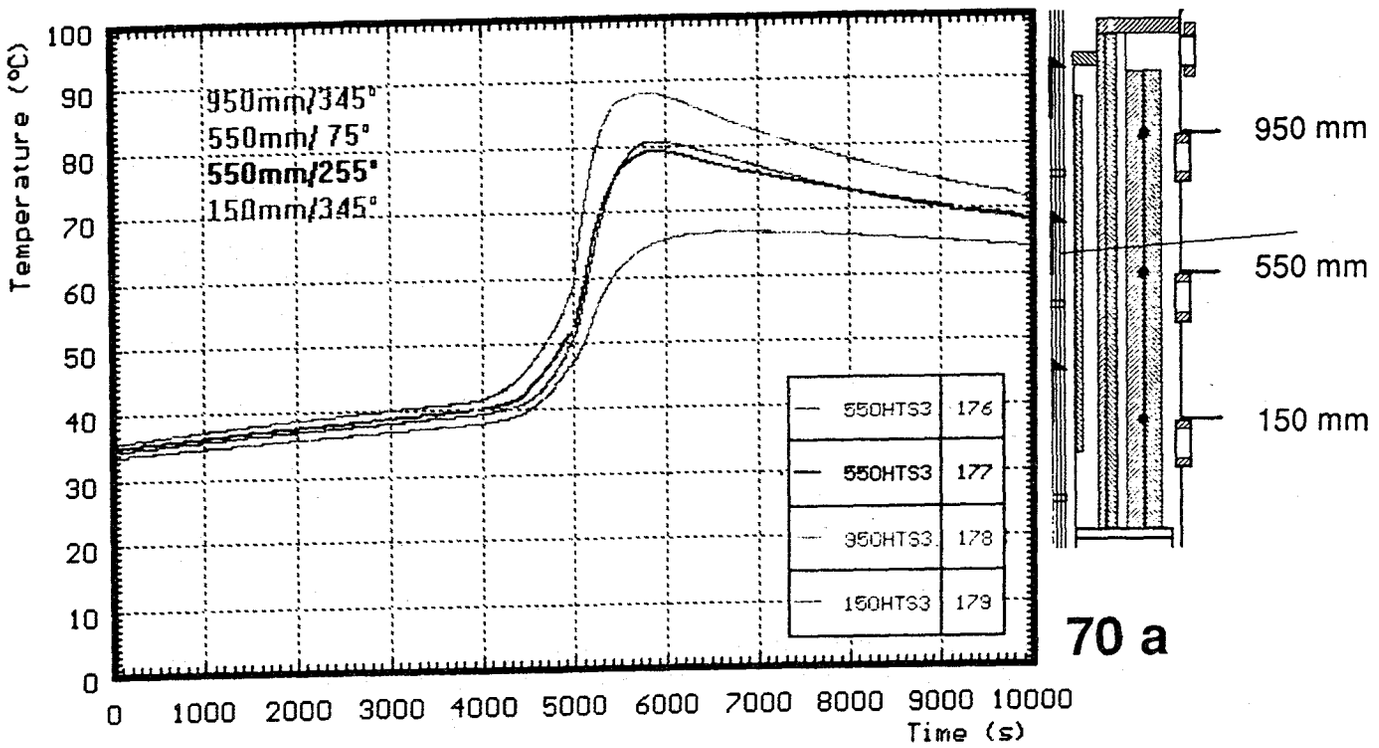

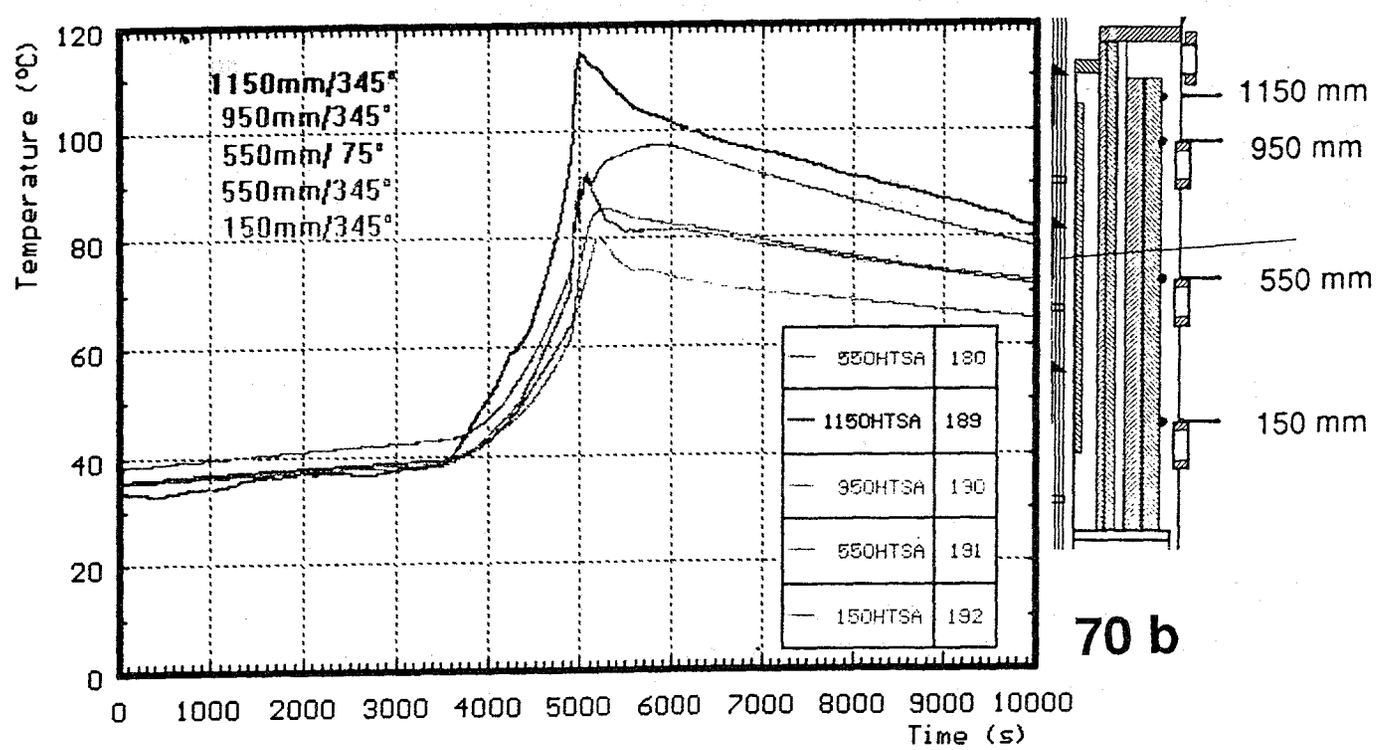

Fig. 70: Temperature of HTS (CORA-13); (a) 255 mm radius, (b) 293 mm radius

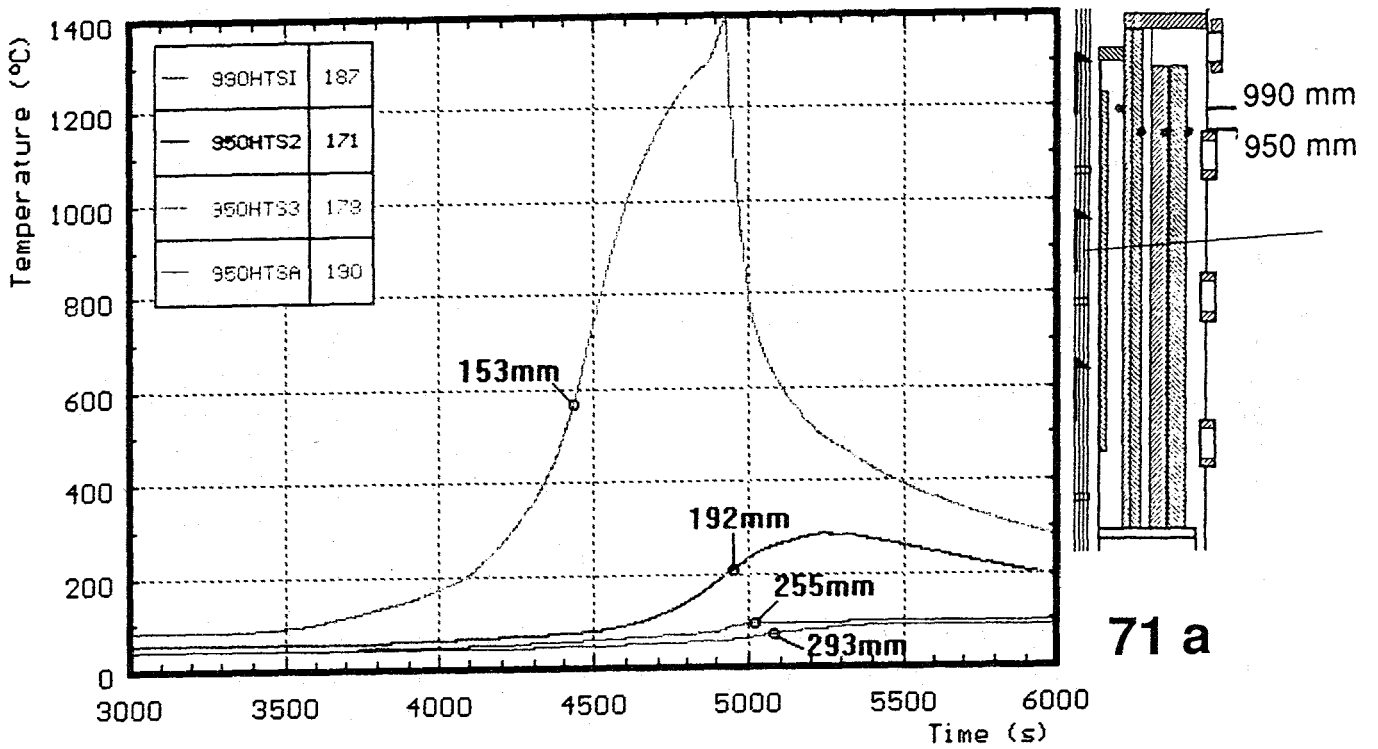

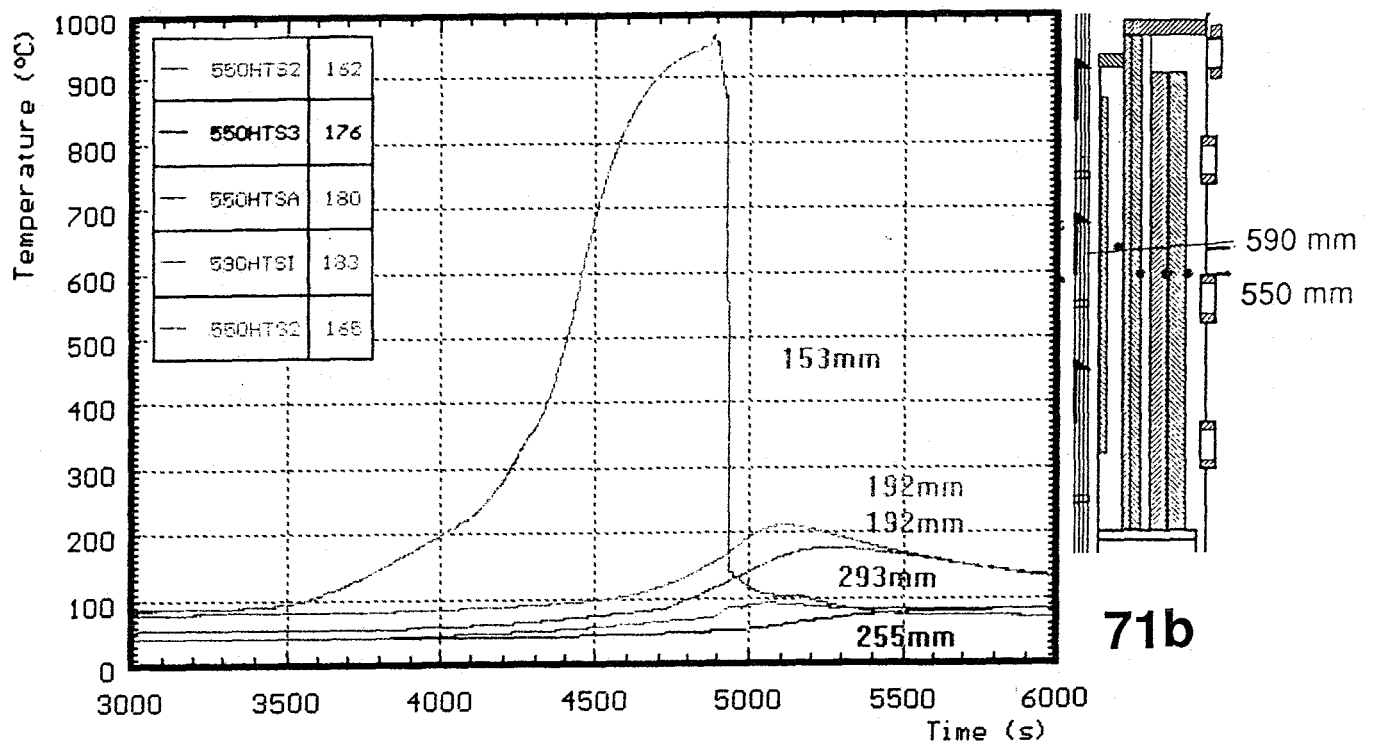

Fig. 71: Temperature of HTS (CORA-13); Radial distribution (a) at 950 mm elevation, (b) at 550 mm elevation

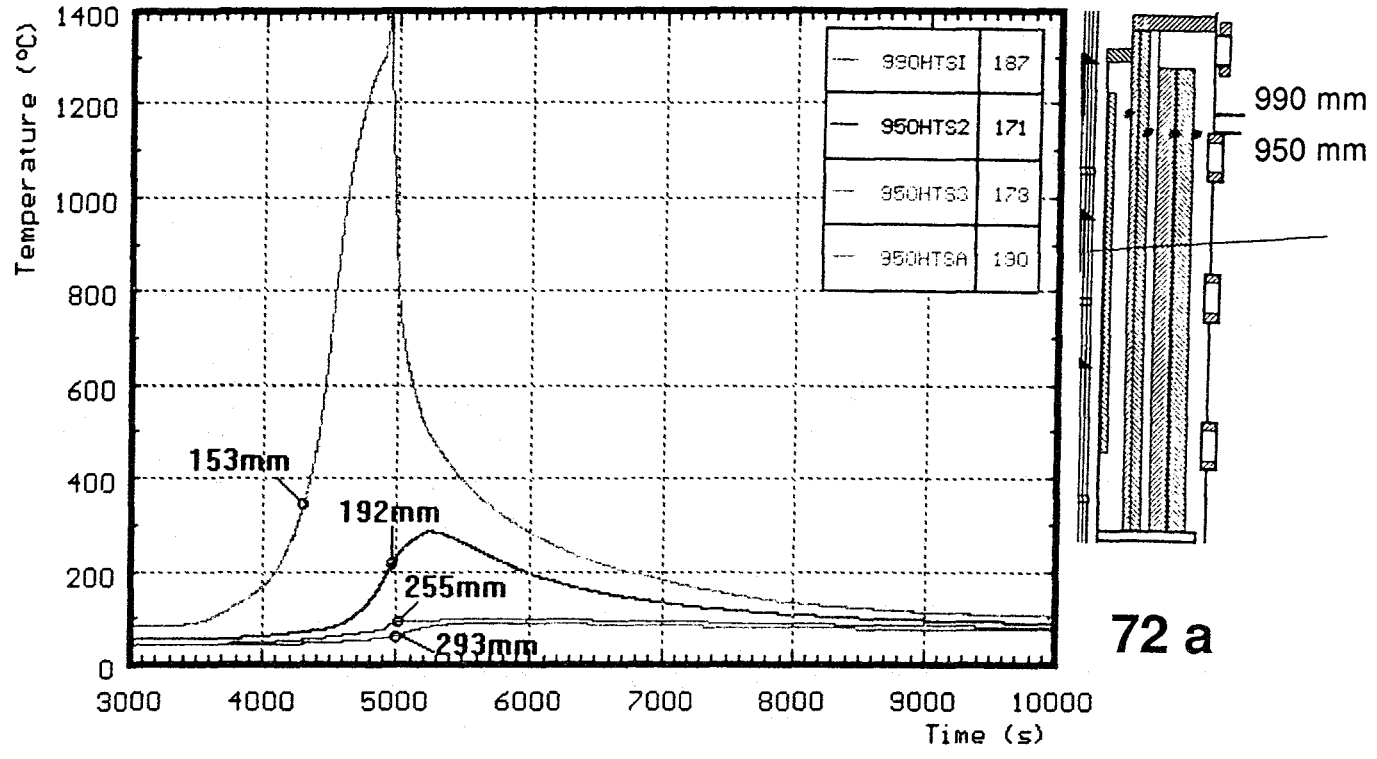

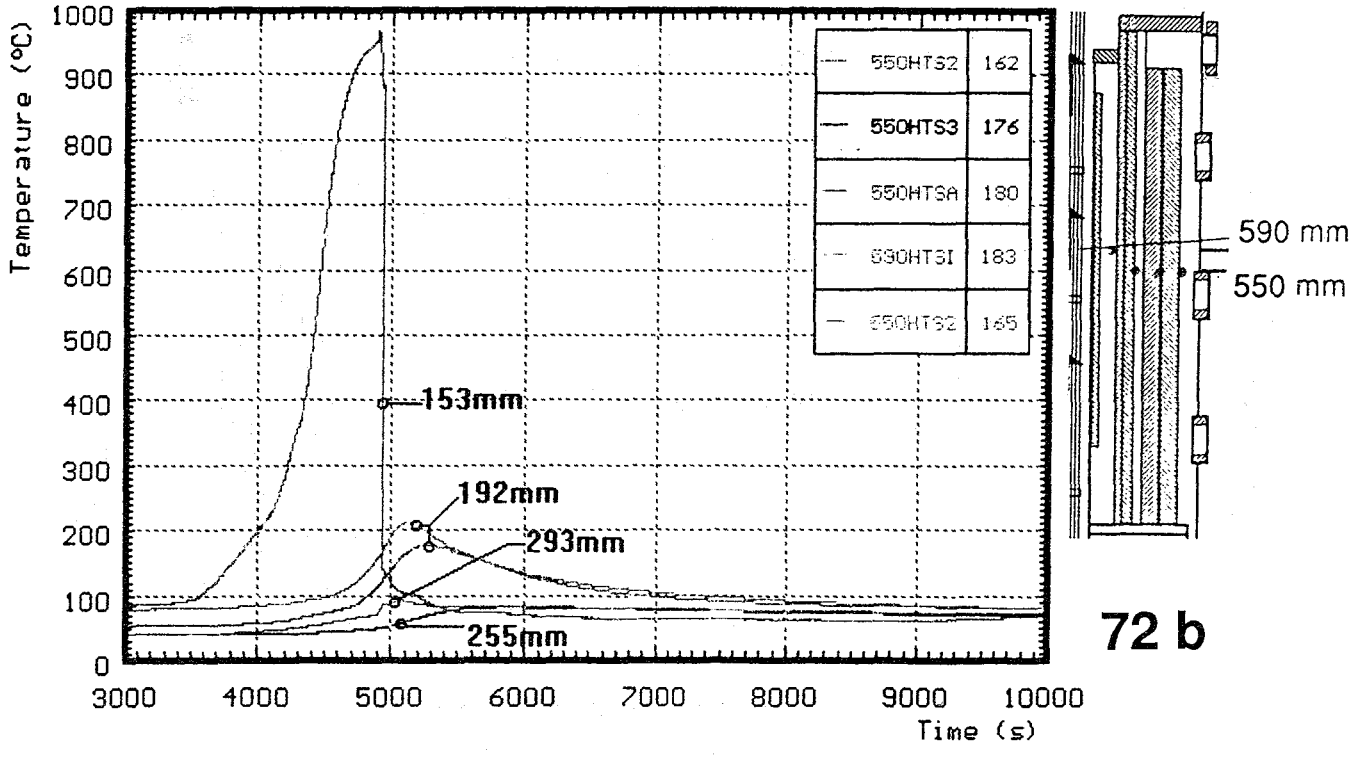

Fig. 72: Temperature of HTS (CORA-13);
Radial distribution (a) at 950 mm elevation,
(b) at 550 mm elevation

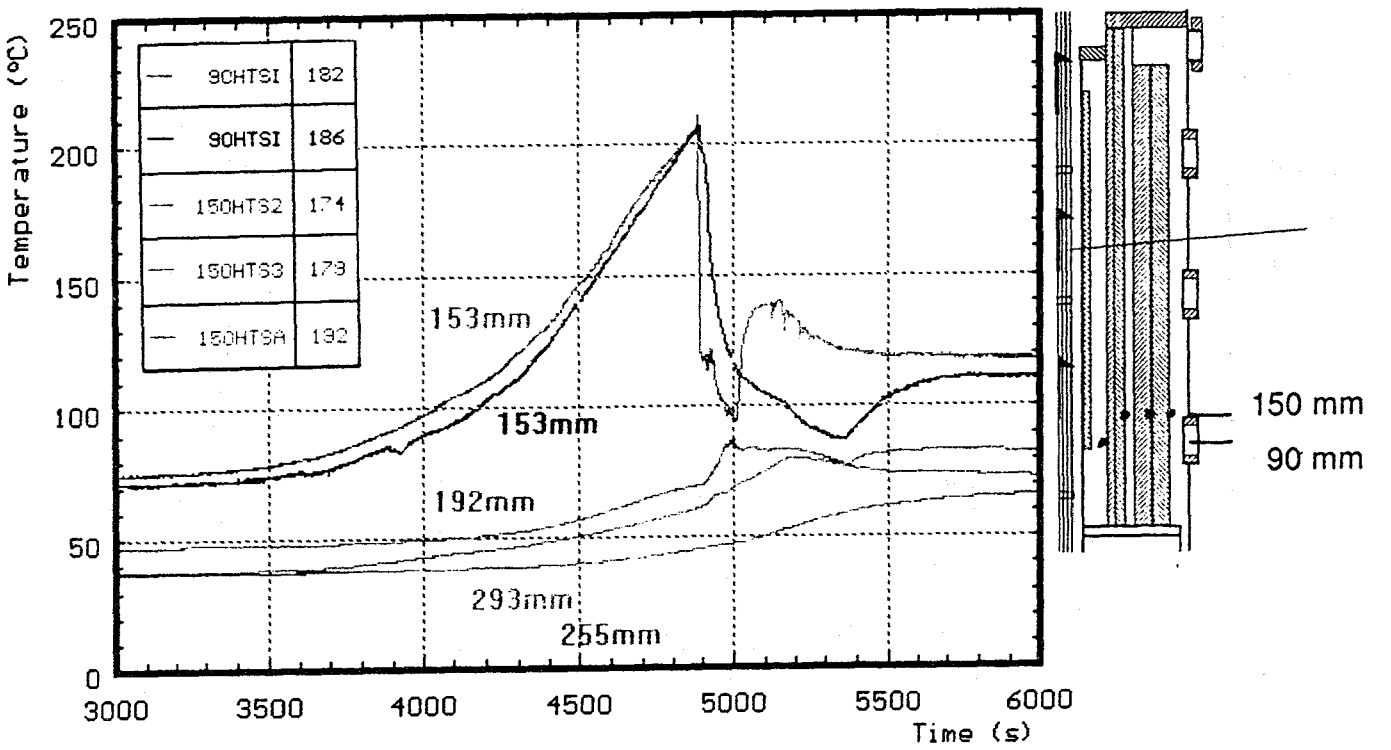

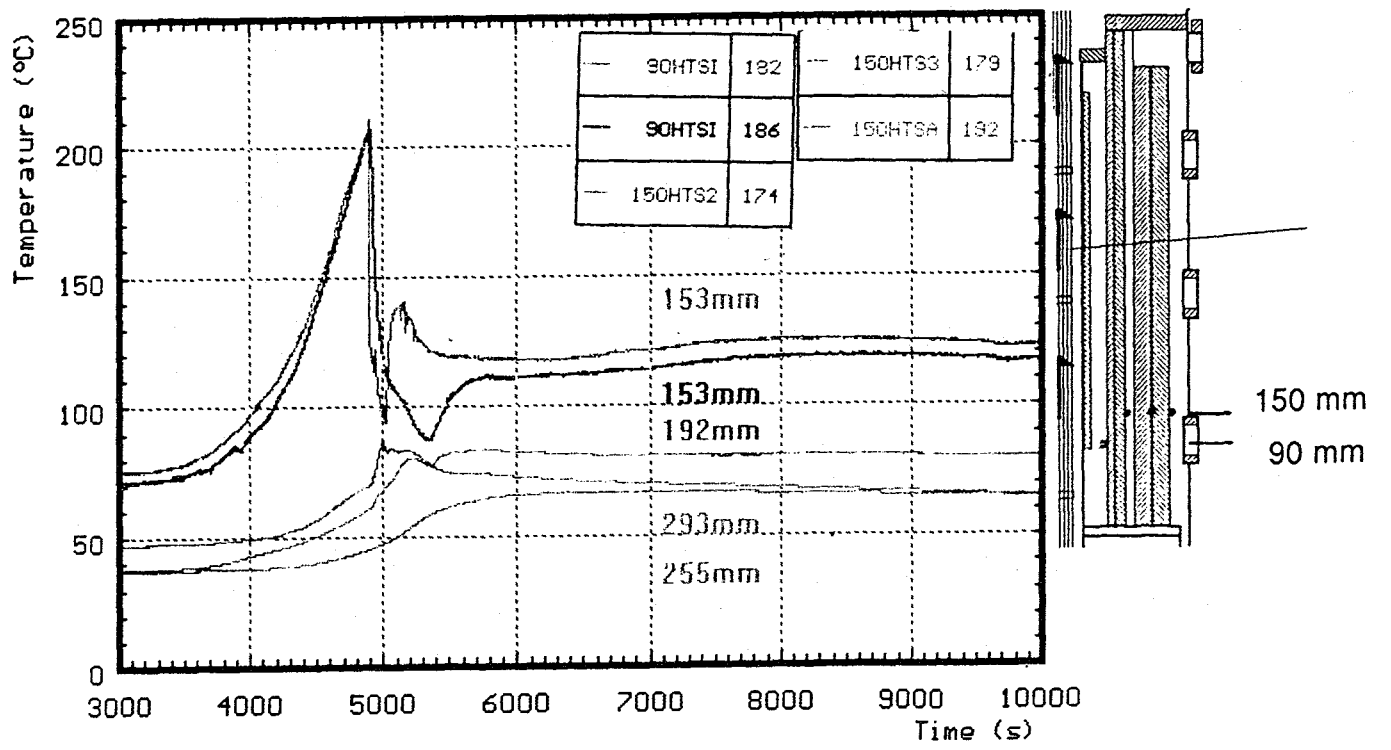

Fig. 73: Temperature of HTS (CORA-13); Radial distribution at about 100 mm elevation during and after the transient

(a)

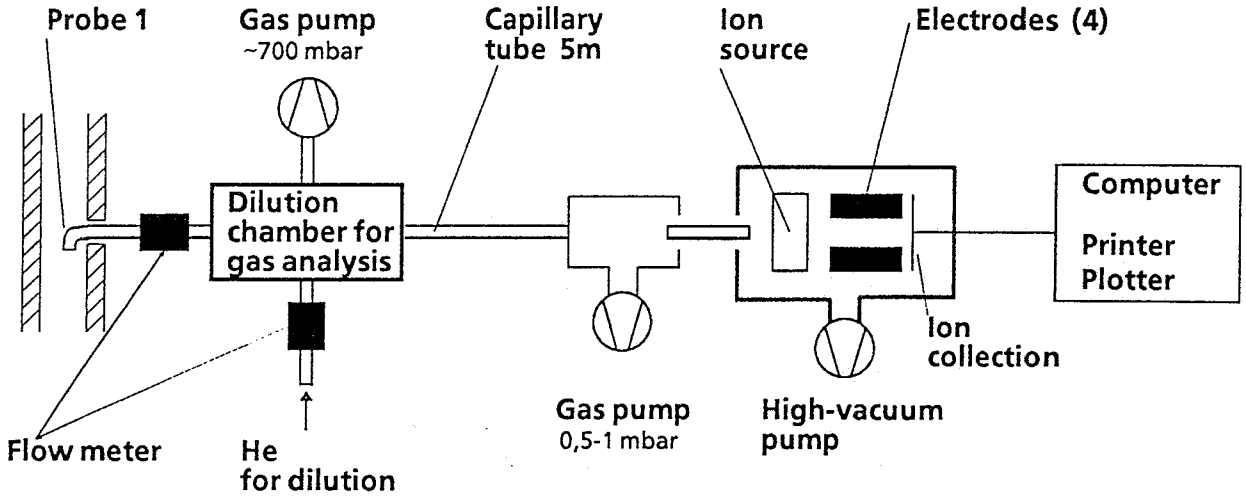

(b)

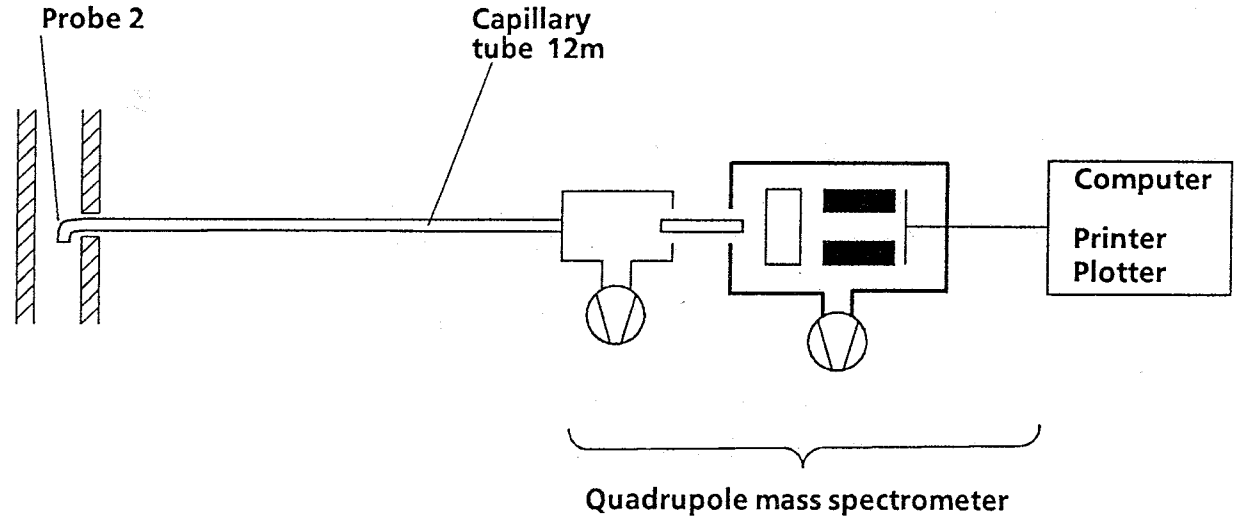

Location (a) : Outlet of test section

Location (b) : Mixing chamber

Fig. 74: Hydrogen measurement

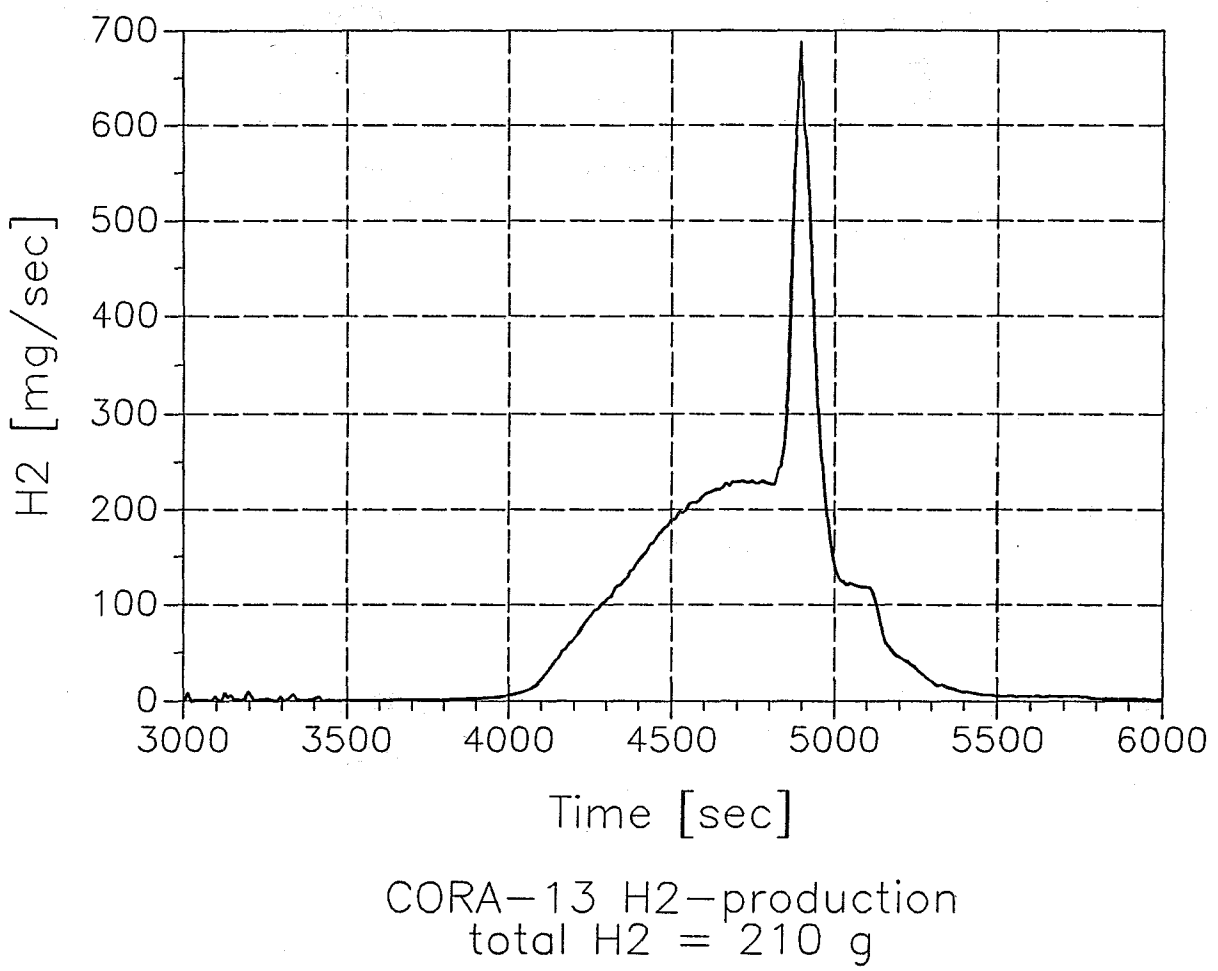

Fig. 75: Hydrogen generation during Test CORA-13

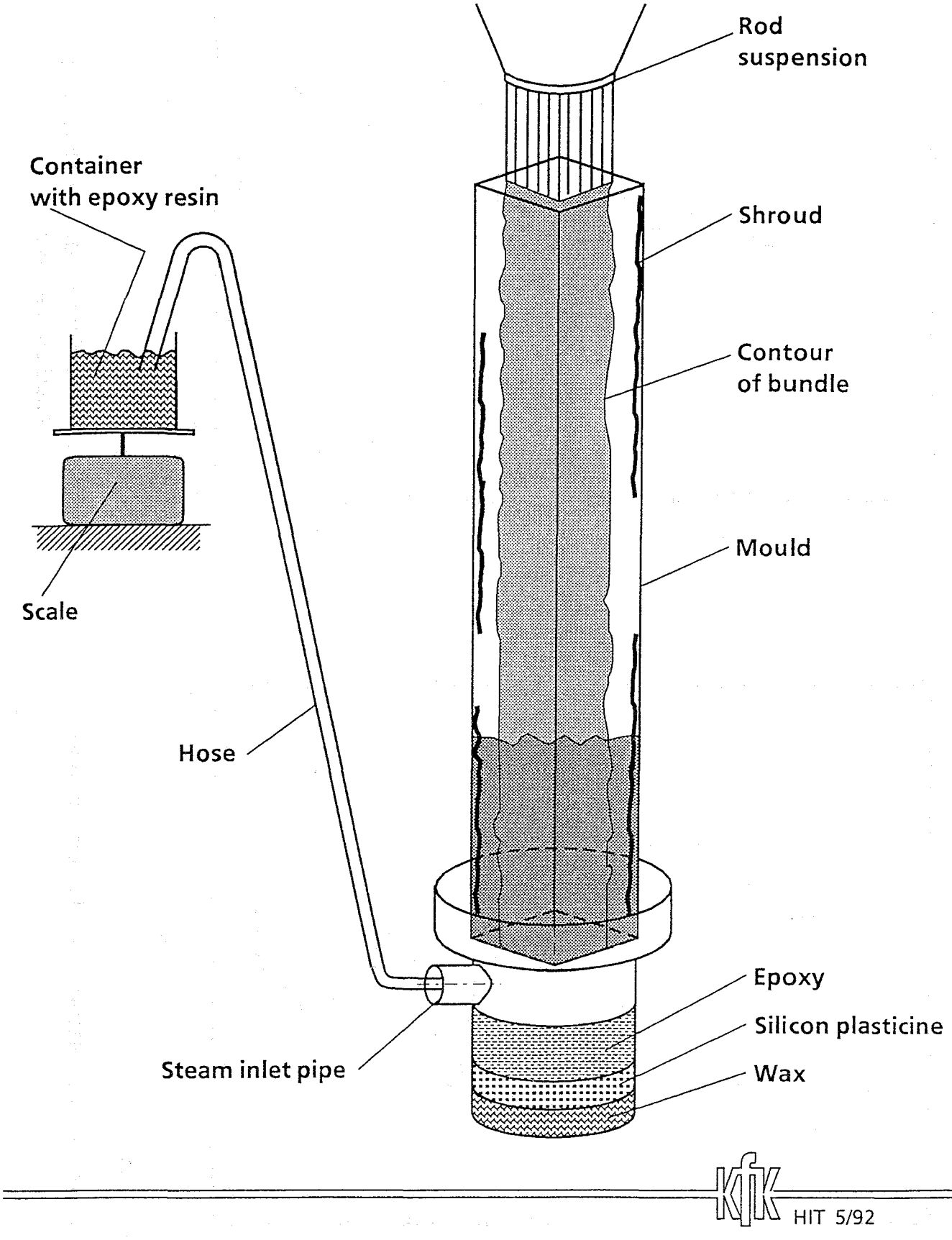

Fig. 76: Epoxying process of the tested bundle

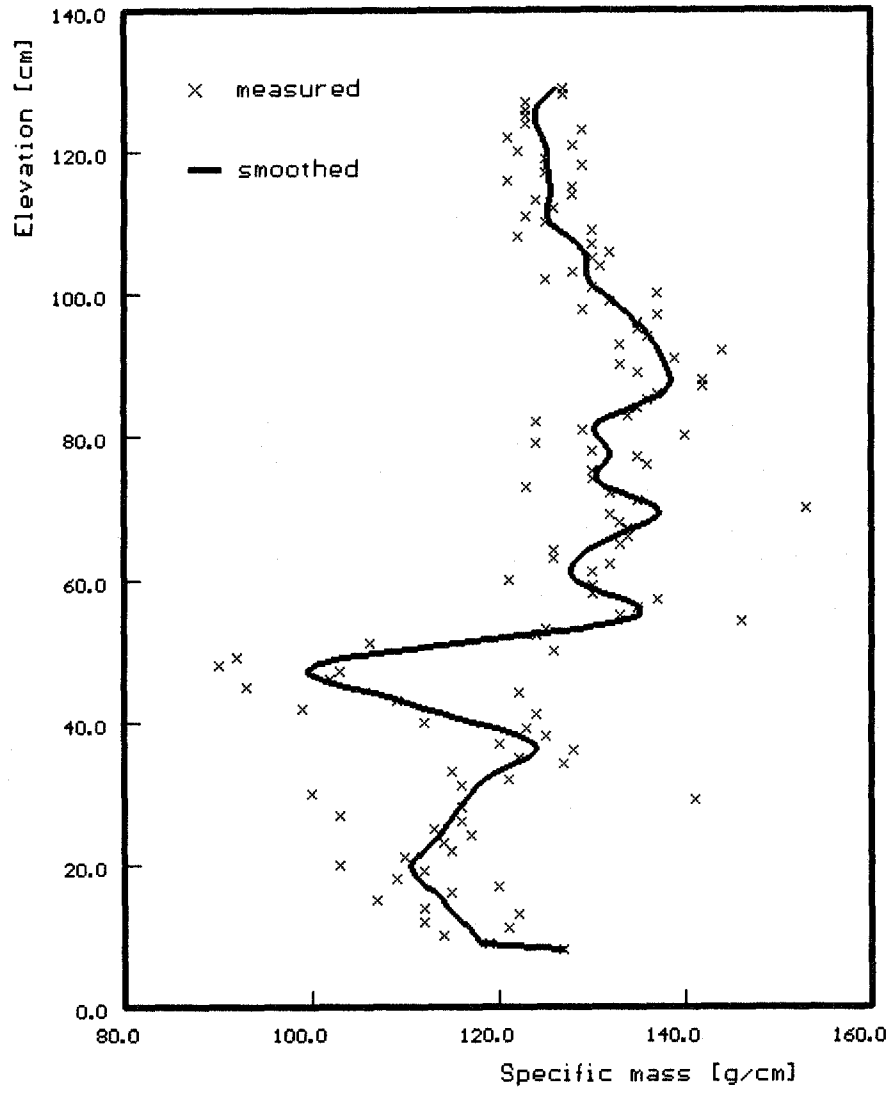

Fig. 77a

CORA 13: Axial distribution of epoxy bundle fill-up

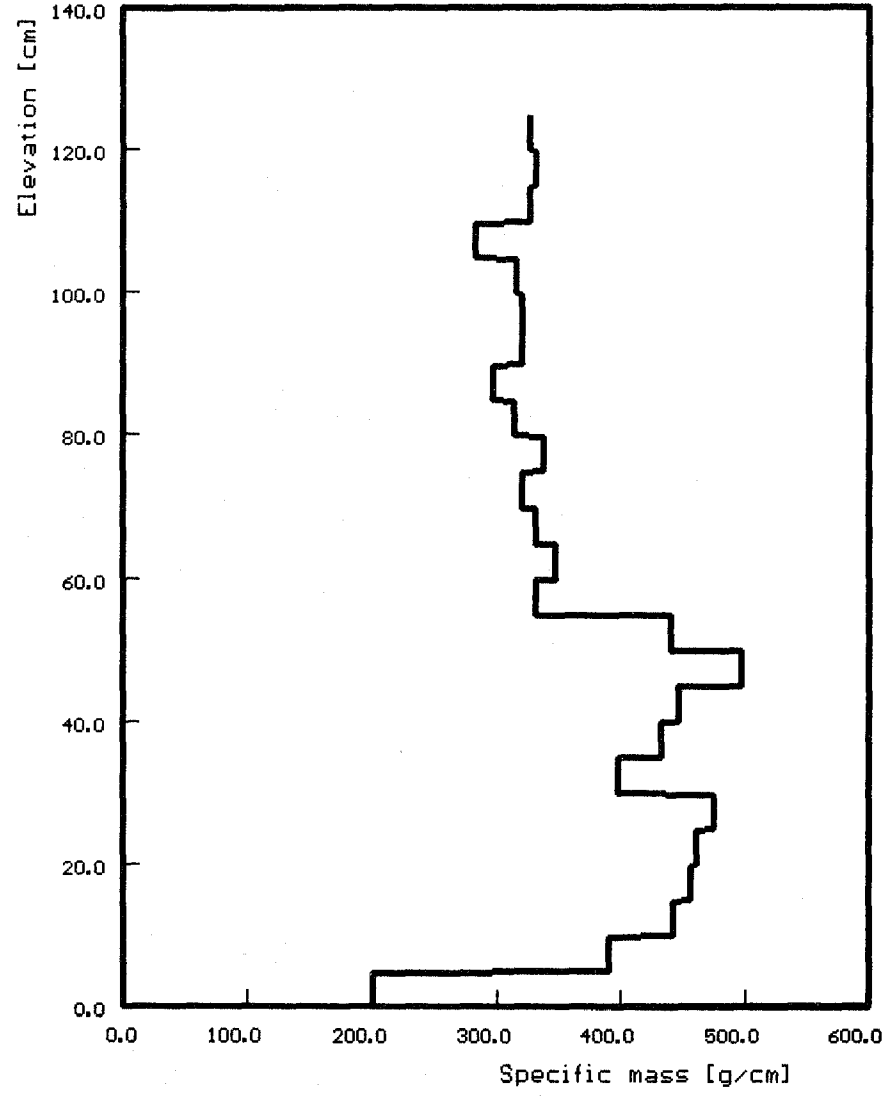

Fig. 77 b

CORA 13: Axial distribution of bundle segments filled with epoxy

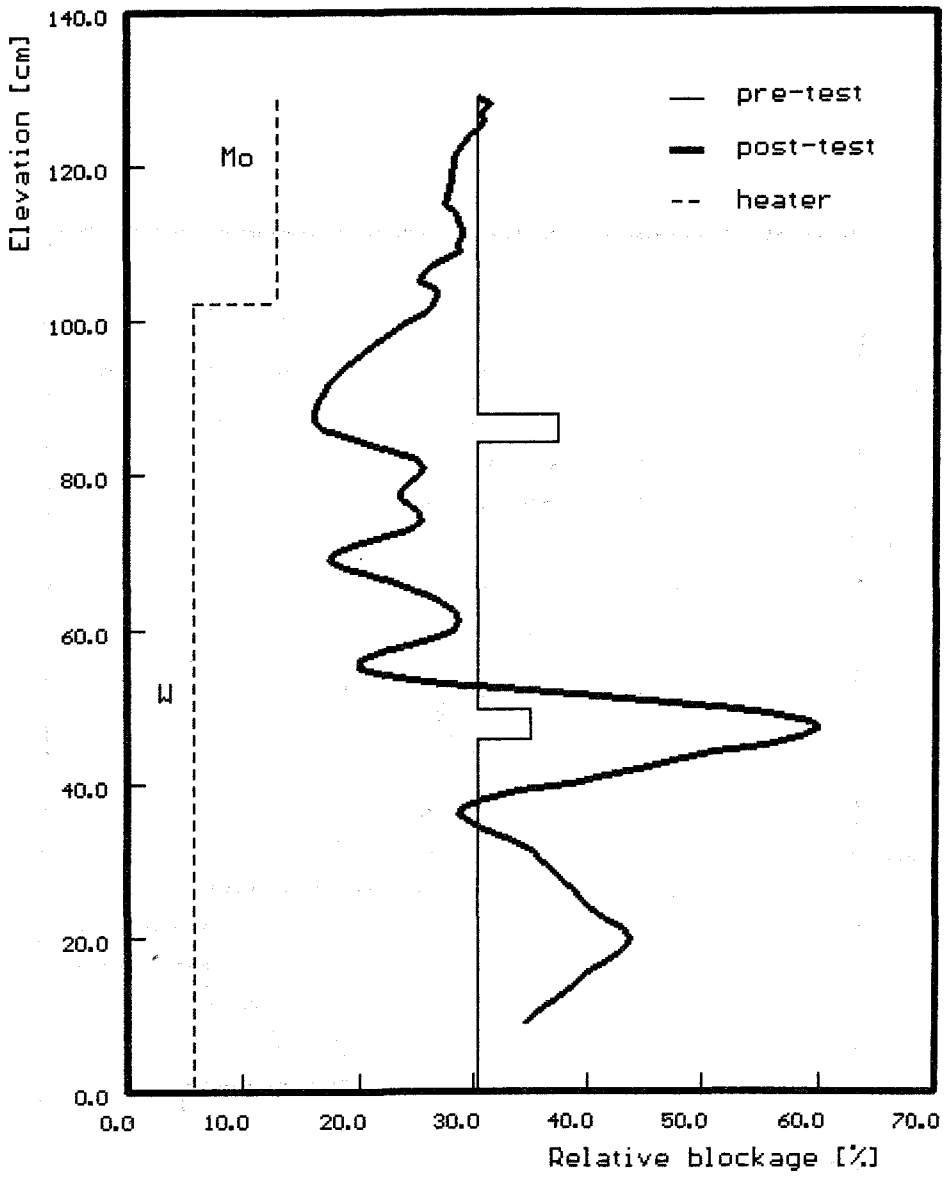

Fig. 78: CORA13: Axial distribution of blocked area inside the shroud

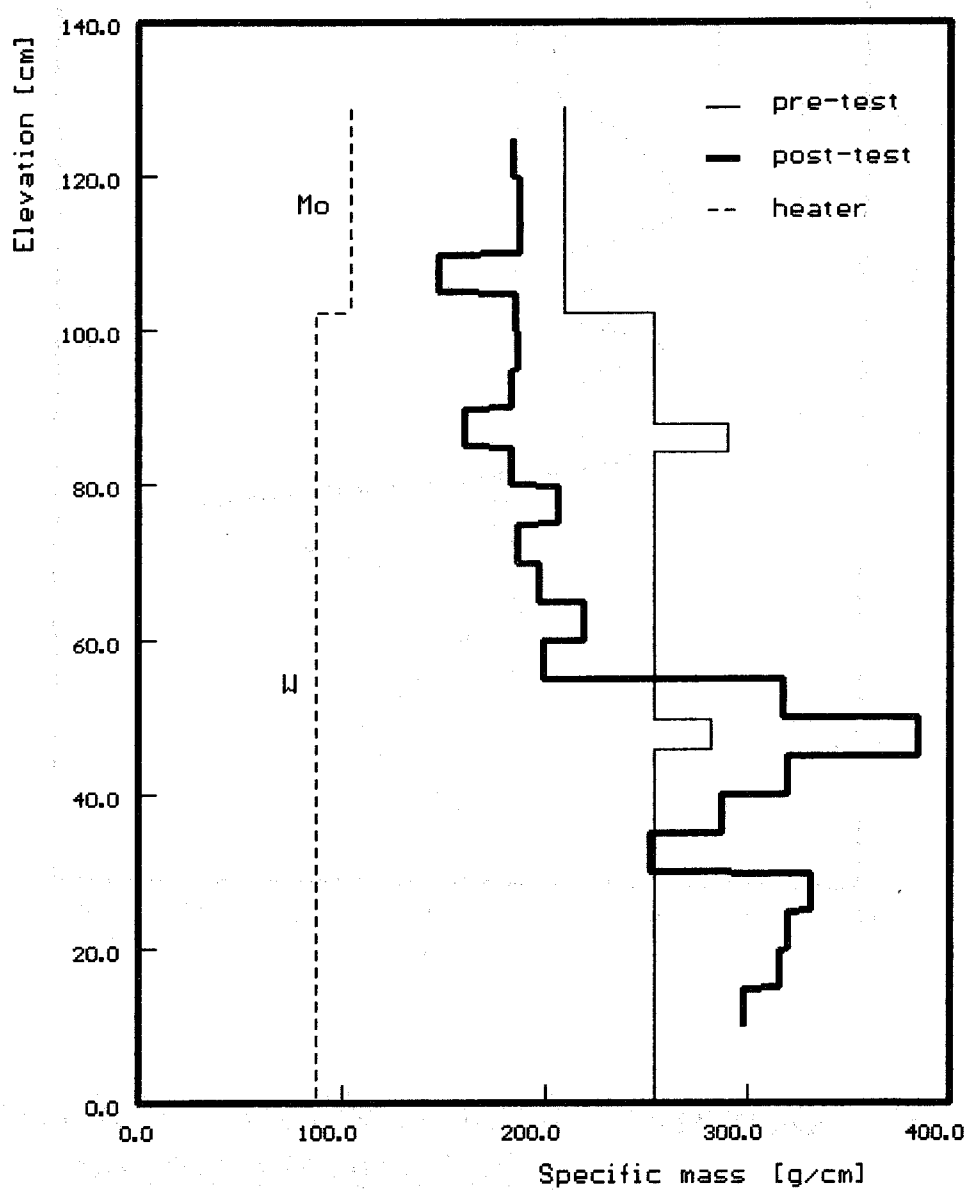

Fig. 79: CORA 13: Axial mass distribution

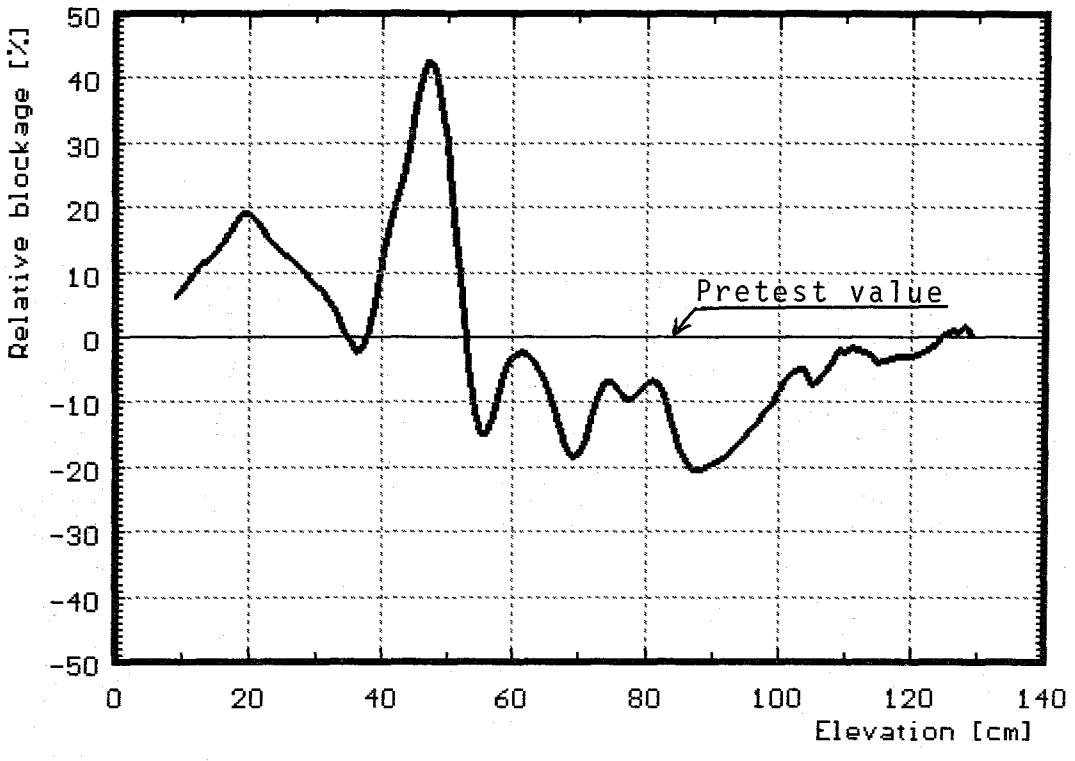

Fig. 78a: CORA13: Relative axial distribution of blocked flow channel

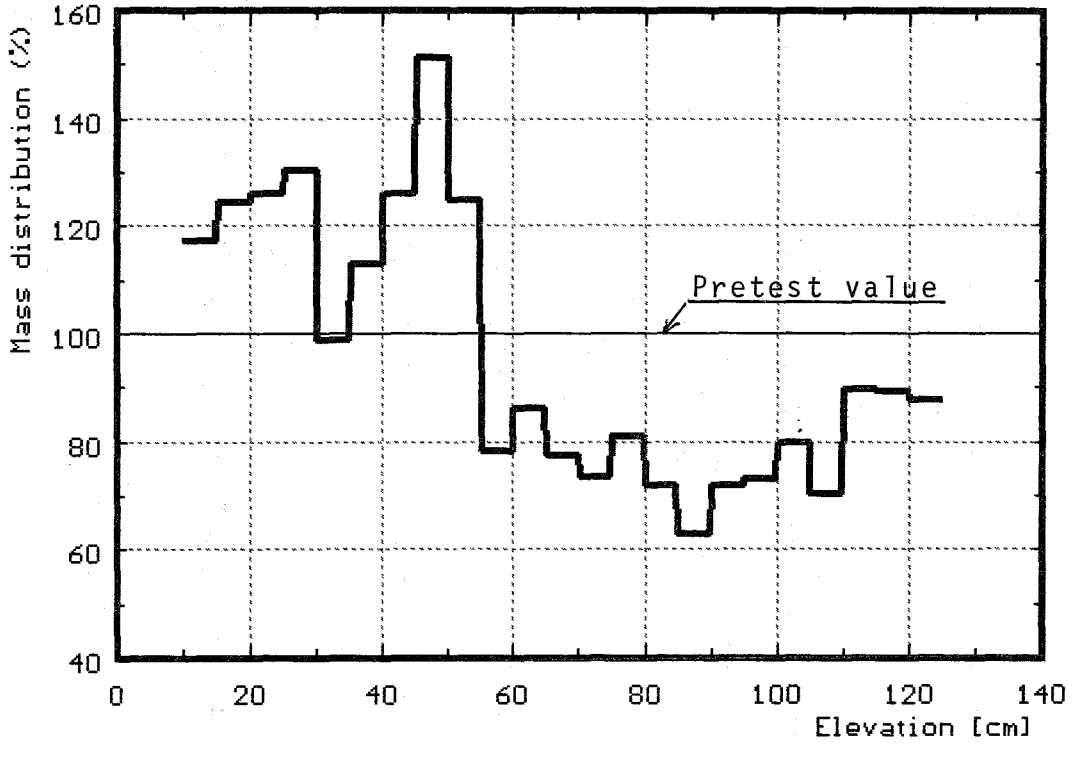

Fig. 79a: CORA13: Relative axial mass distribution

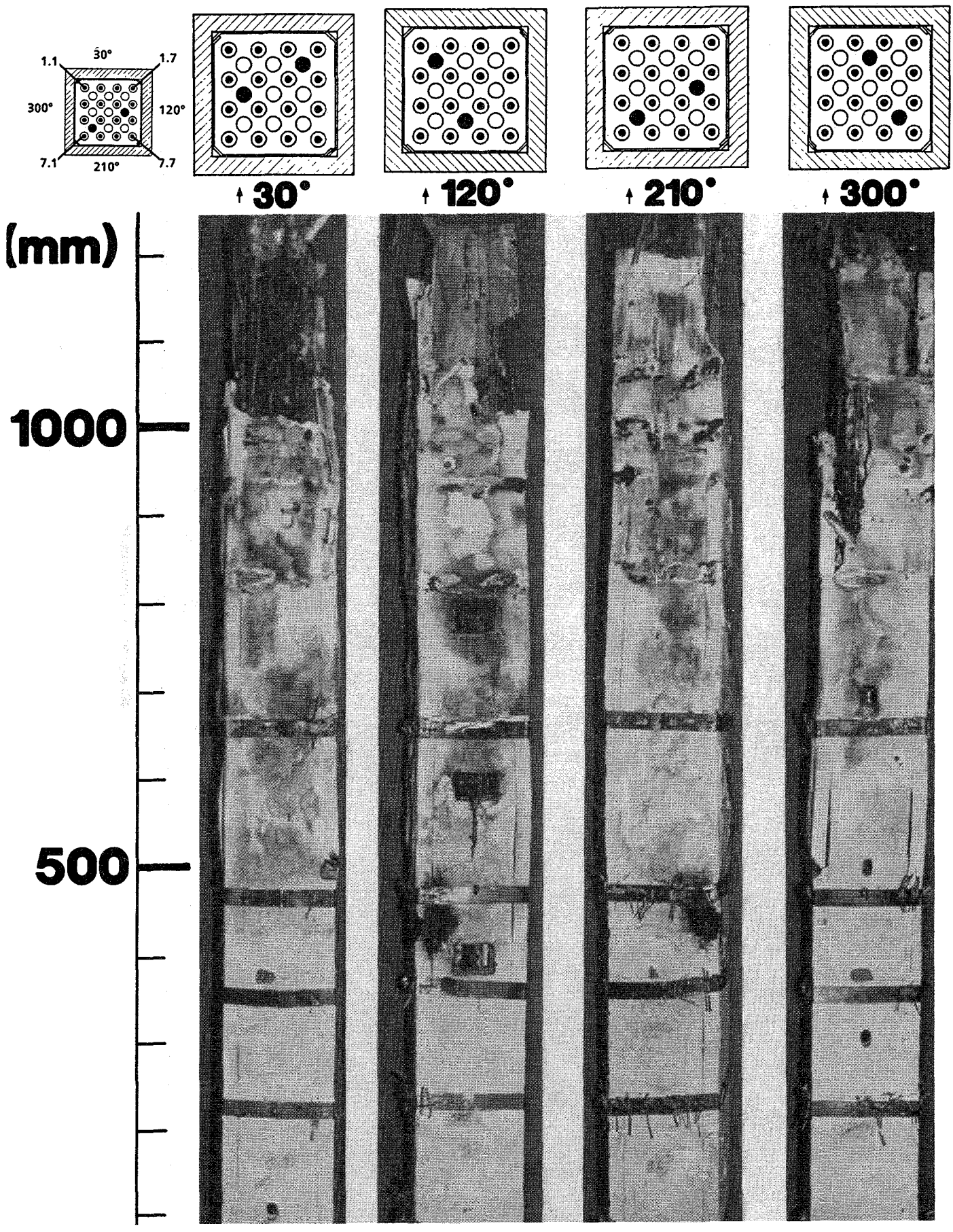

Fig. 80: Posttest appearance of test bundle CORA-13 with shroud insulation

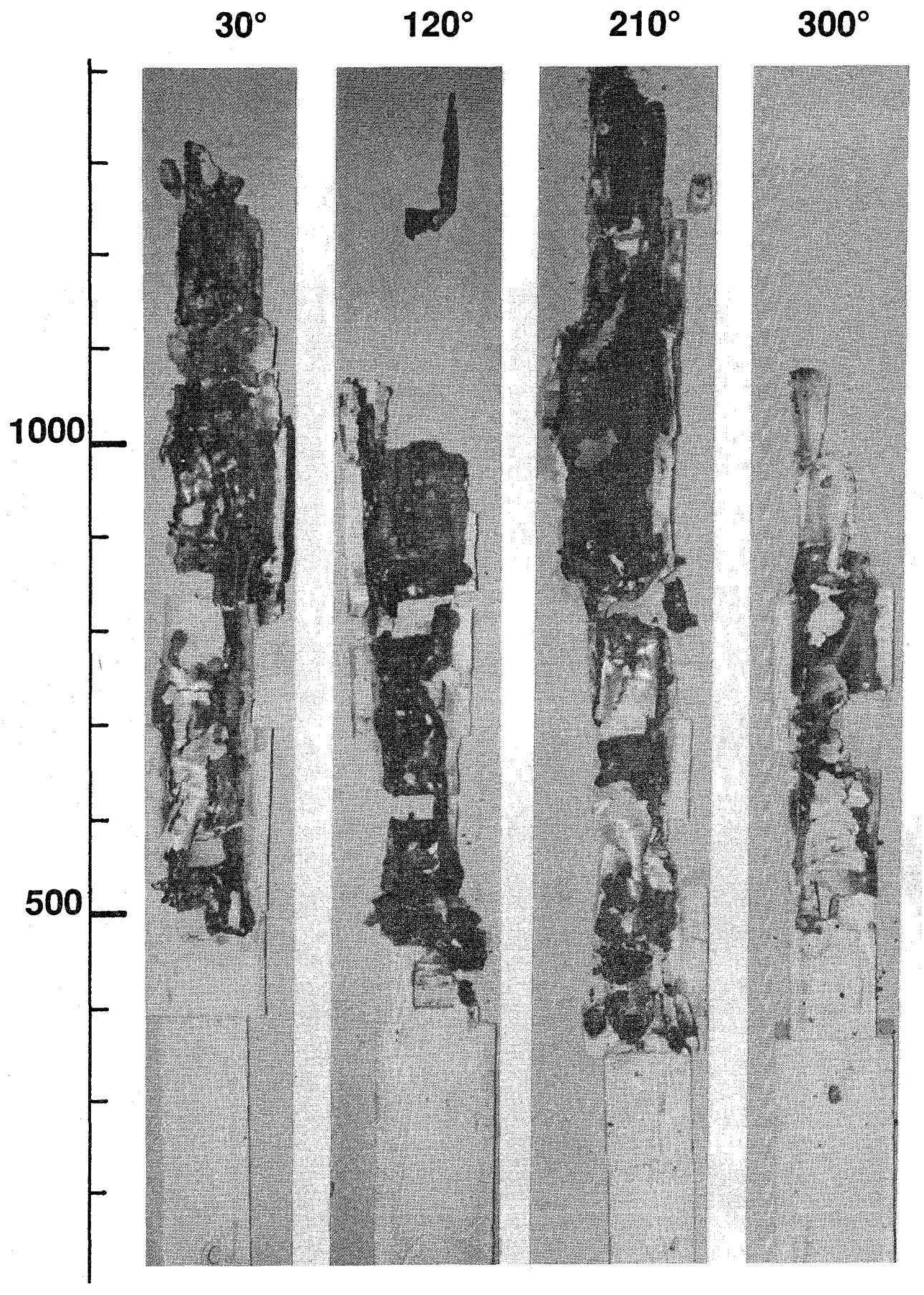

Fig. 81: Inner side of shroud insulation after test CORA-13

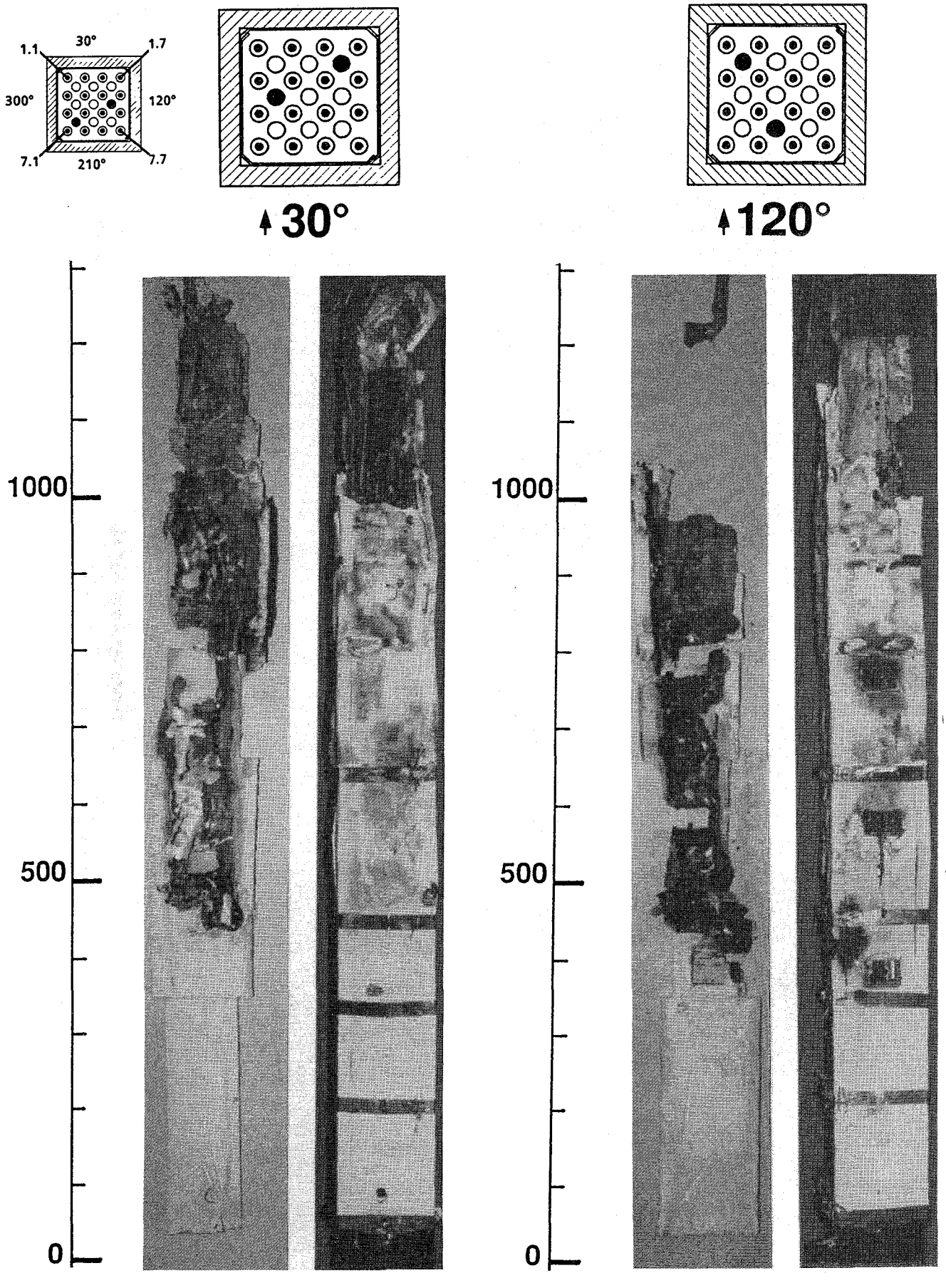

Fig. 82: Inner side and outer side of shroud insulation after test CORA-13

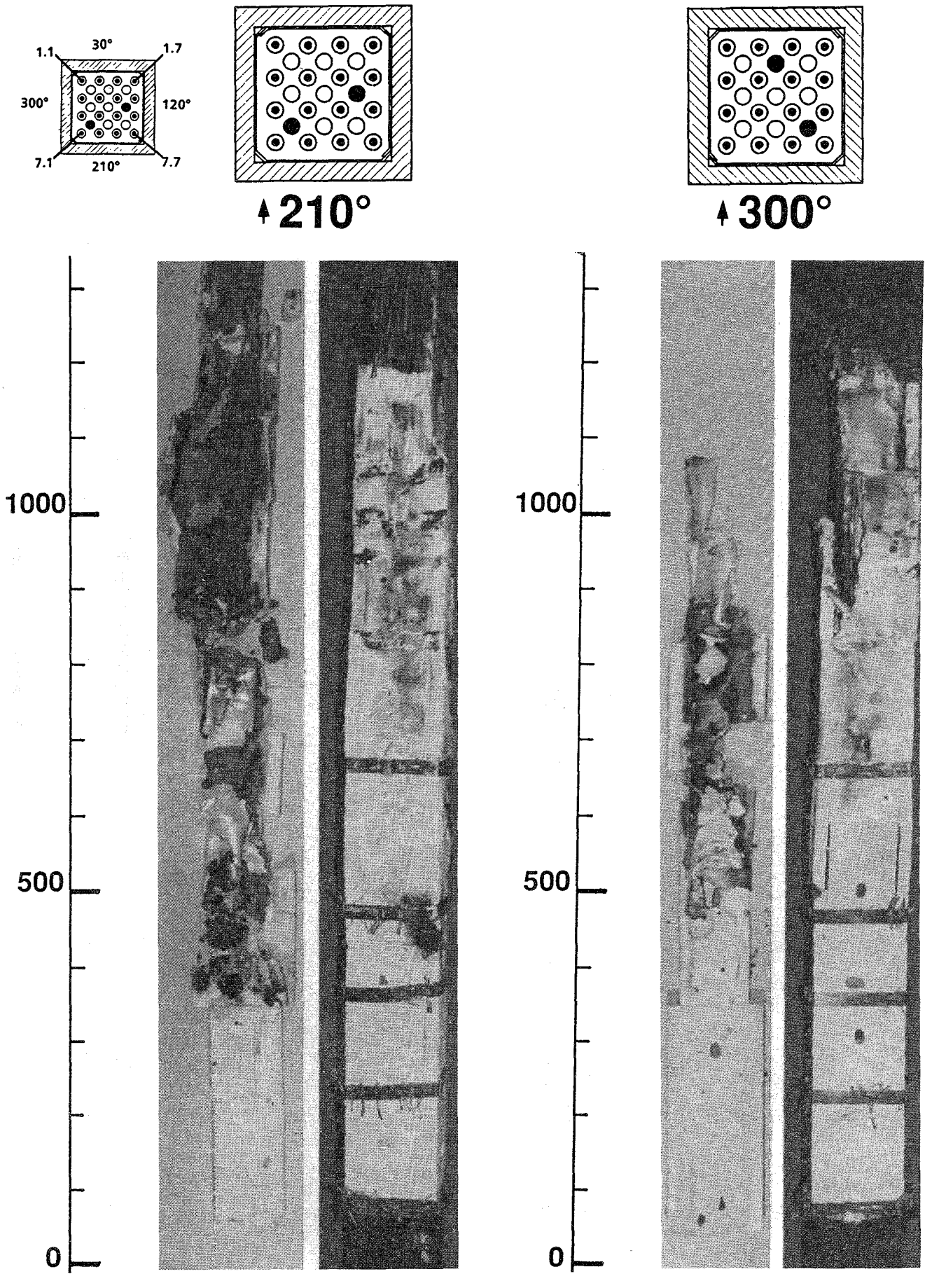

Fig. 83: Inner side and outer side of shroud insulation after test CORA-13

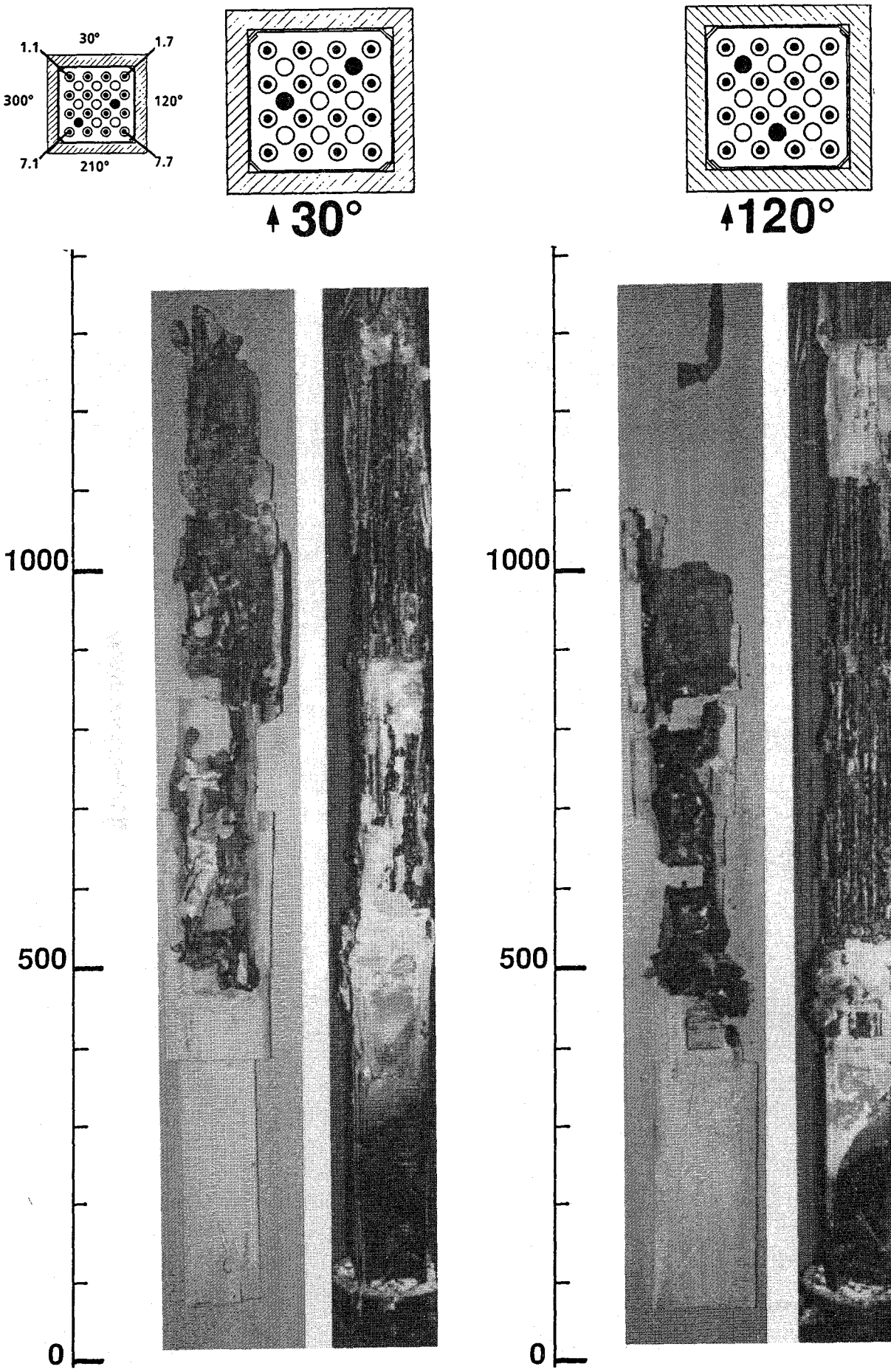

Fig. 84: **Inner side and outer side of shroud insulation after test CORA-13**

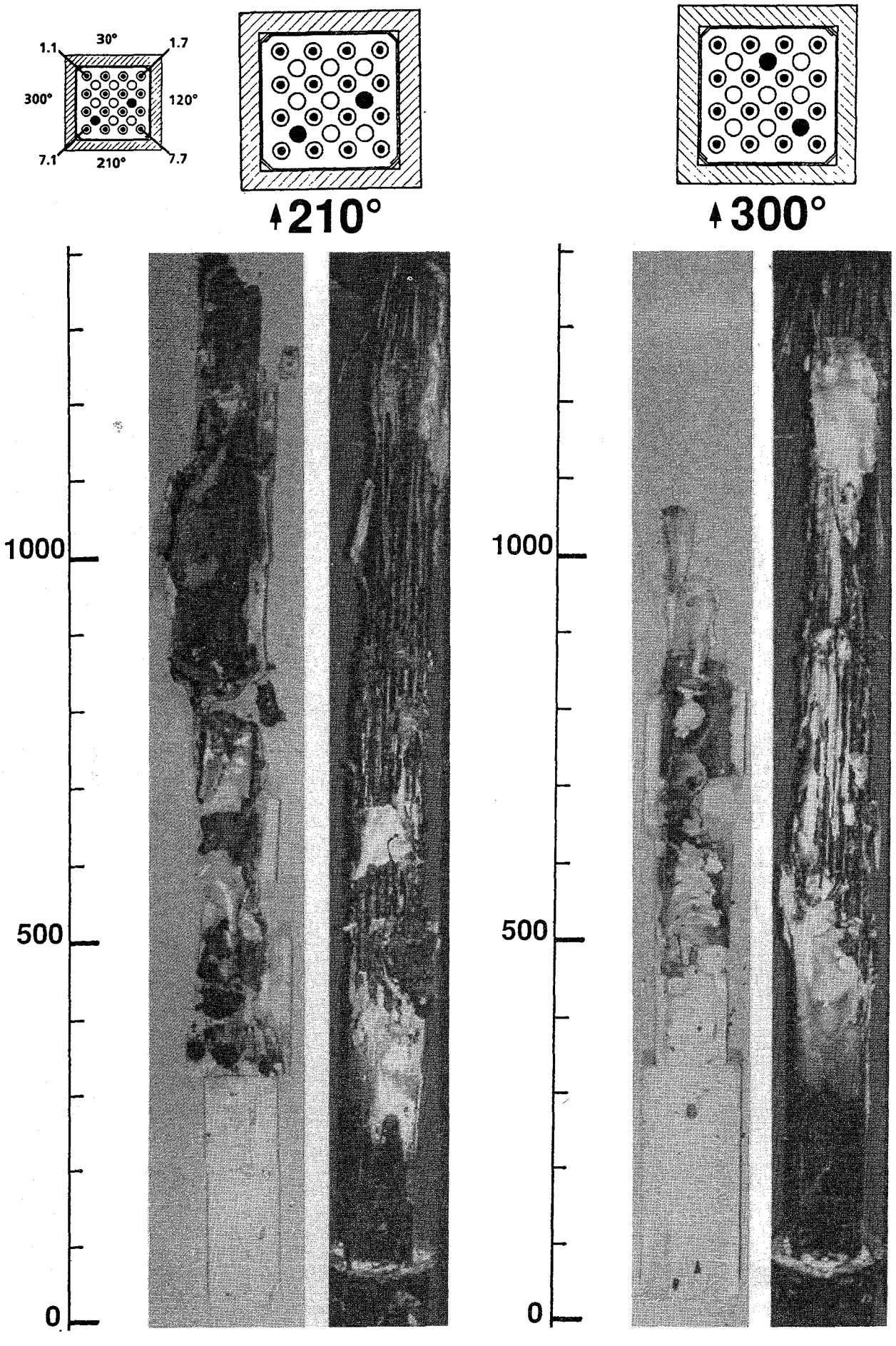

Fig. 85: Inner side and outer side of shroud insulation after test CORA-13

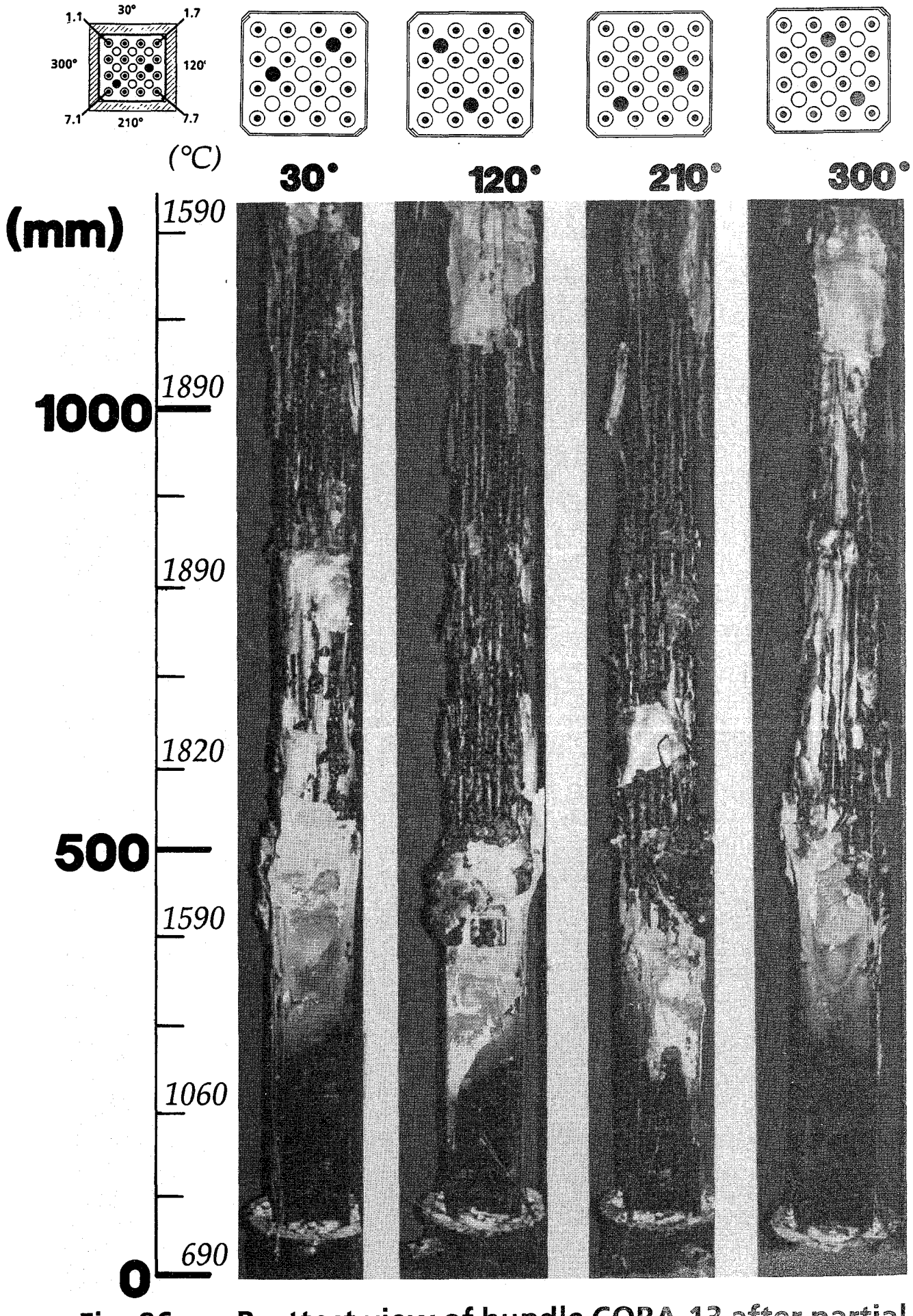

Fig. 86: Posttest view of bundle CORA-13 after partial removal of shroud

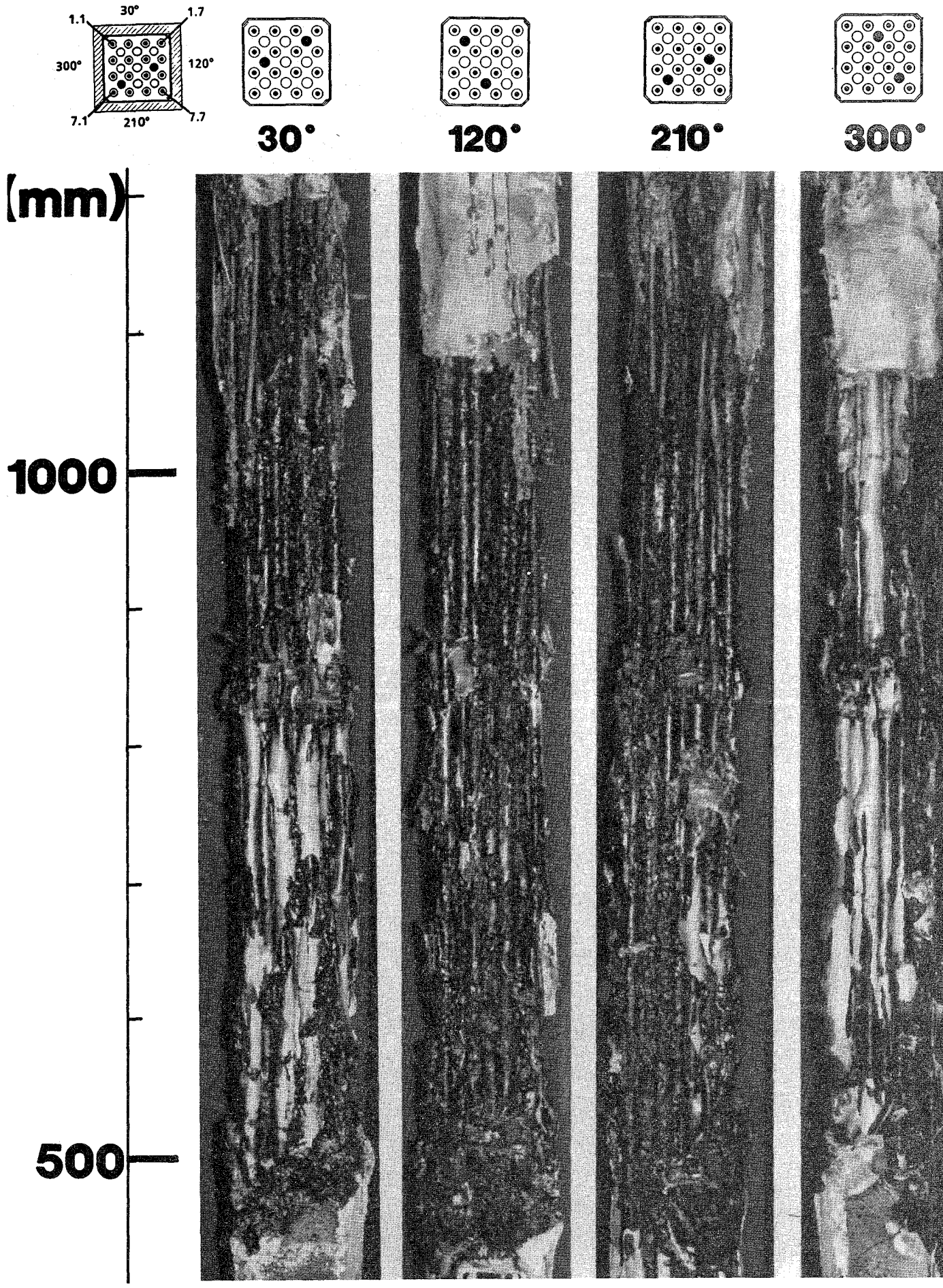

Fig. 87: Posttest view of bundle CORA-13 after partial removal of shroud

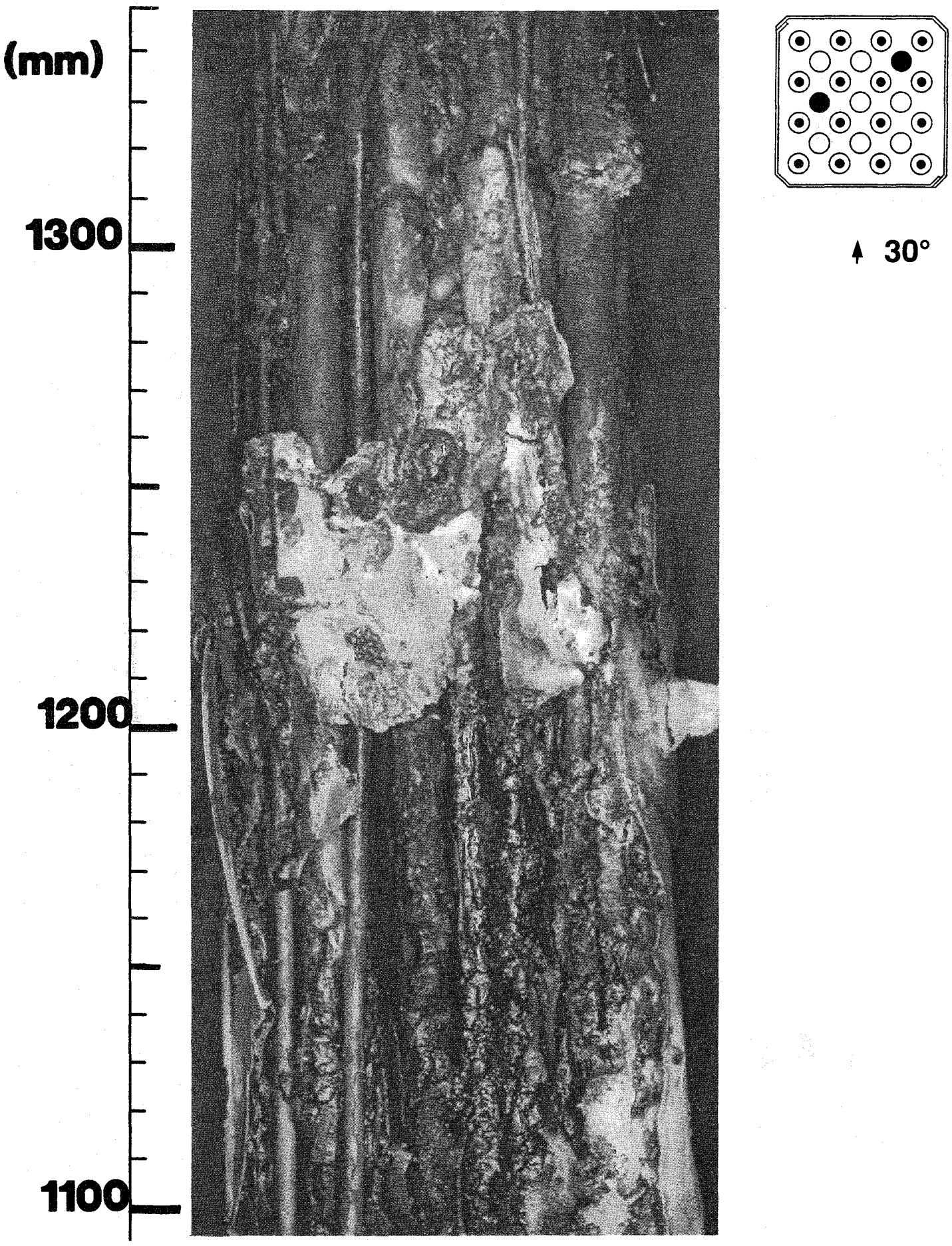

Fig. 88: Posttest view of bundle CORA-13 after partial removal of shroud

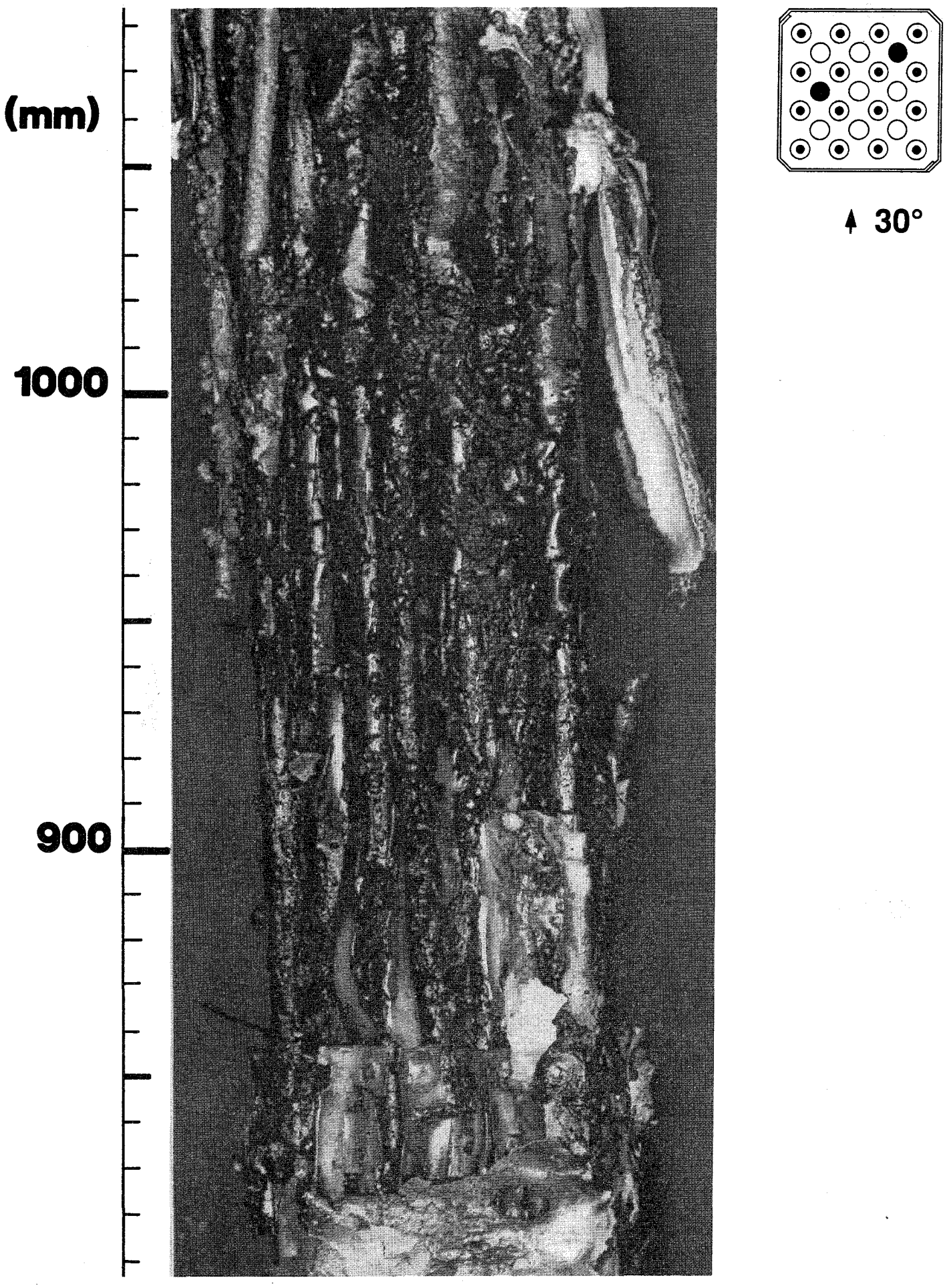

Fig. 89: Posttest view of bundle CORA-13 after partial removal of shroud

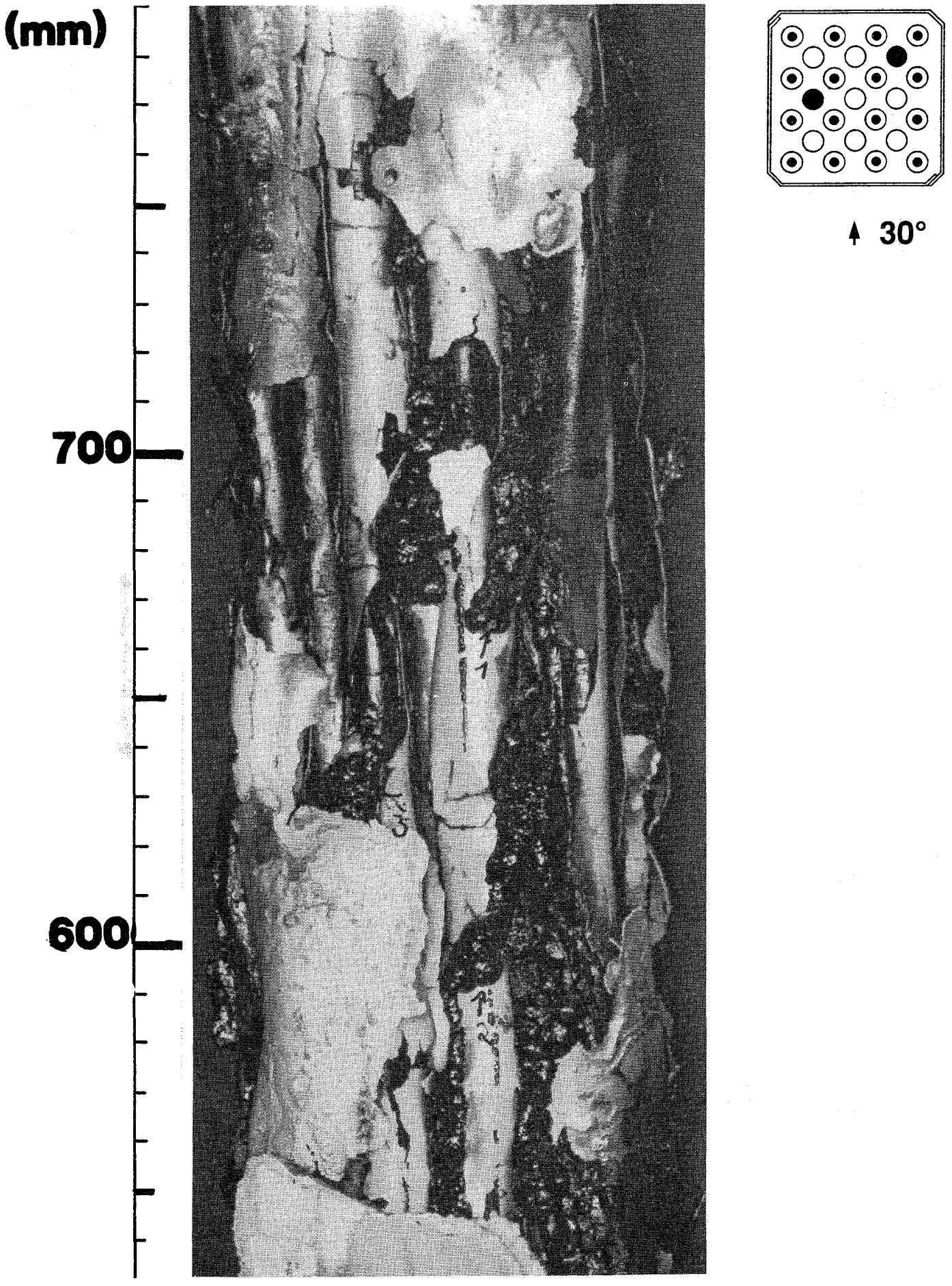

Fig. 90: Posttest view of bundle CORA-13 with shroud remnants

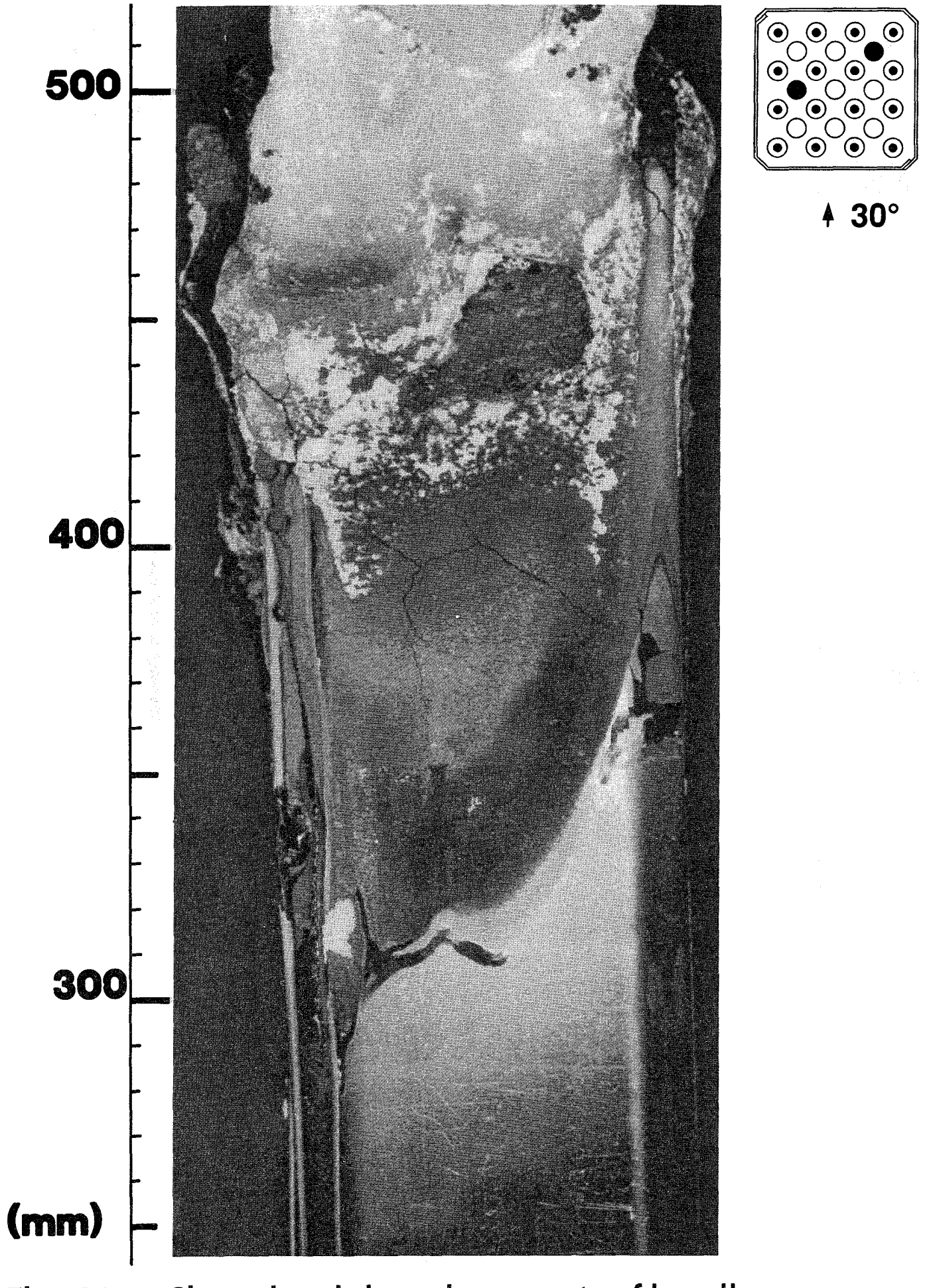

Fig. 91: Shroud and shroud remnants of bundle CORA-13

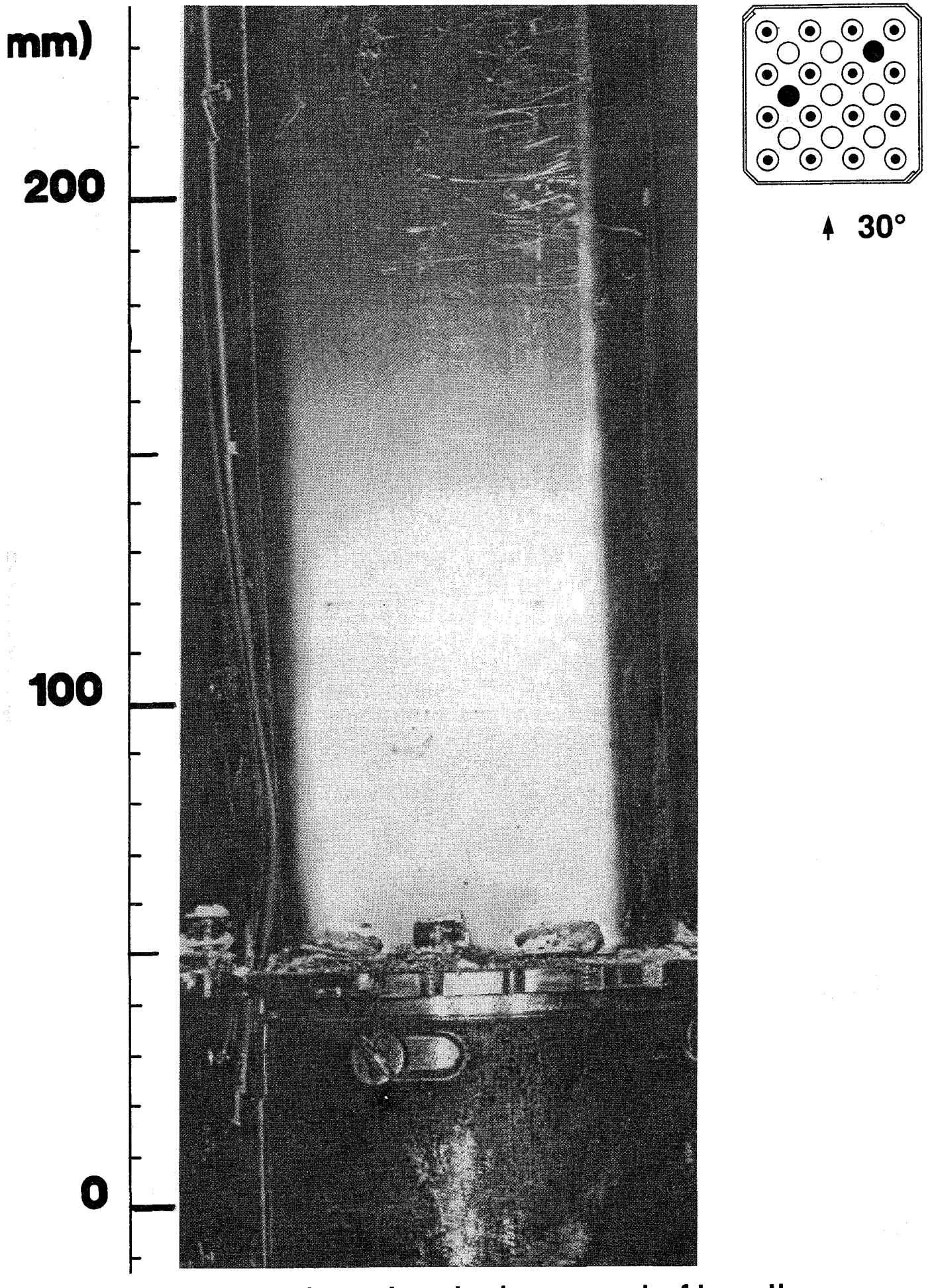

Fig. 92: Intact shroud at the lower end of bundle CORA-13

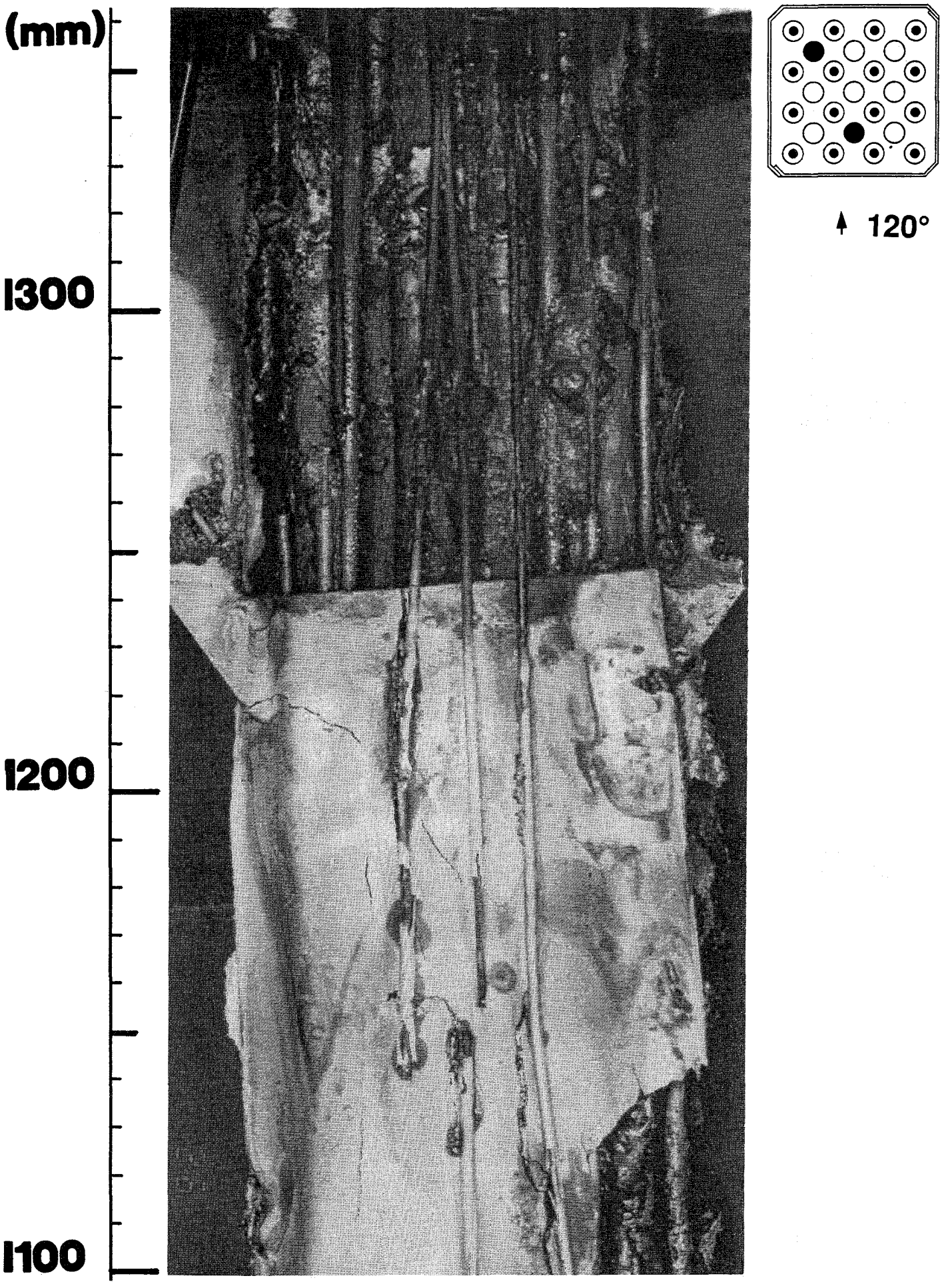

Fig. 93: Posttest view of bundle CORA-13 with shroud

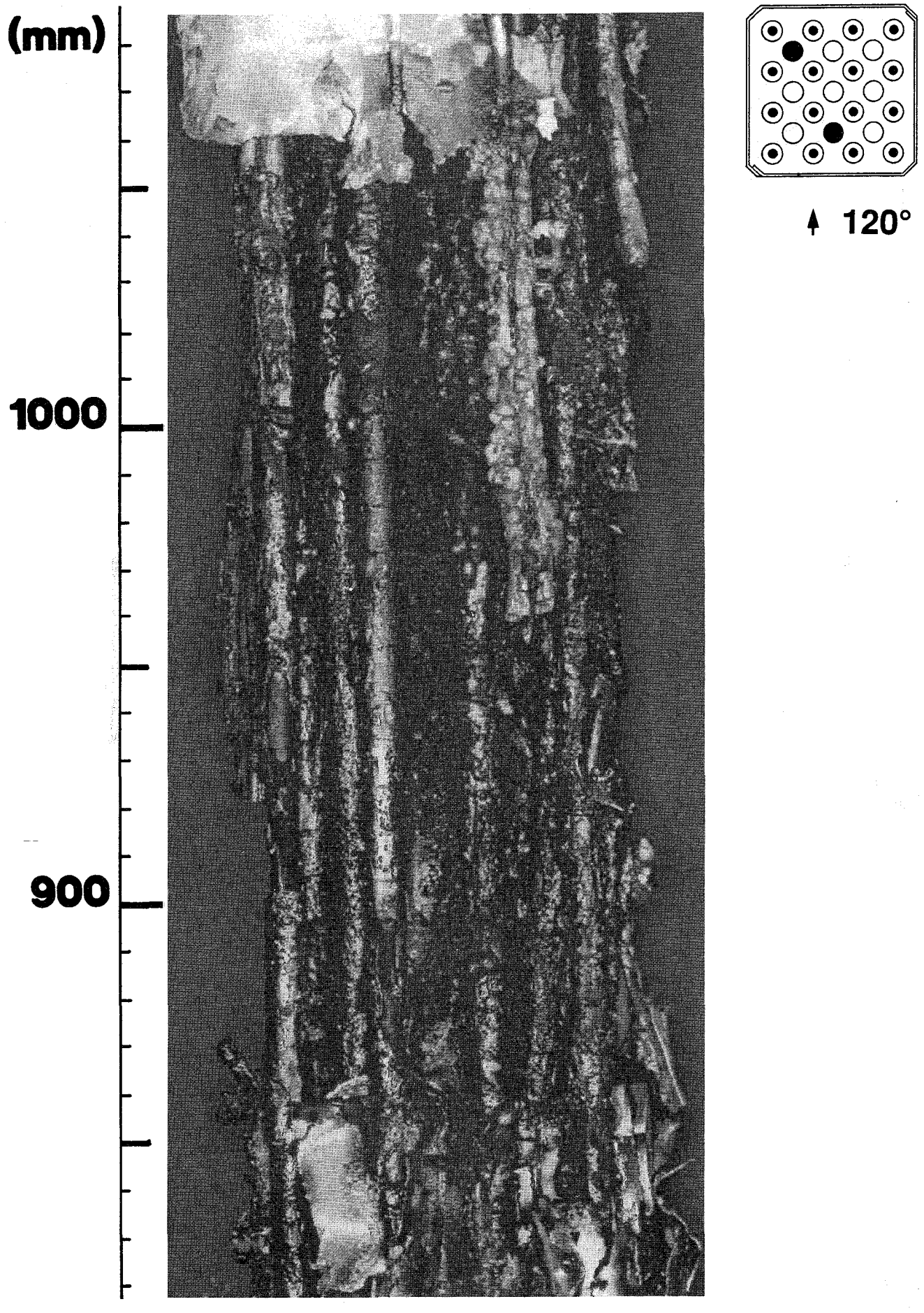

Fig. 94: Posttest view of bundle CORA-13

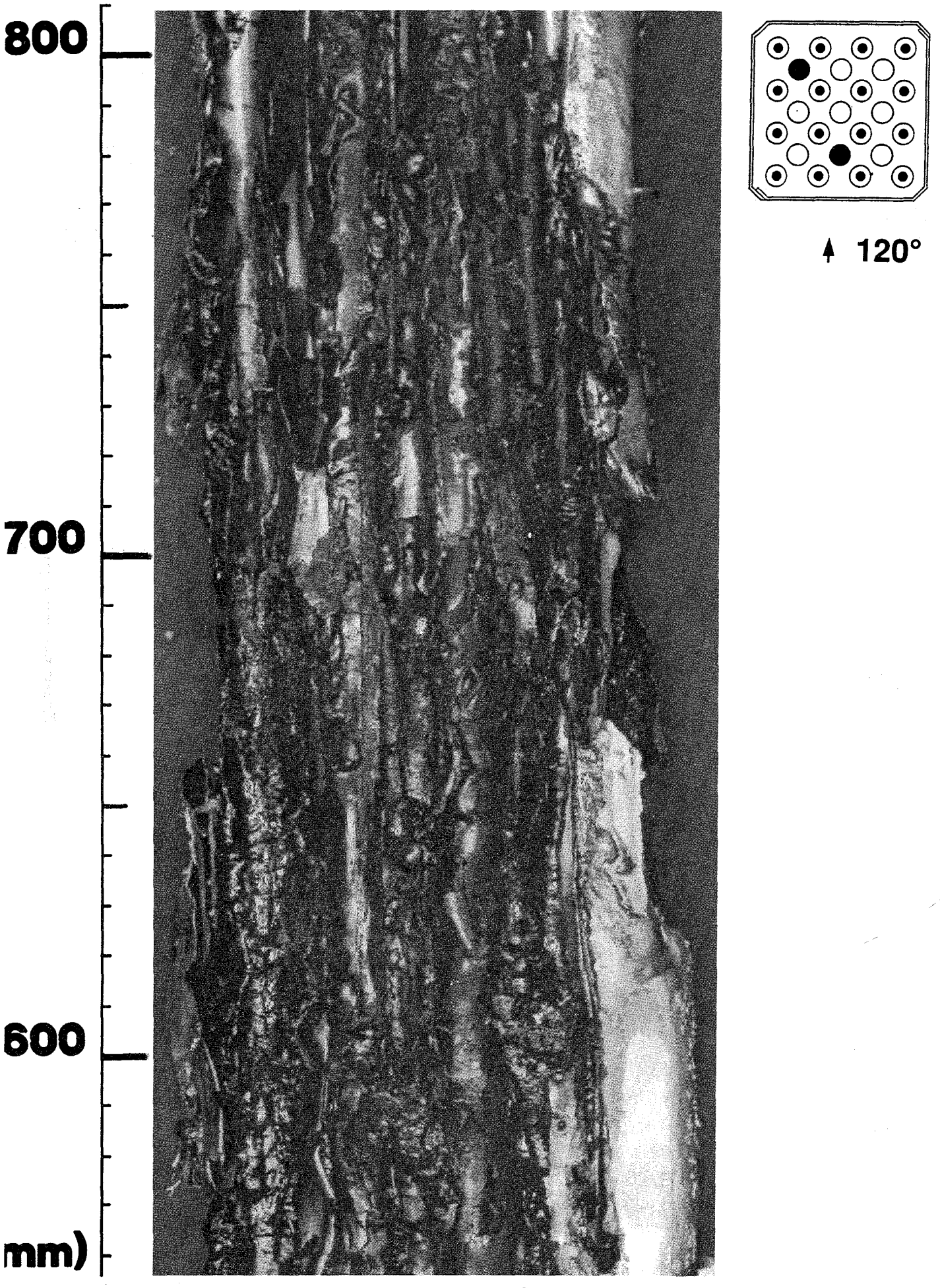

Fig. 95: Posttest view of bundle CORA-13

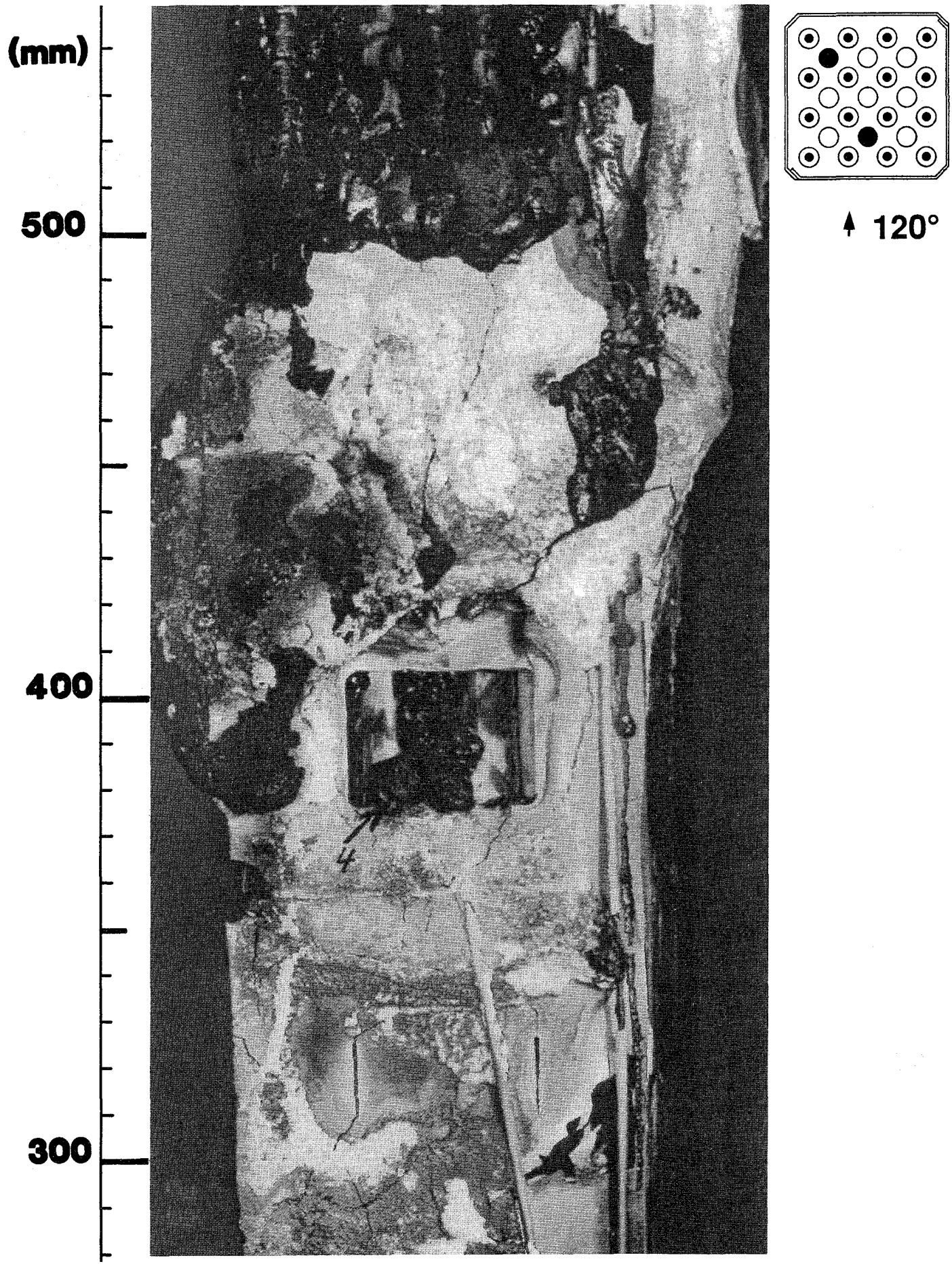

Fig. 96: Posttest view of bundle CORA-13 with shroud remnants

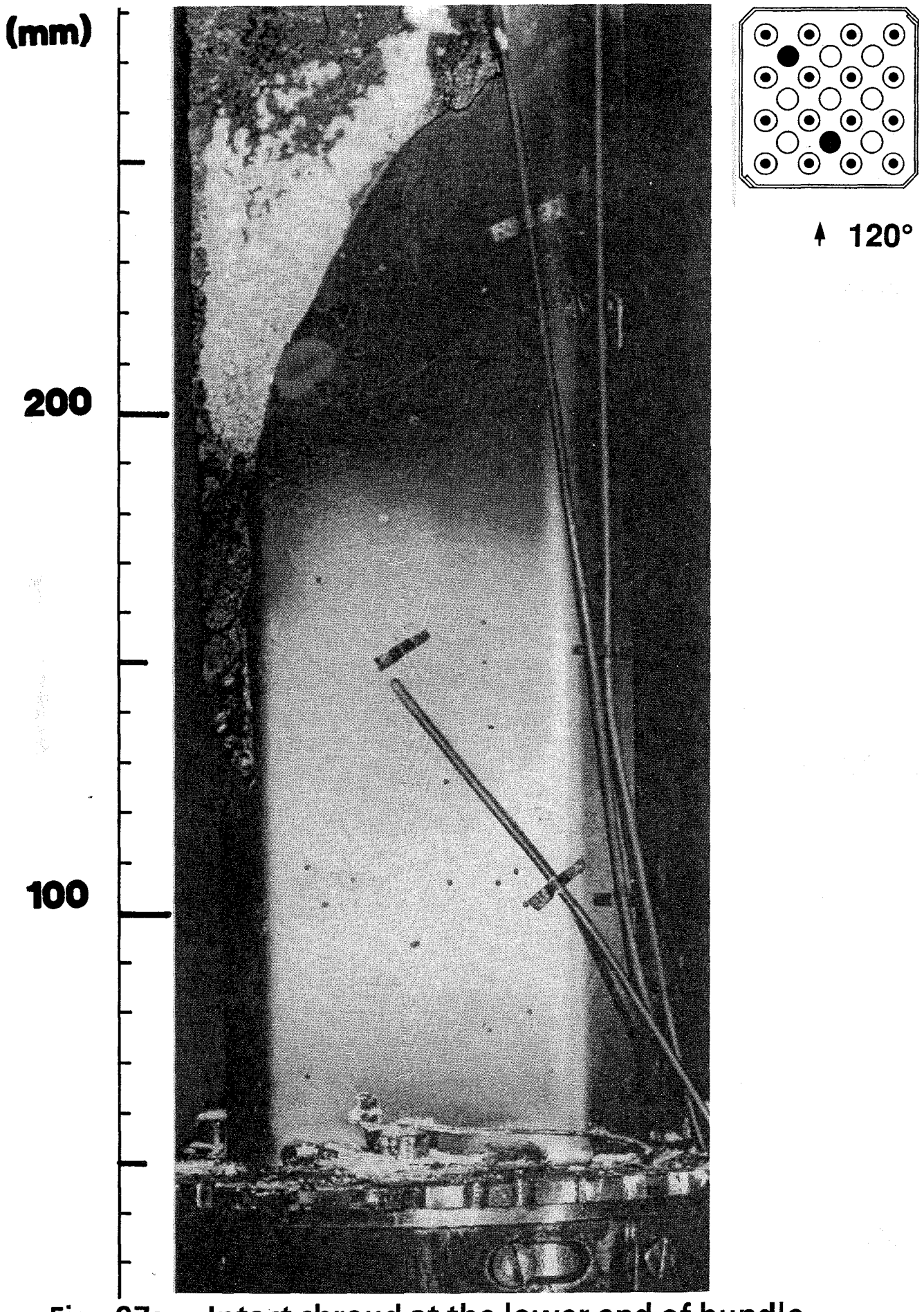

Fig. 97: Intact shroud at the lower end of bundle CORA-13

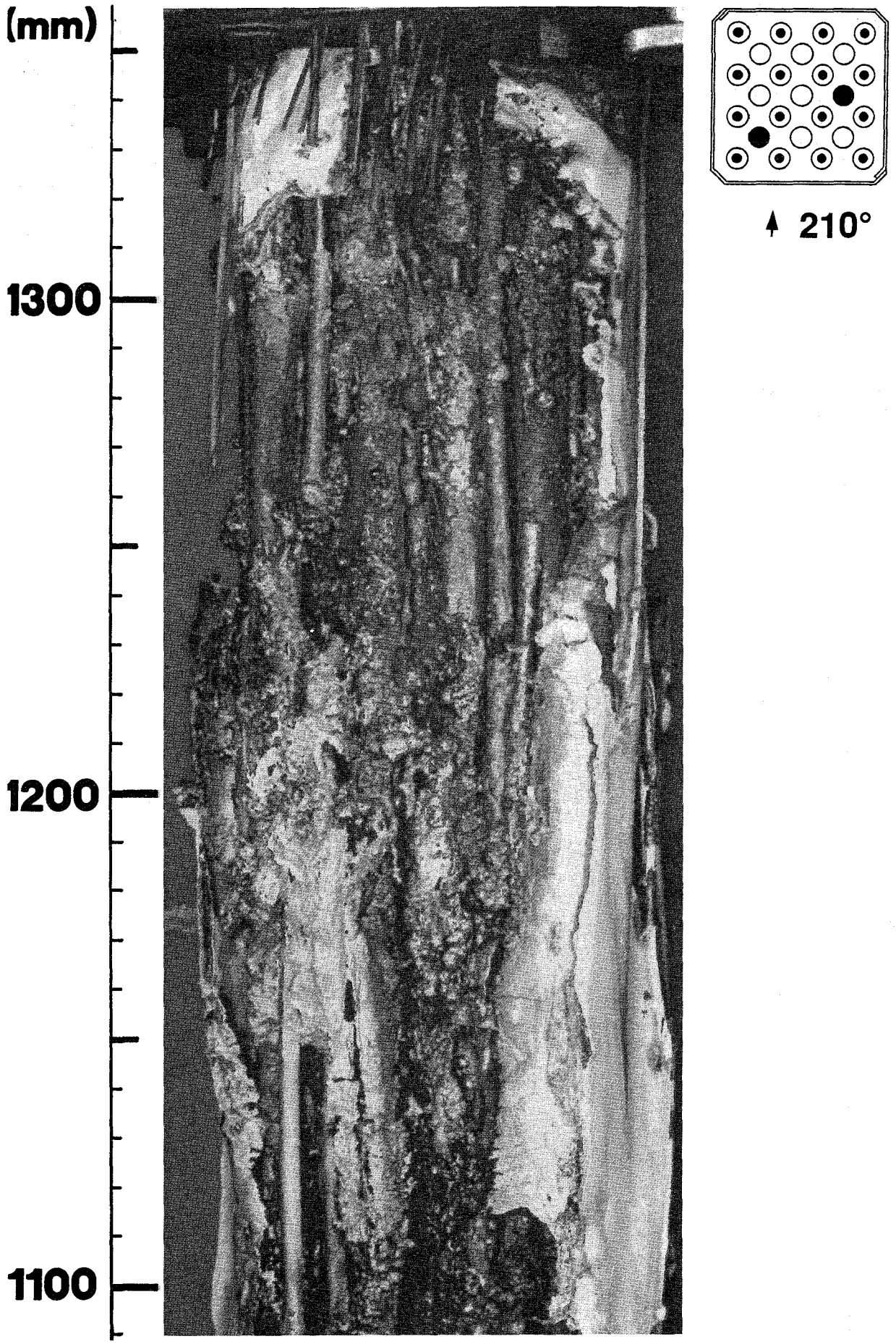

Fig. 98: Posttest view of bundle CORA-13 with shroud remnants

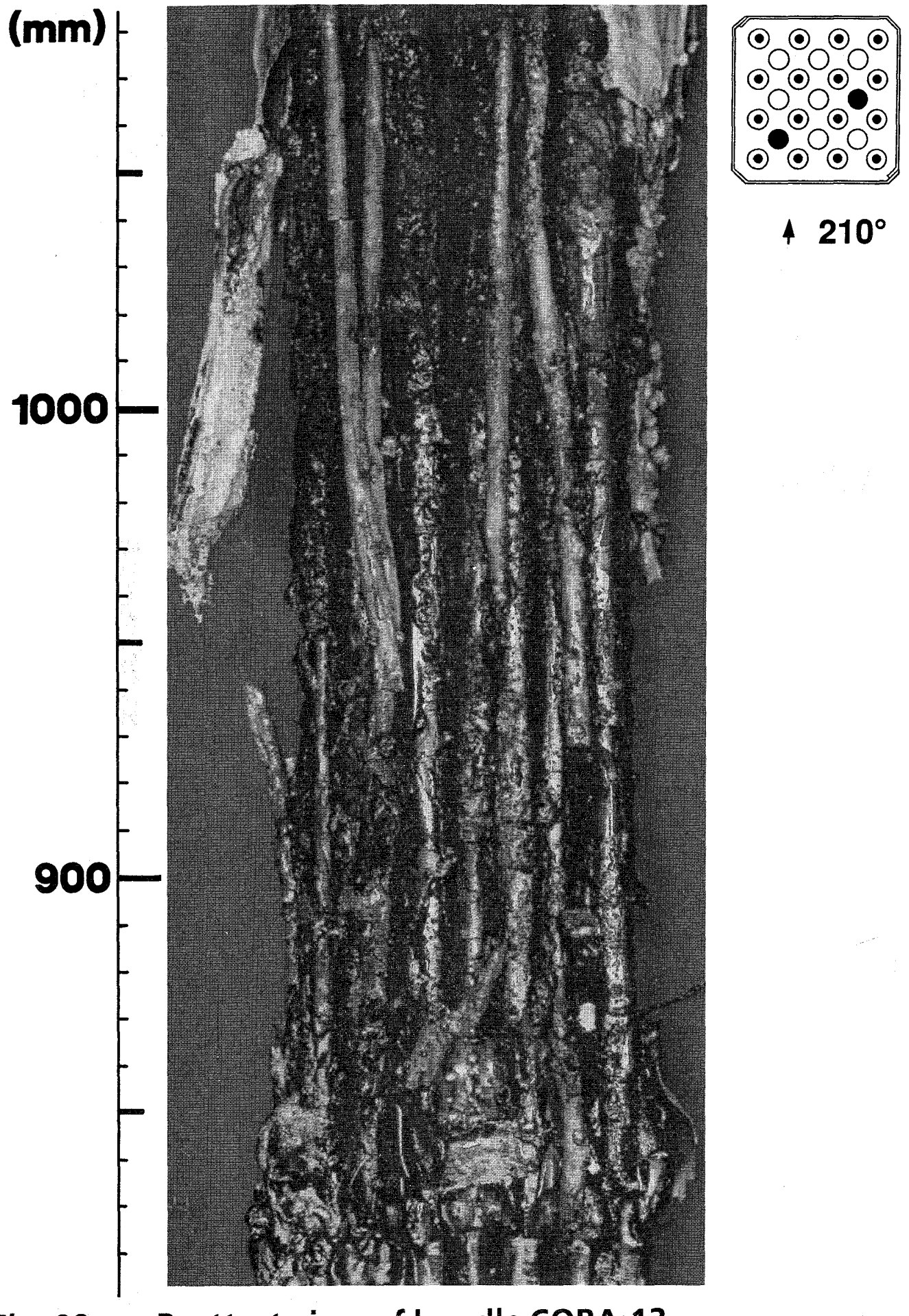

Fig. 99: Posttest view of bundle CORA-13

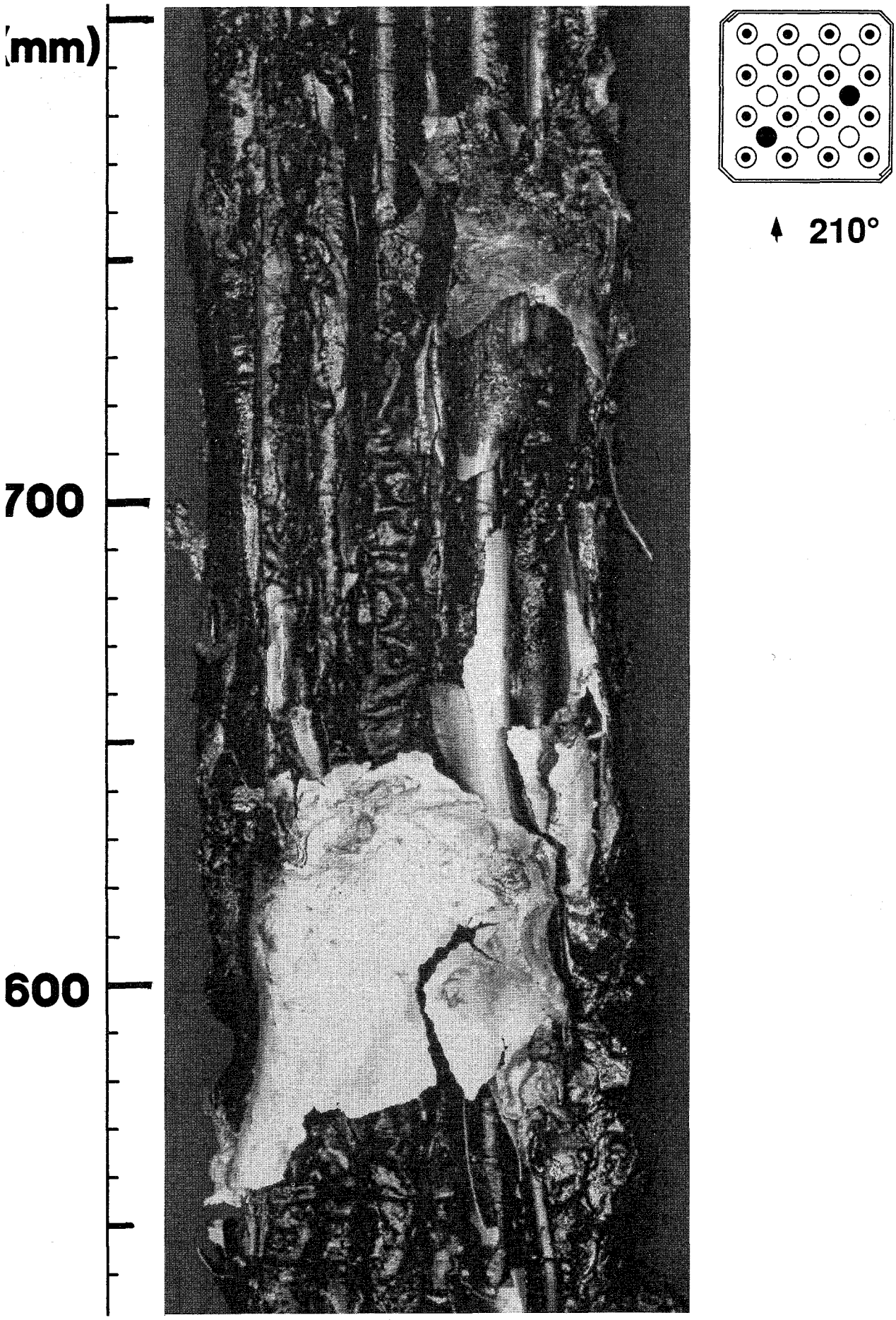

Fig. 100 Posttest view of bundle CORA-13 with shroud remnants

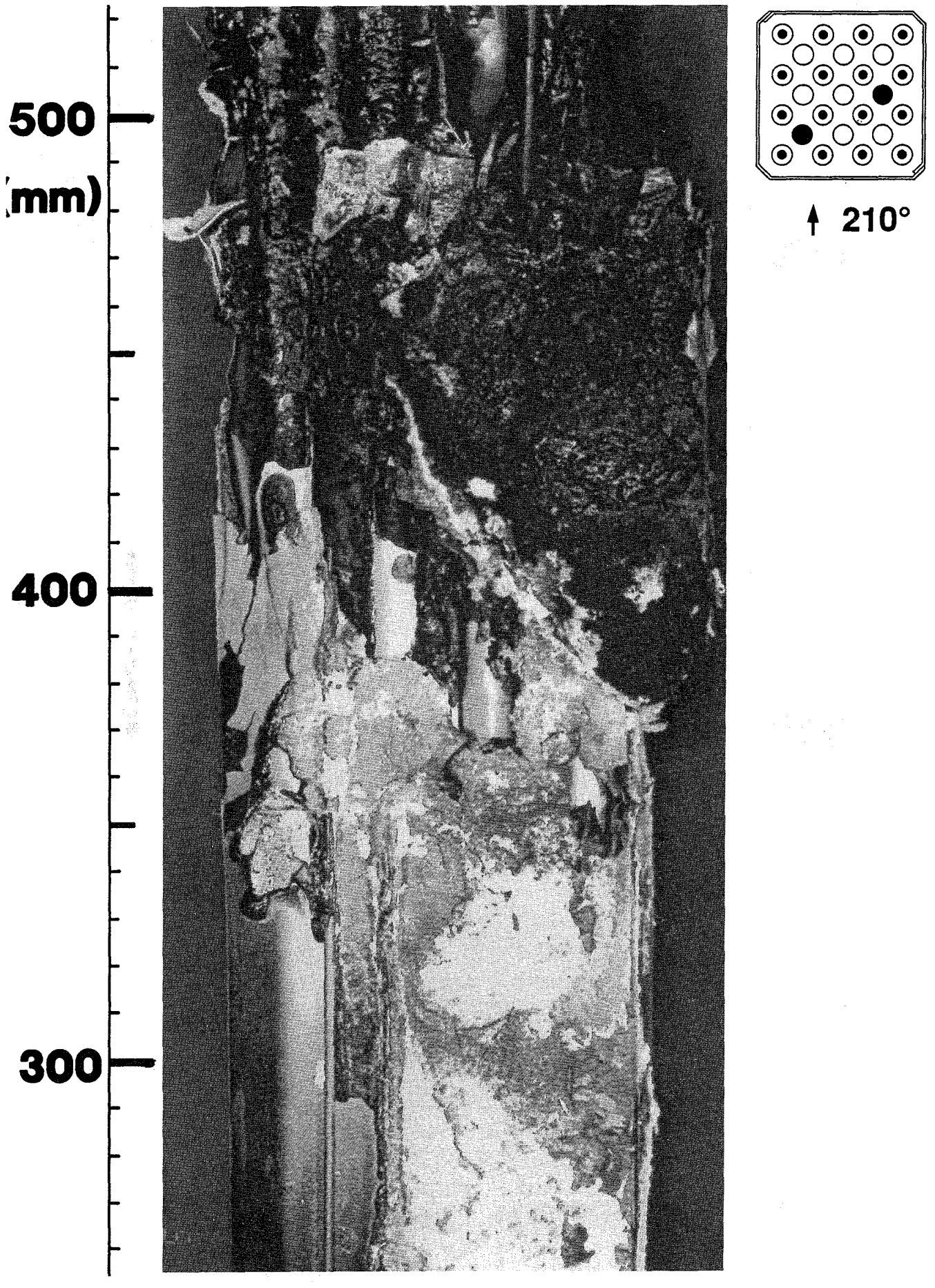

Fig. 101: Posttest view of bundle CORA-13 with shroud remnants

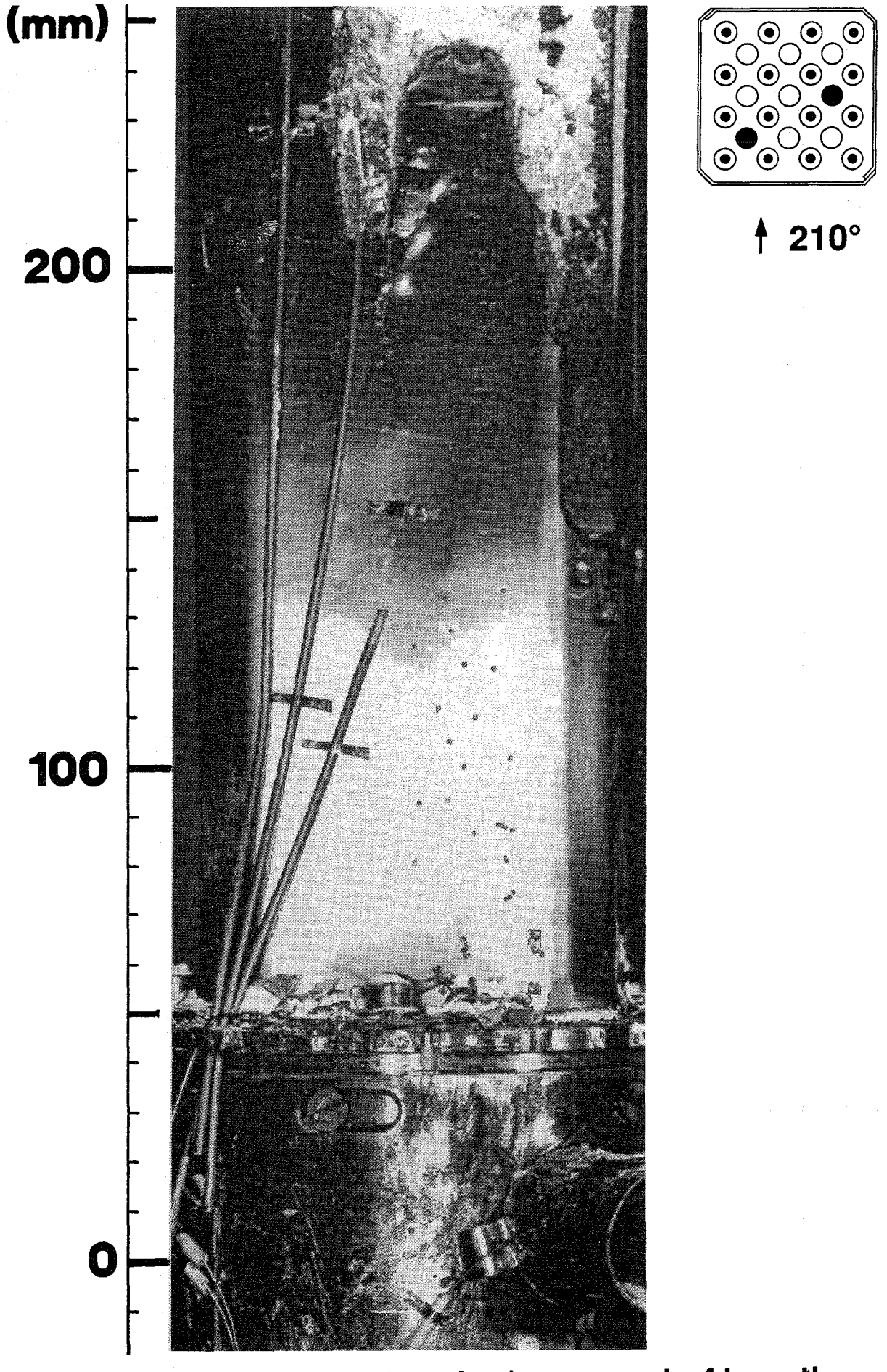

Fig. 102: Intact shroud at the lower end of bundle CORA-13

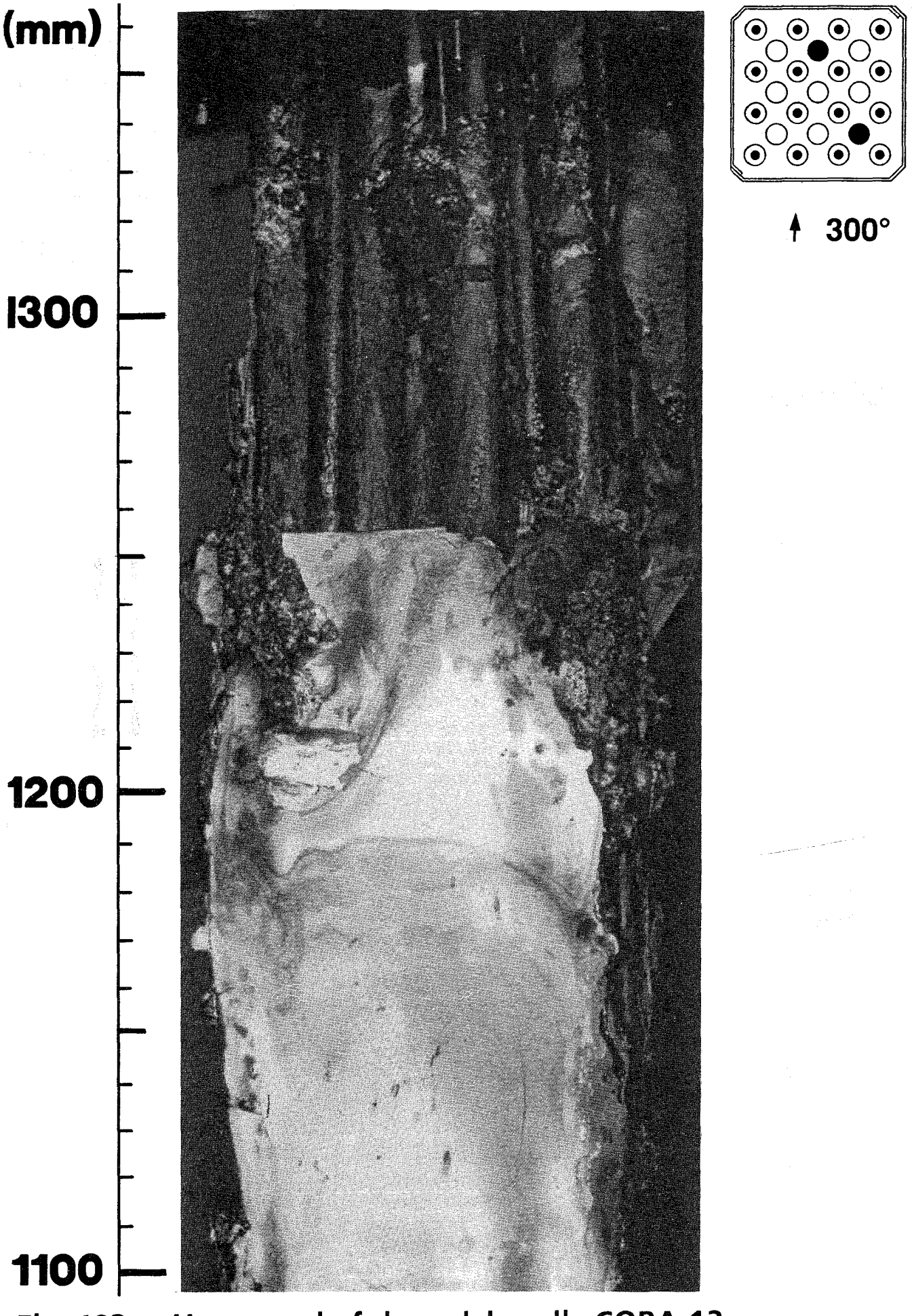

Fig. 103. Upper end of shroud, bundle CORA-13

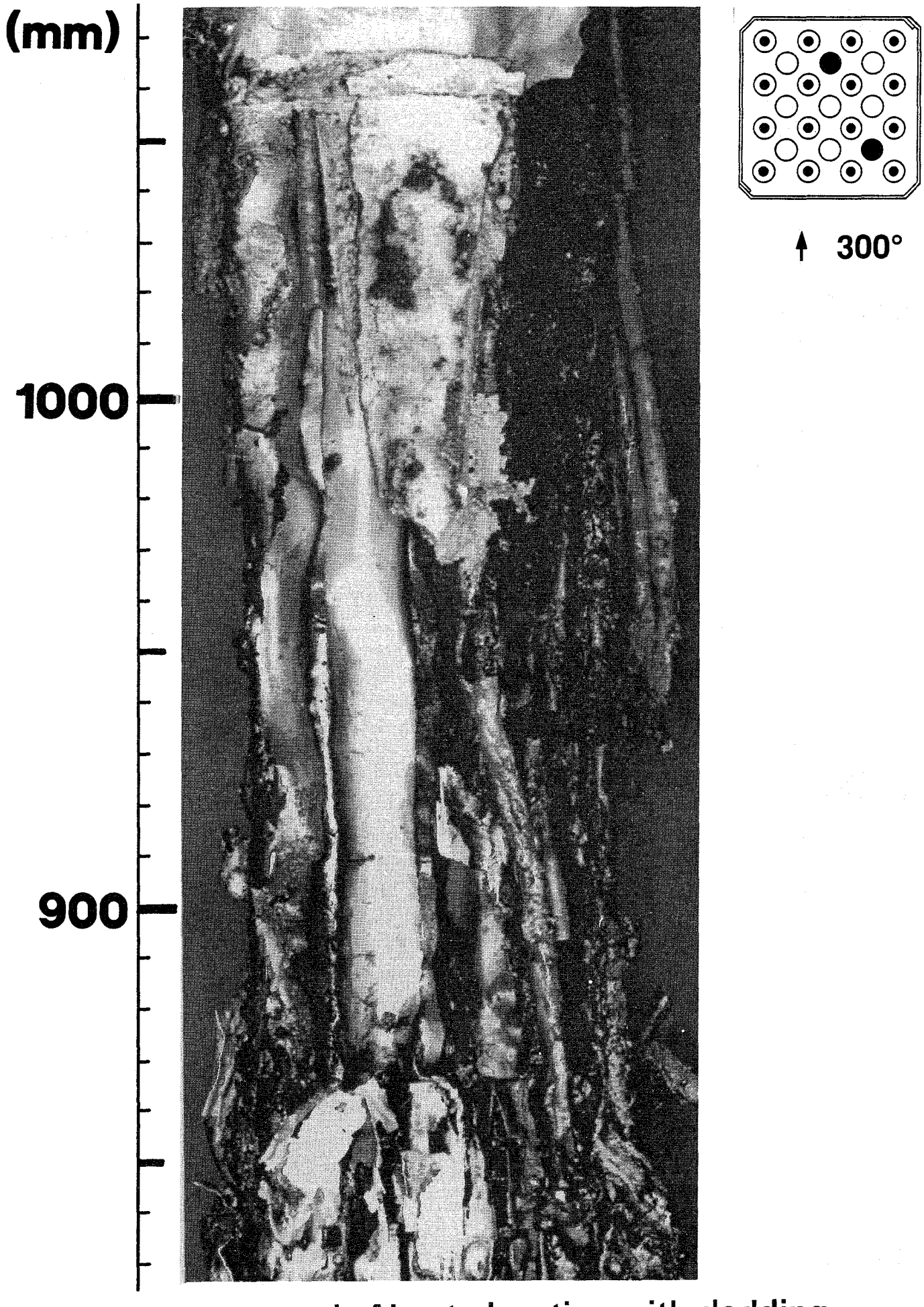

Fig. 104: Upper end of heated section with cladding remnants

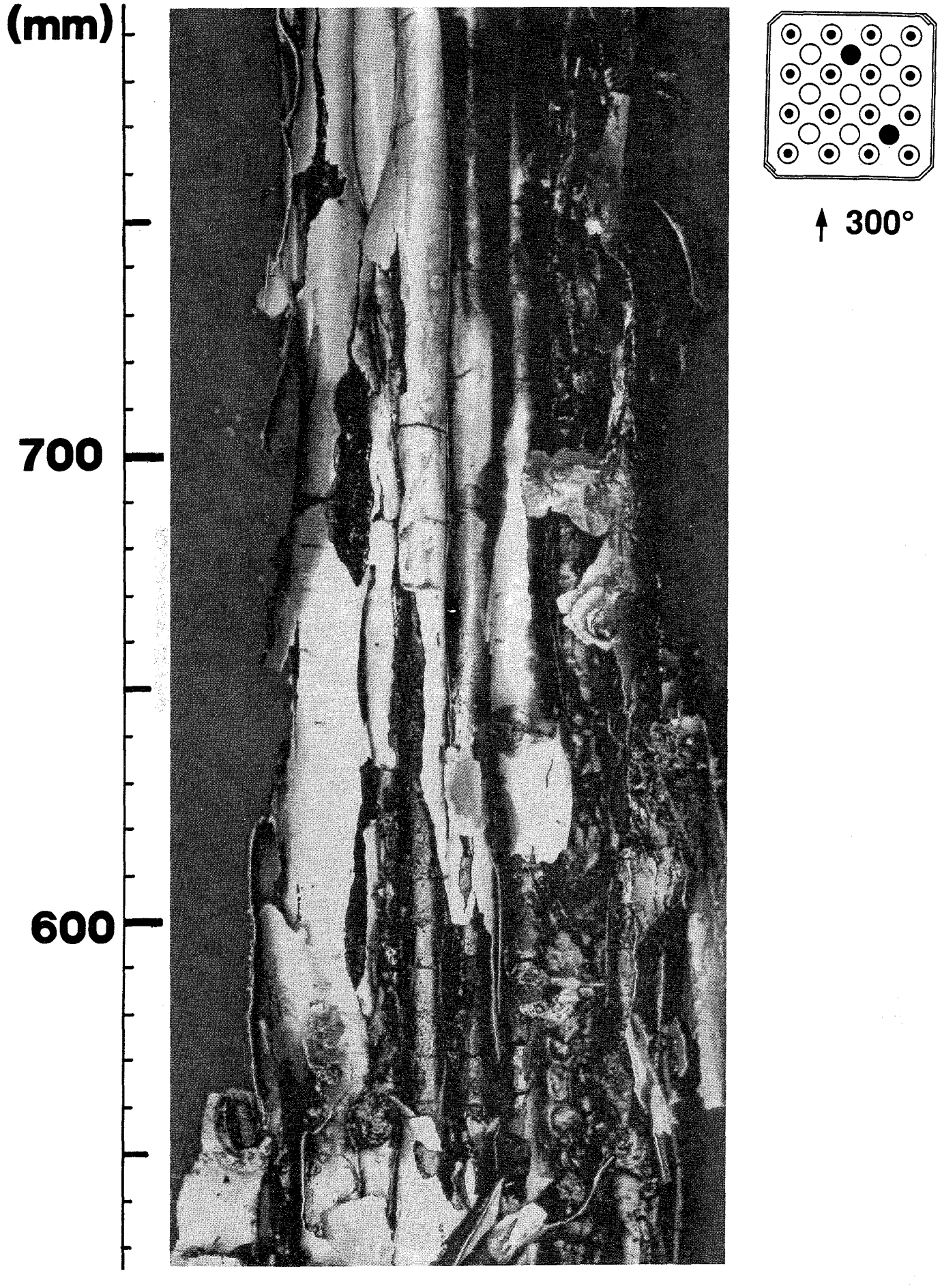

Fig. 105: Oxidized cladding remnants, bundle CORA-13

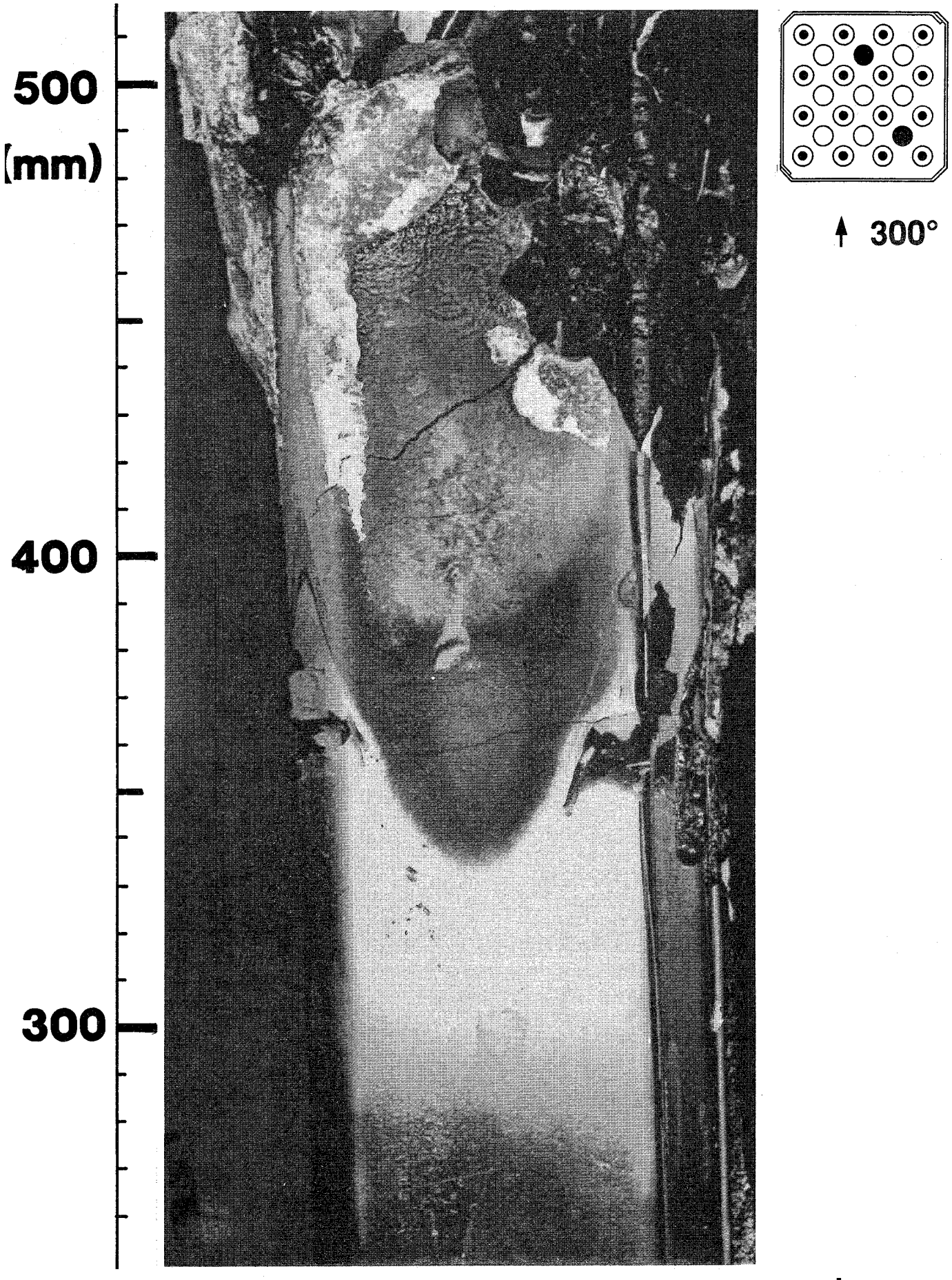

Fig. 106: Transition from intact shroud to interacted shroud, CORA-13

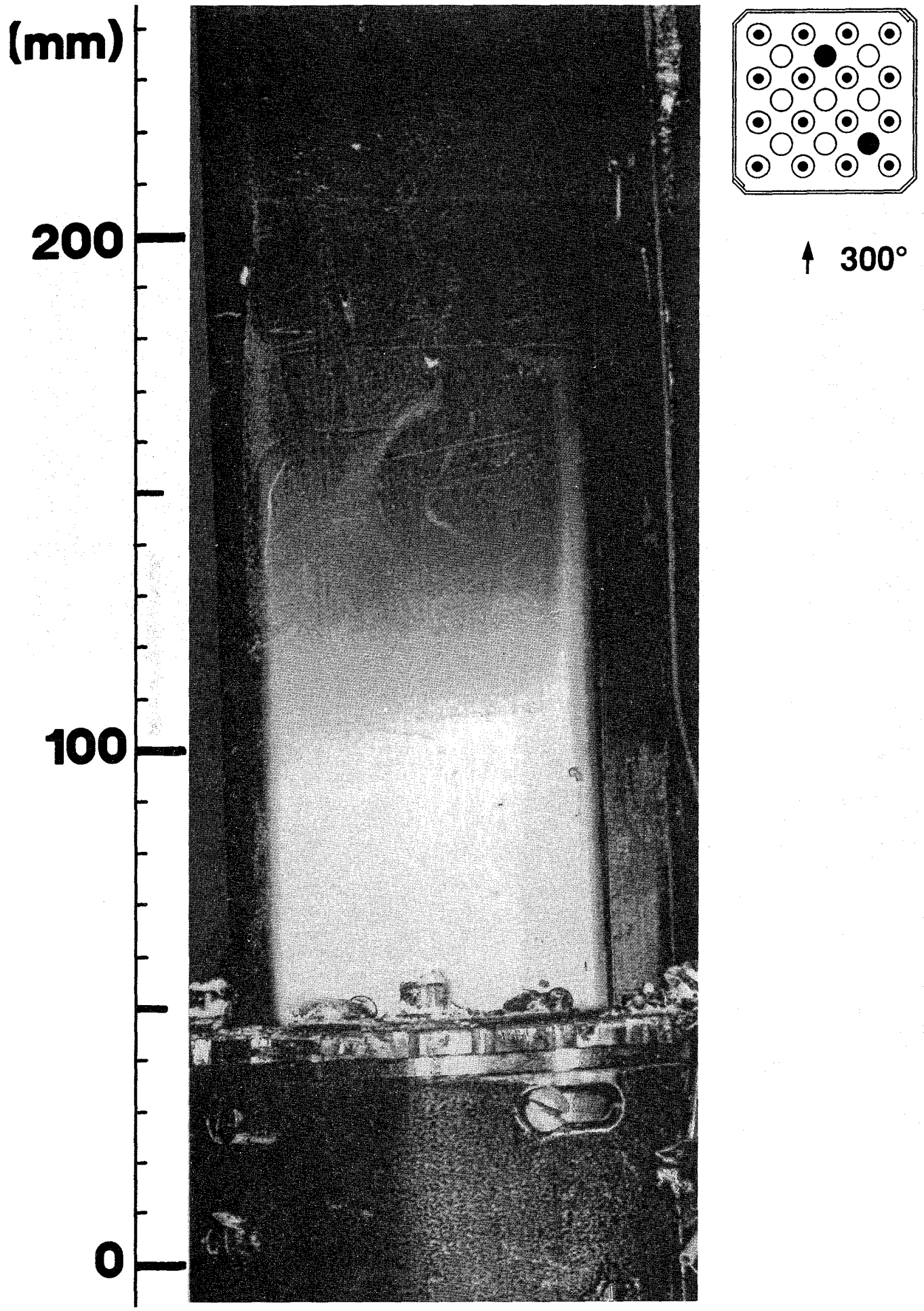

Fig. 107: Intact shroud at the lower end of bundle CORA-13

CORA-13: Horizontal cross section; top view

1248mm

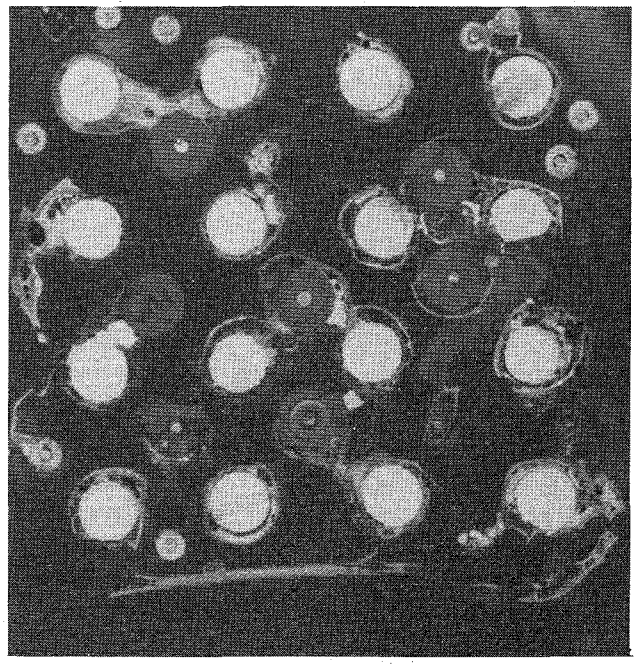

1148mm

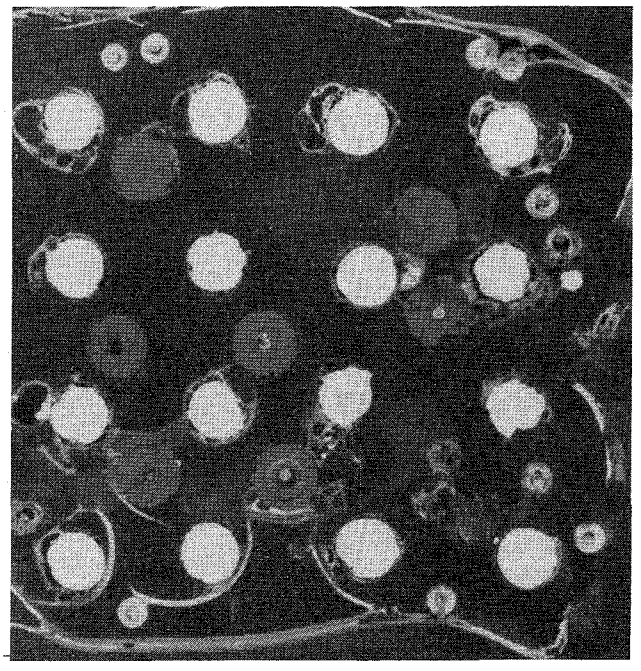

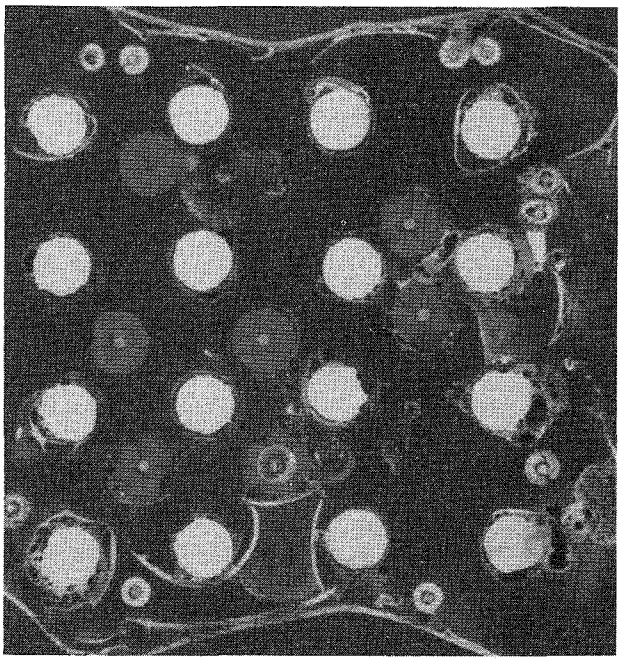

1198mm

Fig. 108: Horizontal cross sections of bundle CORA-13, top view

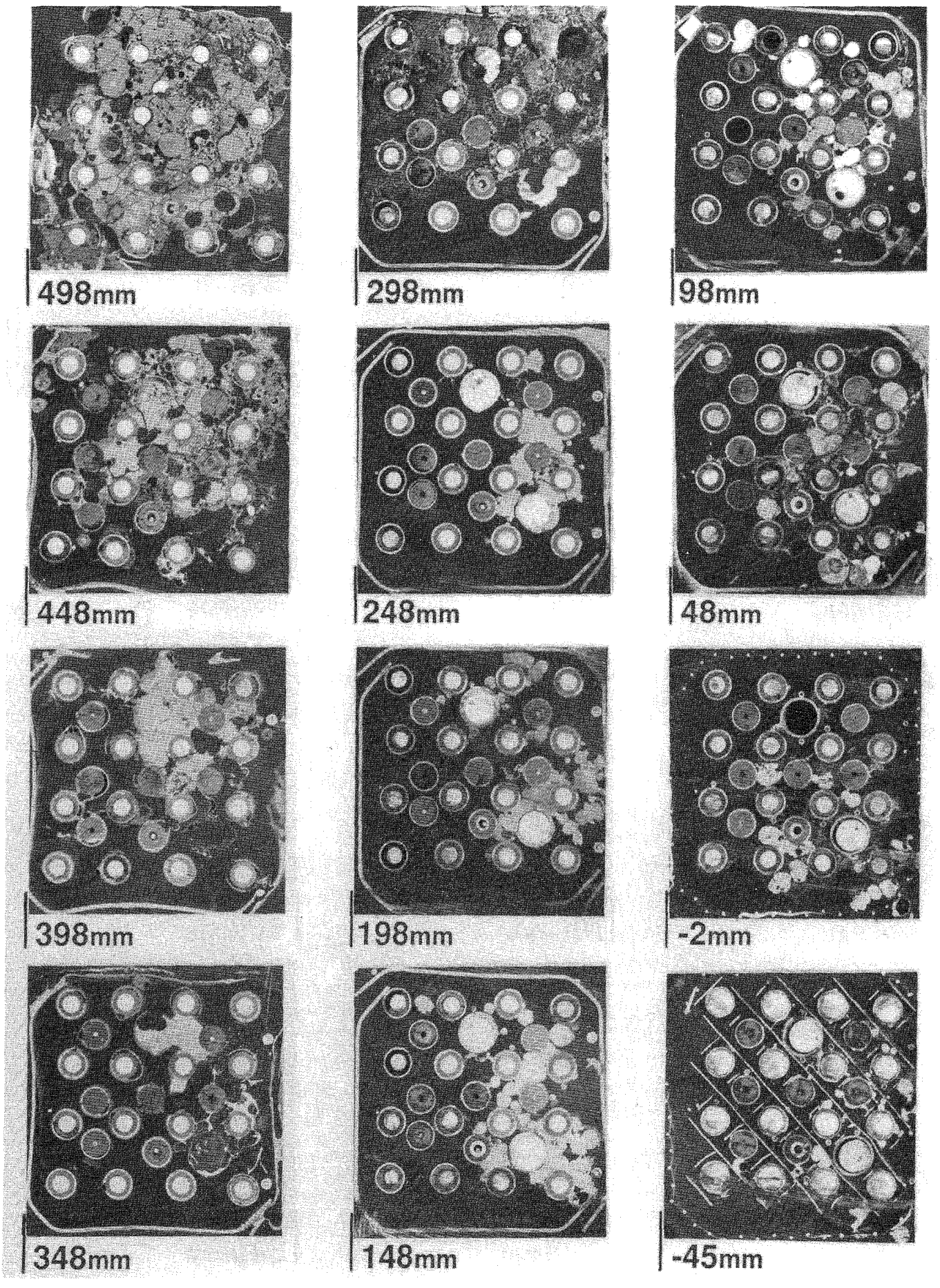

Fig. 109: Horizontal cross sections of bundle CORA-13, top view

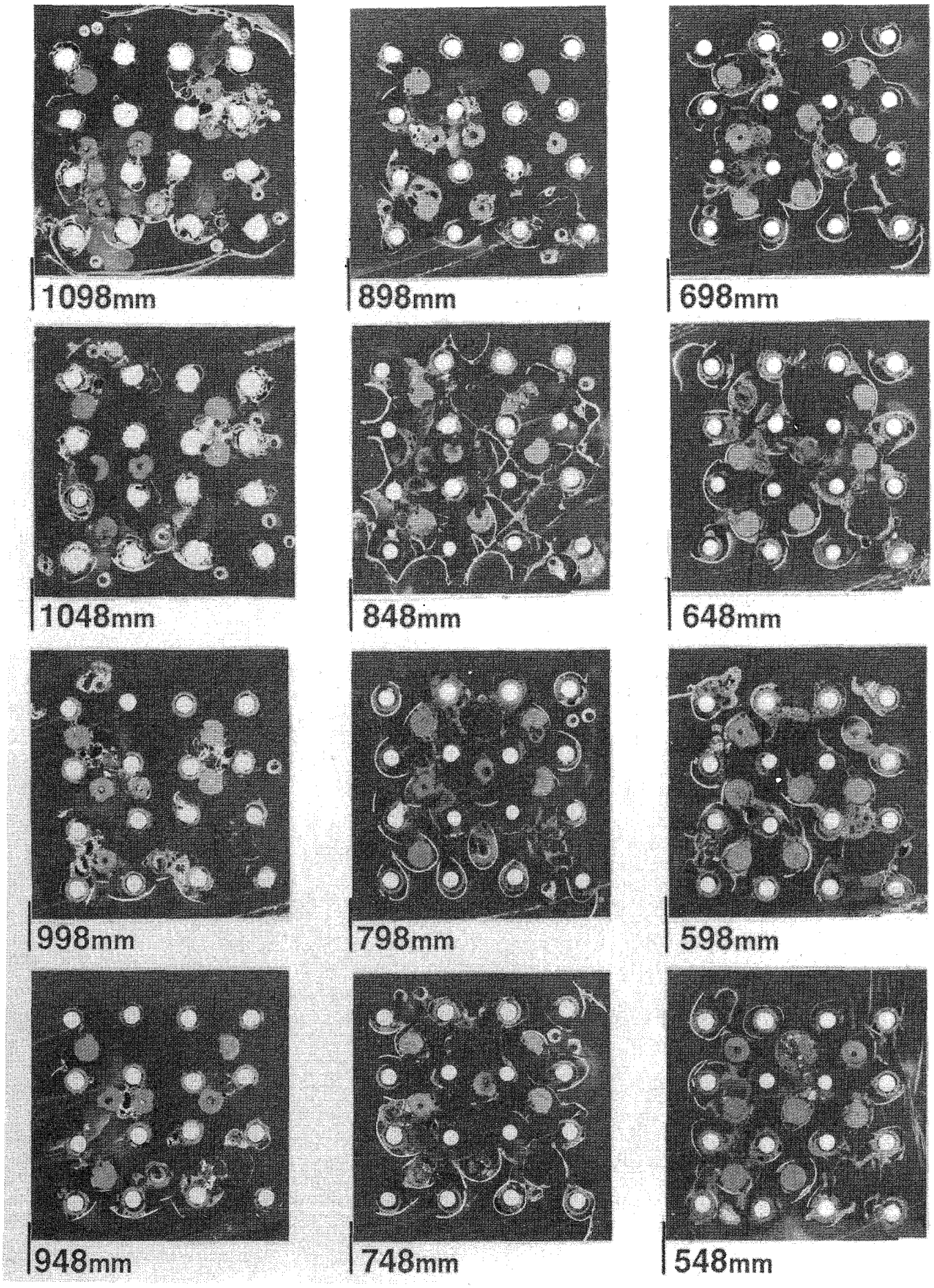

Fig. 110: Horizontal cross sections of bundle CORA-13, top view

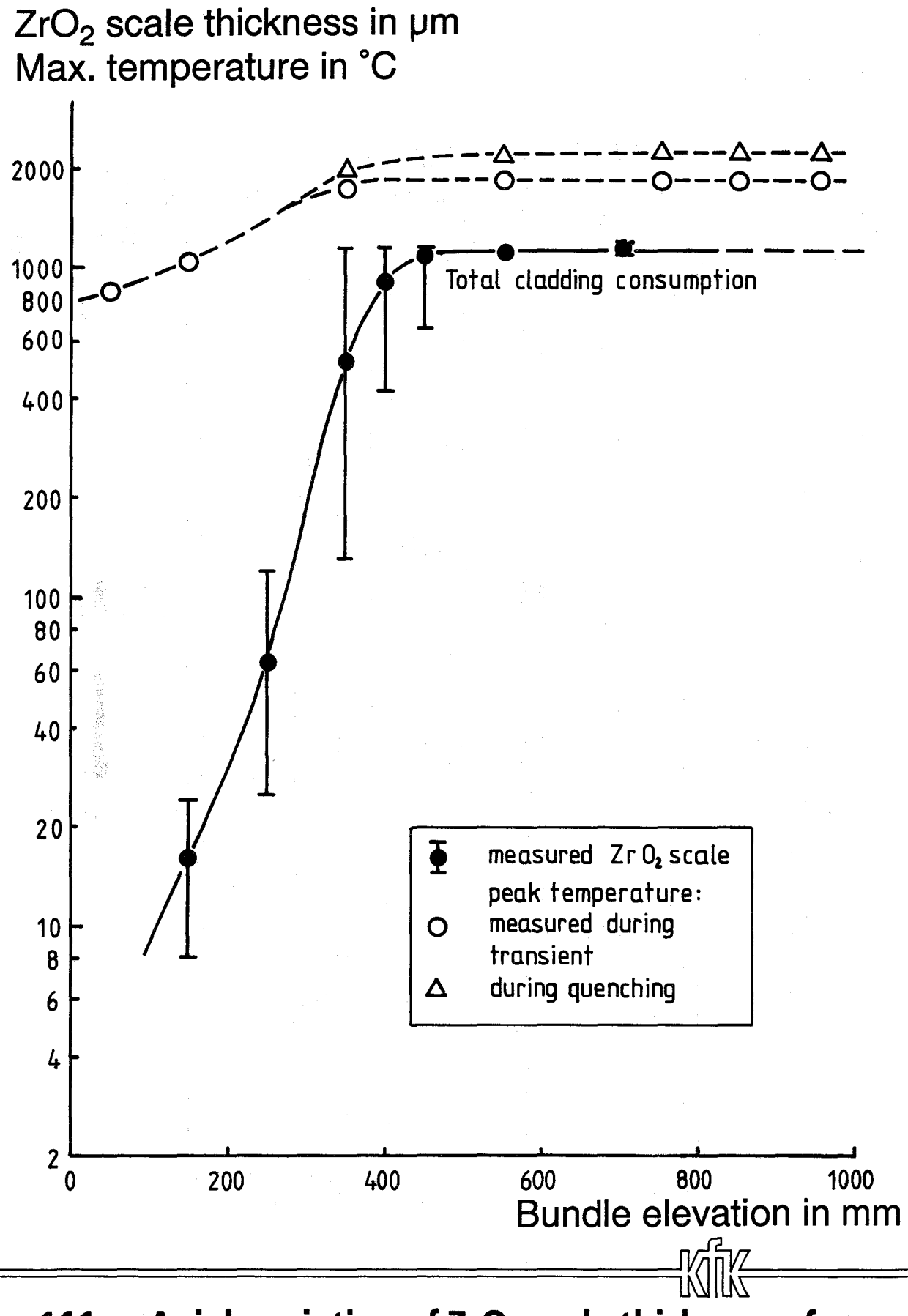

Fig. 111: Axial variation of ZrO_2 scale thickness of the CORA-13 fuel rods in comparison to maximum temperatures

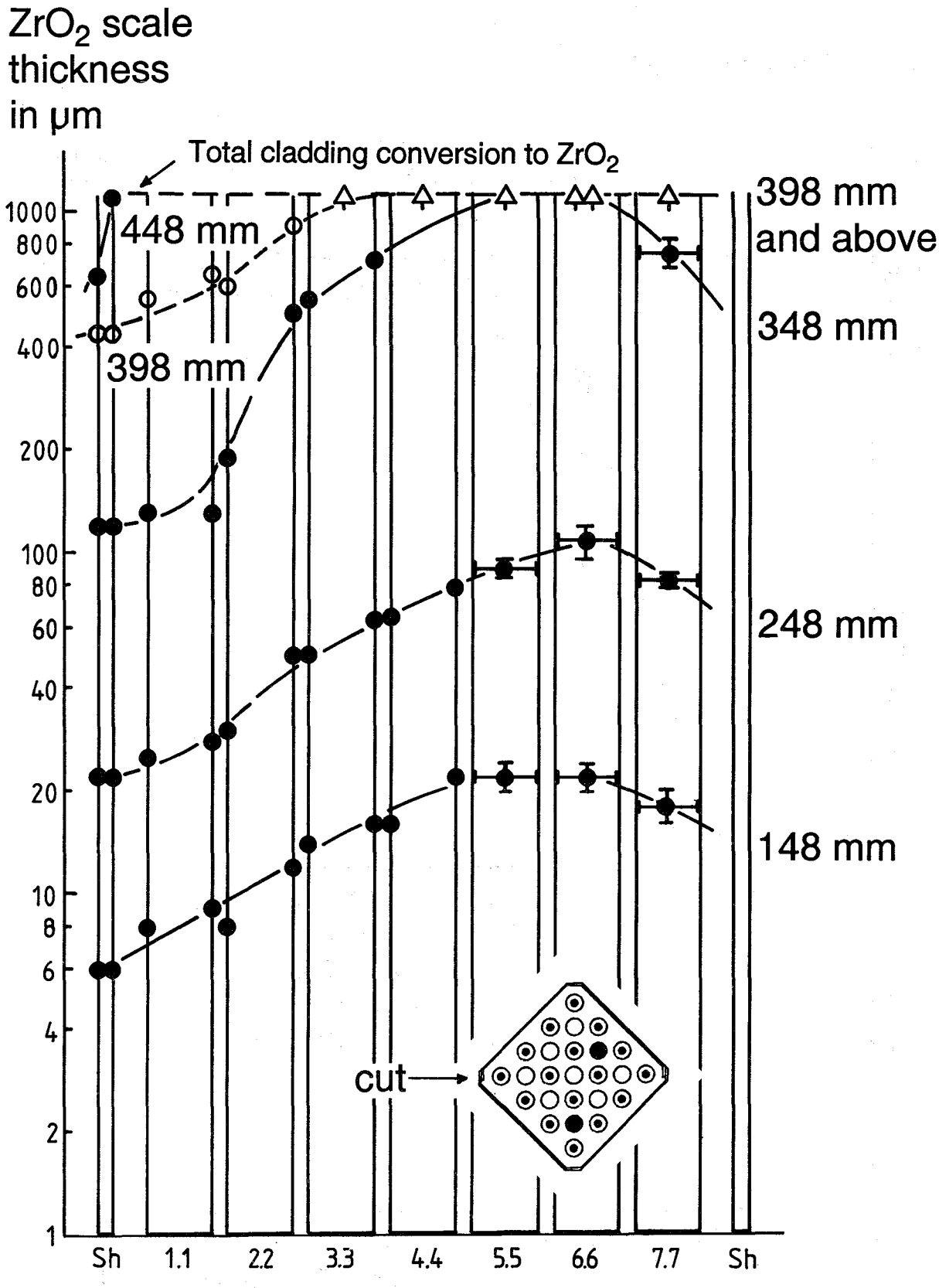

Fig. 112: Lateral variation of ZrO_2 scale thickness, diagonally across the bundle CORA-13, at different axial elevations

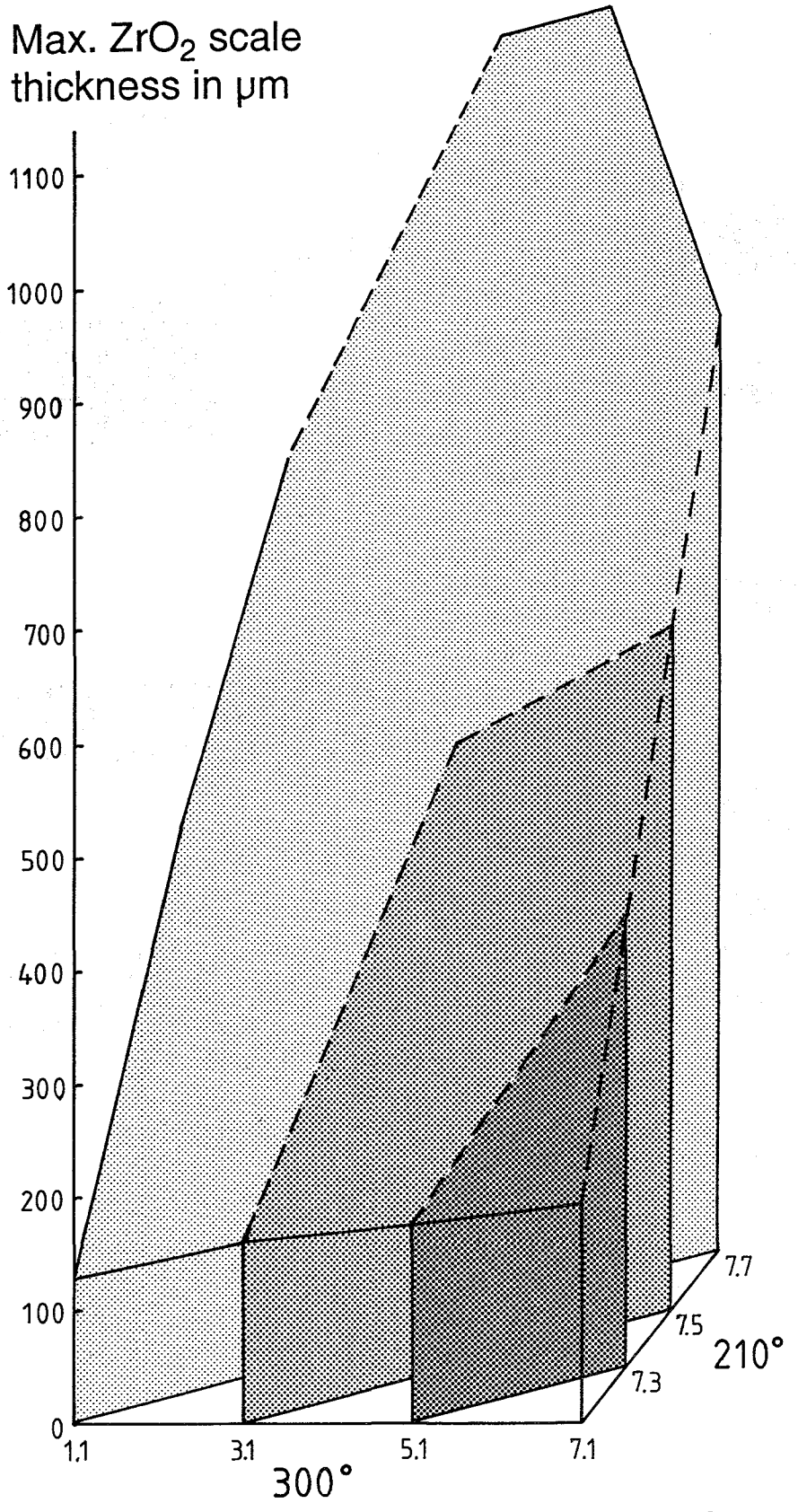

Fig. 113: ZrO_2 scale thickness variation through one half of the bundle CORA-13 at the elevation 348 mm

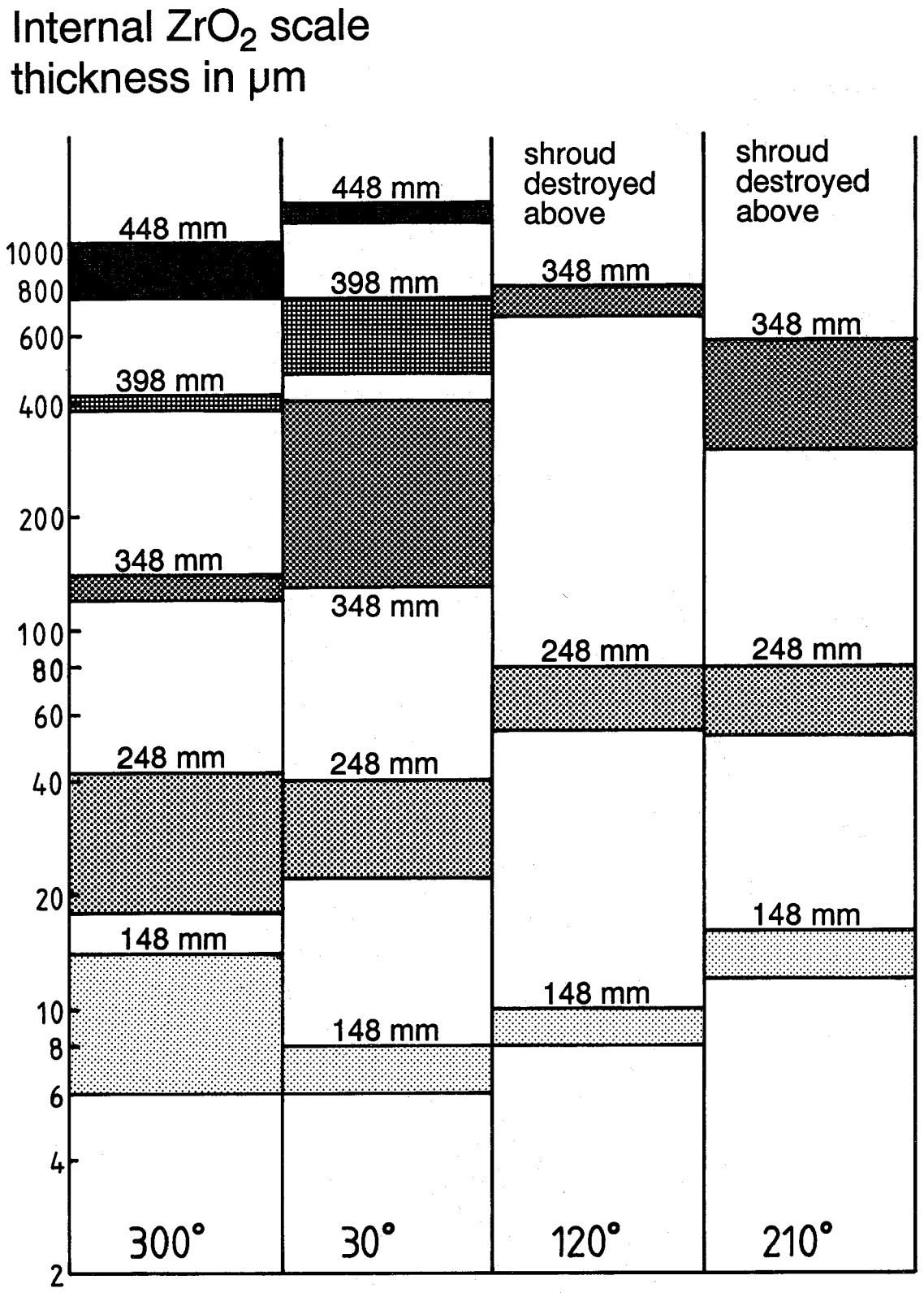

Fig. 114: Variation of internal ZrO_2 scale thickness around the shroud of bundle CORA-13

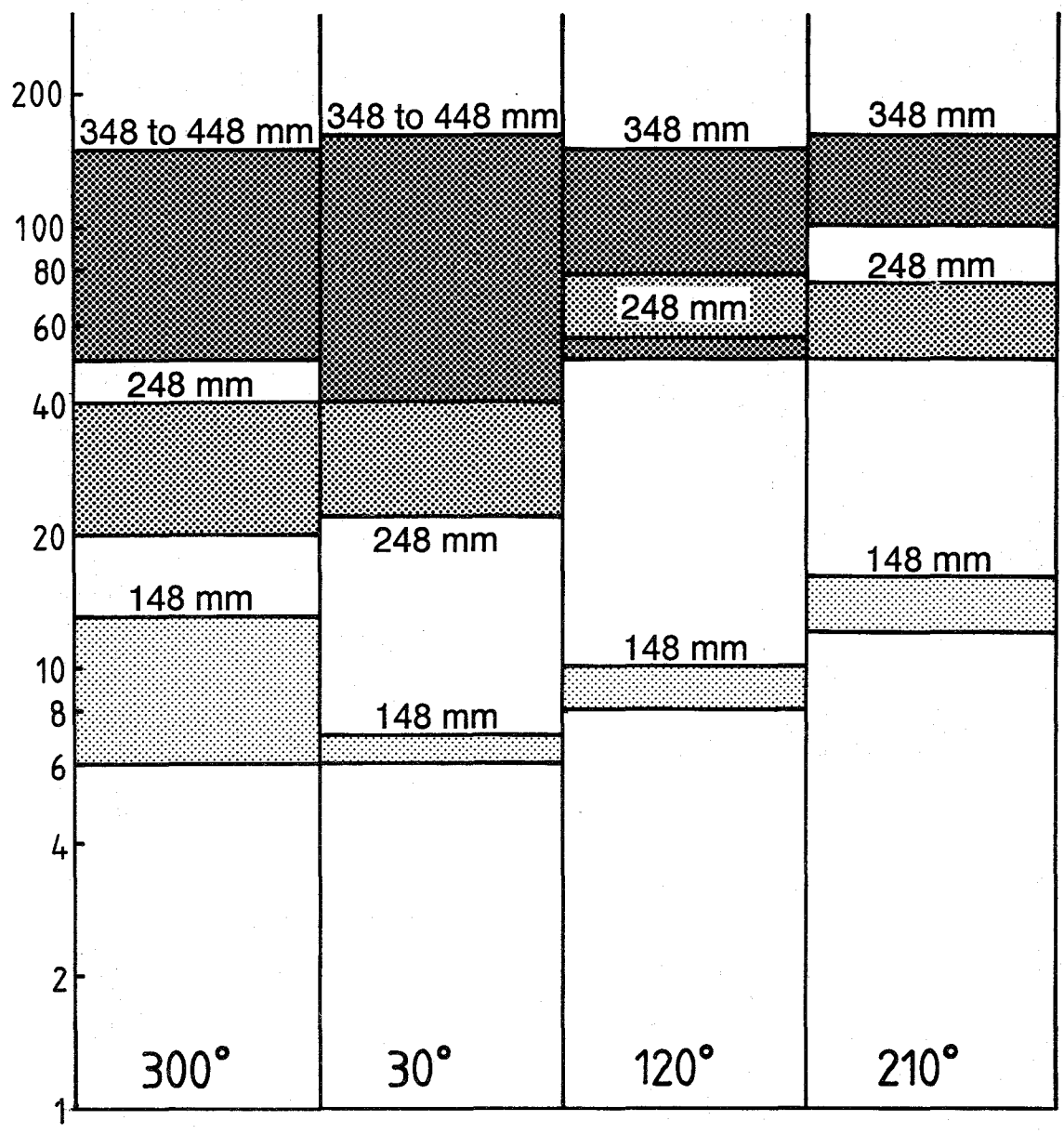

Fig. 115: Variation of external ZrO_2 scale thickness around the shroud of bundle CORA-13

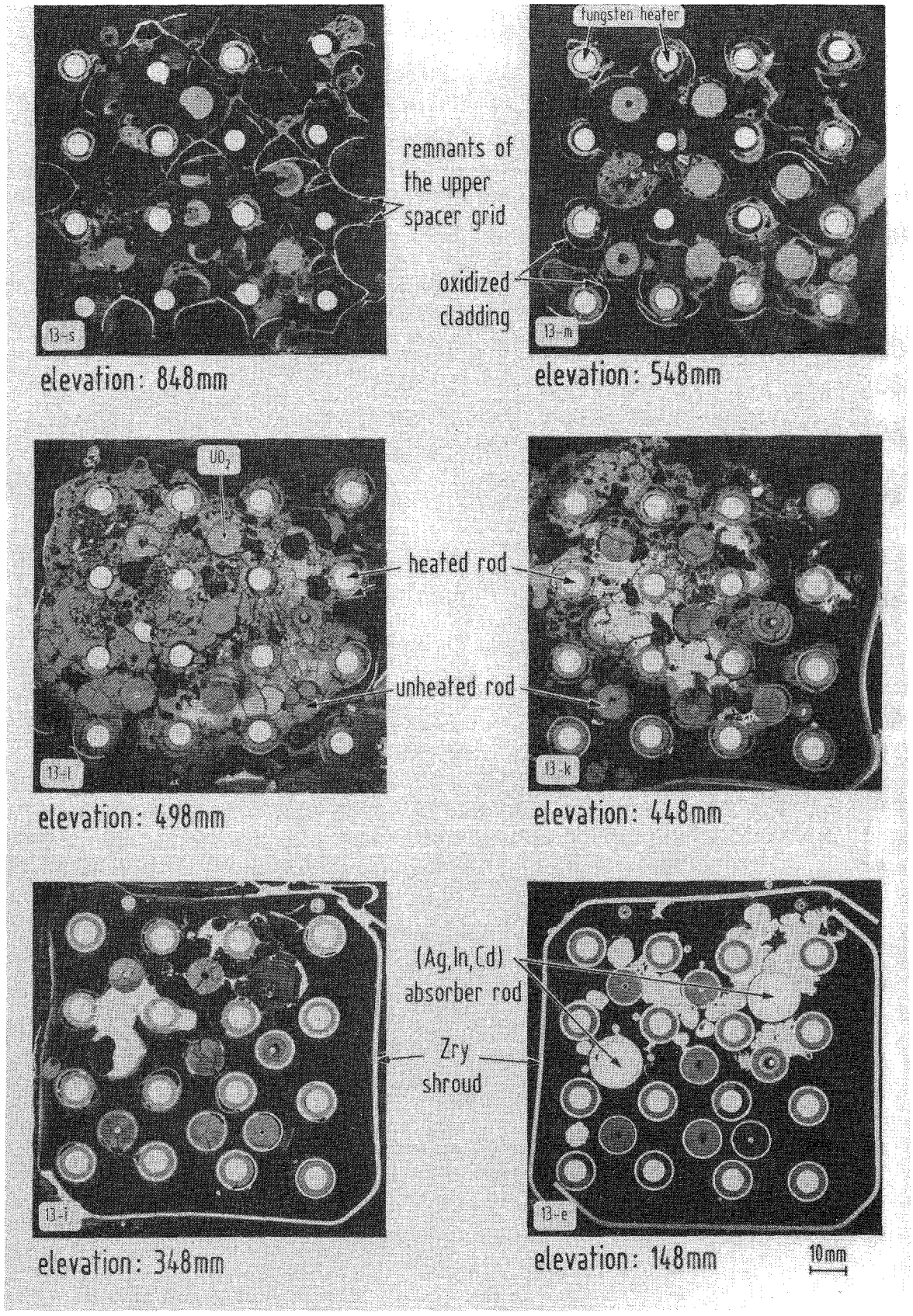

CORA bundle 13; PWR quench test

Fig. 116: Macrostructures of CORA-13 bundle cross-sections (top view)

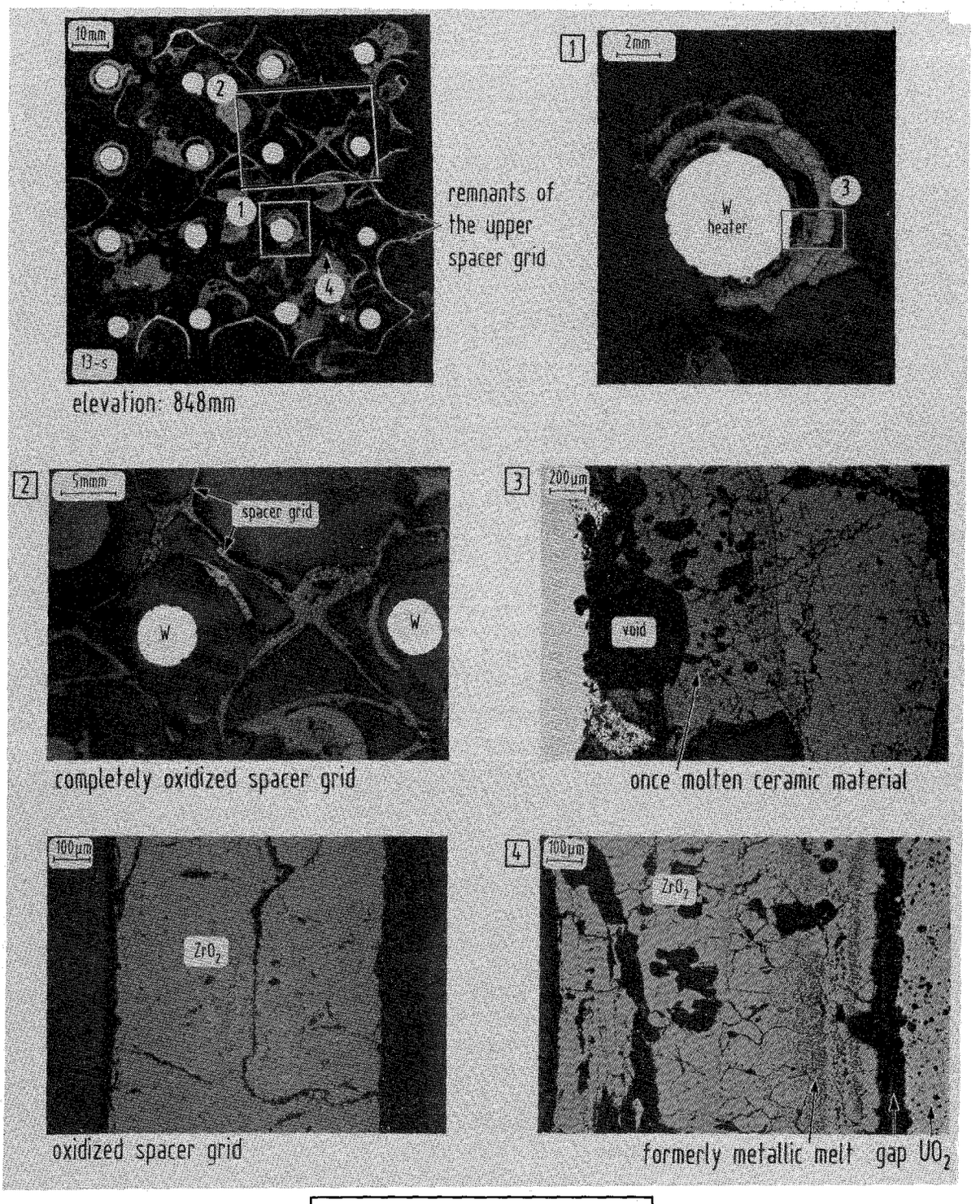

CORA bundle 13; PWR quench test

KfK IMF I 9/92

Fig. 117: Microstructures of CORA-13 bundle at cross-section elevation 848 mm

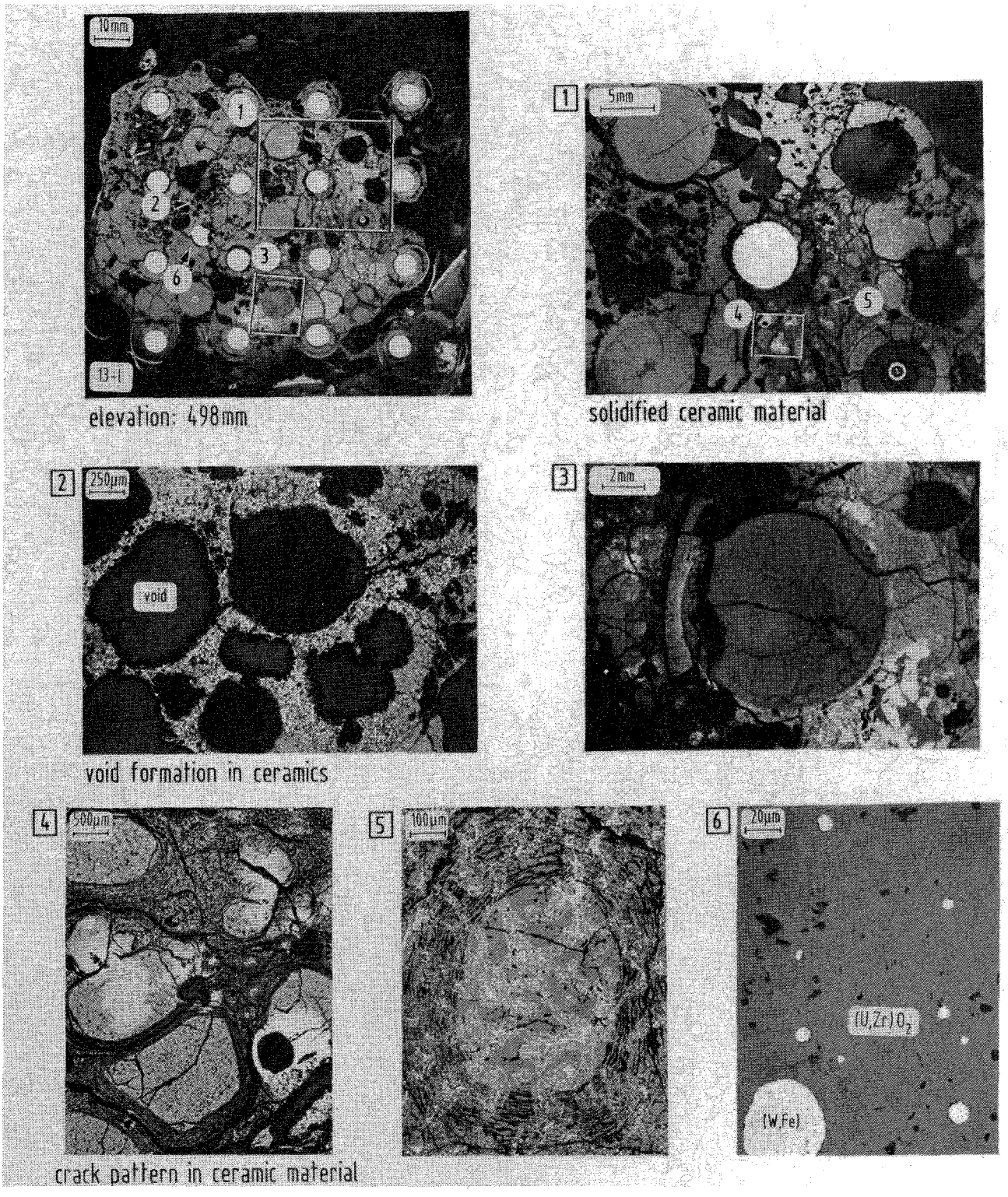

CORA bundle 13; PWR quench test

KfK IMF I 9/92

Fig. 118: Microstructures of CORA-13 bundle at cross-section elevation 498 mm

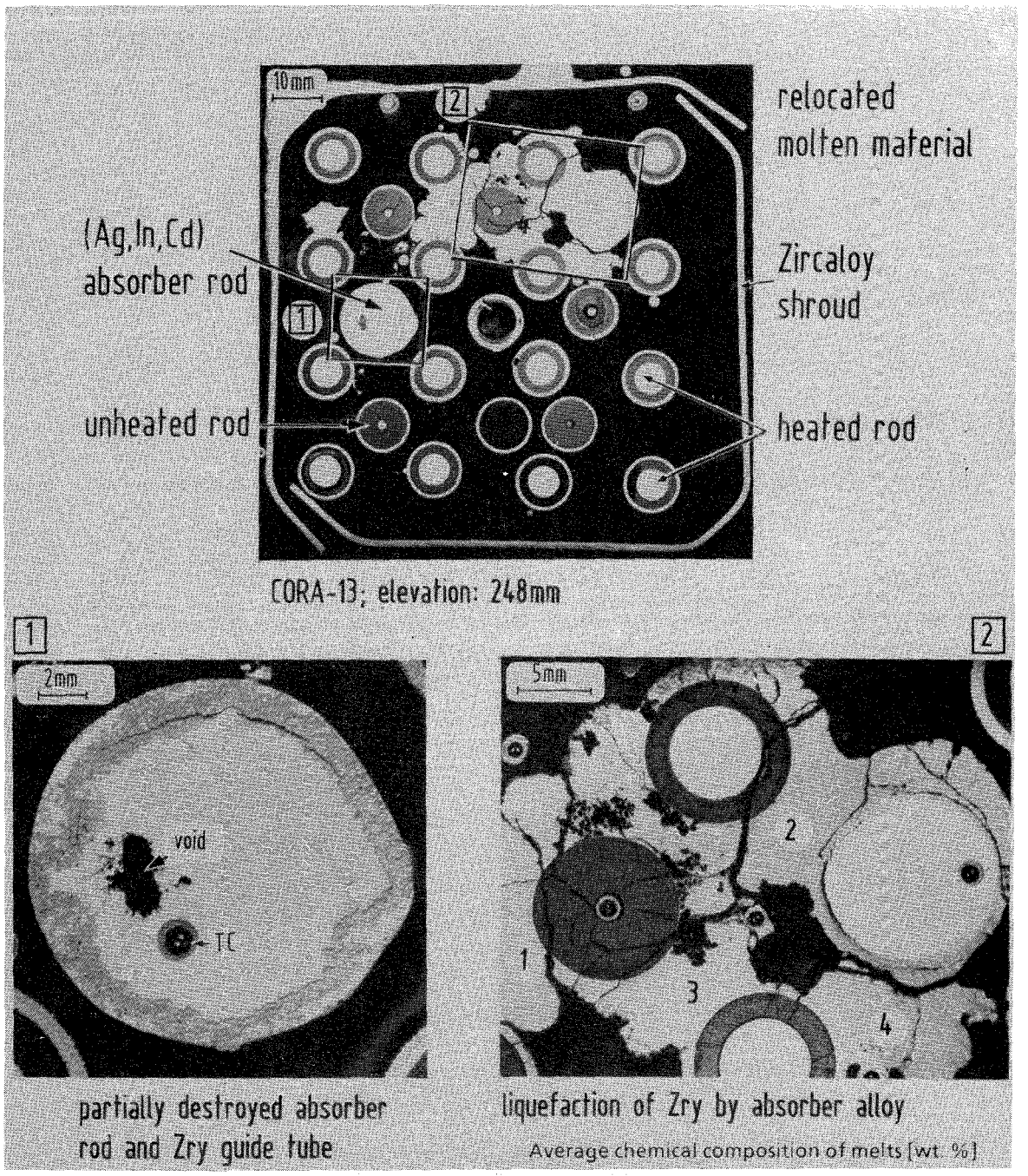

Average chemical composition of melts [wt. %]

melt	Zr	Fe	Cr	Ni	Ag	In	Cd	U
1-4	52	8	2	3	24	5	1	4

KfK IMF I 9/92

Fig. 119: Macrostructures of CORA-13 bundle at cross-section elevation 248 mm

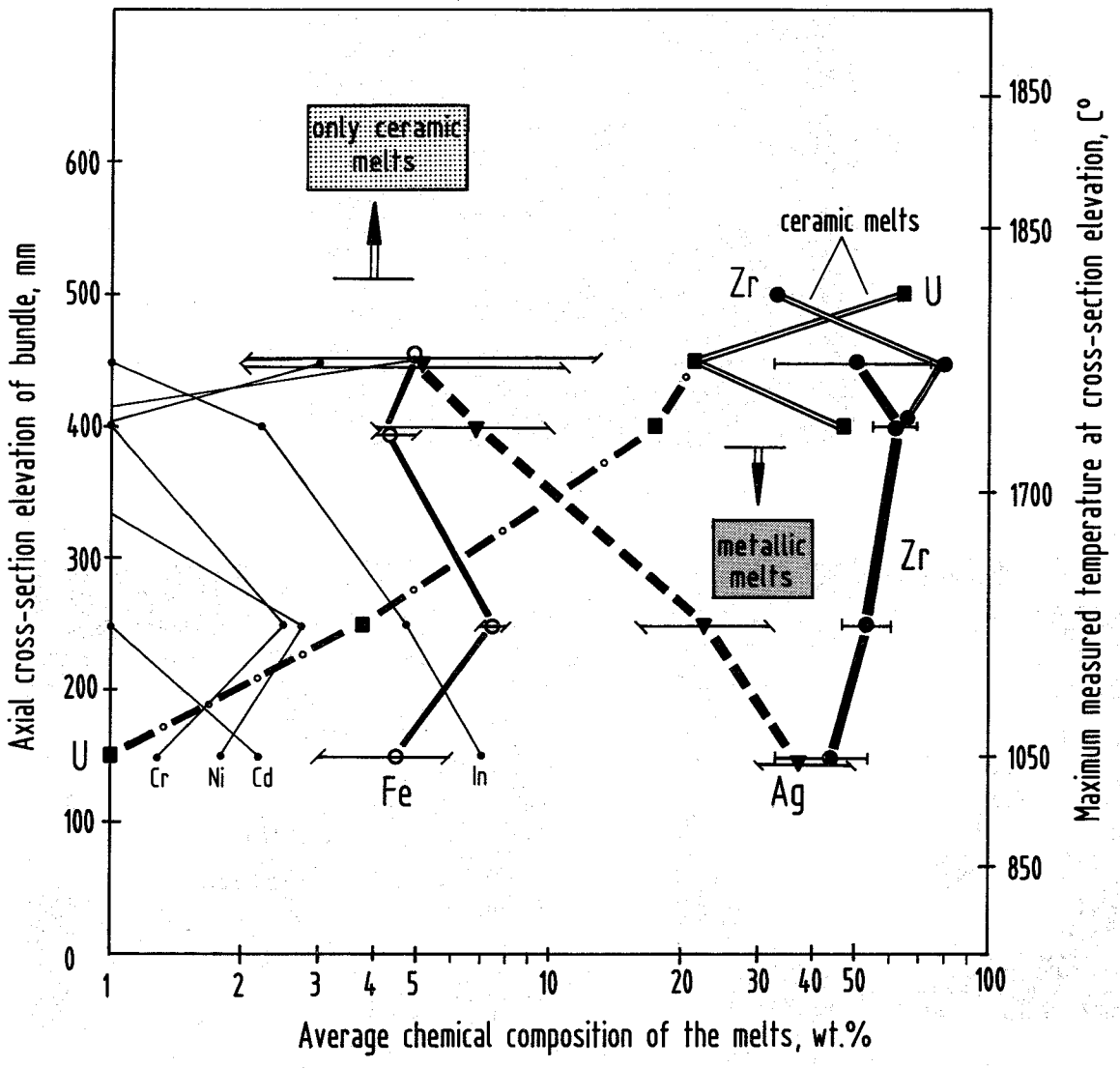

Fig. 120: Chemical composition of melts as function of cross-section elevation

Appendix

Data of the pre-transient phase

of test CORA-13

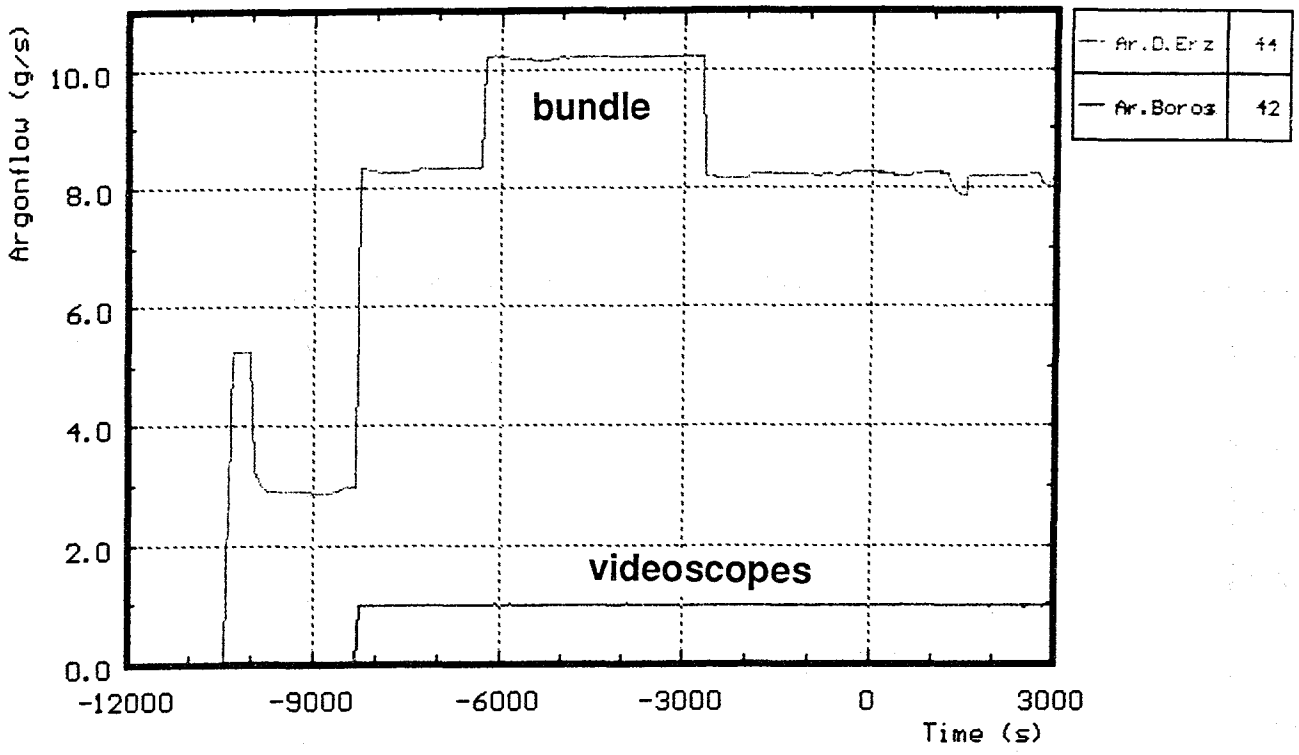

Fig. A1: Argon input prior to test CORA-13

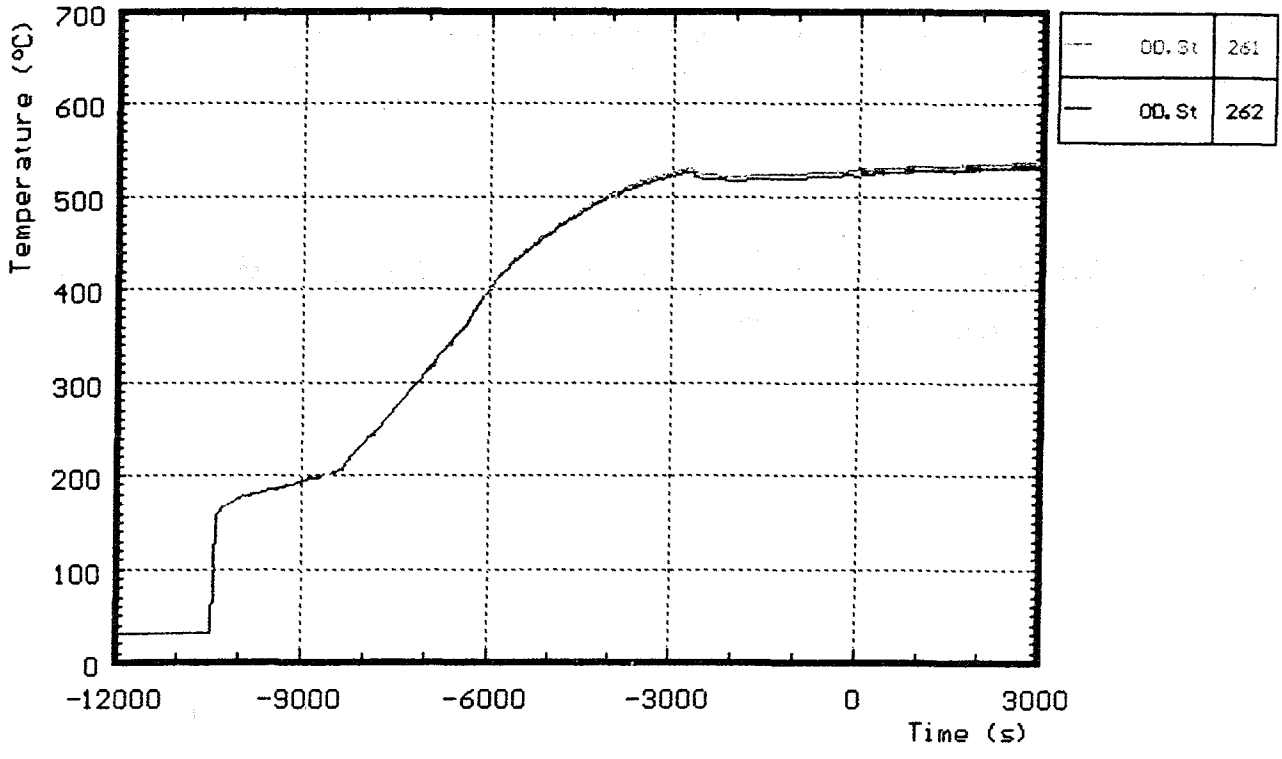

Fig. A2: Temperature at the entrance of the bundle prior to test CORA-13

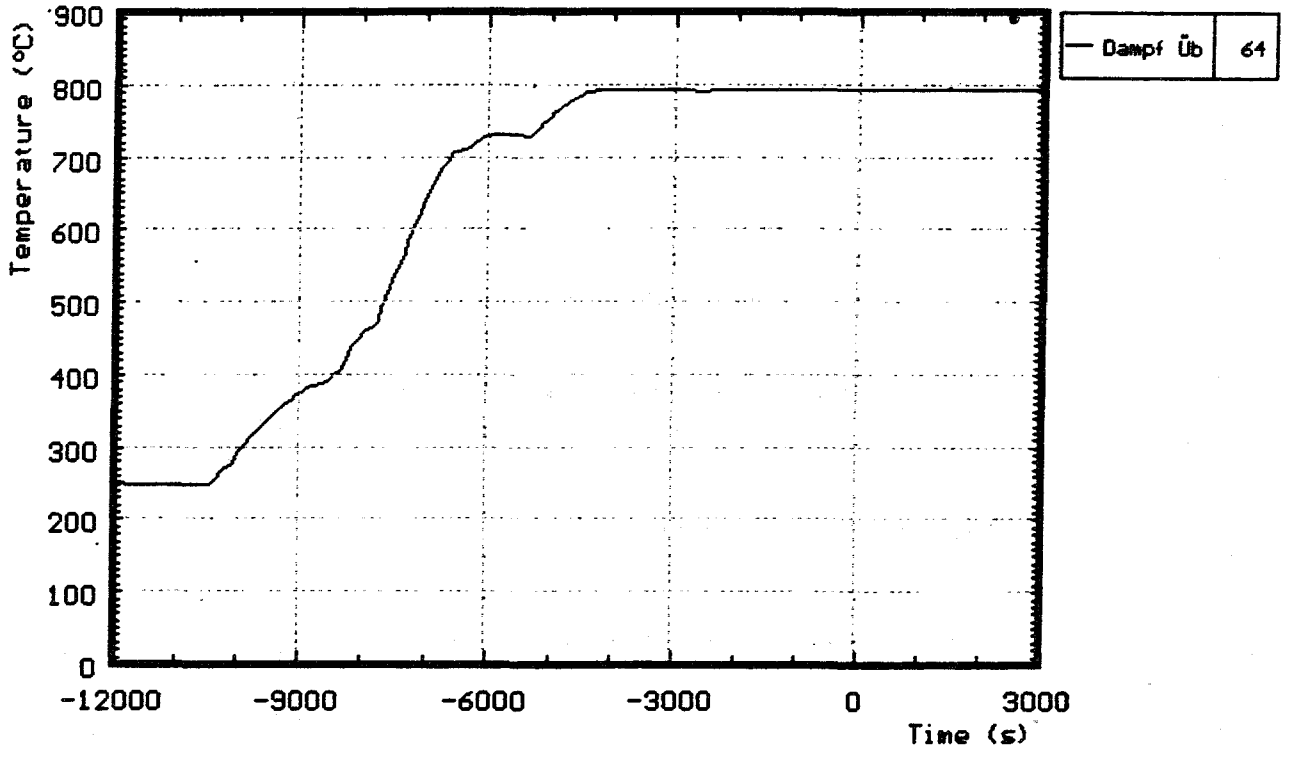

Fig. A3: Temperature of steam superheater prior to the transient of CORA-13

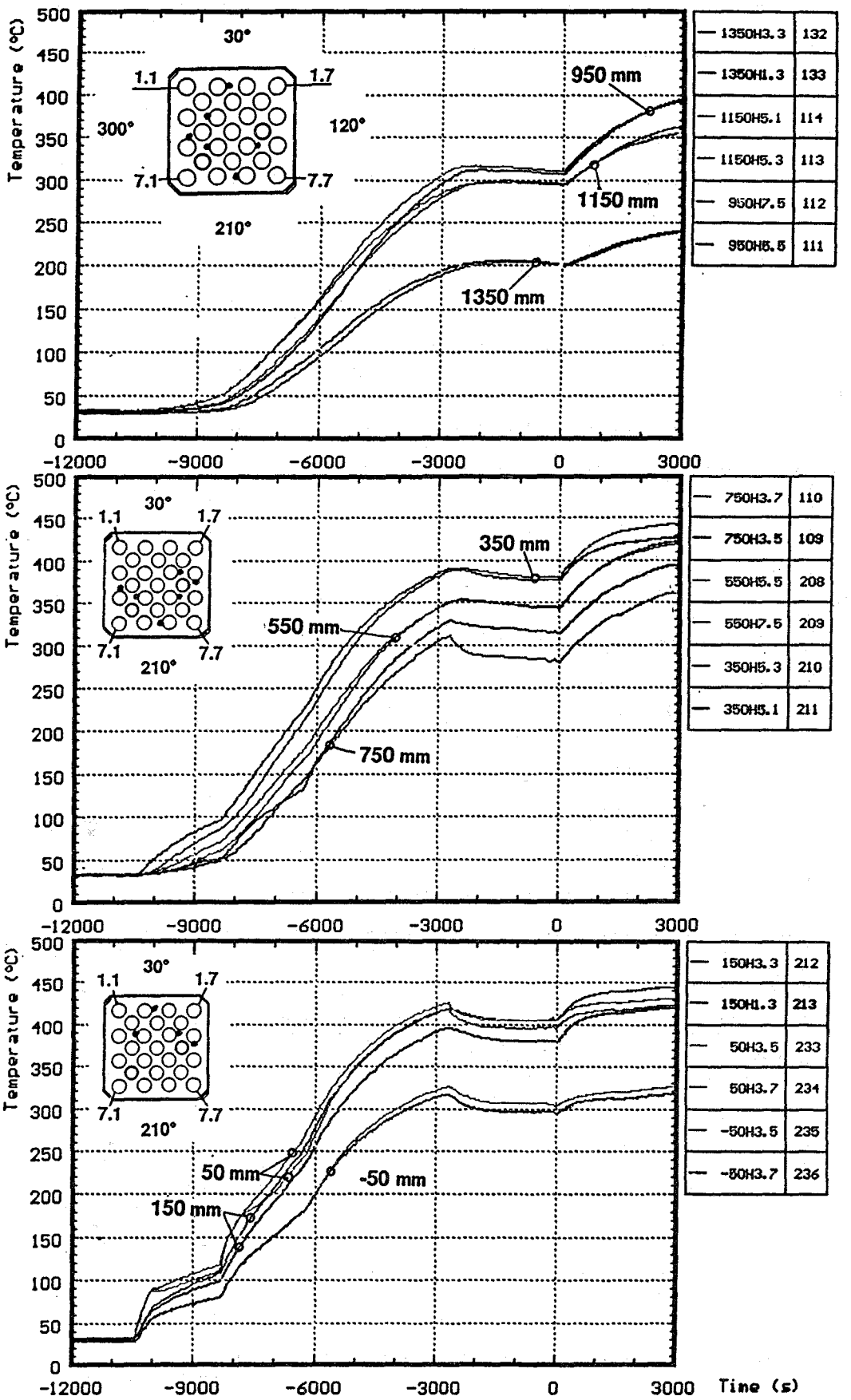

Fig. A4: Temperatures of the heated rods; pre-heat phase (CORA-13)

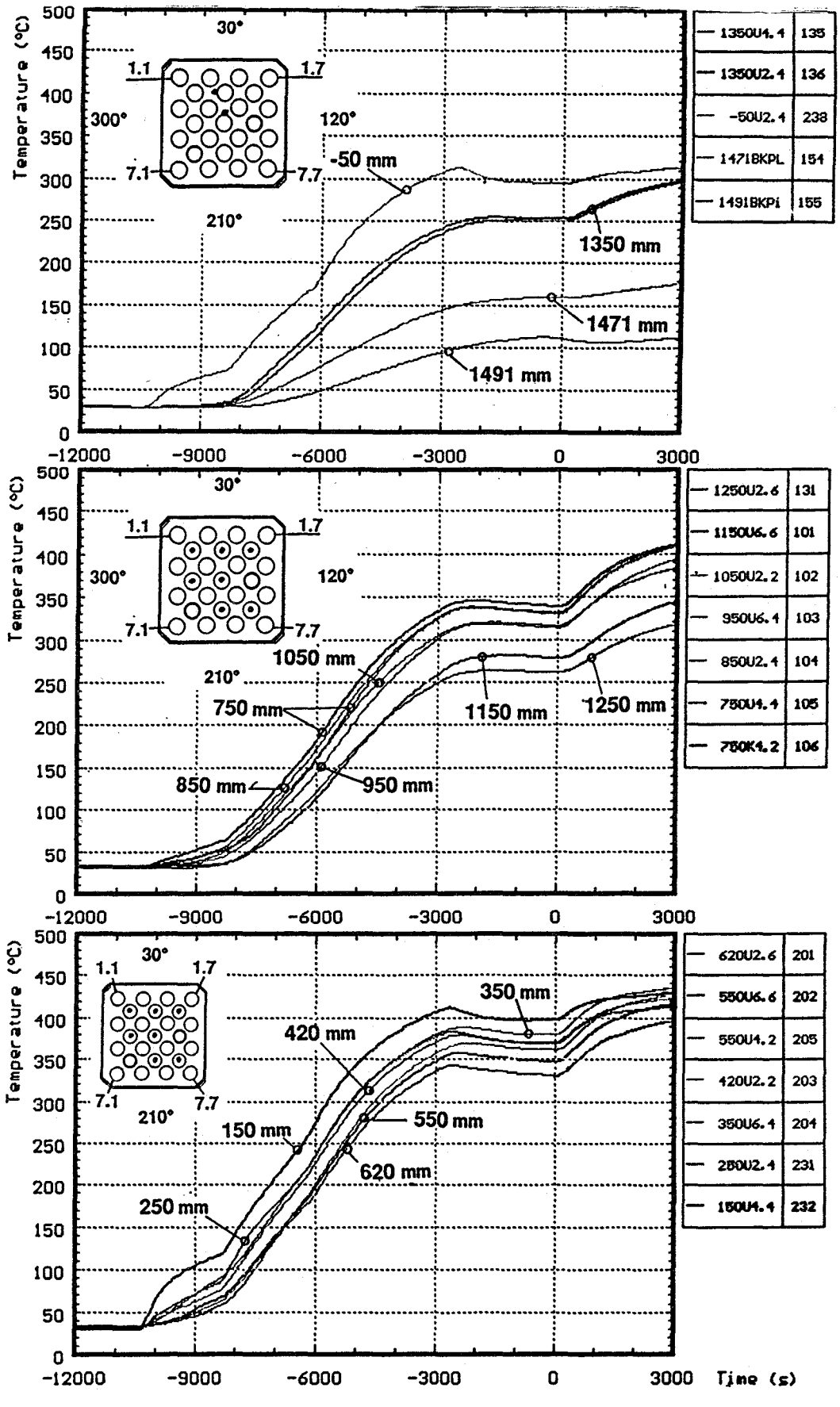

Fig. A5: Temperatures of the unheated rods; pre-heat phase (CORA-13)

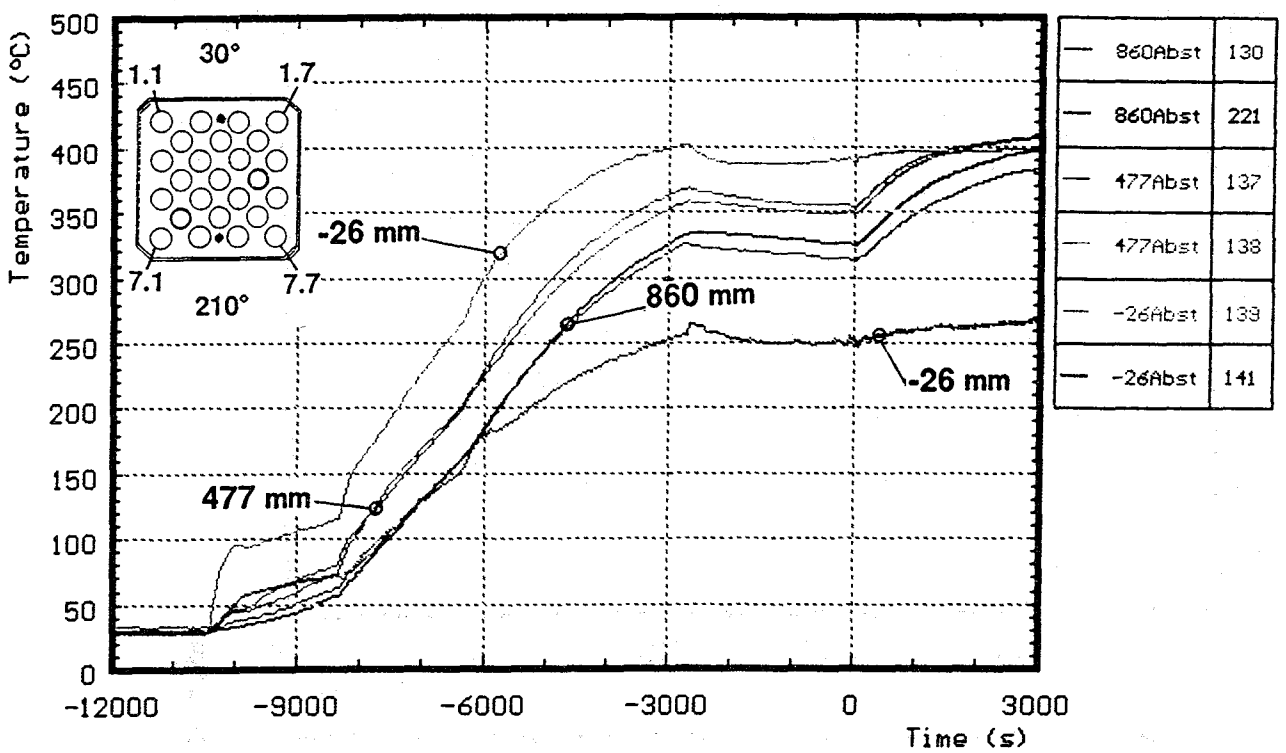

Fig. A6: Temperatures at the spacer; pre-heat phase (CORA-13)

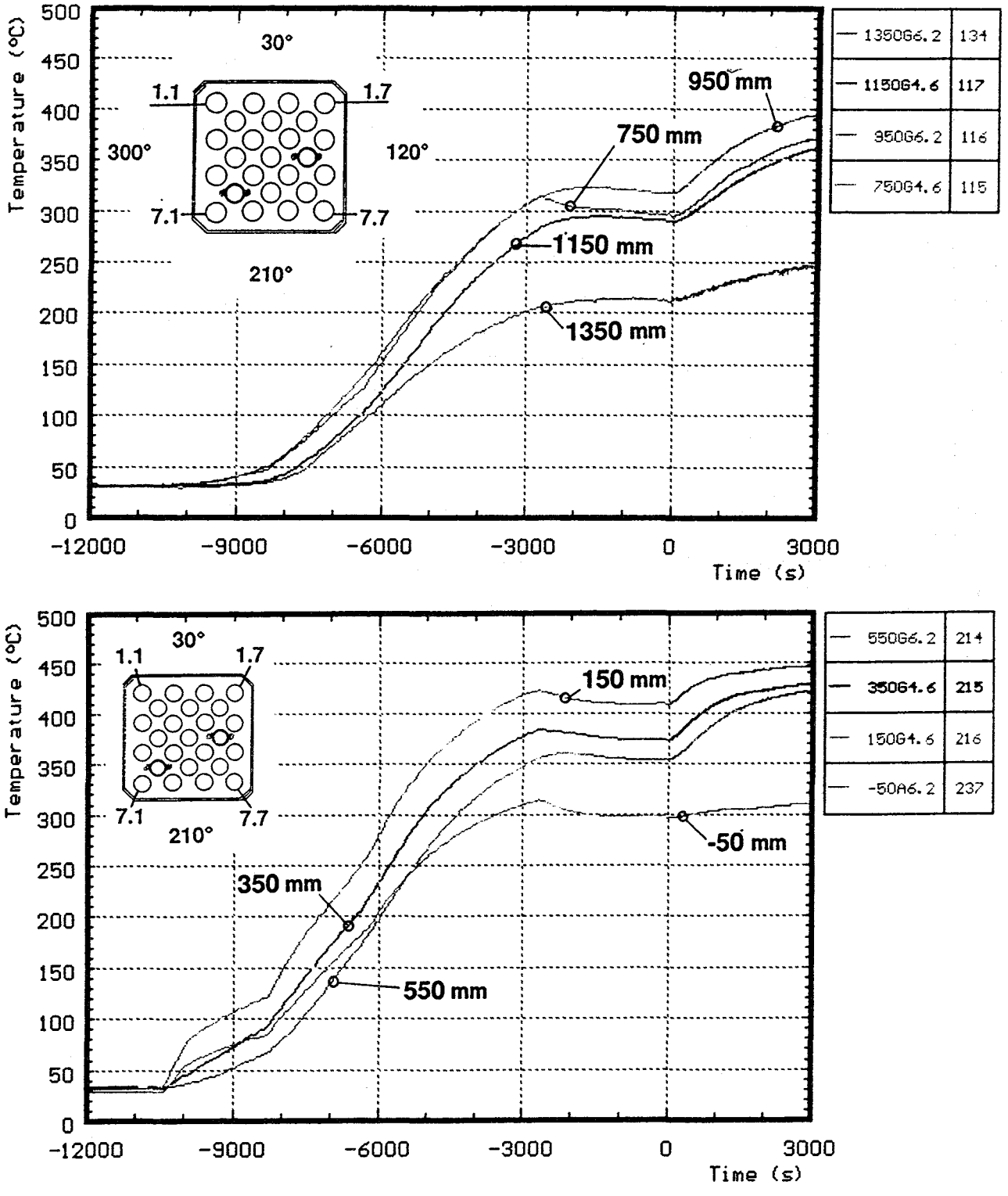

Fig. A7: Temperatures at the guide tube; pre-heat phase (CORA-13)

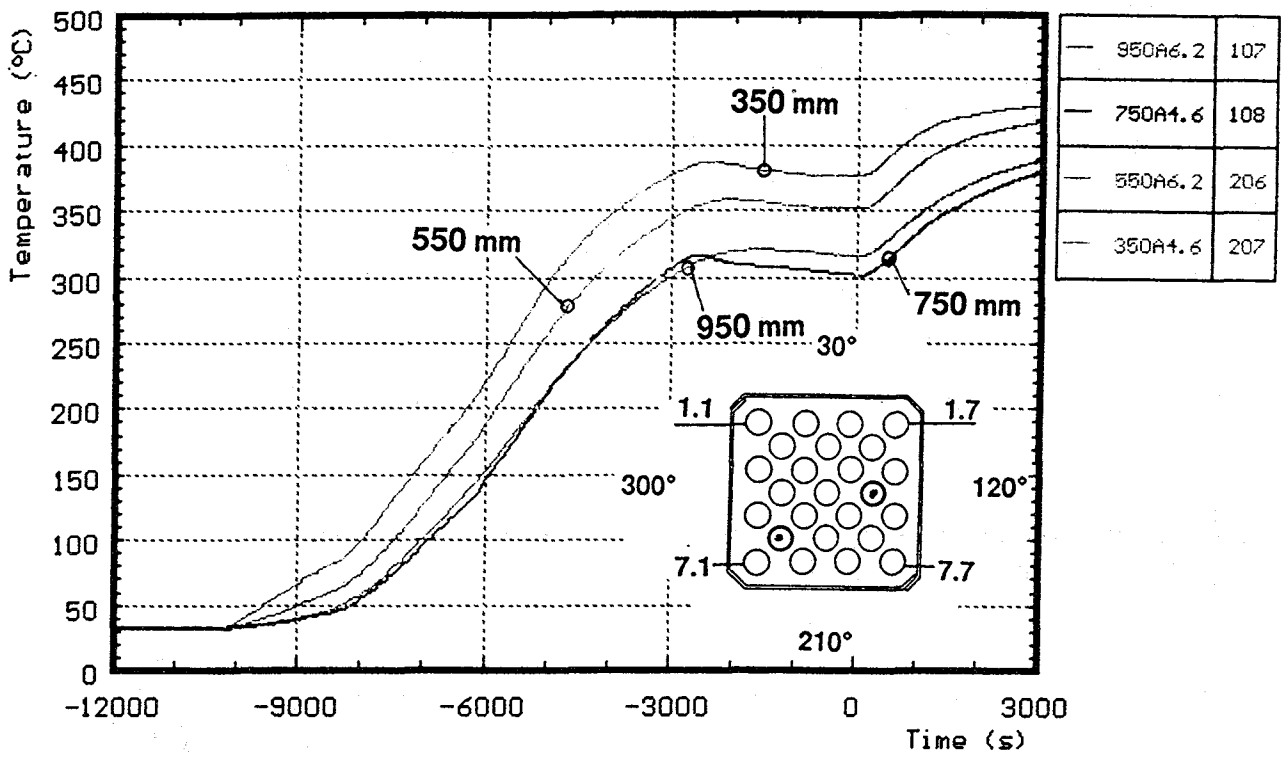

Fig. A8: Temperatures of the absorber rods; pre-heat phase (CORA-13)

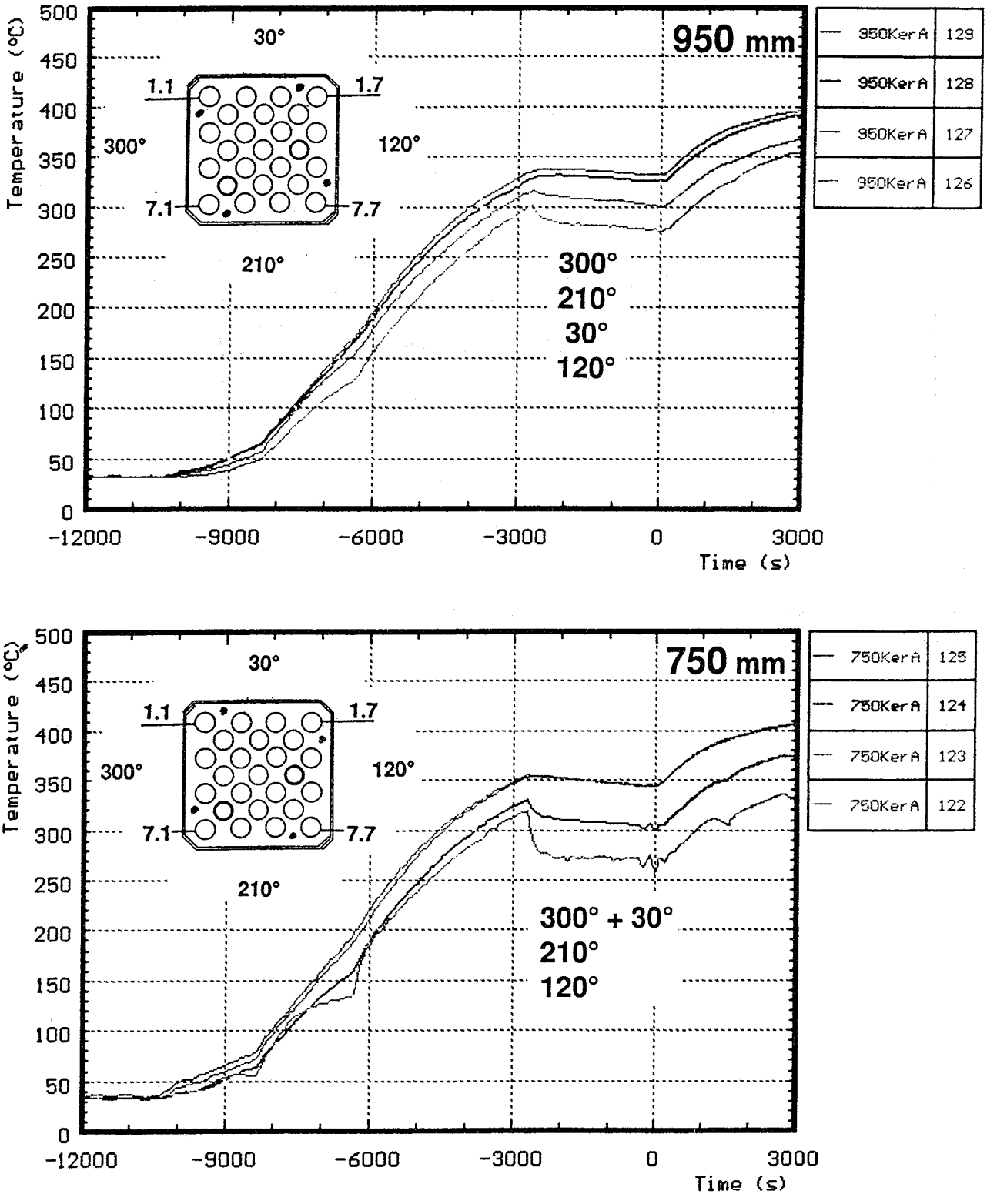

Fig. A9: Temperatures at the outside of the bundle; pre-heat phase (CORA-13)

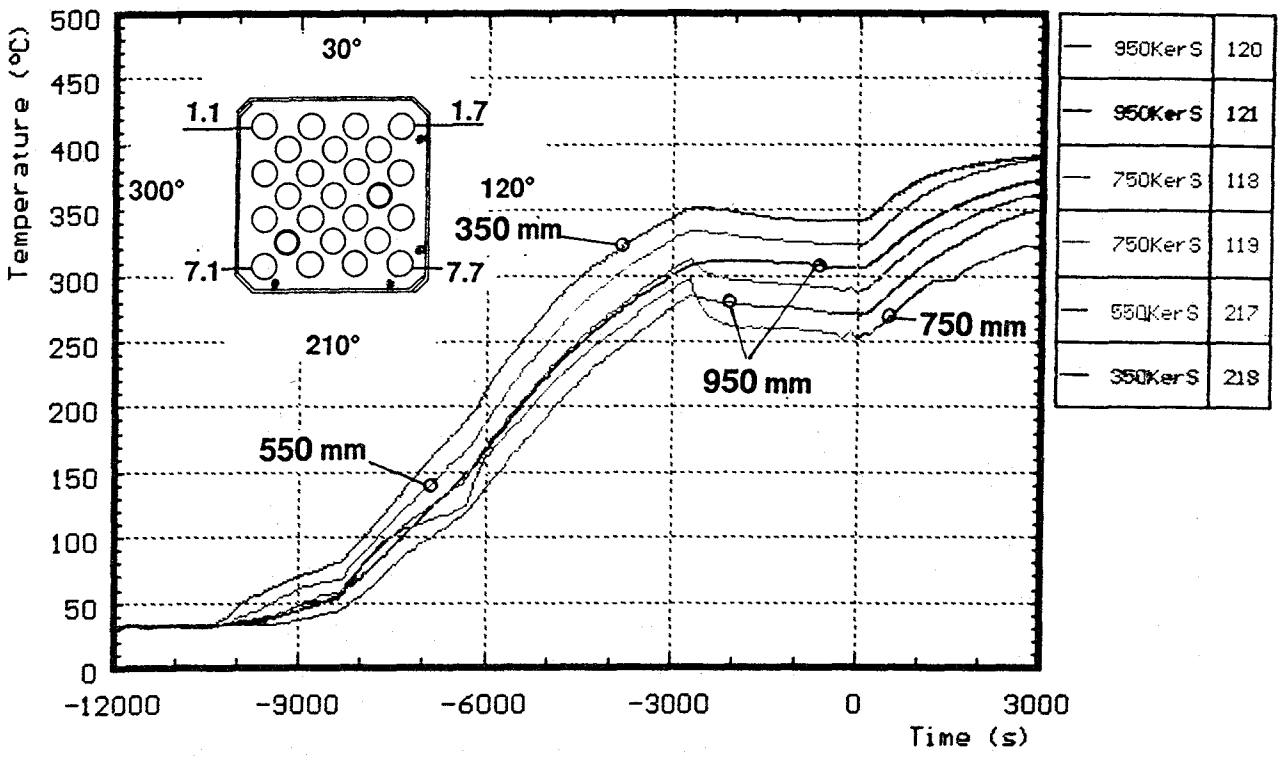

Fig. A10: Temperatures at the inner side of shroud; pre-heat phase (CORA-13)

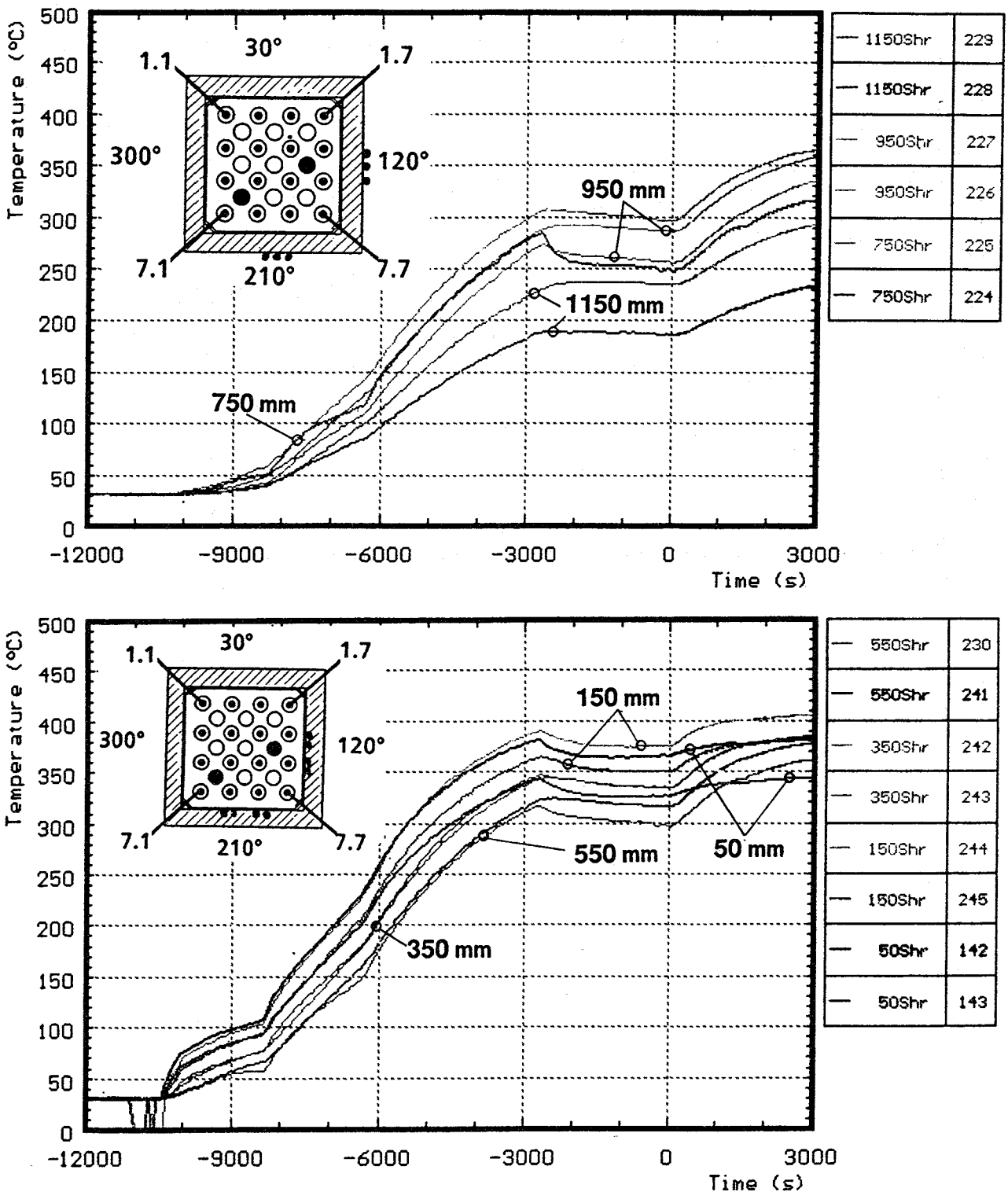

Fig. A11: Temperatures at the outer side of shroud; pre-heat phase (CORA-13)

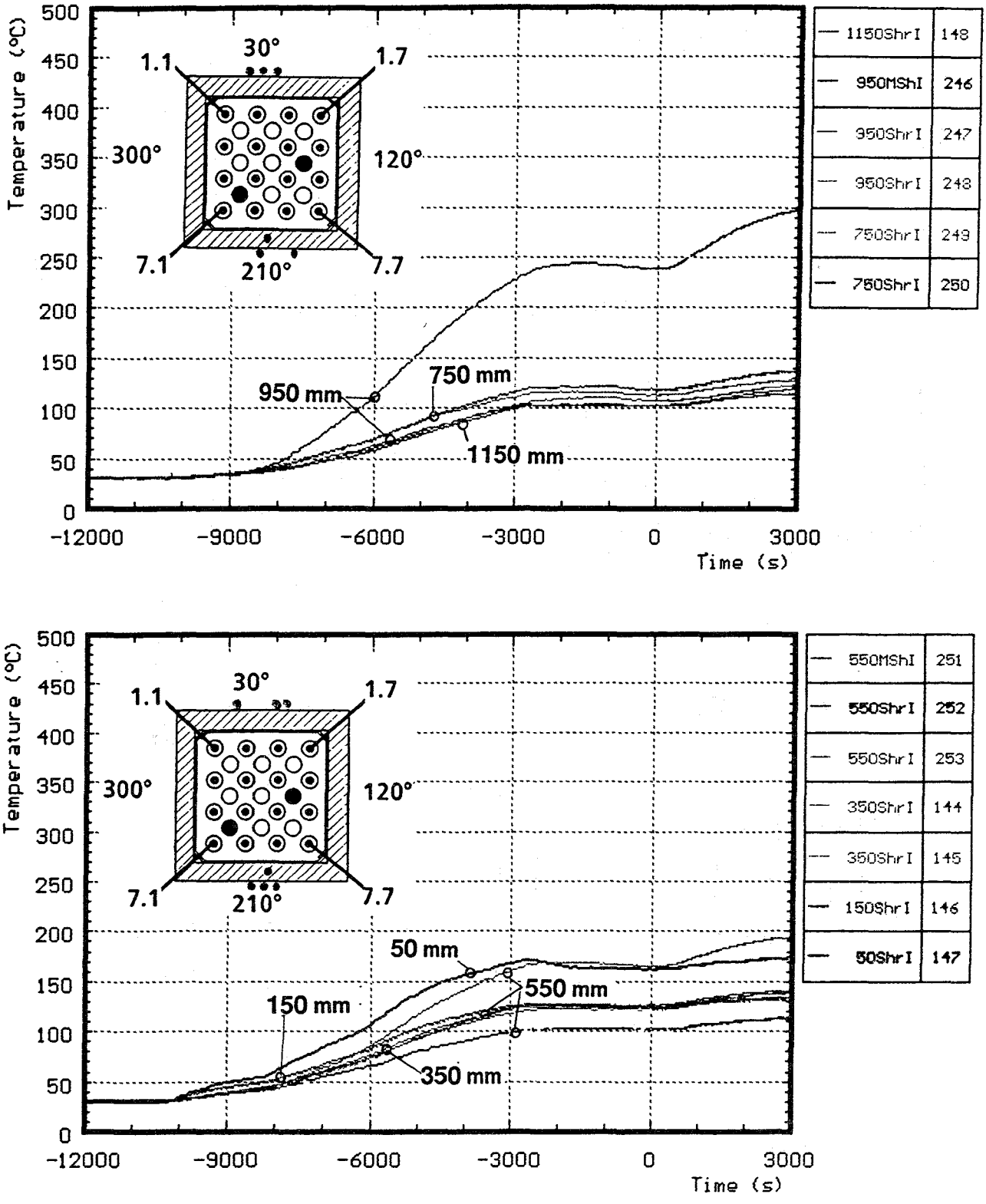

Fig. A12: Temperatures at and within shroud insulation; pre-heat phase (CORA-13)

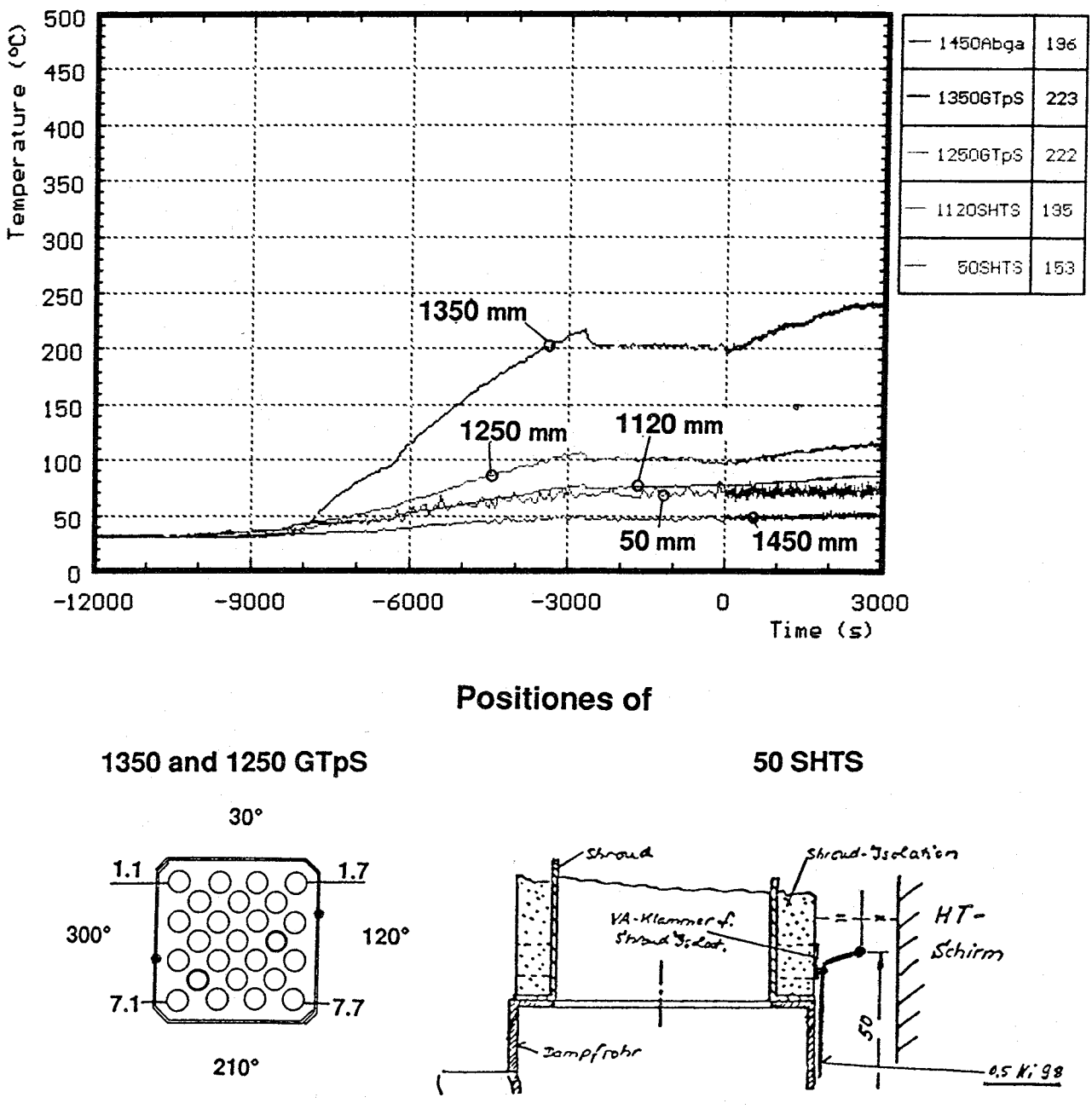

Fig. A13: Gas temperature; pre-heat phase (CORA-13)

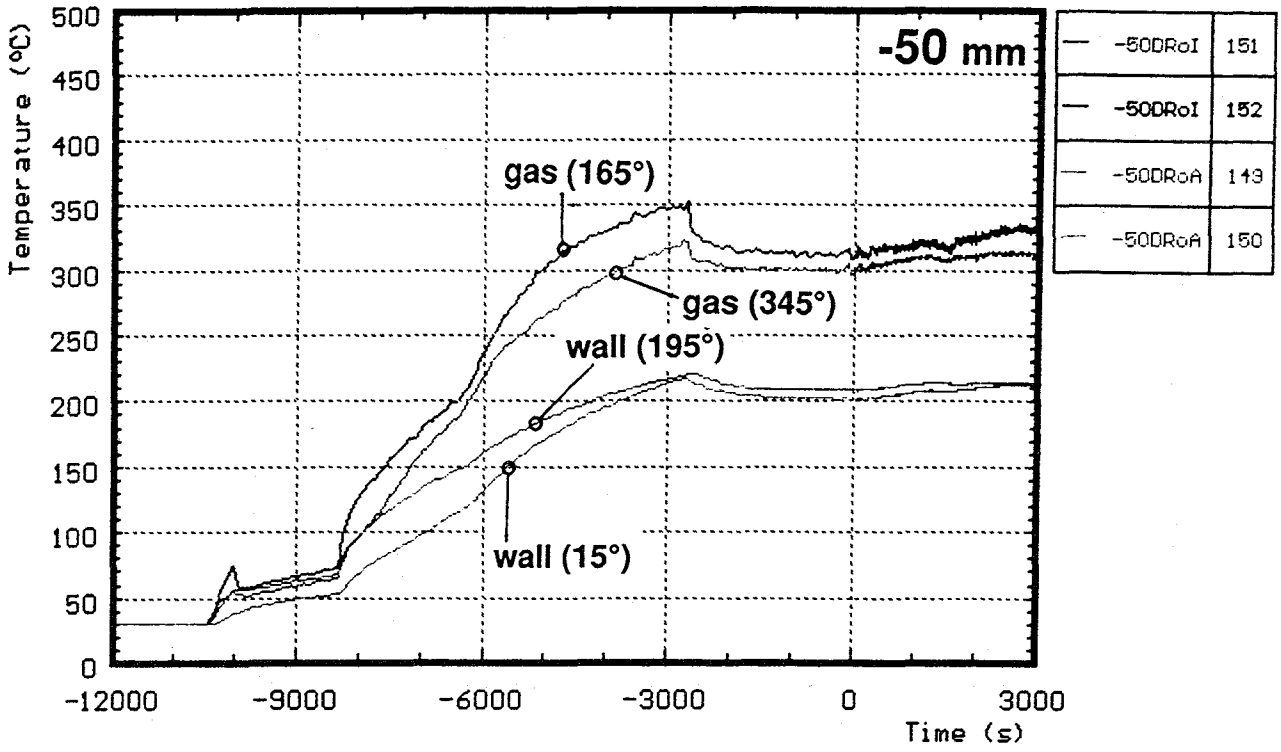

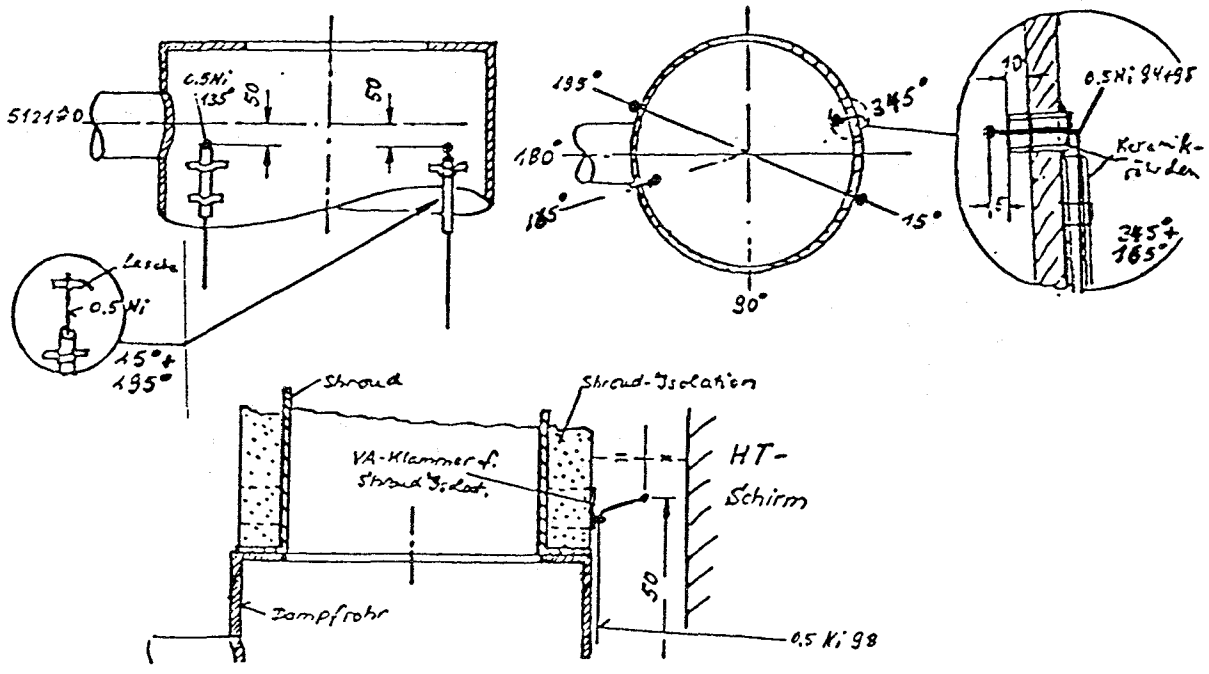

Fig. A14: Temperatures in the steam tube; pre-heat phase (CORA-13)

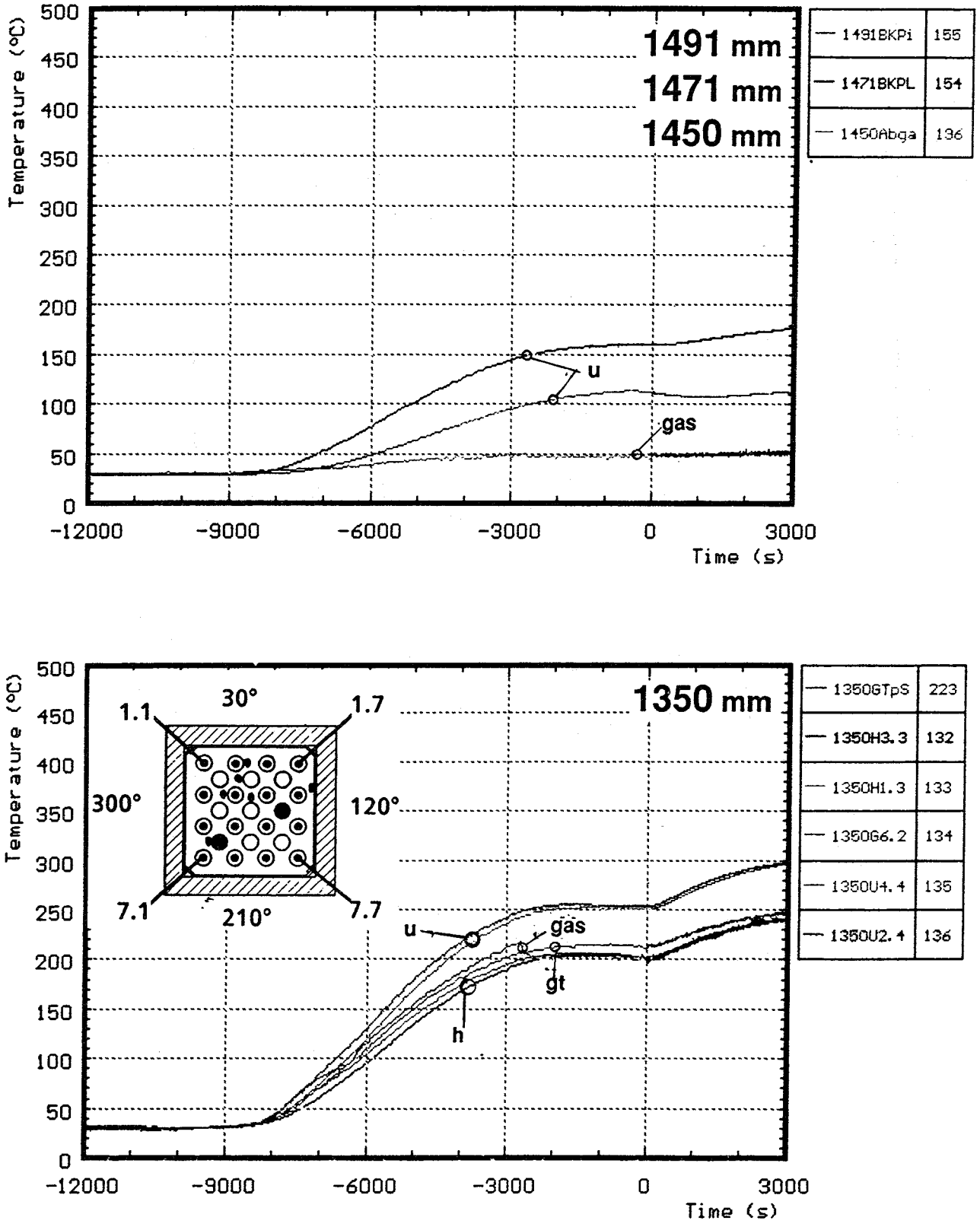

Fig. A15: Temperatures at fixed elevations; pre-heat phase (CORA-13)

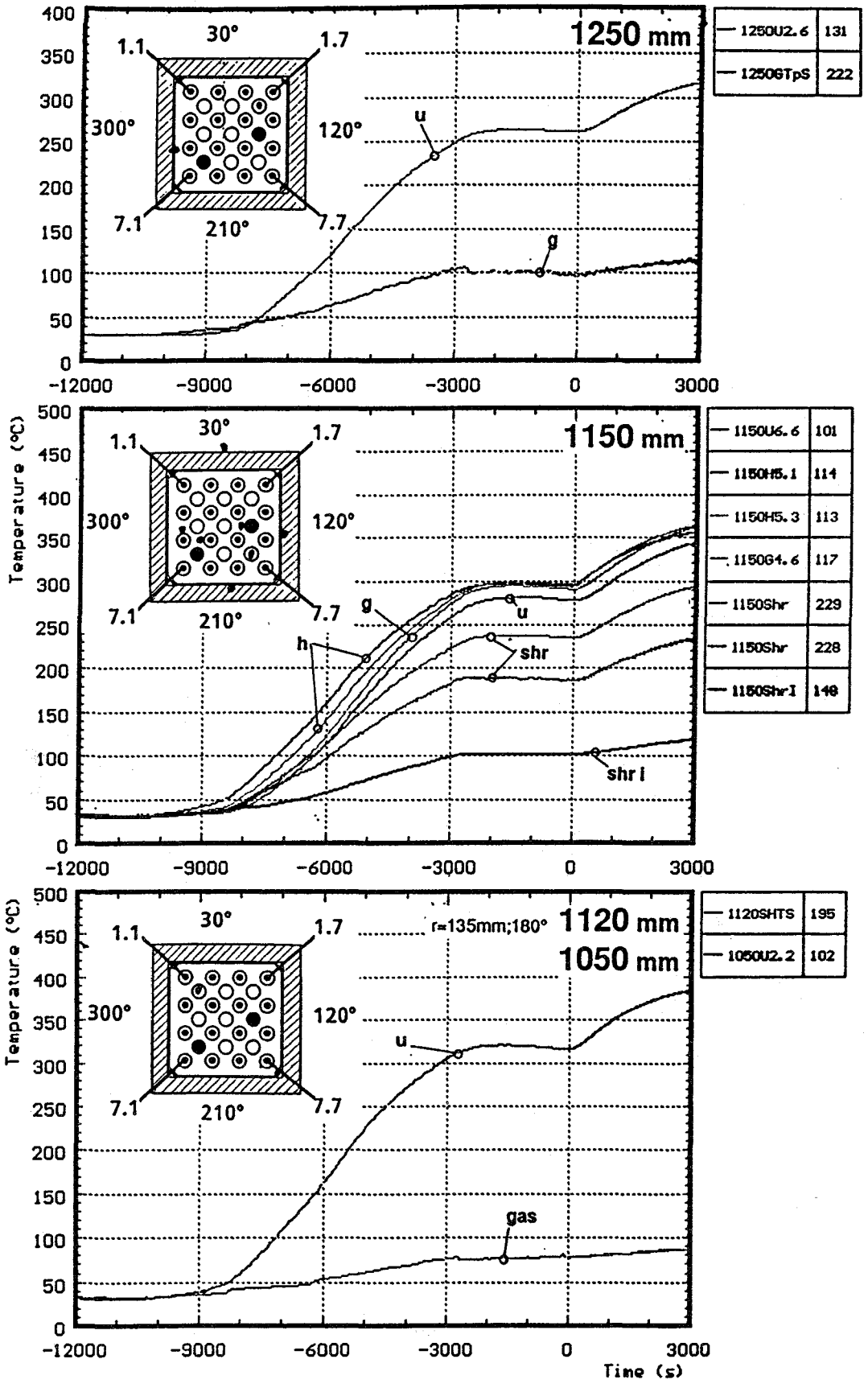

Fig. A16: Temperatures at fixed elevations; pre-heat phase (CORA-13)

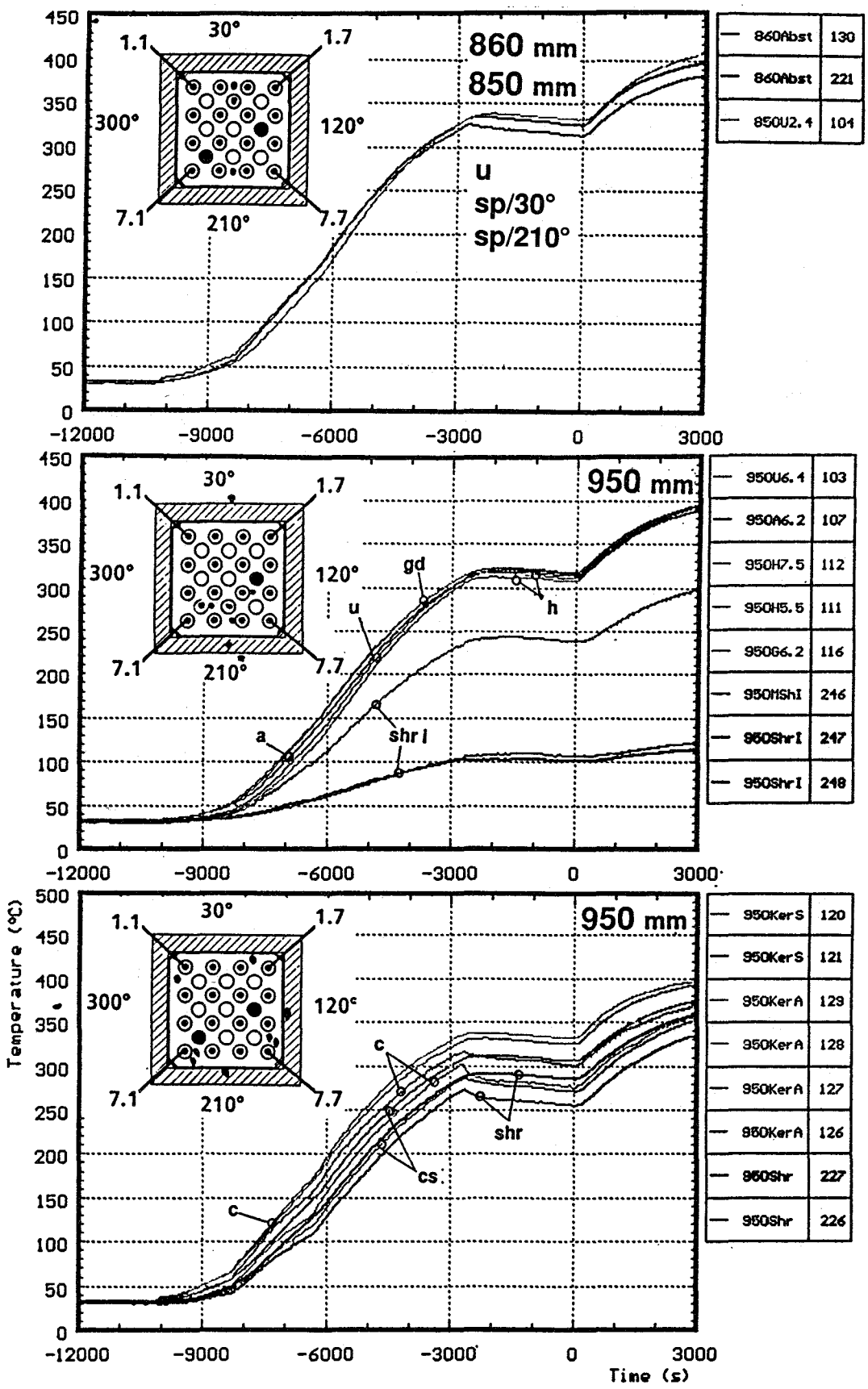

Fig. A17: Temperatures at fixed elevations; pre-heat phase (CORA-13)

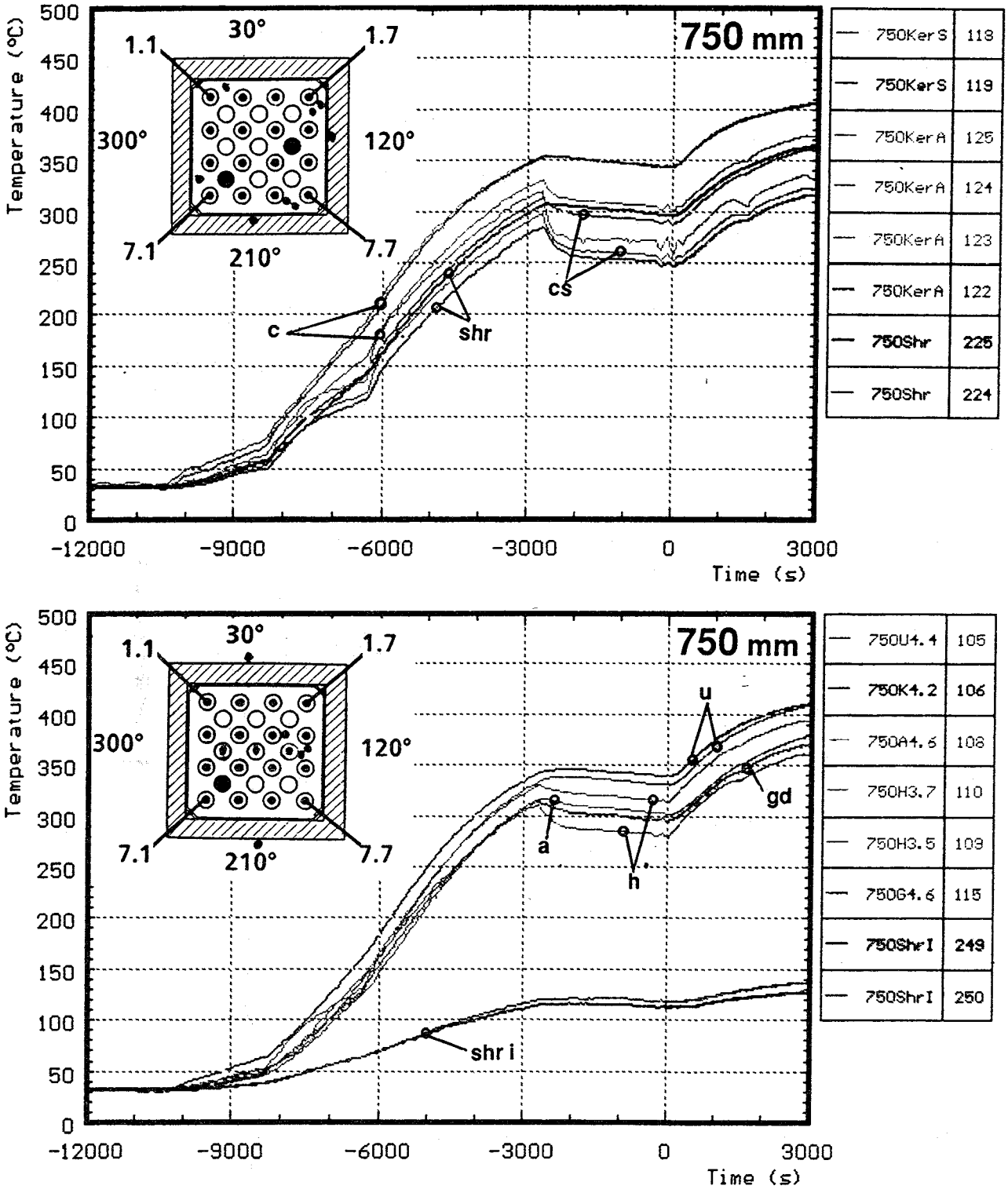

Fig. A18: Temperatures at fixed elevations; pre-heat phase (CORA-13)

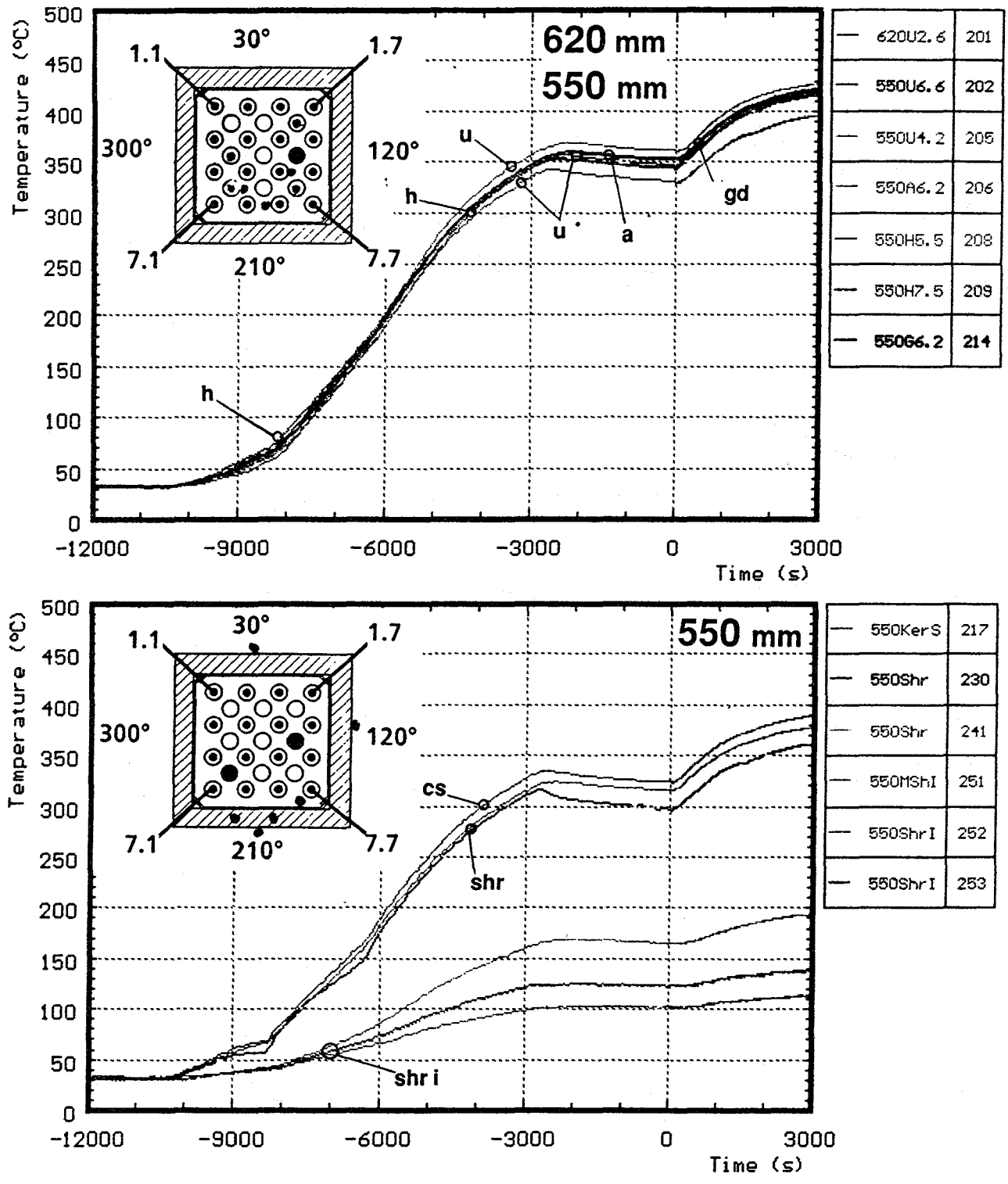

Fig. A19: Temperatures at fixed elevations: pre-heat phase (CORA-13)

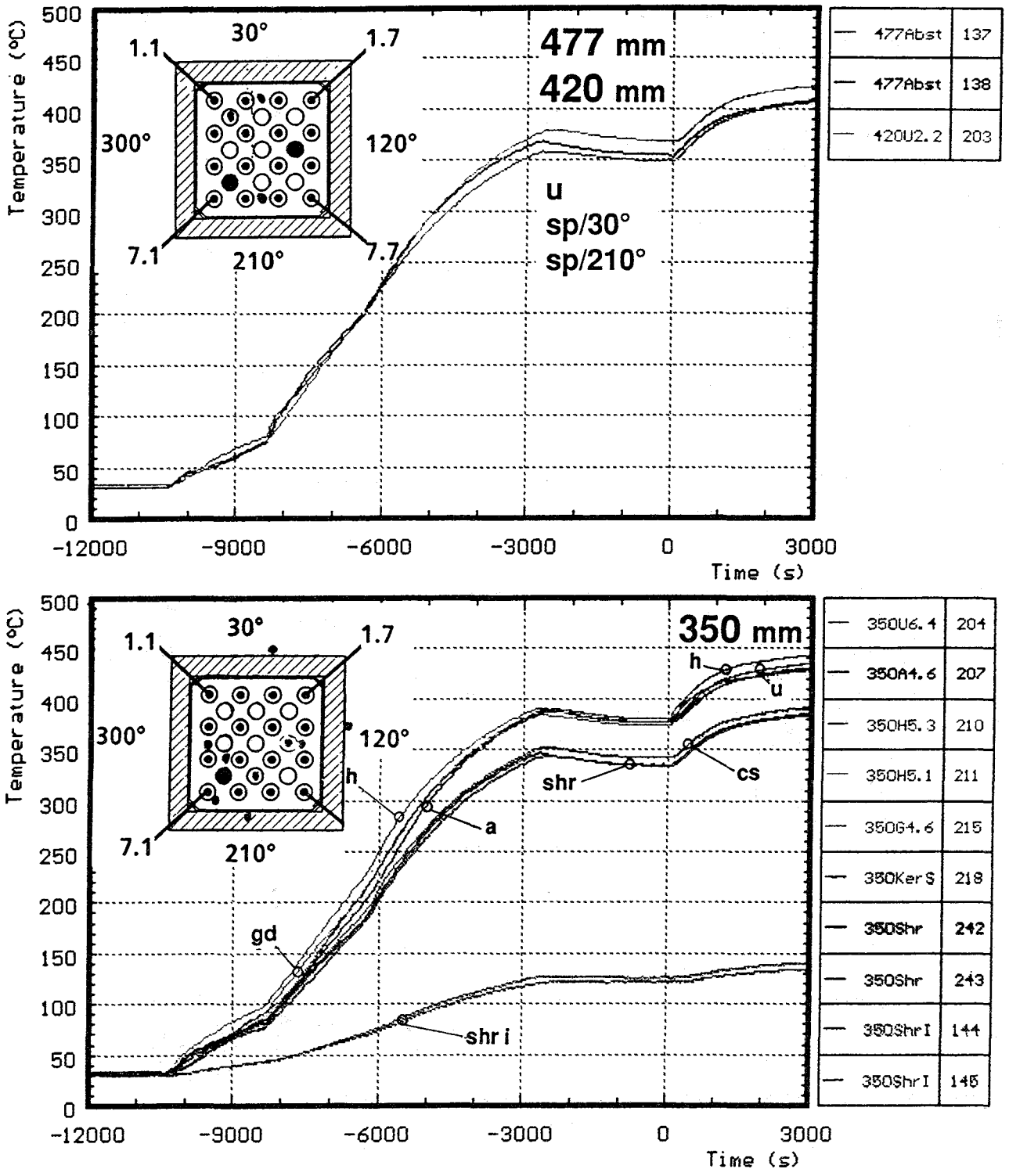

Fig. A20: Temperatures at fixed elevations; pre-heat phase (CORA-13)

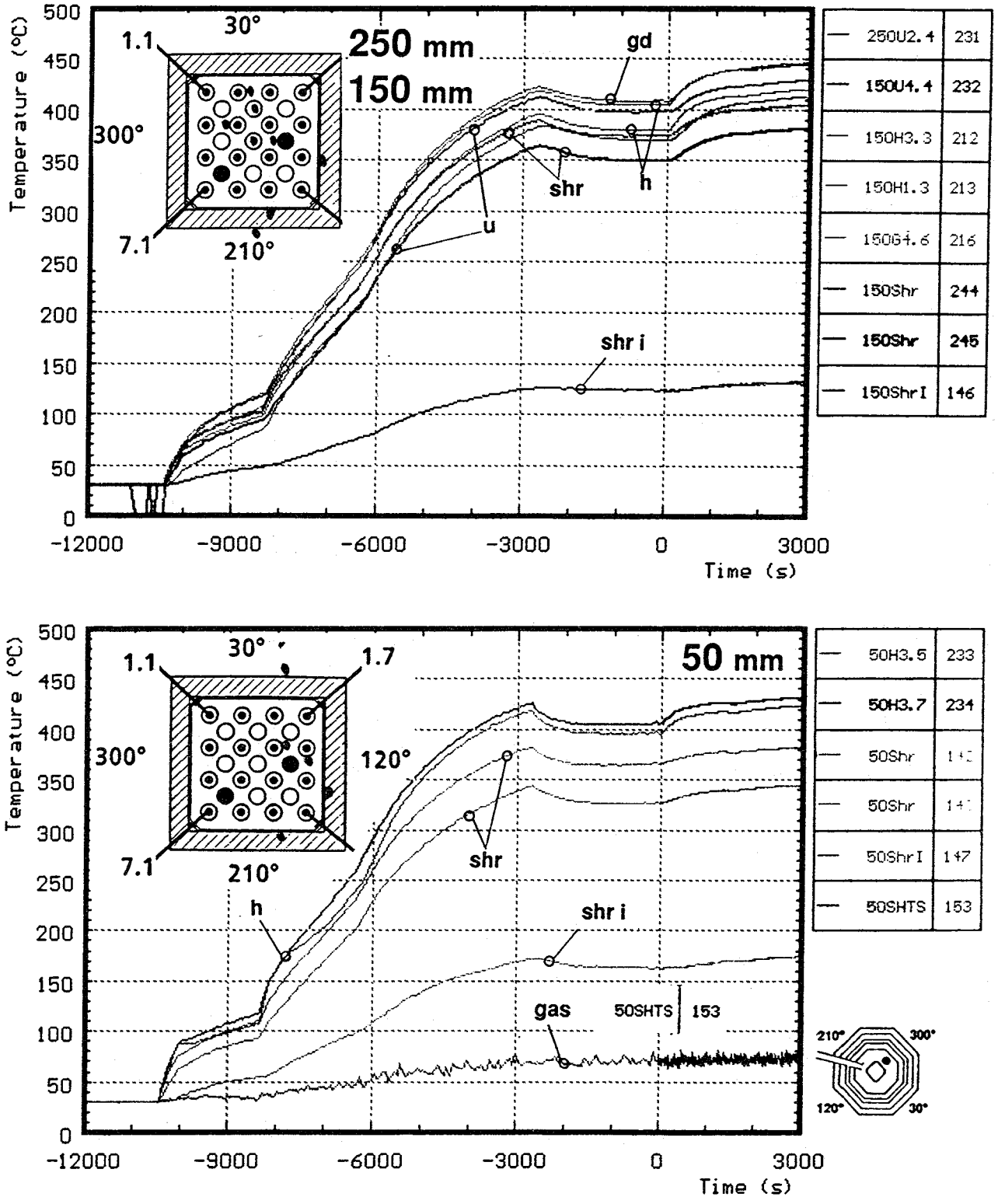

Fig. A21: Temperatures at fixed elevations, pre-heat phase (CORA-13)

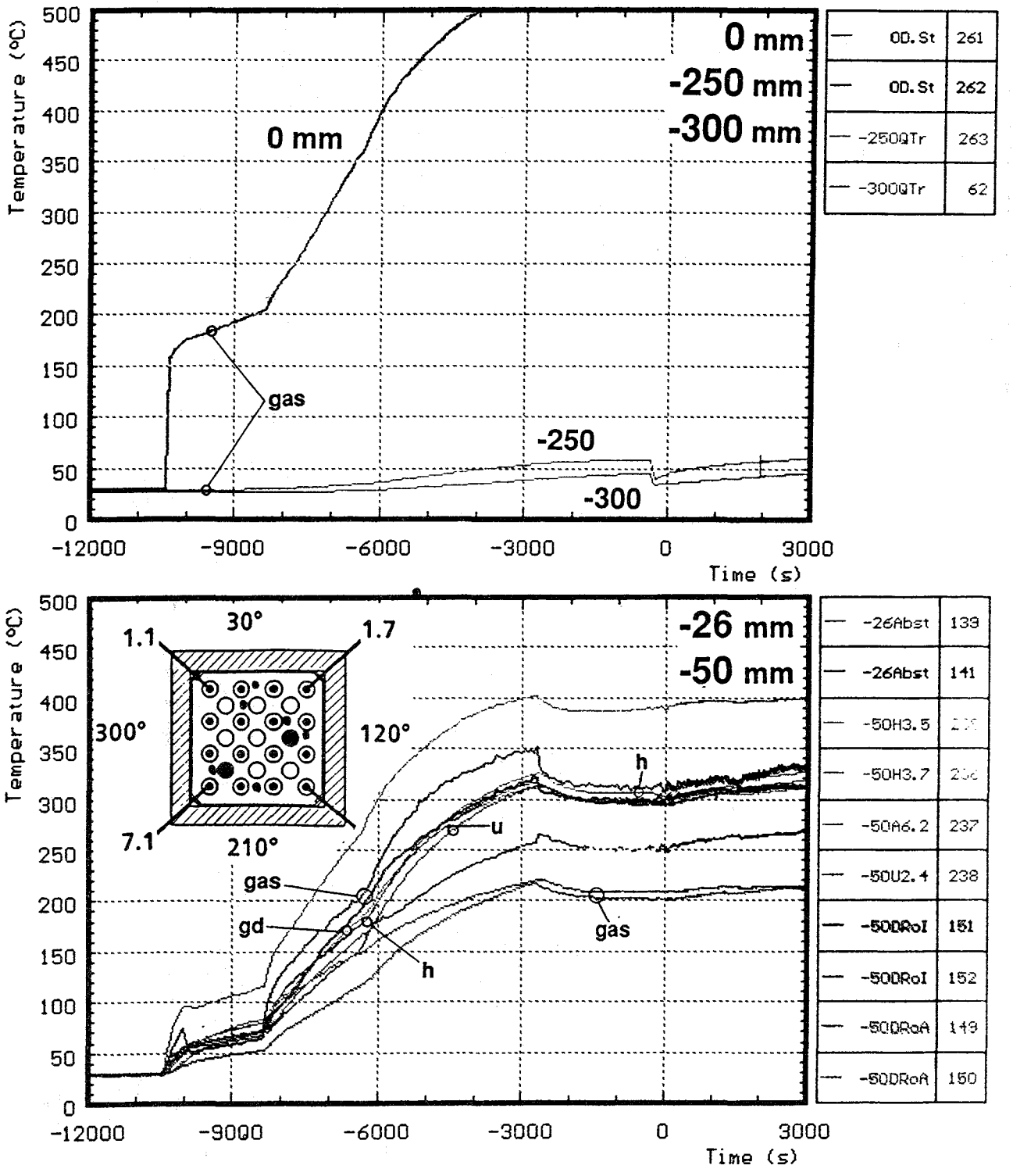

Fig. A22: Temperatures at fixed elevations; pre-heat phase (CORA-13)

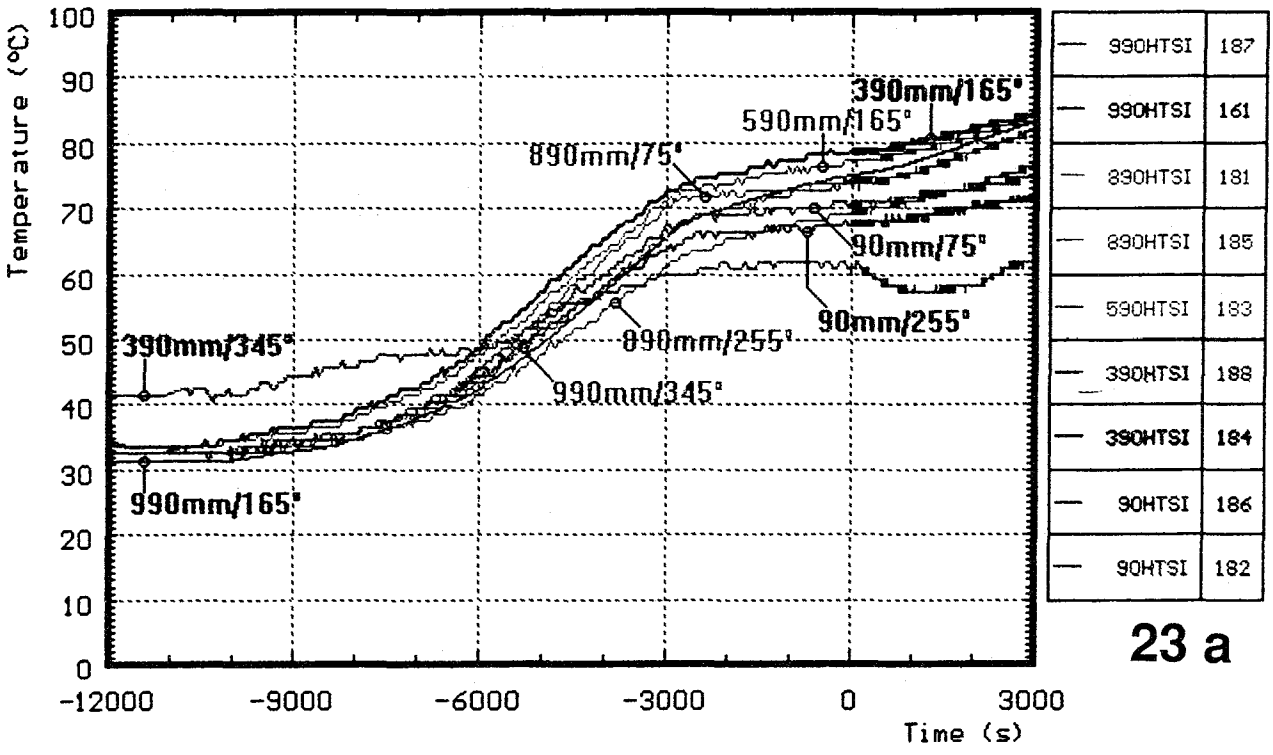

23 a

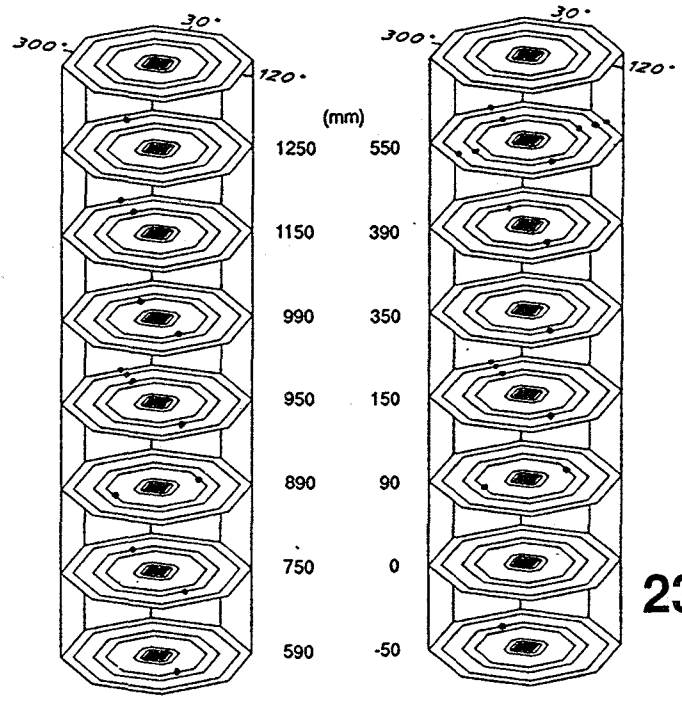

23 b

Fig. A23: Temperatures in the HTS; (a) measurements at 153 mm radius, pre-heat phase, (b) Schematic of TC locations (CORA-13)

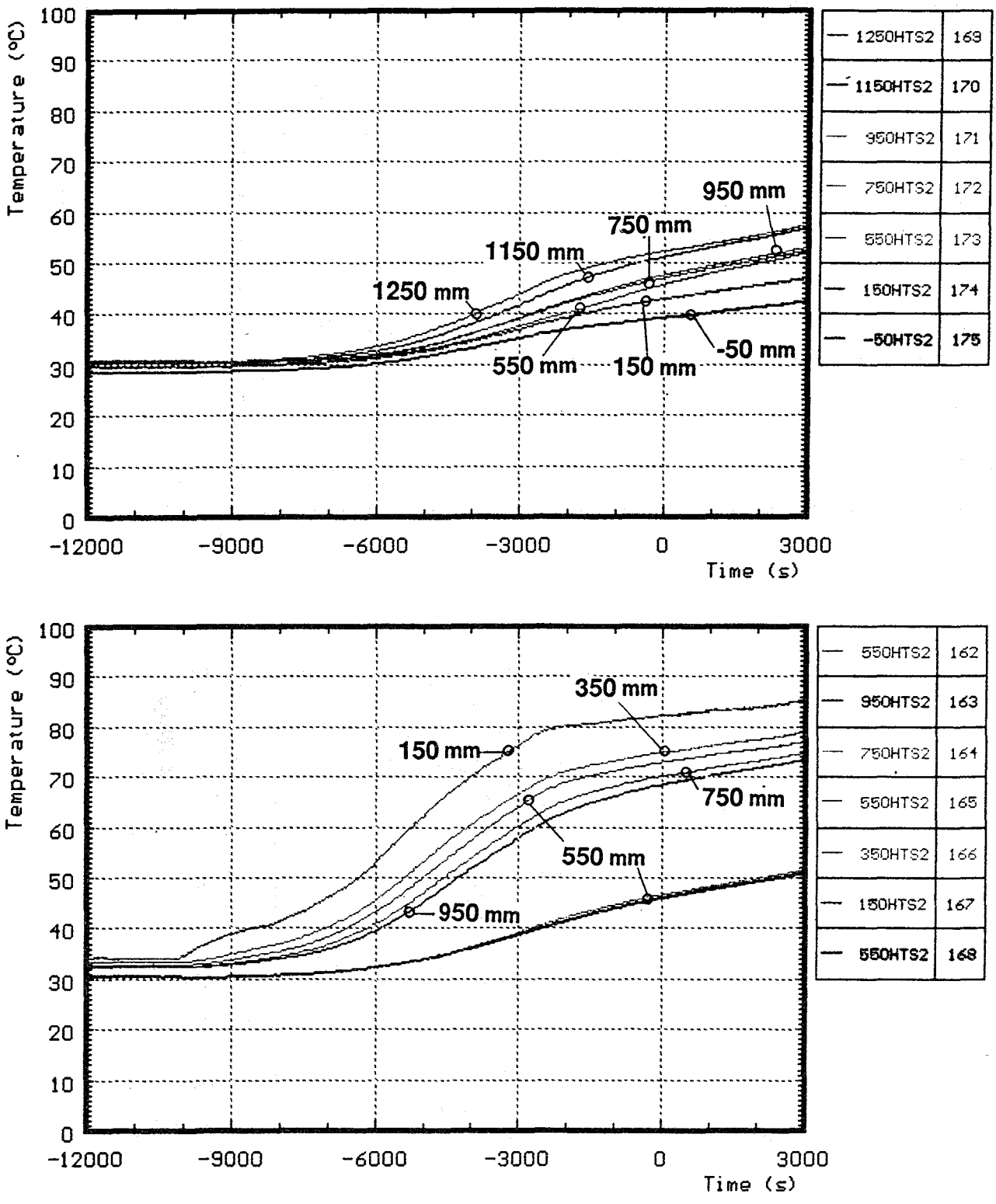

Fig. A24: Temperatures in the HTS; 192 mm radius; pre-heat phase (CORA-13)

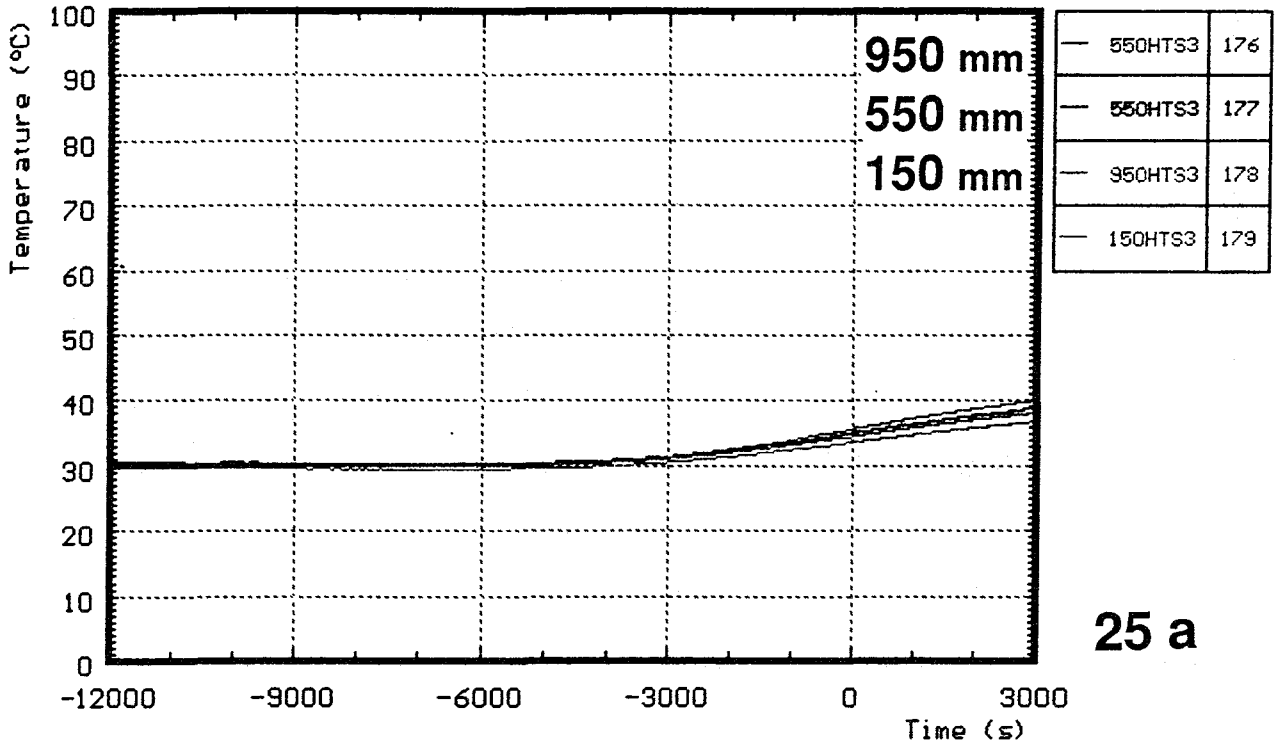

25 a

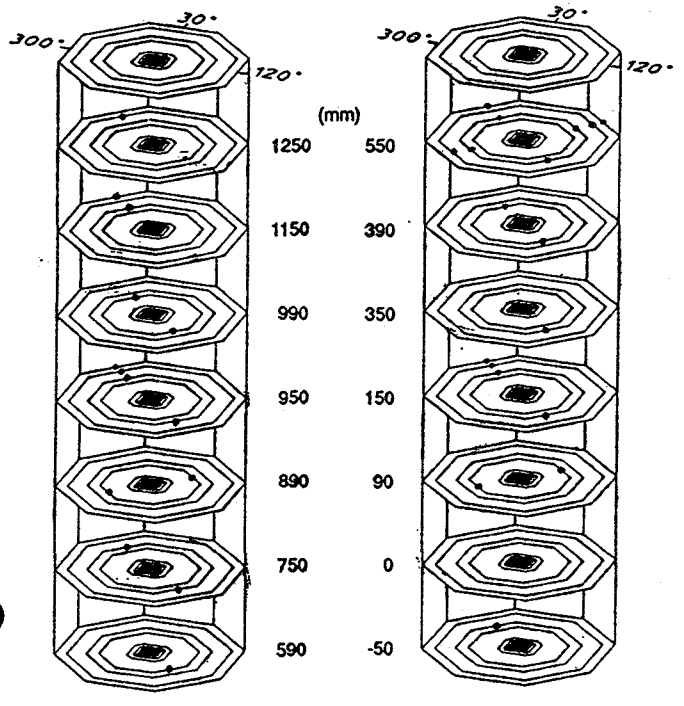

25 b

Fig. A25: Temperatures in the HTS; (a) measurements at 255 mm radius; pre-heat phase (CORA-13) (b) Schematic of TC locations

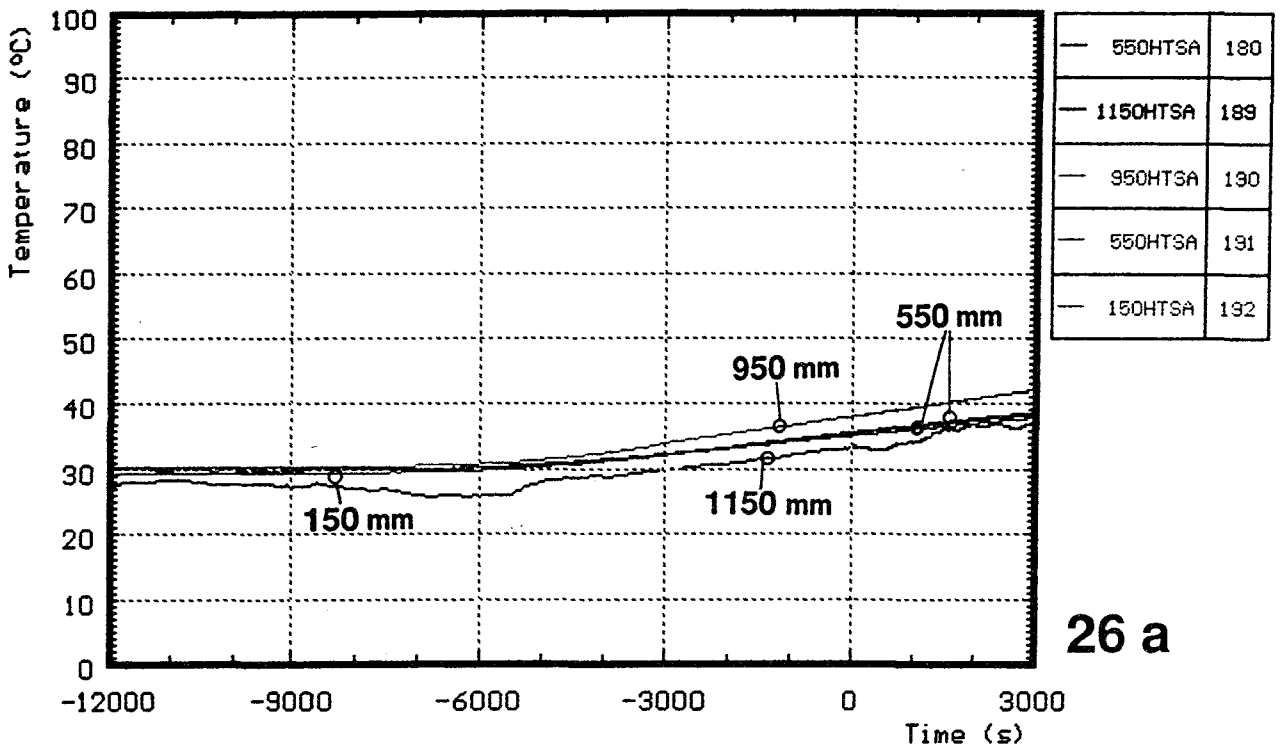

26 a

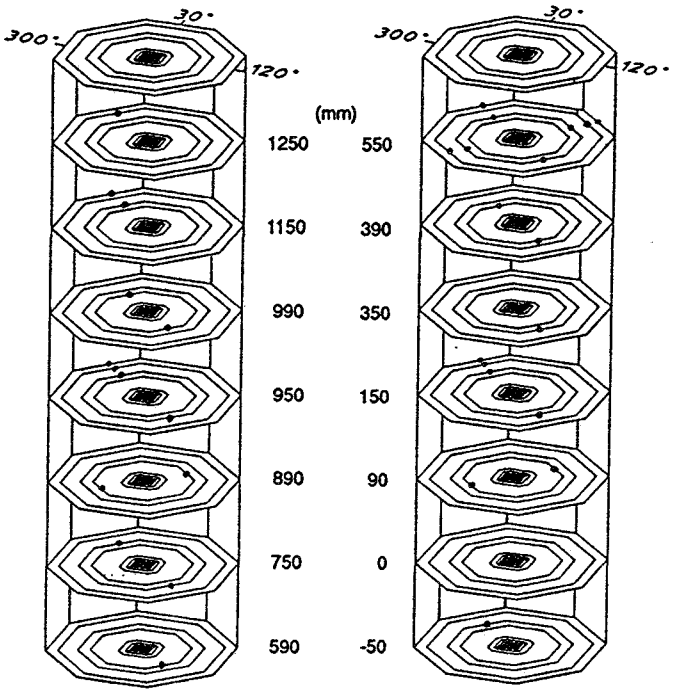

26 b

Fig. A26: Temperatures in the HTS; (a) measurements at 293 mm radius, (pre-heat phase CORA-13), (b) Schematic of TC locations